Modélisation du comportement hydromécanique des réservoirs fracturés à double porosité et double perméabilité.

Hong Lam Dang

UNIVERSITÉ D'ORLÉANS

ÉCOLE DOCTORALE
ENERGIE, MATERIAUX, SCIENCES DE LA TERRE ET DE L'UNIVERS

LABORATOIRE PRISME

THÈSE présentée par :

Hong Lam DANG

Soutenue le : **21 février 2018**

pour obtenir le grade de : **Docteur de l'Université d'Orléans**

Discipline : Génie Civil

A hydro-mechanical modeling of double porosity and double permeability fractured reservoirs

THÈSE dirigée par :

Dashnor HOXHA	Professeur, Université d'Orléans

RAPPORTEURS :

Philippe COSENZA	Professeur, Université de Poitiers
Jian-Fu SHAO	Professeur, Université de Lille 1

JURY:

Jian-Fu SHAO	Professeur, Université de Lille 1, Président/Rapporteur
Philippe COSENZA	Professeur, Université de Poitiers, Rapporteur
Kun SU	HDR, TOTAL, Examinateur
Sylvie GENTIER	HDR, BRGM, Examinateur
Dashnor HOXHA	Professeur, Université d'Orléans, Directeur de thèse
Duc Phi DO	MCF, Université d'Orléans, Co-encadrant

ACKNOWLEDGEMENT

Foremost, I would like to express my sincere gratitude to my advisors Prof. Dashnor HOXHA and Dr. Duc-Phi DO at the University of Orleans for the interesting topic and for their patience, motivation, enthusiasm, and immense knowledge. Their guidance helped me in all the time of research and writing of this thesis.

Besides my advisors, I would like to thank the rest of my thesis committee: Prof. Philippe COSENZA at the Univeristy of Poitiers, Prof. Jian-fu SHAO at the Univerisity of Lille 1, Dr. Sylie GENTIER at the BRGM and Dr. Kun SU at the TOTAL for their encouragement, insightful comments, and hard questions.

My sincere thanks also to Dr. Giap NGUYEN at the University of Orleans, Prof. Thomas WICK at the University of Leibniz and all members in the DEAL.II developer for supporting me on the open source code C++ and DEAL.II. I also thank my fellow labmates in the Civil Engineering team, PRISME laboratory for the stimulating discussions and for all the fun we have had in the last years.

Last but not least, I would like to thank my family: my wife, my daughter and my son for giving birth to me at the first place and supporting me spiritually throughout my life.

CONTENTS

LIST OF FIGURES

LIST OF TABLES

ABSTRACT

Fractured rock masses modeling is a issue in many field of industry including but not limited to oil and gas exploitation. In the literature, fractured rock masse is in many cases recognized as double permeability medium in which fracture network provides the primary permeability and rock matrix plays as the second one. The idea of dissociation of flow inside the fracture network and the matrix, the double permeability, is still challenged for fractured reservoirs. Numerous contributions on this issue have been presented in the past could be cast in two main approaches: continuum media approach and discontinuum approach. Each approach has its advantages and limitations. To overcome the limitation and to take advantage of these two approaches, the Embedded Fractured Continuum Approach (EFCA) which borrows the concept of continuum models and also incorporates the effect of explicit fractures is considered in this thesis. The principal idea of this approach lies on the concept of fracture cell representing a porous medium that has their own properties calculated from the properties of porous matrix and fractures intersecting it.

The development in this work was conducted by using the library source code DEAL.II https://www.dealii.org/. The accuracy of EFCA was investigated through different verifications. Through some applications: determination of effective hydro-mechanical properties of an actual site, estimation of well production in which necessary fractures are modeled explicitly, we demonstrate the performance of the EFCA in the modeling fractured rock masses as well as the effect of double porosity and double permeability on behaviours of fractured reservoirs.

Keywords: *fractured reservoirs, fracture network, hydro-mechanical modeling, double porosity, double permeability, fracture cell, embedded fractured continuum approach, finite element method, DEAL.II, hanging node.*

RÉSUMÉ

La modélisation des massifs rocheux fracturés est un problème important dans de nombreux secteurs industriels, y compris, mais sans s'y limiter à l'exploitation pétrolière et gazière. Dans la littérature, les roches fracturées sont reconnues comme des milieux à double porosité et double perméabilité dans lesquels le réseau de fractures fournit la perméabilité primaire et la matrice rocheuse la perméabilité sécondaire. L'idée de la dissociation de l'écoulement à l'intérieur du réseau de fractures et de la matrice, la double perméabilité, est toujours contestée pour les réservoirs fracturés. De nombreuses contributions sur cette question ont été présentées dans la littérature et les méthodes utilisées pourraient être classées dans deux approches principales : approches continues et discontinues. Chaque approche a ses avantages et ses limites. Pour surmonter les limites en gardant les avantages de ces deux approches, une approche nommée Embedded Fracture Continumm Approach (EFCA) qui emprunte le concept du modèle continu et intègre également l'effet des fractures explicites est considérée dans cette thèse. L'idée principale de cette approche repose sur le concept de la « cellule fracturée » représentant un milieu poreux qui a ses propres propriétés calculées à partir des propriétés de la matrice poreuse et des fractures qui la traversent. Le code de calcul développé dans le cadre de ce travail est basé sur la bibliothèque source DEAL.II https://www.dealii.org/. L'exactitude de l'EFCA a été étudiée à travers différents tests. Plusieurs applications traitées dans ce travail comme la détermination des propriétés hydro-mécaniques effectives d'un site réel, estimation de la production de puits dans laquelle les fractures sont modélisées explicitement, démontrent la performance de l'EFCA dans la modélisation des roches fracturées ainsi que l'effet de la double porosité et de la double perméabilité aux comportements des réservoirs fracturés.

Mots-clés: réservoirs fracturés, réseau de fractures, modélisation hydromécanique, double porosité, double perméabilité, cellule de fracture, approche du continuum fracturé intégré, méthode des éléments finis, DEAL.II, nœud suspendu.

GENERAL INTRODUCTION

In the context of oil field recovery, waste disposal, CO2 storage, geothermal exploitation, a geologic reservoir represents a geological massif whose porous space is susceptible to deserve as a storage for fluids. For these reservoirs, a huge amount of fluid is trapped in natural porous and fractured rocks. Fractures make the flow in reservoir quite complex and significantly impact the production rate as well as elapsed time on oil recovery or geothermal sources. The porosity of the matrix constitutes the primary porosity and the essential storage capacity of reservoir while the capacity storage of fractures represents only some fraction of the total porosity. Likewise, the hydraulic conductivity of such fractured reservoirs is composed by the conductivity of the rock matrix (pores and their connectivity) and the conductivity of cracks/fractures; the later one is of some orders greater than the former. The idea of dissociation of flow inside the fracture network from that of the matrix is first proposed by Barenblatt and Zheltov (1960) and almost simultaneously by Warren and Root (1963). Since, the double permeability system is still used as a common nomination for fractured reservoirs.

Albeit a huge number of studies on fractured reservoirs in the past, their modeling is yet a challenging and dynamic research topic, with two principal trends grouping continuum and discontinuum approaches.

Following the first approach the effect of fractures (double porosity/double permeability) is considered implicitly to reservoirs by equivalent parameters of the effective media (Royer et al., 2002; Marmier, 2007). The problem is then solved as a problem of effective media using various techniques of upscaling. This approach allows solving large scales problems with high densities of fractures. However, their results may be sensitive to the domain's size especially when the studied domain is smaller than the representative elementary volume. Otherwise, this approach cannot capture correctly the behaviour of fractured reservoir particularly near well and hence the well productivity may be different from reality. A particular form of continuum approach is dual-continued model in which the fractures and the porous matrix are represented as two distinct and interacting continua, one consisting of the network of fractures and the other of the porous blocks (Kazemi et al., 1976; Bibby, 1981; Huyakorn, 1983; Arbogast, 1993; Karimi-Fard and Firoozabadi, 2001; Gong, 2007). The main drawbacks of the dual-porosity model are the limitation of its use only for conditions when the sugar-cube representation of fractured reservoirs is acceptable and the difficulties to evaluate the transfer function between matrix and fractures.

In the second approach the fractures network is taking into account explicitly by modeling the fractured medium as an assemblage of blocks (discrete elements) bounded by a number of

intersecting discontinuities (interface between blocks). Although this approach can better describe the behaviour of fractured medium at small scale, it can be very expensive on computer memory and time simulation particularly for the problem at large scale. The main issue for this approach is the reproduction by numerical models of the complexity of in field fractures. In fact, because of the complexity and variation of fracture properties at a given site, the statistics of geometric characteristics and the properties of fractures/cracks are issued from limited and potentially biased field measurements, (e.g. one-dimensional (1D) borehole imaging or two-dimensional (2D) outcrop mapping). The challenge here is not only how to input a great number of fractures in to model but also the conceptual model to express fracture network and its connectivity. Numerous studies in the past which used low-dimensional element (Bruel, 1995; Watanabe, 2011; Watanabe et al 2000, 2012; Taleghani, 2009; Mohammadnejad, 2013, Blum et al., 2003, 2005; Min and Jing, 2003; Min et al., 2004a, 2004b, 2005; Eloranta 2000; Anderson et al., 2005, Baghbanan 2008) to express fractures in porous medium. This method has advantages of express fractures with a reduced number of cells as compared to the equidimensional elements (or called instructed grid) (Tatomir, 2007; Monteagudo et al., 2011). However, this method may be difficult to be applied for complex behaviours such as cracking propagations.

To overcome the limitations as well as to take advantage of these two approaches, another method which borrows the concept of continuum models and also incorporates the effect of fractures explicitly is considered in this thesis work. The principal idea of this approach (called Embedded Fractured Continuum Approach, EFC approach) lies on the concept of fracture cell which represents a cell in grid mesh intersected by one or many fractures. Due to the presence of fractures, the properties of fracture cell which are no longer ones of the porous matrix will be determined as properties of an equivalent porous medium (porous matrix and fractures). This approach was studied and applied successfully for flow problems (Svensson, 2001; Lee et al., 2010; McKenna & Reeves, 2006; Reeves et al., 2008a, b; Botros et al., 2008; Li & Lee 2008; Moinfar 2013; Shakiba, 2014; Xu 2015; Sakhaee-Pour & Wheeler, 2016; Gong, 2016, Yan et al. 2016). However, coupled hydro mechanical modeling is still challenging and there are relatively few studies (Moinfar, 2013; Moinfar et al., 2013; Figueiredo et al., 2015, 2017). Principal features which were not studied in literature are evaluation of accuracy of EFC approach for inclined fractures as well as coupled hydro mechanical behaviour of fractures.

In this context, developing a new home made numerical code for coupled hydro mechanical modeling for not only fractured reservoirs but also for heterogeneous porous medium is of great importance, allowing to add complex features in further studies. The open source library used as a base for developing the FEM software for EFC implementation is

Differential Equation Analysis Library (DEAL.II) (Bang and Kanschat, 1999; Bang et al 2007) because of some its advantages such as a common versatile environment (C++), many available documents, strong mathematical tools in solving equations and existing works on phase field method implemented (Wick et al, 2014; Wheeler et al, 2014; Heister et al, 2015; Mikelic et al 2014, 2015; Lee et al 2016).

The main objective of this thesis ***is to develop, implement and evaluate an approach for modeling of hydromechanical behaviour of large scale fractured porous rock masses/reservoirs***. For that, based on DEAL.II library, the modules for modeling HM behaviour porous media is firstly performed. While modeling of simple hydraulic or simple mechanical behaviour of continuous media in DEAL.II, is an easy task, there is no coupling HM approach already implemented and the above cited problems are solved separately.

As a first step to achieve the main objective, the coupling of hydraulic and mechanical response of porous media must be performed as well as a very flexible input data mechanism should be adopted/adapted. As a first result a FEM code is developed, making possible input of a variety of data such as isotropic and transversely isotropic material, heterogeneous media properties following a given spatial distribution of properties, as well as a variety of calculation options: mechanics only, hydraulic only or hydro mechanical coupling. In particular, the input should be flexible enough to allow the description of heterogeneous materials given a spatial distribution of material properties.

As a second step towards the main objective, the fracture /discontinuity modeling using alternative approach is performed. The difficulties of some commercial software to deal with dead bound cracks/fracture, were overpassed using some numerical strategies offered by the environment of DEAL.II. The crack propagation under stress and/or pore pressure are discussed in an exploration attempt of the effects of hydromechanical coupling on this phenomenon.

As a third step the EFC approach in framework of hydro mechanical coupling should be developed and implemented in DEAL.II. The problem of evaluation of properties of fracture cell as a function of matrix properties and fracture geometry and properties is a challenging task that will be performed using various theories and strategies.

Finally, in order to illustrate, in one hand the behaviour of double permeable/double porosity media, and in the other hand the capacities of the EFC and that of the developed software, a large scale, real fractured rock mass site is considered.

This dissertation is organized as follows:

Chapter 1 devotes to present the definition of fractured reservoirs, double porosity and also double permeability. Concept models for modeling fractured reservoirs are outlined.

Governing equations for hydro mechanical coupling of fractured reservoirs are summarized for isotropic and anisotropic material.

Chapter 2 overviews and summaries briefly the current status of the open source DEAL.II. The coupling of mechanical and hydraulic calculations developed in DEAL.II is presented here. Several verifications were carried out to ensure the correct of coupling process in the developed code.

Chapter 3 contains the implementation of embedded fracture continuum approach in DEAL.II including how to assemble fractures in to the code which is developed in the chapter 2 and the development of the EFC approach for fracture modeling. Hanging node and refined mesh method is selected and implemented in the developed code to enhance the accuracy, performance and robustness of the EFC approach. Some fundamental tests were done to evaluate the accuracy and to point out some items which affect to the accuracy of the EFC approach.

Chapter 4 presents an application of the versatile software to model a fractured rock mass and a fractured reservoir. The methodology of generation of fracture network is presented based on overall information of the well-known Sellafield site. The effective mechanical properties and permeability of fractured rock masses in which fracture network is introduced explicitly are calculated and compared to other available results conform again the accuracy, performance and robustness of the EFC approach. The effect of double porosity and double permeability of fractured reservoir through comparison results between two models: homogenized model and explicit fracture model will be highlighted in this chapter.

Finally, the general conclusions of the thesis point out the achievements as well as the further perspectives of this work.

CHAPTER 1: BIBLIOGRAPHIC STUDY ON HYDRO MECHANICAL MODELING OF FRACTURED RESERVOIR

1.1 Introduction of double porosity and double permeability fractured reservoirs

Significant oil and gas production is recorded from the various types of fractured reservoir (Saidi, 1987) as in the following examples: basement granite in Amarillo (Texas), Mara-la-Paz, (Venezuela); Jurassic metamorphic schists in Los Angeles area (California), Permian Siltstones in Spraberry (Texas), Ordovician carbonates in Scipio-Albion trend (Michigan), Oligocene-Miocene Asmari limestones in Iran and Iraq, Miocene Monterey Chert in Santa Maria district (California). Carbonate rocks commonly display various typologies of fractures, characterized by different statistical behaviours (Guerriere et al, 2013); for example, some fracture sets show a self-similarity of morphology whilst some others are size restricted. Fractures do also behave statistically significantly different with respect to spatial fracture distribution (e.g. random, clustered, and regular) and probability distribution of fracture aperture, length, orientation and location (figure 1-1a). Bear and Berkowitz (1987) distinguish between primary porosity (porosity of the rock matrix) and secondary porosity (porosity of fractures). The rock matrix provides the primary storage of fluid (or production) while fractures serve very little fluid and provide a high permeability (Moinfar et al., 2013). Such reservoirs are identified typically as double-porosity system.

In such fractured reservoirs, the fractures connect themselves and create a network. The permeability of fracture network system plays a role in the overall permeability of fractured reservoirs. The idea of dissociation of flow inside the fracture network and the matrix is first proposed by Barenblatt and Zheltov (1960), Warren and Root (1963). Double permeability system is still named for fractured reservoirs up to now.

Fractured reservoirs have been still received attention from oil and gas industry. A huge amount of hydrocarbon is trapped in natural fractured carbonate reservoirs. Fractures add complexity into reservoir flow and significantly impact the production rate and ultimate recovery (Lei, 2016). Albeit, plenty of studies in fractured reservoirs in the past, the modeling of fractured reservoir is still a challenging and dynamic research topic. In this context, fractured reservoirs are of a great interest in many fields of research: oil field prediction and recovery, CO2 storage, nuclear waste storage, hydraulic fracturing risk assessment and prediction (Figure 1-1b).

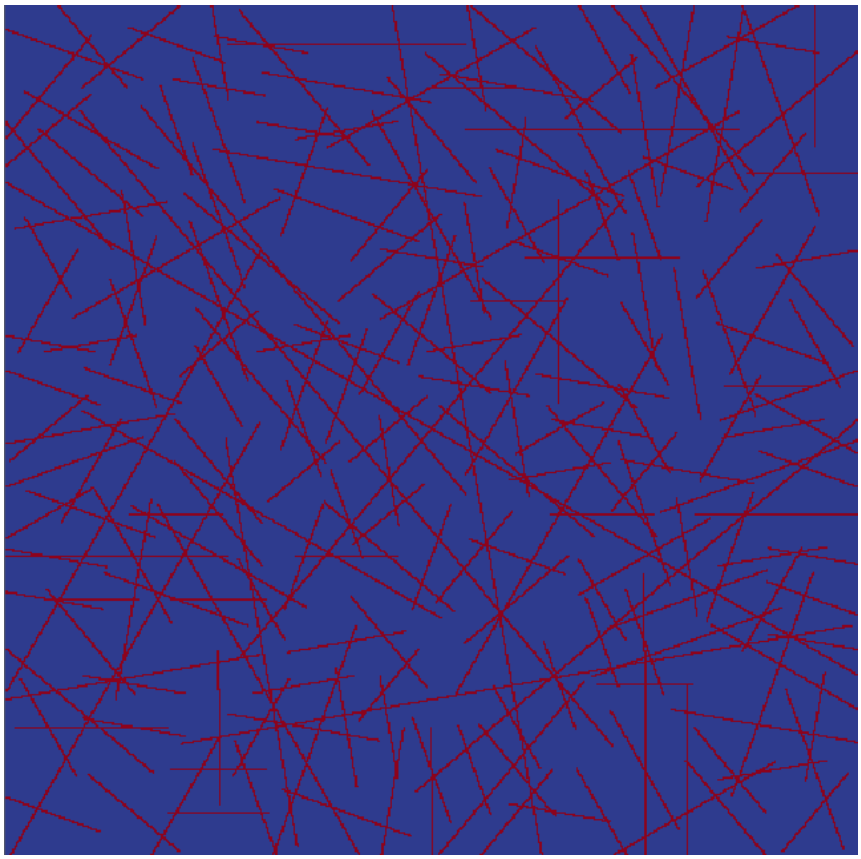

(a) An example of representative volume of fractured reservoirs

(Legend: red color denotes fractures and green color denotes matrix)

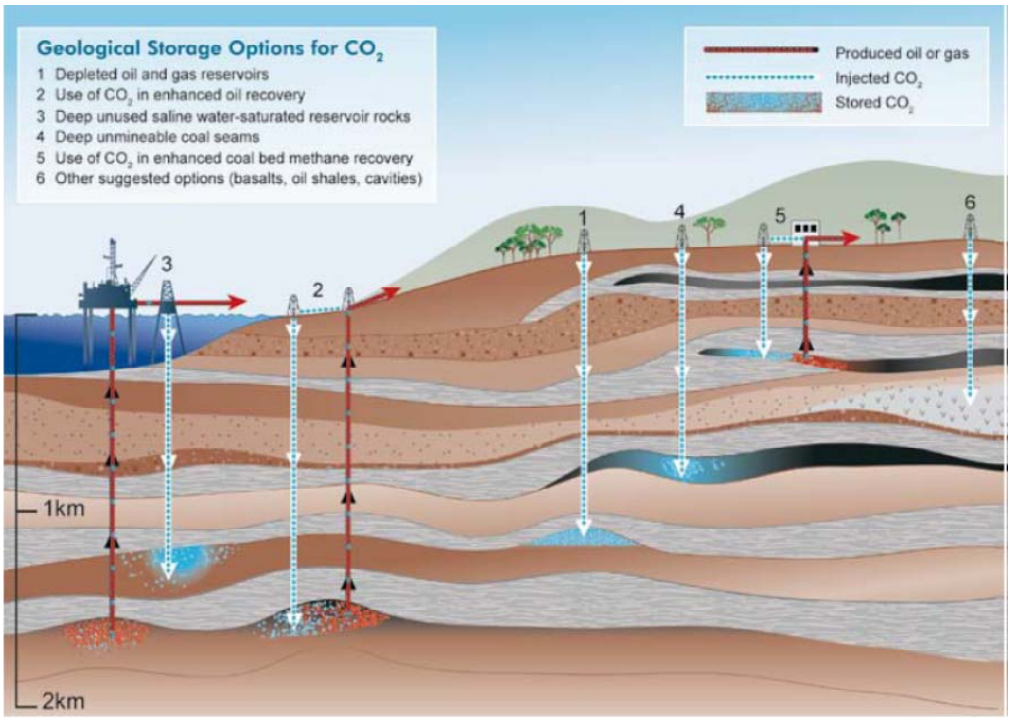

(b) Options for storing CO2 in deep underground geological formations (IPCC Special Report and Cook, 1999).

Figure 1-1: An example of representative volume of fractured reservoirs (a) and options for storing CO2 in deep underground geological formations (b)

1.1.1 Porous media

A porous medium is composed of a matrix (solid phase) and a porous space, the latter could eventually be filled by a fluid (Coussy, 2004). The connected porous space is the space through which the fluid actually flows and whose two points can be joined by a path lying entirely within it so that the fluid phase remains continuous. The matrix is composed of both a solid part and a possible occluded porosity, whether saturated or not, but through which no filtration occurs. The connected porosity is the ratio of the volume of the connected porous space to the total volume. In what follows the term 'porosity', used without further specification, refers to the entire connected porosity.

In the following we present several main assumptions adopted by Coussy (1995), Coussy (2004) which may be considered as the basic framework for development of the poroelastic models. Full version of assumptions is provided in above mentioned references

- The porous media is considered as a continuous and homogeneous solid-fluid mixture which consists of the matrix and the porous space filled fully or partially by fluids and the fluids can freely move through the connected pores. Accordingly, as illustrated in figure 1.2, any infinitesimal volume can be treated as the superimposition of two material particles.

  The first is the skeleton particle formed from the matrix and the connected porous space of fluid drained.

  The second is the fluid particle formed from the fluid saturating the connected porous space and from the remaining space without the matrix.

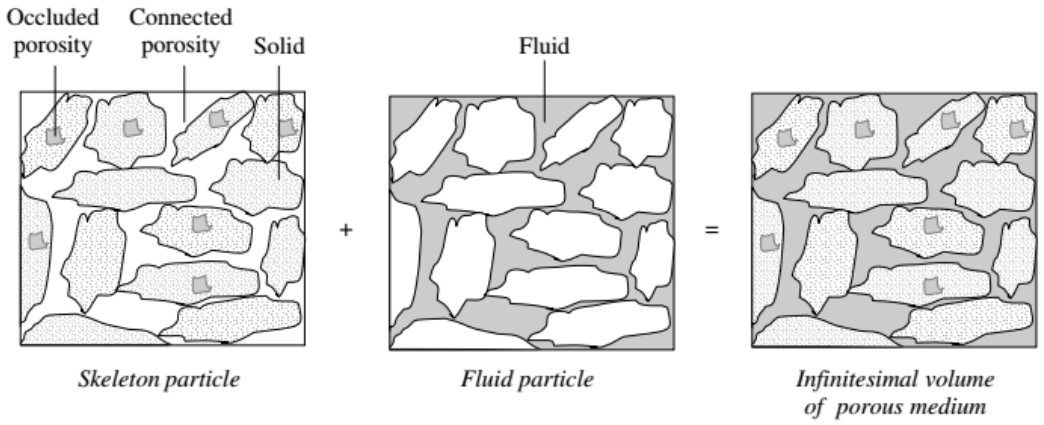

Figure 1-2: A schematic of the porous media idealization (Coussy, 2004)

- The strain-stress relations obey the small deformation theory and followed Hooke's law in elastic behaviour.
- The interstitial fluid flow is assumed to be laminar and can be described by Darcy's law

1.1.2 Fractures and fracture network

According to different points of view various definitions can be given, but from a strict geo-mechanical point of view a fracture is the surface in which a loss of cohesion has taken place (Van Golf-Racht, 1982). In general, two main kinds of fractures are fault and joint. A fracture in which relative displacement has occurred can be defined as a fault, while a fracture in which no noticeable displacement has occurred can be defined as a joint (Figure 1-3).

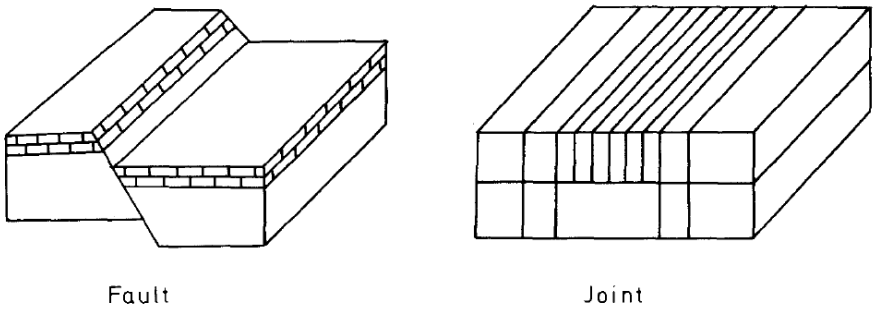

Figure 1-3: Schematic presentation of a fault and a joint in (Van Golf-Racht, 1982).

A fracture can also be defined, in a more general way, as the discontinuity which breaks the rock beds into blocks along cracks, fissures, joints or whatever they may be referred to as, and along which there is no displacement parallel with the planes of discontinuity (Van Golf-Racht, 1982). Basically, whether a fracture is considered a joint or a fault depends on the scale of investigation, but in general, that is called a fracture corresponds to a joint (Van Golf-Racht, 1982). Figure 1-4 is an example of fractures in which fractures can be found on the whole range of scales (Bonnet et al. 2001; Silberhorn-Hemminger 2002; Tatomir, 2007).

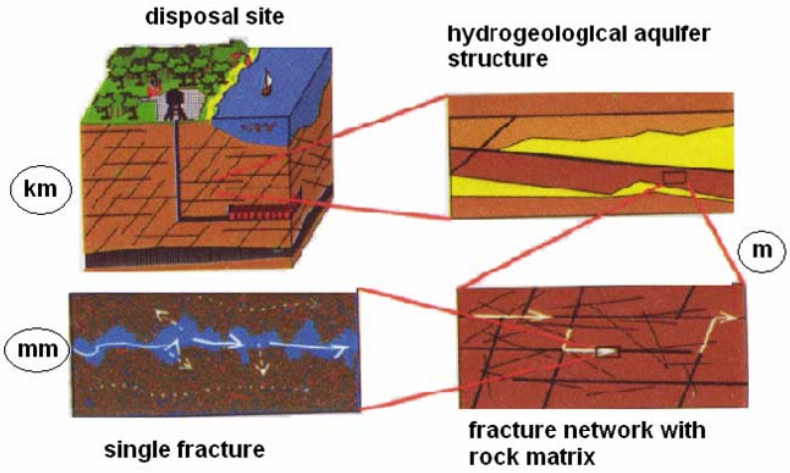

Figure 1-4: Fractures occurring on different scales (Silberhorn-Hemminger, 2002; Tatomir, 2007)

It is a challenging issue the understanding and modeling the impact of fractures to the hydromechanical properties (e.g. strength, deformability, permeability and anisotropy) of highly disordered geological formations (Zimmerman and Main, 2004). A variety of engineering applications including the extraction of hydrocarbons, the production of

geothermal energy, the remediation of contaminated groundwater, and the geological disposal of radioactive waste (Rutqvist and Stephansson, 2003) related to the presence of fracture on rock masses. Three main key issues on fractured rock characterization and modeling are summarized by Lei (2016) as below:

The first problem is how to characterize and represent the geometry complex three-dimensional (3D) discontinuity systems based on limited and potentially biased field measurements, e.g. one-dimensional (1D) borehole imaging or two-dimensional (2D) outcrop mapping (Dershowitz and Einstein, 1988). Fracture statistics are usually obtained from lower-dimensional observations with respect to density, trace lengths, orientation, spacing, and frequency. 2D or 3D synthetic discrete fracture networks (DFN) can be created stochastically (Long et al., 1985; Long and Billaux, 1987) and the DFN can be generated by conducting Monte Carlo simulations.

The second problem is how to take into account the discontinuous behaviours of rock media. These behaviours are the interaction of multiple discrete bodies (Jing, 2003), the fracturing and fragmentation of intact rocks (Hoek and Martin, 2014), the opening, shearing and dilation of rough fractures (Bandis et al., 1983; Barton et al, 1985), and the fluid flow through fractured reservoirs (Berkowitz, 2002), and the coupled hydromechanical or multi-physical processes (Rutqvist and Stephansson, 2003; Figueiredo et al, 2017).

The third issue concerns upscaling method in which the results of small scale modeling are used for large-scale simulation and application. Effective medium theory has been developed to estimate mechanical and hydraulic properties of fractured rocks (Long et al. 1982; Kachanov, 1992) on a homogenisation scale. However, in homogenization method, the geological system may not have any representative elementary volume due to the fractal and scaling of natural fracture patterns (Bonnet et al. 2001). Thus, other upscaling methods based on small-scale simulation results to predict multiscale, multiphysical properties of fractured rocks are used for engineering applications.

1.2 Modeling concepts of fractured reservoirs

The modeling of fractured rock masses in generally and fractured reservoirs in particular, could be performed using various approaches based on various concepts and assumptions such as continuum effective medium, dual porosity or/and dual permeability media, discrete fractures network or discrete fractures on a porous continuum media. Figure 1-5 shows the sketch of models as in Dietrich et al (2005)

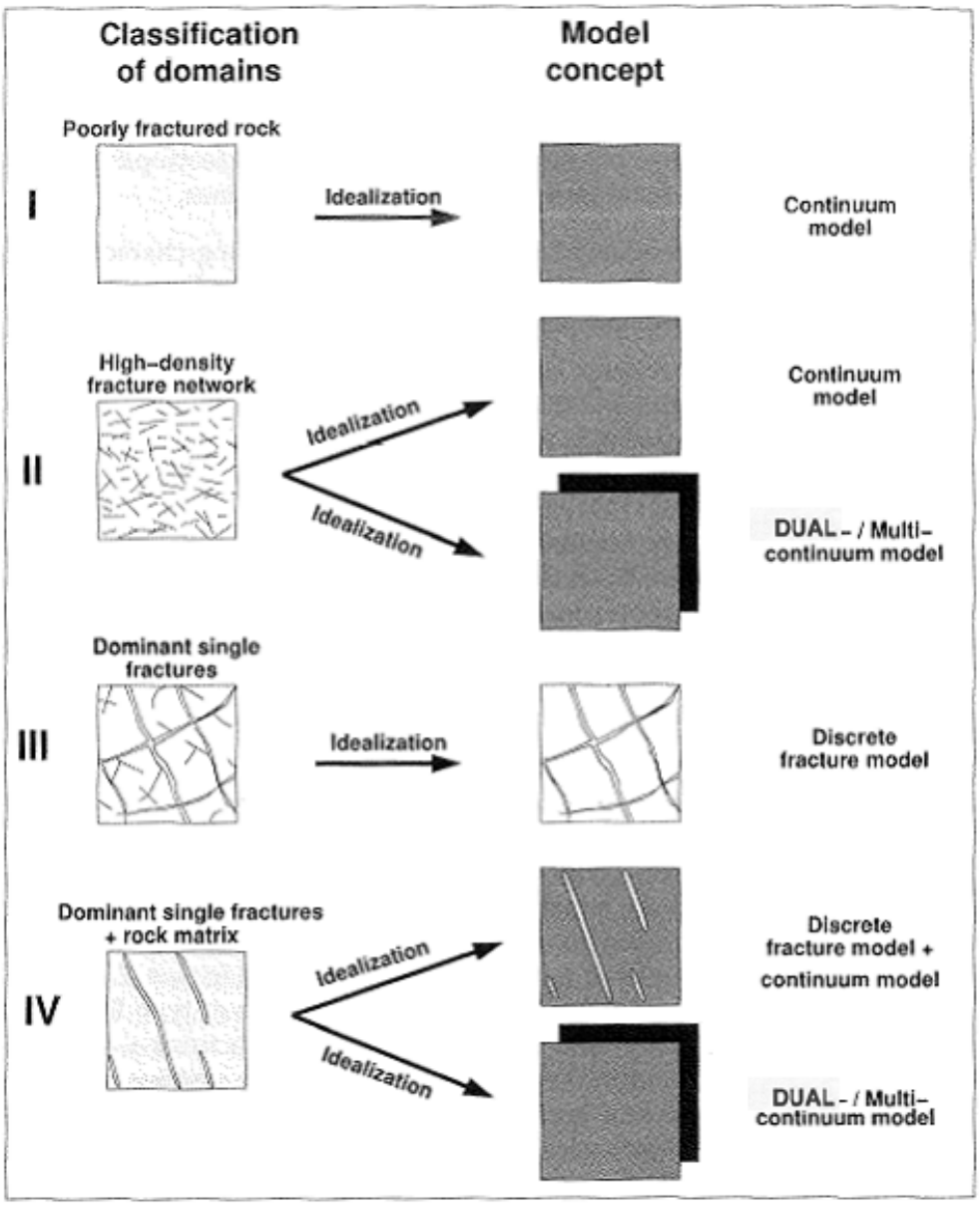

Figure 1-5: Model concepts for the description of fractured porous media (Dietrich et al, 2005)

Each model/approach is distinguished by how it takes into account the fracture density (or equivalent statistics), at which scales these fractures are considered and how the spatial and distribution of fractures is.

Depending on the kind of problem treated in one study, on the same rock masses various approaches could be followed (figure 1-6). For instance on the rock masses schematically presented in the figure 1-6 for a problem treated in cut-out A a continuum model could be used. For the cut-out B one could consider using a continuum model with an equivalent flow and transport properties or dual-porosity or/and dual-permeability model. The problems in cut-out C can be treated using a discrete fracture model, while for problems in cut-out D a combination of discrete fractures model and continuum model or dual continuum model could be a good approach

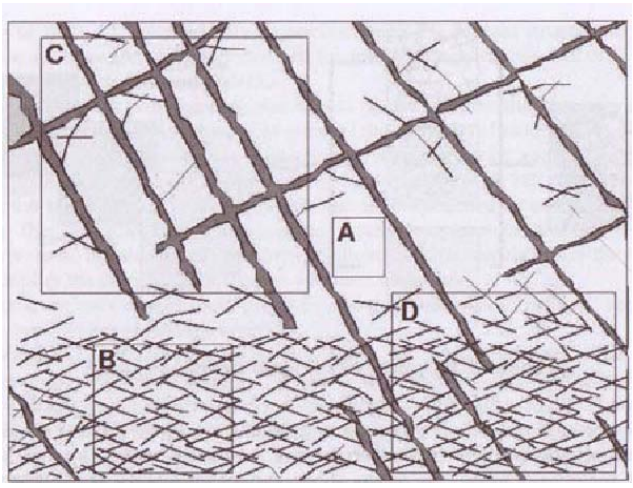

Figure 1-6: Fractured groundwater aquifer with different discontinuities (Silberhorn-Hemminger, 2002; Tatomir, 2007)

These modeling concepts are briefly described in the following. In general, the modeling one could distinguish two main trends in fractured rock modeling: equivalent continuum approach and discrete fracture approach.

1.2.1 Equivalent continuum approach

Averaged parameters for rock matrix and fractured systems are used in the equivalent continuum approach. The transport problem is transformed from the microscopic level to a macroscopic scale at which the problem is expressed in terms of averages of the microscopic quantities. The size of representative elementary volume (REV) must be much larger than the heterogeneity size and much smaller than the macroscopic length-scale. It means that an REV needs to be determined in an equivalent continuum approach (Royer et al., 2002; Marmier, 2007)

Two kinds of continuous models are usually used: single-continuum model and dual-continuum model.

+ *The single-continuum model:* the whole fracture porous domain is represented as an equivalent porous medium. The single-porous model (or single-continuum model) provides the accuracy, but it is not practical due to very large number of grids. A large number of grids are required because of the two different length scales (matrix size and fracture thickness). When the ratio of the two length scales are in a fractured system, the single-porosity approach becomes very inefficient numerically (Tatomir, 2007). Royer et al. (2002) presented a method of homogenization for upscaling by multiple scales expansions and obtained different macroscopic single-continuum transport models.

+ *The dual-continuum model:* the fracture porous media is represented as two distinct and interacting continua, one consisting of the network of fractures and the other of the porous blocks. The first idea which dissociates the flow inside the fracture network and the matrix;

and models the exchange between the two-media's using a transfer function is dual-porosity model from Barenblatt and Zheltov (1960), Warren and Root (1963) (figure 1-7). A complete set of equations for slightly compressible single-phase flow was written for both the fractures and the matrix by Barenblatt and Zheltov (1960), and transfer between them was assumed to occur at pseudo-steady state (Gong, 2007). Warren and Root (1963) presented a practical model for fractured systems in which a set of identical rectangular parallelepipeds, representing the matrix blocks, is separated by fractures. Kazemi et al. (1976) presented an extension of the dual-porosity model of Warren and Root (1963) to two-phase flow. For transport of contaminant, dual-continuum model has been employed in Bibby (1981) and Huyakorn et al. (1983). Despite of originally developed based on physical considerations, the dual-porosity model has since been derived rigorously using two-scale homogenization procedures (Gong, 2007) for example Marmier (2007) and Arbogast (1993) considered single and two-phase flow in uniformly fractured systems and showed that the dual-porosity description is recovered via homogenization.

The main advantage of dual porosity model is cheap computational time in compared with discretely fractures model. However, a number of approximations were commonly used in these models that are not always appropriate. For example, spatial variation within local matrix regions was neglected in many dual-porosity implementations; i.e., they modeled pressure and saturation as constant within the matrix (Gong, 2007). The disadvantage of the dual-porosity model is that they can be mainly used for sugar-cube representation of fractured media (Karimi-Fard and Firoozabadi, 2001). Another limitation is that the method cannot be applied to disconnected fractured media and cannot represent the heterogeneity of such a system. Another shortcoming is the complexity in the evaluation of the transfer function between the matrix and the fractures (Tatomir, 2007).

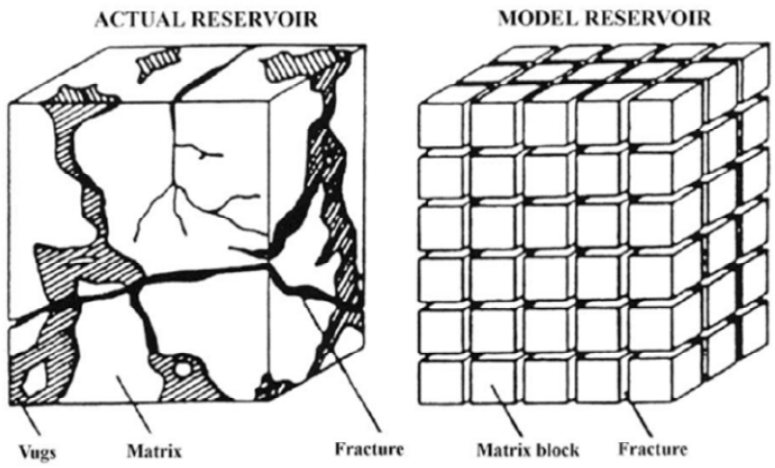

Figure 1-7: An idealized sugar cube representation of a fractured reservoir (Warren and Root, 1963).

A special case of continuum media approach is stochastic continuum modeling in which an equivalent homogeneous porous medium is obtained with a random spatial function of

regions (blocks) hydraulic conductivities (Niemi et al., 2000; Ohman and Niemi, 2003) due to the various scales of fractures, and their statistics distribution (density, trace lengths, orientation, spacing, and frequency). This approach is more applicable to densely fractured rock masses and larger scales. Limitations on the available data and computational resources promote the stochastic continuum approach as an alternative approach for modeling flow and transport in fractured media (Botros et al., 2008)

1.2.2 Discrete fractures approaches

Discrete fracture model is required when the continuum approach to the description of the transport problem is not applicable. In the discrete model, fractures are considered as discrete structures. This kind of modeling open the possibility to model flow and transport the process in a very similar way as it happens in the nature (Reichenberger et al. 2004). Fractures can be modeled as equidimensional elements (which implies very high demands on fracture network generation and the numerical tools for solving the resulting equation system) (Tatomir 2007), or lower dimensional elements (also referred in literature as mixed dimensional elements (Bruel (1995), Watanabe (2011) and Watanabe et al (2010, 2012)). Some of the literatures for the discrete fractured model have been reviewed in Sahimi (2011).

The Figure 1-8 shows an example of modeling fractured reservoir as equidimensional element by finite element method (FEM) (left) and phase field method (right). In the FEM, conformed mesh is required along fracture intersection (Tatomir, 2007). The limitations of this method are (1) fined mesh around fractures and (2) re-fined mesh if cracking propagation is considered.

A development of FEM is ***Phase Field Method*** that uses a very simple and versatile way to describe the fracture network: a phase field function is used and defined such that its value is 0 for fractures or 1 for porous matrix. This method introduces an energy to be minimized with respect to the admissible displacements and to the fracture itself. The energy function that is minimized in practice is a Γ-convergent approximation. This energy regularizes the displacement field based on a phase field variable that interpolates between the unbroken and the broken states of the material (Formaggia et al, 2013). This method has simplicity in indicating fracture areas and re-mesh is not required during cracking propagation, so the method is used preferentially in crack propagation context. Using phase field method, and based on the Griffith energy (1921) theory for crack propagation, Heister et al (2015) studied the crack propagation in a linear elastic medium by implementing a fully coupling between state variables of continuum medium and variables of phase field. Borden et al (2012) uses phase field method to investigate the dynamic brittle fracture. Wick et al (2014), Wheeler et al (2014), Mikelic et al (2014, 2015) and Lee et al (2016) implemented and developed phase field method to solve hydro mechanical coupling of isotropic porous medium.

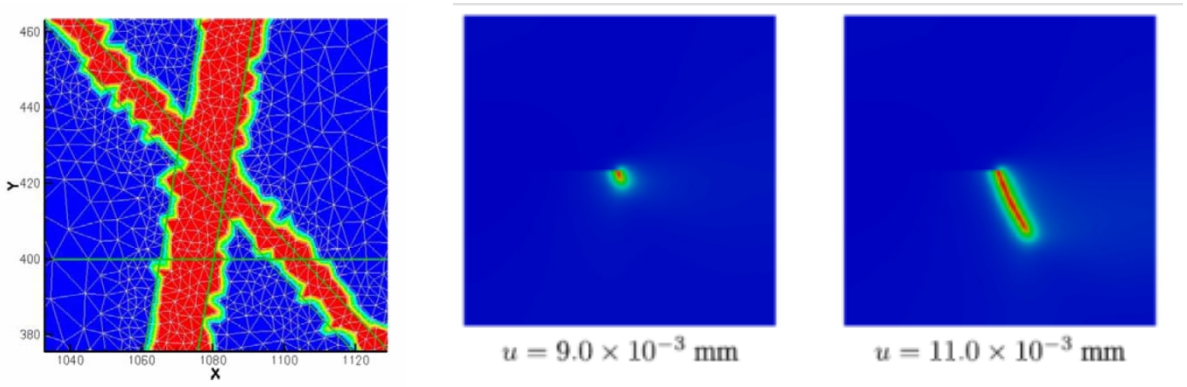

a) FEM method. b) Phase field method

Figure 1-8: Modeling fracture by equidimension element: a) FEM by Tatomir (2007) and b) Phase field method by Borden et al (2012)

For modeling fractured reservoir as low-dimensional element, eXtended Finite Element Method (XFEM) in which fractures are expressed by enrichment elements is suggested. The Figure 1-9 shows an example of modeling fractured reservoir as low-dimensional element by XFEM (Taleghani, 2009; Mohammadnejad and Khoei, 2013). Although the re-mesh is not required in XFEM, the enrichment of elements involved cracking propagation is required and complicated.

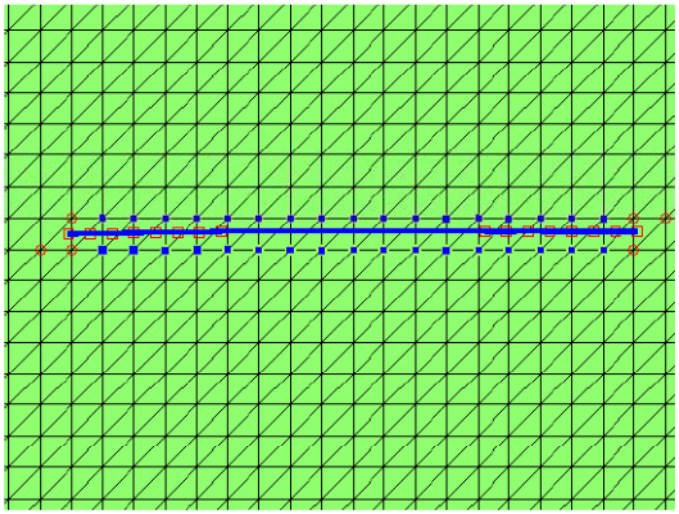

Figure 1-9: Modeling fracture by low-dimensional element (XFEM in Taleghani (2009))

One of the discrete fractures approaches is discrete fracture network model (DFN) developed to address network-scale fluid flow and solute transport behaviour. This approach assumes that fluid flow through a low-permeability rock mass is controlled by interconnected fractures of a network with negligible contribution from the rock matrix (Indraratna, 1999). This means fluid flow can only occur within fractures for a DFN simulation. Hence, detailed site characterization is required for the identification and inclusion of deterministic structures into the model domain.

The DFN requires property information of the fracture network such as distribution of fracture size, orientation. Due to the uncertainty of fracture network, stochastic introduction of background features is commonly required for discrete fracture simulations (Munier, 2004). This approach is computationally intensive and requires large number of input parameters; therefore, DFN simulations become limitation to applications where large scales are required, although extensions based on particle travel statistics have been developed (Schwartz and Smith, 1988).

A relatively new trend in the family of discrete fracture approaches, used in modeling flow through fractured reservoir, is used under different names: “fracture continuum approach” (Svensson 2001a, 2001b; McKenna and Reeves, 2006; Botros et al. 2008) or “fracture-cell model” (Sakhaee-Pour & Wheeler, 2016; Gong, 2016) or “embedded discrete fracture model” (Lee et al., 2010; Li & Lee, 2008; Moinfar, 2013; Shakiba, 2014; Xu, 2015; Yan et al., 2016)

Fracture continuum approaches (Svensson 2001a, 2001b) are based on the conversion of discrete fractures, or more commonly fracture zones, to permeability structures on a model grid instead of representing discrete fractures as continuous line elements in 2-D or planes in 3-D. However, this technique is limited to a sparsely fractured rock with a conductivity field dominated by major fractures and fracture zones. In the worst case, when fractures are inclined, in relation to the grid, a difference up to 16% between the finite-difference grid and DFN in the simulated flow was reported. Commonly, the origin of these differences is thought to be from the non-correspondence of the fracture (aperture), in relation to the grid size. In order to minimize the error, this author recommended that the fracture zones modeled by this approach should have widths comparable to grid cell size (i.e., the ratio of fracture width and grid cell size is suggested not to decrease below 0.1). The selection between a discrete fracture network model (DFN) and fracture continuum approach model (FC) is dependent on scale; DFN models are favored at smaller scales where they remain computationally feasible and FC models are used for larger-scale models (Svensson, 2001b). However, comparisons between DFN and FC models have shown that both methods are equally capable of capturing key aspects of flow and transport in fractured crystalline rock masses (Svensson, 2001b).

McKenna and Reeves (2006) also developed another fracture continuum technique, which they called fractured continuum model (FCM). This model is based on the DFN model with the help of stochastic continuum approach. They assumed the critical properties of the fracture network to be spatially random variables and assigned these random variables to finite-difference grid elements. As summarized by Botros et al. (2008), the critical properties of this model are the number of fractures within each grid block, coordination number (a

measure of fracture connectivity), and the permeability class for each grid block (a flag to show if the cell is a fracture cell or a matrix cell). All three random variables are defined at each grid block and derive a hydraulic conductivity value for the grid blocks which is then used to get the effective medium. Grid block conductivities are assumed isotropic.

A number of simple fracture network cases, a group of fractures that connect two opposite faces or simple fracture networks (uniform fracture size, random orientation, and uniform transmissivity), were studied and converted to continuum models using one of these fracture continuum approaches by Svensson (2001a, 2001b), McKenna and Reeves (2006) among others. The results of the flow problem on the DFN and the continuum grid were studied and compared for these simple cases. However, there is no comparison between the flow prediction from the DFN approach towards the same predictions from the continuum grid for more complicated networks; therefore, the evaluation of the pertinence of these approaches is yet an open question. Reeves et al., (2008) and Botros et al., (2008) developed a new fracture continuum approach for fully saturated single-phase flow system in which some of the limitations of the previous approaches in Svensson (2001a, 2001b) and McKenna and Reeves, (2006) are avoided. The condition of ratio of fracture width to cell size pointed out as a source of error in Svensson (2001a, 2001b), is not any more a problem; different fracture densities and orientations can be modeled reasonably well in Botros et al., (2008). Basically, the approach proposed by these authors consists of mapping the fracture network onto a grid where a hydraulic conductivity is modified for each grid cell in each direction such that the total flow is conserved (figure 1-10). Therefore, two correction factors are introduced to ensure equivalence between the total flow of the grid and the original fracture network in Reeves et al., (2008) and Botros et al., (2008). The first correction depends on the fracture alignment with the grid due to the difference between the flow path in the actual fracture and the representative path. The other correction acounts for areas in the grid where high fracture density is occurred. The same idea, using a correction factor when mapping fracture onto grid, is used and further developed on Sakhaee-Pour & Wheeler (2016) and Gong (2016) for curved fractures under the named “fracture-cell model”.

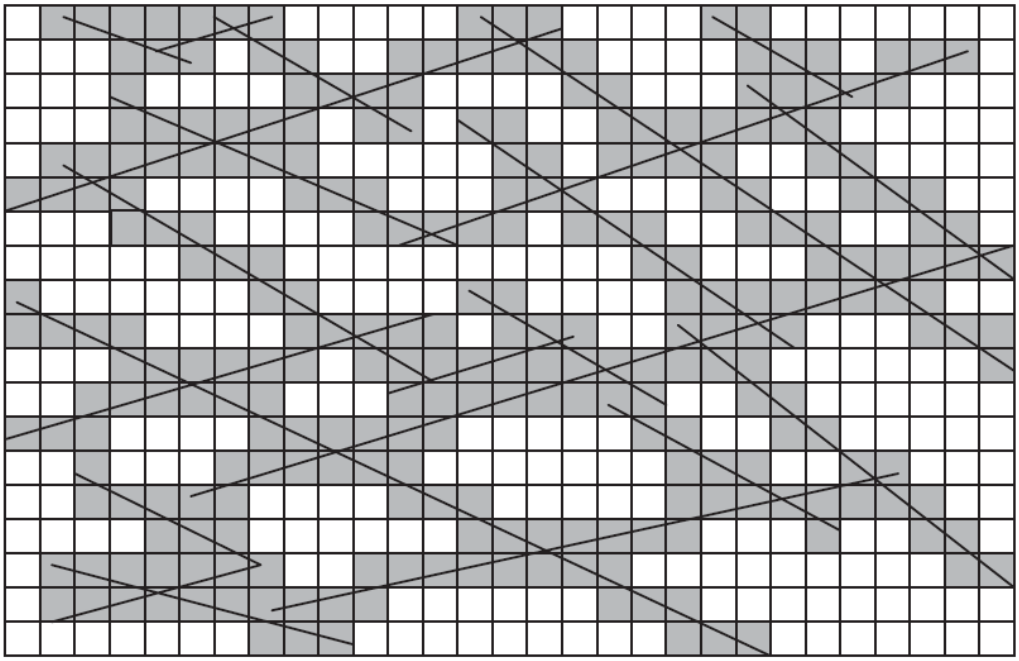

Figure 1-10: Sketch of a hypothetical rock fracture network (Reeves et al., 2008a,b).

Likewise, the alternative approaches that do not use mapping of the fracture onto the grid, the equivalent permeability of a regular fracture-matrix system is obtained using also some kind of correction factor for equivalent permeability (Parsons, 1966; Sarkar et al., 2004). Of course, there is no coincidence between these correction factors since their physical meaning is not the same: for the mapping-of- fracture-onto-grids approach this correction factor acounts for a longer fracture path in mapped situation as compared to real flow Reeves et al., (2008a, b), Botros et al., (2008), Sakhaee-Pour & Wheeler (2016) and Gong (2016). For the equivalent permeability approach, the correction factor acounts for differences of the gradient pressure on corresponding grid direction (Parsons, 1966; Sarkar et al., 2004).

Note that all above studies based on “fracture continuum approach” or “fracture-cell model” or “embedded discrete fracture model” are focused on the hydraulic behaviour of rock masses or flow in the fracture network system, with no mention on mechanical behaviour.

Studies on hydro-mechanical coupling in fractured reservoir, fractured rock masses have been conducted using different numerical methods, such as discrete and combined continuum–discrete fracture models. As reviewed by Figueiredo et al. (2015), discrete fracture models are more realistic for discontinuous media such as fractures. However, discrete fracture models have the limitation of not considering permeable intact rock and are time consuming for modeling hydro-mechanical behaviour of fractured rock domains

The equivalent parameters of fracture cell, joint model for mechanical behaviour and Poisseuille’s law for hydraulic behaviour, were used for fractures with filling material to the simulation of hydro mechanical coupling in Figueiredo et al. (2015) (see figure 1-11). The results indicated that the equivalent permeability of the fractured rock domain is most

sensitive to the fractures normal stiffness, the permeability of the tension failure regions and the power-law exponent for permeability change. Further, Figueiredo et al. (2017) used this approach, to study how geological structures such as confining formations, pre-existing bedding planes and faults influence fracture propagation during hydraulic fracturing operations. A model based on degradation of material properties is implemented in FLAC3D (Itasca, 2012) by these authors, to simulate fracture propagation in a continuous medium. Through this study, the effectiveness of using a continuum based model to simulate the fracture propagation, influence of complex geological settings (e.g. confining formations, a pre-existing bedding plane and fault) to fracture propagation and the changes of pore pressure and permeability induced by the interaction between the propagating fracture and preexisting geological structures were highlighted.

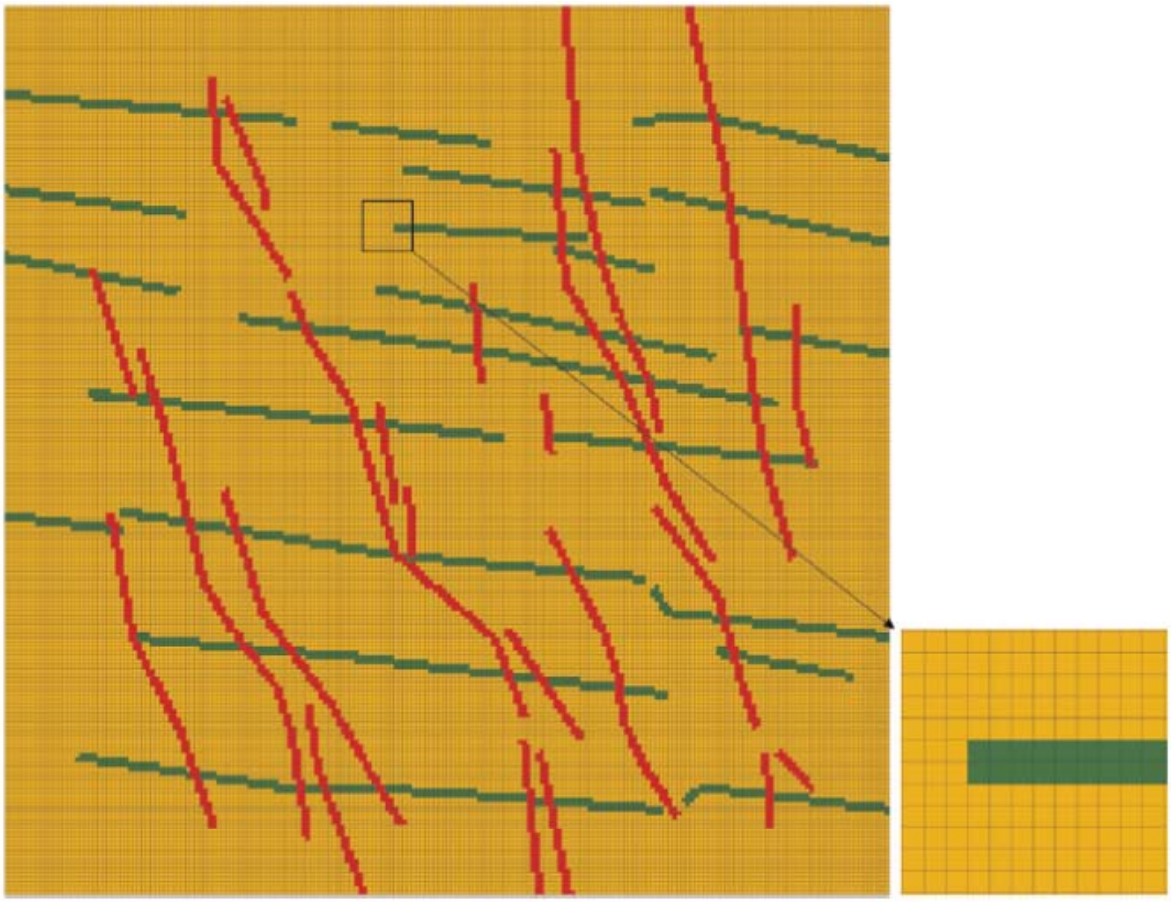

Figure 1-11. Mesh of the finite-difference model to study the hydro-mechanical behaviour of the fractured rock domain in Figueiredo et al. (2015)

1.3 Governing equations of hydro mechanical coupling of fractured reservoir

The term "hydro mechanical (HM) coupling" denotes to the physical interaction between hydraulic and mechanical processes (Rutqvist and Stephansson, 2003). In geological media (e.g., soils and rocks), HM interactions commonly occur because such medium contains pore and/or fractures which are filled by fluid and are deformable. In general, a porous medium or a fractured rock can deform as a result either of change in the external load or of change in the internal pore-fluid pressure (Figure 1-12).

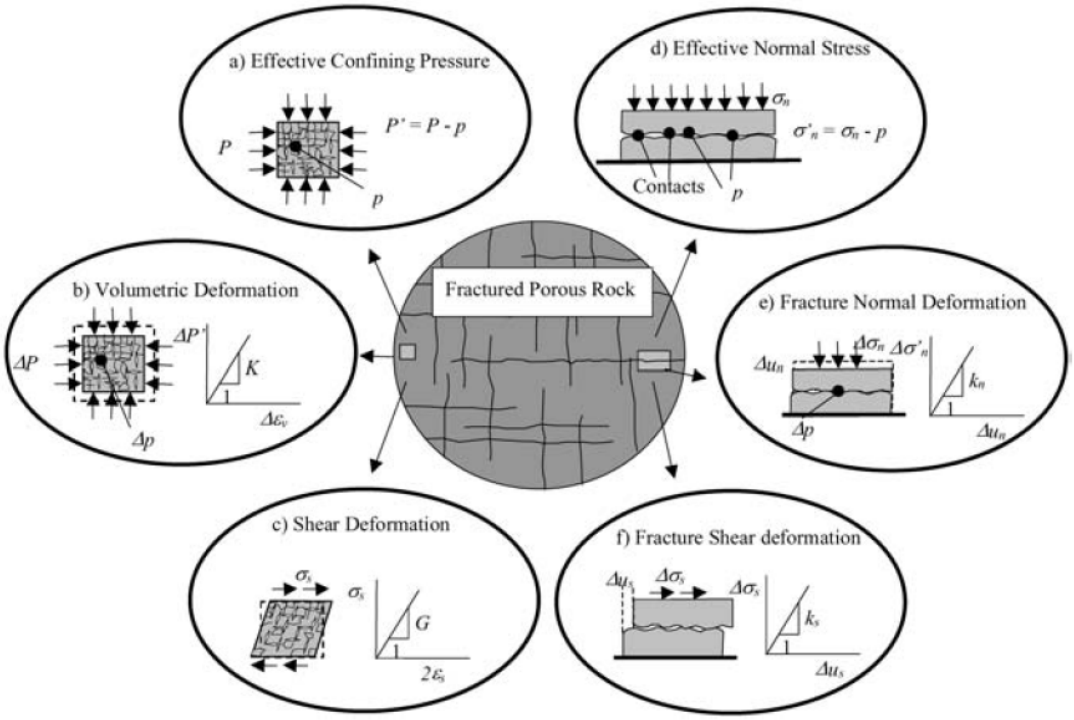

Figure 1-12: Schematic overview of a fractured geological medium composed of an intact porous rock matrix and macrofractures in Rutqvist (2003)

1.3.1 Linear mechanical behaviour

Under the quasi-static assumption for earth displacement, the governing equation for mechanical deformation of the solid-fluid system can be expressed stress equilibrium equations as below

$$\sigma_{ij,j} = -f_i \text{ or } \nabla.\sigma + \rho g = 0 \qquad (1.1)$$

where

σ_{ij} denote the Cartesian components of the symmetric stress tensor

$f_i = \rho g_i$ is the body force per unit volume of the bulk material, $\rho = (1-\varphi)\rho_s + \varphi\rho_f$ is the bulk density, ρ_s is the solid density, ρ_f is the fluid density and φ is the porosity.

$\nabla.$ is the divergence operator, σ is the Cauchy total stress tensor, g is the gravity vector.

Linear, isotropic mechanical behaviour is the simplest constitutive model for a material and could be taken as a base for a first approach as described in abound literature (Detournay and Cheng (1993), Coussy (1995)). In the framework of linear elasticity, the rock masses behaviour could be described reasonably well by an orthotropic elastic solid for which three mutually perpendicular planes of symmetry exist at any point. For a such material, the stress-strains relation is given by equation (1.2).

$$\sigma = \mathbb{D}^e \varepsilon \tag{1.2}$$

in which $\mathbb{D}^e$ is drained elastic modulus tensor that is given by following relation (Cheng, 1997):

$$\mathbb{D}^e = \begin{pmatrix} M_{11} & M_{12} & M_{13} & 0 & 0 & 0 \\ M_{12} & M_{22} & M_{23} & 0 & 0 & 0 \\ M_{13} & M_{23} & M_{33} & 0 & 0 & 0 \\ 0 & 0 & 0 & M_{44} & 0 & 0 \\ 0 & 0 & 0 & 0 & M_{55} & 0 \\ 0 & 0 & 0 & 0 & 0 & M_{66} \end{pmatrix} \tag{1.3}$$

The inverse of the stress-strains relation is commonly written as

$$\begin{pmatrix} \varepsilon_{xx} \\ \varepsilon_{yy} \\ \varepsilon_{zz} \\ 2\varepsilon_{xy} \\ 2\varepsilon_{xz} \\ 2\varepsilon_{yz} \end{pmatrix} = \begin{pmatrix} \frac{1}{E_x} & -\frac{\upsilon_{yx}}{E_y} & -\frac{\upsilon_{zx}}{E_z} & 0 & 0 & 0 \\ -\frac{\upsilon_{xy}}{E_x} & \frac{1}{E_y} & -\frac{\upsilon_{zy}}{E_z} & 0 & 0 & 0 \\ -\frac{\upsilon_{xz}}{E_x} & -\frac{\upsilon_{yz}}{E_y} & \frac{1}{E_z} & 0 & 0 & 0 \\ 0 & 0 & 0 & \frac{1}{G_{xy}} & 0 & 0 \\ 0 & 0 & 0 & 0 & \frac{1}{G_{xz}} & 0 \\ 0 & 0 & 0 & 0 & 0 & \frac{1}{G_{yz}} \end{pmatrix} \begin{pmatrix} \sigma_{xx} \\ \sigma_{yy} \\ \sigma_{zz} \\ \sigma_{xy} \\ \sigma_{xz} \\ \sigma_{yz} \end{pmatrix} \tag{1.4}$$

where E_i is the Young's modulus along axis i.

G_{ij} is the shear modulus in direction j on the plane whose normal is in direction i.

υ_{ij} is the Poisson's ratio that corresponds to a contraction in direction j when an extension is applied in direction i.

Note that $E_x\upsilon_{yx} = E_y\upsilon_{xy}$; $E_x\upsilon_{zx} = E_z\upsilon_{xz}$; $E_y\upsilon_{zy} = E_z\upsilon_{yz}$

Under plane strain conditions (2-dimensional plane), $\varepsilon_{zz} = 0$, Hook's law for an orthotropic material takes the form of equation (1.5) or (1.6).

$$\begin{pmatrix} \varepsilon_{xx} \\ \varepsilon_{yy} \\ 2\varepsilon_{xy} \end{pmatrix} = \begin{pmatrix} \frac{1-\upsilon_{xz}\upsilon_{zx}}{E_x} & -\frac{\upsilon_{yx}+\upsilon_{zx}\upsilon_{yz}}{E_y} & 0 \\ -\frac{\upsilon_{xy}+\upsilon_{zy}\upsilon_{xz}}{E_x} & \frac{1-\upsilon_{yz}\upsilon_{zy}}{E_y} & 0 \\ 0 & 0 & \frac{1}{G_{xy}} \end{pmatrix} \begin{pmatrix} \sigma_{xx} \\ \sigma_{yy} \\ \sigma_{xy} \end{pmatrix} \tag{1.5}$$

$$\begin{pmatrix} \sigma_{xx} \\ \sigma_{yy} \\ \sigma_{xy} \end{pmatrix} = \begin{pmatrix} \frac{E_x}{m}(1-\upsilon_{yz}\upsilon_{zy}) & \frac{E_x}{m}(\upsilon_{yx}+\upsilon_{zx}\upsilon_{yz}) & 0 \\ \frac{E_y}{m}(\upsilon_{xy}+\upsilon_{zy}\upsilon_{xz}) & \frac{E_y}{m}(1-\upsilon_{xz}\upsilon_{zx}) & 0 \\ 0 & 0 & G_{xy} \end{pmatrix} \begin{pmatrix} \varepsilon_{xx} \\ \varepsilon_{yy} \\ 2\varepsilon_{xy} \end{pmatrix} \tag{1.6}$$

with $m = (1-\upsilon_{xz}\upsilon_{zx})(1-\upsilon_{yz}\upsilon_{zy}) - (\upsilon_{yx}+\upsilon_{zx}\upsilon_{yz})(\upsilon_{xy}+\upsilon_{zy}\upsilon_{xz})$

For sedimentary rocks, very often the properties in one plane (generally the stratification plan) are isotropic (e.g. xz plan in figure 1-13, also known as the isotropic plane) whereas the properties in the direction normal to this plane are different. These materials are known as transversely isotropic materials.

In a transversely isotropic material, with axis of symmetry coinciding with y axis, one could write $E_x = E_z$; $\upsilon_{zx} = \upsilon_{xz}$, $\upsilon_{yx} = \upsilon_{yz}$, $\upsilon_{xy} = \upsilon_{zy}$ and $\frac{\upsilon_{yx}}{E_y} = \frac{\upsilon_{xy}}{E_x}$. The Hook's law for an transversly isotropic material takes the form of equation (1.7) or (1.8).

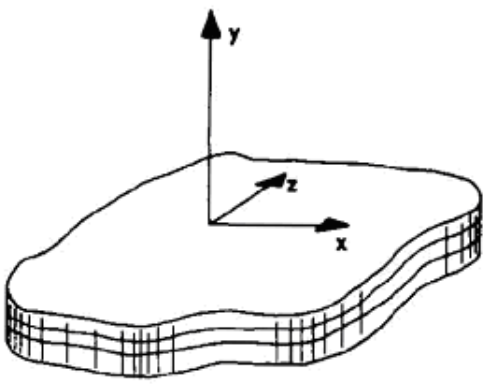

Figure 1-13: A stratified (transversely isotropic) material

$$\begin{pmatrix} \varepsilon_{xx} \\ \varepsilon_{yy} \\ 2\varepsilon_{xy} \end{pmatrix} = \begin{pmatrix} \frac{1-\upsilon_{xz}^2}{E_x} & -\frac{\upsilon_{yx}(1+\upsilon_{zx})}{E_y} & 0 \\ -\frac{\upsilon_{xy}(1+\upsilon_{xz})}{E_x} & \frac{1-\upsilon_{yx}\upsilon_{xy}}{E_y} & 0 \\ 0 & 0 & \frac{1}{G_{xy}} \end{pmatrix} \begin{pmatrix} \sigma_{xx} \\ \sigma_{yy} \\ \sigma_{xy} \end{pmatrix} \tag{1.7}$$

$$\begin{pmatrix} \sigma_{xx} \\ \sigma_{yy} \\ \sigma_{xy} \end{pmatrix} = \begin{pmatrix} \frac{E_x}{m}(1-\upsilon_{yz}\upsilon_{xy}) & \frac{E_x}{m}\upsilon_{yx}(1+\upsilon_{zx}) & 0 \\ \frac{E_y}{m}\upsilon_{xy}(1+\upsilon_{xz}) & \frac{E_y}{m}(1-\upsilon_{xz}^2) & 0 \\ 0 & 0 & G_{xy} \end{pmatrix} \begin{pmatrix} \varepsilon_{xx} \\ \varepsilon_{yy} \\ 2\varepsilon_{xy} \end{pmatrix} \tag{1.8}$$

with $m = (1-\upsilon_{xz}^2)(1-\upsilon_{yz}\frac{E_x\upsilon_{yz}}{E_y}) - \upsilon_{yz}(1+\upsilon_{xz})\frac{E_x\upsilon_{yz}}{E_y}(1+\upsilon_{xz})$

The isotropic material has the property which is invariant under translation and rotation. For linear isotropic poroelastic solid skeleton case, $\mathbb{D}^e$ is become in (1.9)

$$\mathbb{D}^e = \begin{bmatrix} \lambda+2\mu & \lambda & 0 \\ \lambda & \lambda+2\mu & 0 \\ 0 & 0 & \mu \end{bmatrix} \tag{1.9}$$

Thus, the input parameters for 2-dimensional problem are

+ $E_x = E_y = E$ and $\upsilon_{yz} = \upsilon_{yx} = \upsilon_{xz} = \upsilon$ for isotropic material.

+ $E_x, E_y, G_{xy}, \upsilon_{xz}, \upsilon_{yz}$ for transversely isotropic material which is transversed of axis y

1.3.2 Hydraulic behaviour

The hydraulic behaviour of fractures is perhaps the the most discussed in the literature including mathematical model formulations of the complex flow behaviour for single -phase flow fracture systems. Multi-phase flow systems are described in literature by Chen et al (2006) and are not expressed in the thesis. Flow in porous media is treated by Darcy's law while Navier-Stokes, Stokes or the local cubic law (Poisseuille) could be applied for modeling flow in fractures.

a) Darcy's law

The flow of a fluid through a porous medium can be described by the well-known Darcy's law. The law was proposed in 1856 by Henry Darcy based on the results of experiments on the water flow through sand layers. Based on the assumptions of the laminar and Newtonian

flow, and a nonslip boundary condition of fluid-solid interfaced at the microscopic scale (Bear, 1972; Detournay and Cheng, 1993; Chen et al, 2006), the generalized Darcy's law describes the movements of fluid in the porous media. The velocity vector v is related to the gradient of the pressure p by equation (1.10)

$$v = -\frac{\mathbb{K}}{\mu}(\nabla p - \rho g) \tag{1.10}$$

where μ represents the dynamic viscosity, p the pressure, and the $\mathbb{K}$ the intrinsic permeability tensor. We neglect the effect of gravity and assume that $\mathbb{K}$ is a diagonal tensor. The velocity vector becomes

$$v = -\frac{\mathbb{K}\nabla p}{\mu} \tag{1.11}$$

where

$$\mathbb{K} = \begin{pmatrix} k_{xx} & 0 & 0 \\ 0 & k_{yy} & 0 \\ 0 & 0 & k_{zz} \end{pmatrix} = diag(k_{xx}, k_{yy}, k_{zz})$$

If $k_{xx} = k_{yy} = k_{zz} = k$, the porous medium is isotropic.

b) Navier-Stokes equations;

The Navier-Stokes equations which express momentum and mass conservation over the fracture (Brush and Thomson, 2003) for the steady laminar flow of a Newtonian fluid with constant density and viscosity through a fracture with impervious walls. The equation of the momentum conservation in fracture is expressed by equation (1.12)

$$\rho(u.\nabla)u = \mu\nabla^2 u - \nabla p \tag{1.12}$$

Where ρ is the fluid density,

μ is the fluid viscosity,

$u = (u_x, u_y, u_z)$ is the velocity vector at point (x,y,z),

$p(x, y, z)$ is the hydrodynamic pressure.

And, mass conservation in fracture is equation (1.13):

$$\nabla u = 0 \tag{1.13}$$

The Navier Stokes equations form a nonlinear system of partial differential equations that are difficult to solve in irregular geometries and even in domains with simple geometry (Tatomir, 2007). Hence, some expressions are derived from the Navier- Stokes equations by making

certain assumptions and simplifications which are proposed to model flow in fractures such as Stockes equation or Poisseuille equation.

c) Stokes equation

The fist level of simplification is to assume that the inertial forces in the flow field are negligibly small compared with the viscous and pressure forces. The momentum conservation of Stokes equation becomes to equation (1.14) and the mass conservation equation is kept as equation (1.13) in fracture

$$0 = \mu \nabla^2 u - \nabla p \tag{1.14}$$

To ensure the neglecting of inertial forces, a common measure of the relative strength of inertial forces to viscous forces in flowing fluids is the Reynolds number. The critical Reynolds number marking the beginning of turbulence and the dominance of inertial forces in the flow field is approximately 1200 based on experimental observations of flow through smooth parallel plates (Brush and Thomson, 2003; Tatomir, 2007)

d) Poisseuille equation

Poiseuille flow is a pressure-driven flow between stationary parallel plates which presented in Zimmerman and Bodvarsson (1996). Incorporating the no-slip condition (u=0) at the fracture walls, the resulting parabolic velocity distribution given by equation (1.15) is shown on the right of Fig 1-15.

$$u_x(y) = \frac{\left|\overline{\nabla P}\right|}{2\mu}\left[y^2 - \left(\frac{H}{2}\right)^2\right] \tag{1.15}$$

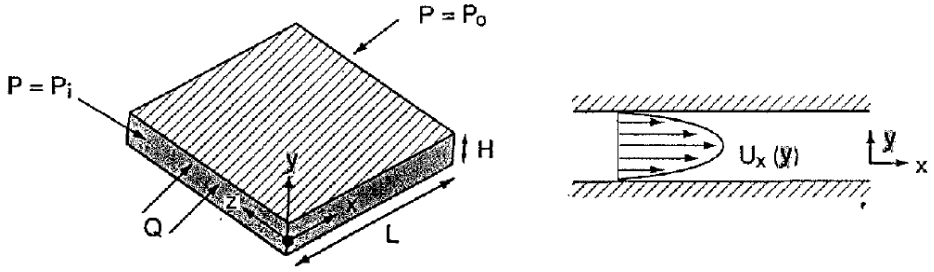

Figure 1-14: Parallel-plate fracture of aperture h, with uniform pressures Pi and Po imposed on two opposing faces.

The average velocity is found by dividing the flux by the cross-sectional area

$$U_x = -\frac{H^2}{12\mu}\nabla P \tag{1.16}$$

Where H is the local aperture parallel to the y-axis

In general, permeability of fracture is in form of tensor. $\mathbb{K}^{poi} = \begin{pmatrix} k_{xx} & 0 & 0 \\ 0 & k_{yy} & 0 \\ 0 & 0 & k_{zz} \end{pmatrix}$

The flow along fracture can be equaled to Darcy's law with the average permeability as below

$$k_{xx} = k^{poi} = \frac{H^2}{12} \tag{1.17}$$

The flow perpendicular fracture k_{yy} can be equaled to the value in longitudinal direction. Hence, the hydraulic behaviour of fractures can be isotropic.

1.3.3 Hydro mechanical coupling theory of porous media

The concept of the poroelastic medium had first appeared in the works of Karl von Terzaghi. Since then, it was later interpreted generally in the works of Maurice Anthony Biot. During the years of 1935-1957, Biot developed the theory of dynamic poroelasticity also called Biot's theory. In his theory of linear poroelasticity, Biot's theory has employed by Detournay and Cheng (1993), Verruijt (2013) and Coussy (2004) in the following equations: (1) equations of linear elasticity for the solid matrix is the stress-strain relation in which changes in total stress and fluid pressure are related to changes in strain and fluid content by Biot's theory such as Biot (1941), Coussy (2004) and (2) diffusion equations for fluid is the equation that comes from mass and linear-momentum conservation laws. We assume single-phase flow of a slightly compressible fluid, small deformation, isotropic and anisotropic materials in this study. The hydro mechanical theory of unsaturated porous media is expressed in chapter 6 of Coussy (2004) and is not included in this thesis.

(1) Equations of linear elasticity for the solid matrix

The stress equilibrium equations with the consideration of pore pressure are based on Biot theory as follow:

$$\sigma - \sigma_0 = \mathbb{D}^e \mathbb{E} - \mathbb{B}(p - p_0) \tag{1.18}$$

Where σ and σ_0 are the Cauchy total stress tensor at the current status and the initial status

$\mathbb{D}^e$ is stress strain tensor

$\mathbb{E}$ is the strain tensor

$\mathbb{B}$ is the Biot tensor

p and p_0 are the pressure at the current status and the initial status

(2) Diffusion equations for fluid

The diffusion equation for fluid is combined with the continuity equation of fluid, constitutive equation and transport law. Considerations of mass conservation of a compressible fluid yields the local continuity equation

$$\frac{\partial \zeta}{\partial t} + q_{i,i} = \gamma \tag{1.19}$$

where γ is the source density (the rate of injected fluid volume per unit volume of the porous solid).

ζ is variation of fluid content per unit volume of porous media

The transport law is conformed to the Darcy's law for the flow of fluid through the porous matrix which is introduced in item 1.3.2. The fluid volume flux, $v = q / \rho_{f,0}$, is given by Darcy's law

$$v = -\frac{\mathbb{K}\nabla p}{\mu} \tag{1.20}$$

where $\mathbb{K}$ is the permeability tensor,

μ is fluid viscosity.

Constitutive equations for porous media:

$$p - p_0 = M\left(\zeta - \mathbb{B} : \mathbb{E}\right) \tag{1.21}$$

in which

p and p_0 are the pressure at the current status and the initial status

$\mathbb{B}$ is the Biot second ordre tensor

$\mathbb{E}$ is the Cauchy second order strain tensor

M is the Biot modulus

The equation (1.21) is rewritten

$$\zeta = \mathbb{B} : \mathbb{E} + \frac{1}{M}(p - p_0) \tag{1.22}$$

For isotropic material, $\mathbb{B} = b\mathbb{I}$ where $\mathbb{I}$ is the identity tensor, the equation (1.22) becomes

$$\zeta = b\varepsilon_v + \frac{1}{M}(p - p_0) \tag{1.23}$$

For orthotropic material, the equation (1.22) can be rewritten:

$$\zeta = b_{xx}\varepsilon_{xx} + b_{yy}\varepsilon_{yy} + b_{zz}\varepsilon_{zz} + \frac{1}{M}(p - p_0) \tag{1.24}$$

Combination of Darcy's law (1.20), the continuity equation (1.19), and the constitutive relation (1.23), we have the diffusion equation for isotropic material (Detournay and Cheng, 1993) with the neglecting of source density

$$\frac{1}{M}\frac{\partial p}{\partial t} + \nabla.(-\frac{\mathbb{K}\nabla p}{\mu}) = -b\frac{\partial \varepsilon_v}{\partial t} \tag{1.25}$$

In generalization, combination of Darcy's law (1.20), the continuity equation (1.19), and the constitutive relation (1.22), the diffusion equation for orthotropic material can be written with the neglect of source density

$$\frac{1}{M}\frac{\partial p}{\partial t} + \nabla.(-\frac{\mathbb{K}\nabla p}{\mu}) = -\mathbb{B}:\frac{\partial \mathbb{E}}{\partial t} \tag{1.26}$$

Thus, the Biot parameters for 2-dimensional problem are

+ Biot modulus M and Biot coefficient b for isotropic material.

+ Biot modulus M and Biot coefficient in two directions b_{xx} , b_{yy} for isotropic transversely material with isotropic axis coinciding with one of this axis

1.3.4 Hydro mechanical coupling theory of fractured reservoirs

Hydromechanical effects within fractured media is a major field of scientific interest in geosciences especially the impact of fluid pressure to mechanical response and also aperture variation to fluid flow in fracture (Cappa et al, 2008). At the scale of a fracture network, the understanding of interactions between fluid flow and mechanical processes are complicated due to the complex geometry and the great variability in properties, such as fracture aperture and stiffness (Cappa et al., 2005).

Coupled hydro mechanical behaviours of fractured rock masses are expressed depending on conceptual model used for modeling of fractured rock masses. As presented in the item 1.2, two main approaches can be used to model fractured reservoirs: equivalent continuum approach and discrete fractures approach. For equivalent continuum approach, the effect of fractures will be taken into account by equivalent matrix. In this approach, fractured reservoir will play as porous media and governing equation detailed in item 1.3.3 could be used with the equivalent parameters which combined the properties of matrix and fractures. Additionally, pore pressure changes caused by production from a reservoir or injection into a reservoir can induce rock deformations (Moinfar, 2013). Fluid-flow characteristics of porous

media (especially in case of reservoirs), such as permeability and pore compressibility, can be very sensitive to effective stress changes caused by changes in pore pressure. Several studies in the past such as Settari and Mourits (1998), Chin et al. (2000), Raghavan and Chin (2004), Gutierrez et al. (2001), Samier et al. (2006) and Marmier (2007) attempted to take in to account the effect of mechanics state od rock masses to porosity and permeability of porous media changes by updating porosity of porous media in each elapsed time.

The hydromechanical effects of fractures may be considered as one-way coupling (H->M) in case the mechanical effect to pressure distribution is neglected. On the other hand, the hydro mechanical coupling is generally complete and occurs fracture-fluid interaction (H<->M). For discrete fracture approach, the governing equations are presented hereafter for both approaches.

a) One-way coupling

The mass balance of single phase flow (saturated material), in case of neglecting the mechanical effect to pressure distribution in fractures, is presented in Chen et al (2006) and Mikelic et al (2014). Fracture aperture is kept constant as its initial value in this case

$$\frac{\partial(\varphi_f \rho_f)}{\partial t} + \nabla.(q_f) = \gamma + q_H^+ + q_H^- \tag{1.27}$$

where

φ_f is porosity and equals to 1 in fracture

γ is external source and sinks

q_H^+ and q_H^- are the leak-off flux from each side of the fracture surfaces to the surrounding porous media and are not required to be calculated explicitly (Woodbury and Zhang, 2001; Segura and Carol, 2004; Wantanabe, 2011; Liu et al, 2015).

$q_f = \rho_f u^{poi} \approx \rho_f^0 u^{poi}$ is conformed to the Poisseuille's law presented in the item 1.3.2.

$$q_f = \rho_f^0 v^{poi} = -\rho_f^0 \frac{\mathbb{K}^{poi} \nabla p}{\mu} \tag{1.28}$$

Where

$\mathbb{K}^{poi}$ is the permeability tensor of fracture presented in item 1.3.2d, with *poi* denoting to Poisseuille's law,

ρ_f is density of fluid, for slightly compression flow, we assume $\rho_f = \rho_f^0 \left(1 + c_f (p - p_0)\right)$,

c_f is fluid compressibility

ρ_f^0 and p_0 are the initial density of fluid and initial pressure, respectively.

The diffusion equation for hydraulic behaviour in fractures is combination of mass balance and transport law. Neglect the effect of gravity and external source and sinks, we have

$$c_f \frac{\partial p}{\partial t} - \nabla.\left(\frac{\mathbb{K}_{poi}}{\mu} \nabla p \right) = 0 \tag{1.29}$$

The mechanical equation is similar to (1.18)

$$\sigma - \sigma_0 = \mathbb{D}_F^e \varepsilon - \mathbb{B}_F (p - p_0) \tag{1.30}$$

Where $\mathbb{D}_F^e$ and $\mathbb{B}_F$ are strain stress tensor and Biot tensor of fractures.

b) Two-way coupling

In this case, the variation of fracture aperture can induce a variation of pressure in fracture as well as the fracture's permeability. The volume balance equation for the discrete fracture can be described in its local coordinates, writing in low-dimensional form, from the mass balance law as (Wantanabe, 2011)

$$b_m S_s \frac{\partial p}{\partial t} + b \frac{\partial b_m}{\partial t} + \nabla.\left(b_h q_f \right) + q_H^+ + q_H^- = 0 \tag{1.31}$$

where b is Biot is coefficient for fractures. It denotes the mechanical effect to pressure distribution in fracture.

b_m and b_h denotes a mechanical and hydraulic (hydraulically effective) aperture, respectively.

$S_s = \frac{1}{K^l}$ is specific storage coefficient for a fracture with K^l the compressibility of liquid.

$\nabla.$ is the divergence operator in local coordinate system.

The volumetric change of unit space due to change in the stress field is expressed as $\frac{\partial b_m}{\partial t}$.

q_H^+ and q_H^- are the leak-off flux from each side of the fracture surfaces to the surrounding porous media and are not required to be calculated explicitly (Woodbury and Zhang, 2001; Segura and Carol, 2004; Wantanabe, 2011; Liu et al, 2015).

The term of "writing in low-dimensional form" denotes one-dimensional calculation for two-dimensional problem.

With the ignore of leak-off flux, the mass balance becomes

$$b_m S_s \frac{\partial p}{\partial t} + b\frac{\partial b_m}{\partial t} + \nabla.\left(b_h q_H^-\right) = 0 \tag{1.32}$$

In case fracture length is too long in compared fracture width, the deformation long fracture can be neglected, we have $\frac{\partial b_m}{\partial t} = b_m \frac{\partial \varepsilon_v}{\partial t}$

Assumption of $b_h = b_m$, the mass balance becomes

$$S_s \frac{\partial p}{\partial t} + \nabla.\left(q_f\right) = -b\frac{\partial \varepsilon_v}{\partial t} \tag{1.33}$$

$q_f = \rho_f u^{poi} \approx \rho_f^0 u^{poi}$ is conformed to the Poisseuille's law presented in the item 1.3.2.

Combined equation (1.33) and (1.28), we have diffusion equation for fractures in equi-dimensional form

$$S_s \frac{\partial p}{\partial t} - \nabla.\left(\frac{\mathbb{K}_F(\mathrm{t})}{\mu}\nabla p\right) = -\mathbb{B}_F : \frac{\partial \mathbb{E}}{\partial t} \tag{1.34}$$

The mechanical equation is similar to (1.18)

$$\sigma - \sigma_0 = \mathbb{D}_F^e \varepsilon - \mathbb{B}_F (p - p_0) \tag{1.35}$$

Where $\mathbb{D}_F^e$ and $\mathbb{B}_F$ are strain stress tensor and Biot tensor of fractures.

$\mathbb{K}(\mathrm{t})$ is the intrinsic permeability tensor of fracture at time t.

The hydro mechanical parameters of fracture need to be determined and should be provided to simulate. They include mechanical parameters (E_F ν_F, etc...), hydraulic parameter ($\mathbb{K}_F(\mathrm{t})$) and coupling parameters (M_F, $\mathbb{B}_F$). Determining these parameters is challenging due to the complexity of fractures: nominally planar or rough surfaces. The surfaces are typically in contact with each other in some locations, but separated in others. It is usually classified as a fault if the fracture has undergone substantial shear, otherwise, it is denoted as a joint (Zimmerman and Main, 2004). Some experiments conducted by Makurat and Gutierrez (1996), Cappa et al (2005, 2006) and studies by Lorenz (1999) showed that the transmissivity of fracture depends on normal stress action on that fracture and varies during production. Fractures with stress transfer through surface contacts is a more realistic scenario because it enables to consider changes in fractures aperture caused by changes in the effective stress normal to the fractures. Min et al (2004b) studied the fracture aperture change in a complicated fracture network with an impermeable material using a two-dimensional distinct element method program UDEC (universe distinct element code). Bagheri and Settari (2008), Monteagudo et al. (2011) attempted to update permeability of fractured blocks by calculating

on the basis of the orientation and spacing of fracture sets and aperture of fracture sets from the previous step. There have been very few attempts to couple flow and geomechanics in discrete fractures models. Tao et al. (2009), and Ranjbar et al. (2011) incorporated fracture geomechanics into modeling of naturally fractured reservoirs. Monteagudo et al. (2011) coupled a finite-element poroelastic code with a control volume discrete fracture flow simulator. We briefly introduce some basic theories of modeling closure or opening of fractures as below:

The deformation behaviour of fractures prior to an ultimate failure was studied by Goodman in 1970 (Rutqvist and Stephansson, 2003). He expressed normal and shear deformation of fractures as a function of stiffness and applied stress. The force-displacement law relates incremental normal and shear forces ($\Delta\sigma_n^{'}, \Delta\sigma_s^{'}$) which develop at contacts directly to the amount of incremental relative displacement ($\Delta u_n, \Delta u_s$):

$$\begin{aligned} \Delta\sigma_n^{'} &= k_n \Delta u_n \\ \Delta\sigma_s^{'} &= k_s \Delta u_s \end{aligned} \tag{1.36}$$

where k_n and k_s are the contact normal and shear stiffness

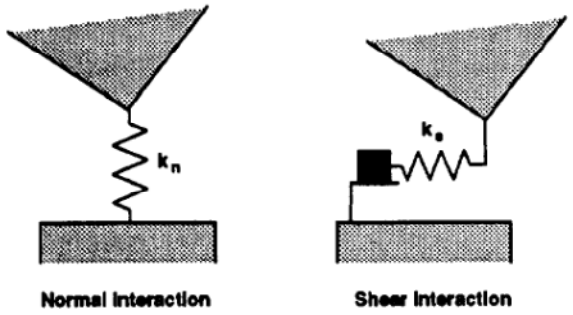

Figure 1-15 Sketch of mechanical behavoir of fracture (UDEC's manual, 1989)

The normal stiffness of a fracture is dependent on the size of the contact area between the fracture surfaces and the quality of the surfaces. The rate of fracture closure and stiffness has been studied in the laboratory by Bandis et al. (1983) and Barton et al. (1985). Based on their experimental data, Bandis et al. (1983) and Barton et al. (1985) suggested a hyperbolic model for the normal deformation of fractures as given below:

$$\sigma_n^{'} = \frac{\mathrm{D}_n}{a - bD_n} \tag{1.37}$$

where $\sigma_n^{'}$ is the effective normal stress and $\mathrm{D}_n = w_{init} - w$ is the normal closure of fracture, w_{init} and w are fracture aperture at initial state and current state $\sigma_n^{'}$. Also, a and b are constants related to two joint parameters, initial normal stiffness and maximum joint closure.

For very large values of normal stress, the fracture closure reaches its maximum in equation (1.38)

$$\mathrm{D}_{n,\max} = \frac{\mathrm{a}}{b} \tag{1.38}$$

where $\mathrm{D}_{n,\max}$ is the maximum normal closure of fracture. Also, joint normal stiffness (k_n) can be obtained from the derivative of equation (1.37)

$$k_n = \frac{\mathrm{d}\sigma_n^{'}}{dD_n} = \frac{1}{a\left(1-\frac{b}{a}D_n\right)^2} \tag{1.39}$$

The normal stiffness at zero effective normal stress is called the initial normal stiffness (k_{init}) can be determined by equation (1.40)

$$k_{init} = \frac{1}{a} \tag{1.40}$$

Hence, with two basic joint parameters, initial normal stiffness and maximum normal closure, we can calculate the normal fracture closure in terms of joint parameters and normal effective stress (using Equations 1.37, 1.38, and 1.40), which is given by equation (1.41)

$$\mathrm{D}_n = \frac{\mathrm{D}_{n,\max}\,\sigma_n^{'}}{k_{init}\,\mathrm{D}_{n,\max} + \sigma_n^{'}} \tag{1.41}$$

By rewriting equation (1.41), we can calculate the fracture aperture by equation (1.42)

$$\mathrm{w} = \mathrm{D}_{n,\max}\frac{k_{init}\,\mathrm{D}_{n,\max}}{k_{init}\,\mathrm{D}_{n,\max} + \sigma_n^{'}} \tag{1.42}$$

Recently, Baghbanan and Jing (2008) proposed another equation to express the normal stiffness as below:

$$k_n = \frac{(10\sigma_n + \sigma_{nc})^2}{9\sigma_{nc}w_{init}} \tag{1.43}$$

where σ_n is the normal stress.

$$\sigma_{nc}[MPa] = 0.487 w_{init}[\mu m] + 2.51 \tag{1.44}$$

The symbols w_{init} and σ_{nc} are initial fracture aperture and critical normal stress, respectively. It can be seen that fracture normal stiffness also is correlated with fracture trace length.

Zimmerman and Bodvarsson (1996) sought to find a way to describe the hydraulic aperture in a more geometrically sound way than the cubic law, which is based on the Navier-Stokes equations and assume laminar flow in smooth parallel plates. A modified form of the cubic law (equation (1.16)) governs fluid flow in fractures (Rutqvist and Stephansson, 2003):

$$q = \frac{(b_{hi} + f\Delta U_n)^3 w\rho g}{12\mu}\nabla h \tag{1.45}$$

where q is the flow rate, b_{hi} is the initial hydraulic aperture at the initial effective stress, f is a factor reflecting the influence of the roughness on the tortuosity of the flow, ΔU_n is the change in the fractures normal displacement, w is the fracture width, ρ is the fluid density, g is the gravitational acceleration, μ is the fluid dynamic viscosity, and h is the gradient in hydraulic head.

1.4 Summary

The literature about characteristics of double porosity and double permeability of fractured reservoirs is reviewed in this chapter. Rock matrix provides the primary storage of production such as oil, gas while the fractures serve as highly conductive flow paths.

In this chapter, the conceptual model as well as previous works for fractured reservoirs is summarized in two main approaches: equivalent approach (or called continuum approach) and discrete fracture approach (or called discontinuum approach). Also, a new approach, which combines the superiority of continuum and discontinuum approaches, identified and studied by some former authors under different names fracture continuum approach, fracture-cell model, or embedded discrete fracture model for hydraulic behaviours is presented briefly.

Finally, governing equations of porous medium and fractured rock masses that will further used in this thesis are briefly described based on major references on the field.

CHAPTER 2 PORO-ELASTIC COUPLING OF POROUS MEDIA: IMPLEMENTATION IN DEAL.II

2.1 Introduction

In this chapter, the implementation of the poro-elastic coupling of the porous media in an open source library will be detailed. The well-known source code DEAL.II which has been utilized and developed since the last two decades (Bang and Kanschat, 1999; Bang et al, 2007; http://www.dealii.org/) will be chosen for this purpose. Thanks for the available mechanical and hydraulic module in this library source code, a sequential strategy to couple the poro-elastic behaviour of the porous geomaterial will be applied. The implementation of this module allows to simulate the hydro-mechanical behaviour of the isotropic as well as the transversely isotropic porous media which will be extended later in the context of the fractured porous media as detailed in the next chapter.

The organization of this chapter is as follows. Firstly, a brief presentation of the open source code DEAL.II is conducted. Then after a bibliographic study on different methods to couple the hydro-mechanical behaviour of the porous media, we will focus on the interactive coupling technique which is widely used in the literature to couple an available geomechanical code with another available fluid flow code. The implementation details of this iterative coupling in DEAL.II will be followed by some numerical investigations which aim to validate the developed procedure.

2.2 Open library source code DEAL.II

DEAL.II or Deal.II (Differential Equation Analysis Library) is a free, open library source code to solve the partial differential equations using the finite element method (FEM). Starting from the pioneering work of Numerical Methods Group at Heidelberg University in Germany with the first public release (version 3.0.0) in 2000, this software has received a lot of contributions of the community scientific (http://dealii.org/authors.html) illustrated by hundreds of publications (http://dealii.org/publications.html) in different fields. The current version 8.5.0 is released in February 2016. The primary maintainers, coordinating the worldwide development of the library, are today located at Texas A&M University, Clemson University and Heidelberg University.

DEAL.II was written and developed based on the principal aims (Bangerth and Kanschat, 1999) as follows:

Flexibility: DEAL.II provided a library which enables users to try and test their ideas in a way as quick as possible. The library is easily extendible with respect to the most common

approaches in numerical analysis, i.e., different variational formulations, different space dimensions, different finite element spaces, and different linear solvers.

High level interfaces: The library is designed as simple to use as possible. The interface shows only the basic data structure and hides the complex data structures. For example, locally refined grids are quite complex data structure and users can use this library without all necessary knowledge about the grid handling details.

Efficiency: The computations involved in finite element calculations are often highly time consuming and their required memories are enormous. Therefore, efficiency has to be considered as well.

Obviously, some of these criteria are contradictory and must be traded against each other. In almost cases, DEAL.II traded efficiency in favor of safety and flexibility. However, some decisions were also made with the performance aspect in mind. One important decision for simplicity against flexibility in DEAL.II was the reduction to hypercube (line, quadrilateral, hexahedron) cells and their transformations to the physical space only. Experiences of running combined mesh of simplicial elements (triangle, tetrahedron) and hypercube elements exhibit complicated data structures and violate the safety. The final decision was only hypercube (line, quadrilateral, hexahedron) cells in DEAL.II. Below some essential aspects of DEAL.II are outlined:

- ✓ This source code uses C++ (http://www.cplusplus.com/info/description/) as the programming language due to some main reasons. Firstly, C++ is widely available and is a compiler that runs on almost any platform, including personal computers for home use, workstations and supercomputers. It is a popular language in nearly all fields of computing, so acquiring skilled programmers is less difficult than with other programming languages. Secondly, C++ is a standardized language, so the programmer is able to rely on language features and can write portable programs that are guaranteed to run in the future as well. Furthermore, with a large library of generic data containers and algorithms C++ allows to program significantly faster than using other languages. Also, C++ is a highly structured software that is fast, opposed to teaching focused languages like Pascal and languages for network and interactive applications like Java. Therefore, it offers features like templates and inline functions, that enable a good compiler to mostly eliminate structural overhead. The last one is in-code documentation. In practice, for a rather small group of developers it is impossible to keep a good technical documentation up to date unless this can happen within the source code itself. Documentation is written directly at the point where modifications occur, making it much easier to keep program and documentation in a matching state.

- ✓ This code treats a huge kind of finite elements of any order: continuous and discontinuous Lagrange elements (Cangiani et al, 2011), Raviart-Thomas elements (Raviart and Thomas, 1977), and other combinations.
- ✓ Parallelization using multithreading through massively parallel using MPI (Message Passing Interface) is implemented in DEAL.II (it has been shown to scale to at least 16,000 processors as confirmed by Bangerth et al. 2011)
- ✓ Mesh refinement in this source code bases on the multigrid method with local smoothing using the adaptively refined meshes (Bangerth and Rannacher, 2003 ; Kanschat, 2004; Janssen and Kanschat, 2011). The adaptive refined meshes with the hanging nodes technique will be presented in the next chapter.
- ✓ All documentation about this code is available online in a logical tree structure which allow users fast access to the information. The documents comprise more than 500 pages of tutorials, several reports, and more than 5,000 pages of programming interface documentation with explanations of all classes, functions, and variables. All documentation comes with the library on user's computer after installation, is available on the World Wide Web http://www.dealii.org/ as well as updated every day.

DEAL.II is structured in different steps and each step solved a particular problem. As for example, the basic steps 1, 2, 3, 4, 5 and 6 talk about the triangulation, degree of freedom, Laplace matrix, boundary condition, adaptive local refinement and hanging node handing etc which are essential to solve each required problem. Based on these six basic steps, users can implement a simple problem by themselves. From the step 7, DEAL.II classified tutorial into some topics: advance techniques, fluid dynamics, solid mechanics, and time-dependent problems. However, this classification is only reference and users need to understand what they want DEAL.II to supply to solve a problem and what DEAL.II can supply. For a complicated problem, users need to combine two or more steps into a unified code. The chart of the step structure in DEAL.II is in the figure 2-1. The other features of DEAL.II will be captured in appendix A to simplify the presentation.

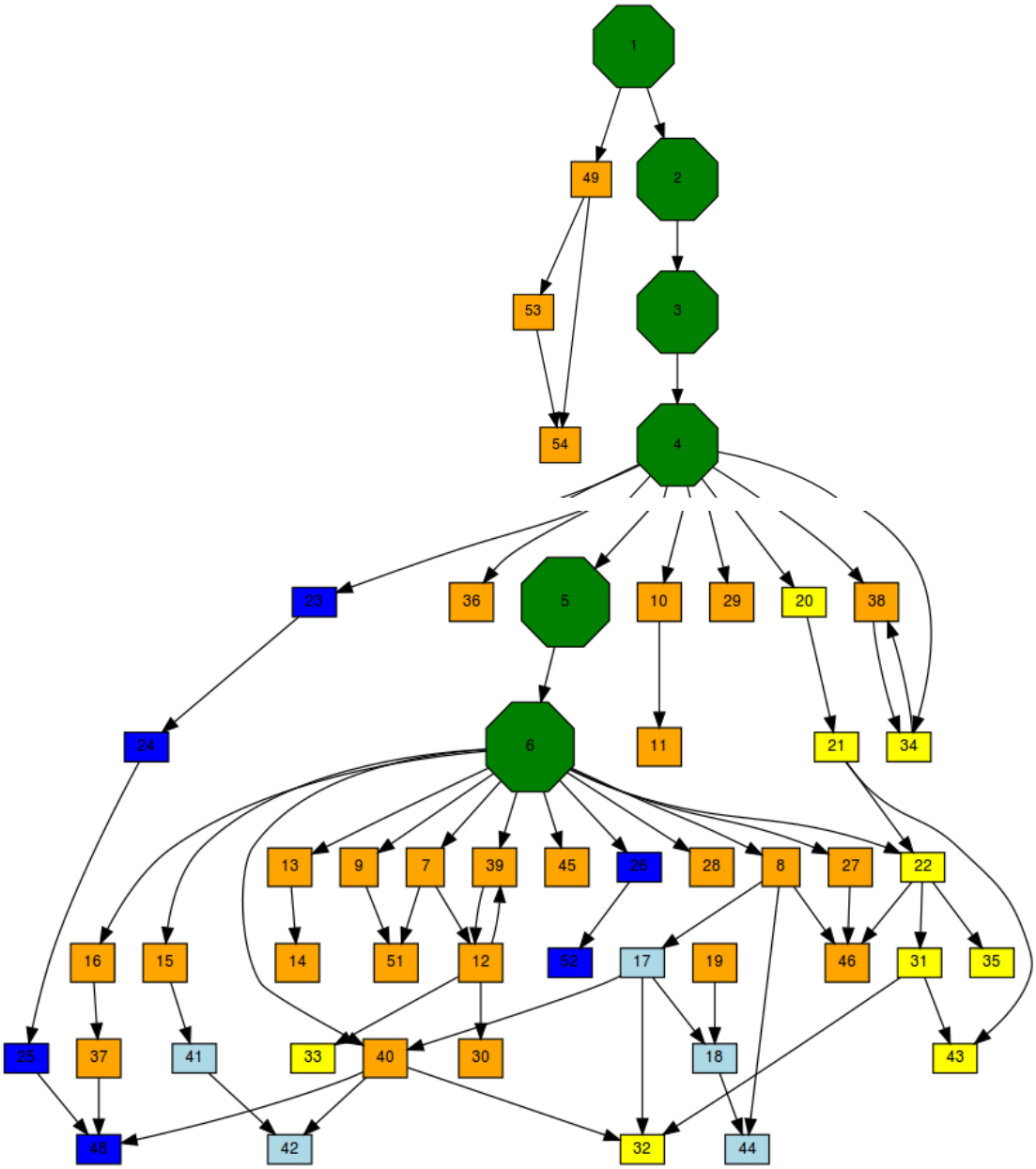

Figure 2-1: Structure of all steps in DEAL.II

Legend:

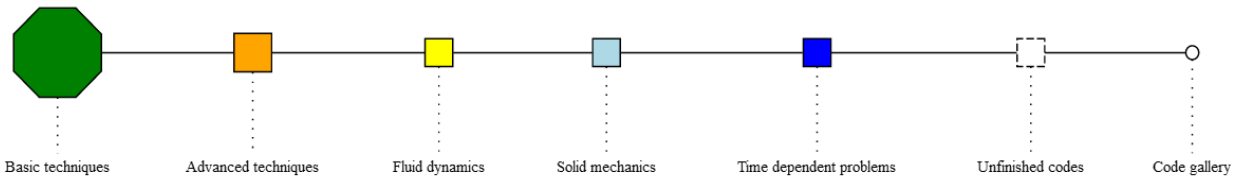

Concerning the hydraulic and mechanical phenomena, DEAL.II provided some steps which solve however separately the corresponding hydraulic and mechanical behaviour of the material which are summarized in table 2-1 and table 2-2, respectively. Hydraulic problems solved in DEAL.II consist of the Darcy, Stoke or Navier Stock diffusion. These equations are solved with some kinds of boundary such as pressure imposed, saturation imposed, velocity

imposed. The obtained results from these steps could be pressure of all nodes and velocity at faces of element. Correspondingly, the mechanical problems solved in DEAL.II are elastic, visco-elastic, plastic and hyper-elastic behaviours of isotropic material. Similar to hydraulic phenomena, the differential equations of the mechanical behaviour can be solved with the provided Newman and Dirichlet boundaries while the obtained results are displacements of all nodes.

Items	Equations solved	Boundary condition	Results
Step 20	Darcy equation (saturated material)	Pressure imposed	Velocities Pressure
Step 21	Darcy equation Balance equation of mass	Saturation and Pressure imposed	Velocities Pressure Saturation
Step 22	Stoke equations	Load imposed	Pressure Velocities
Step 26	Diffusion equation	Pressured imposed	Pressure
Step 35	Navier-Stokes equation in isotropic behaviour	Velocities	Velocities Pressure
Step 43	Darcy equation (unsaturated material)	Saturation and Pressure imposed	Velocities Pressure Saturation

Table 2-1 : Available hydraulic examples implemented in DEAL.II

Items	Equations solved for isotropic material	Boundary condition	Results
Step 8 Step 17	Elastic linear	Displacement imposed	Displacement
Step 18	Visco-elasticity	Displacement and stress imposed	Displacement
Step 42	Elasto-plastic	Stress imposed	Displacement
Step 44	Hyperelasticity	Displacement imposed	Displacement

Table 2-2: Available mechanical examples implemented in DEAL.II

Recently, Heister et al (2015) implemented in this code the phase-field method (which consider two variables: displacement and phase field) to study the cracking-propagation problem in an elastic material by using the fully coupling based on the Griffith energy (1921).

Some other studies of Wick et al (2014), Wheeler et al (2014), Mikelic et al (2014, 2015) and Lee et al (2016) about cracking propagation were also conducted in DEAL.II with an extension for the isotropic porous medium.

Concerning the hydro-mechanical behaviour of fractured porous medium, with the knowledge of authors, until now no development in DEAL.II is available. This issue will contribute as one of the main objectives of the present thesis and will be focused on the next chapter. However, in this chapter, the hydro-mechanical of a homogeneous porous medium is the first important step to obtain this purpose. The available hydraulic and mechanical examples implemented in DEAL. II (steps 8, 26) will be used as the starting point of this coupling. These present steps limited in the isotropic behaviour of the material will be extended in the transversely isotropic for the future applications.

2.3 Hydro-mechanical coupling strategy

There exist in the literature different approaches to couple the fluid flow and geomechanics (hydro-mechanical behaviour) in the porous medium. In general, one can classify them in three main approaches (Gai, 2004; Jha, 2005; Kim et al, 2009, 2011; Kim 2010):

- The first approach known as the fully coupling involves solving all the coupled governing equations (of both hydraulic and mechanical problems) simultaneously and the obtained results at each node after every time step are the pressure and displacements. This strategy of coupling is unconditionally stable but can be computationally expensive when it has substantial local memory and complex solvers. (Wan, 2002; Gai, 2004).

- The second approach called as iterative coupling is a sequential procedure where either the flow or the mechanical problem is solved first and the other problem is solved by using the intermediate solution information. At each step, the procedure is iterated until the solution converges within an acceptable tolerance (Gai, 2004; Jha, 2005; Kim et al, 2009, 2011; Kim 2010). The fully coupled and sequential solutions are expected to be the same for a given time step, at convergence, if they both employ the same spatial discretization schemes of the flow and mechanical problems (Kim et al, 2009). In principle, a sequential scheme offers several advantages (Mainguy and Longuemare, 2002), including working with separate modules for flow and mechanics, each with its own advanced numeric and engineering functionality. It also facilitates the use of different computational domains for the flow and mechanical problems. The schematics of fully coupling and iterative coupling is sketched in figure 2-2. Note that as a special case of the iterative coupling where only one iteration is taken, we can find in the literature the staggered (or single – pass sequential) coupling.

- The third approach is usually called as the loose or explicit coupling. Follow that, the coupling between the two problems is resolved only after a certain number of flow time steps.

As consequence, the results of this strategy of coupling are less accurate in comparison with the fully and sequential coupling.

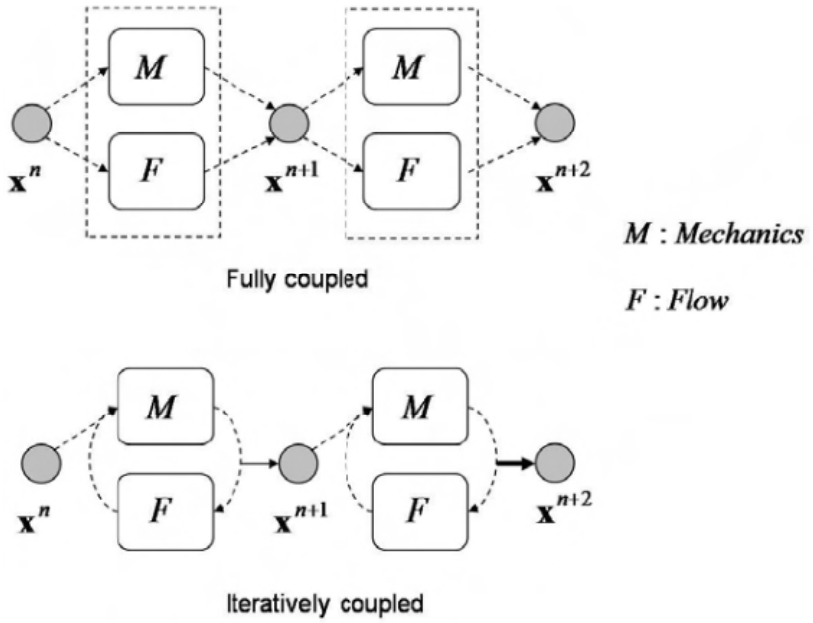

Figure 2-2: Schematics of the fully coupled (top) and the iteratively coupled (bottom) methods (Kim, 2010)

Given the enormous investment in software development and the high computational cost of the fully coupled flow–mechanics simulation, it is desirable to develop the sequential method that can be competitive with the fully coupled approach. The sequential calculation can be done by using the corresponding geomechanics and fluid flow codes or in only one codes with the separate modules for mechanics and flow. This is the main reason why iterative coupling is of interest in many areas of science and engineering. In this work, this coupling strategy is also chosen.

In the sequential coupling, one distinguishes four schemes (Figure 2-3) which are respectively the drained split, the undrained split, the fixed strain split and the fixed stress split. An excellent overview of these schemes can be found for example in (Kim et al., 2009, 2011; Kim, 2010) and below some of these schemes will be briefly presented.

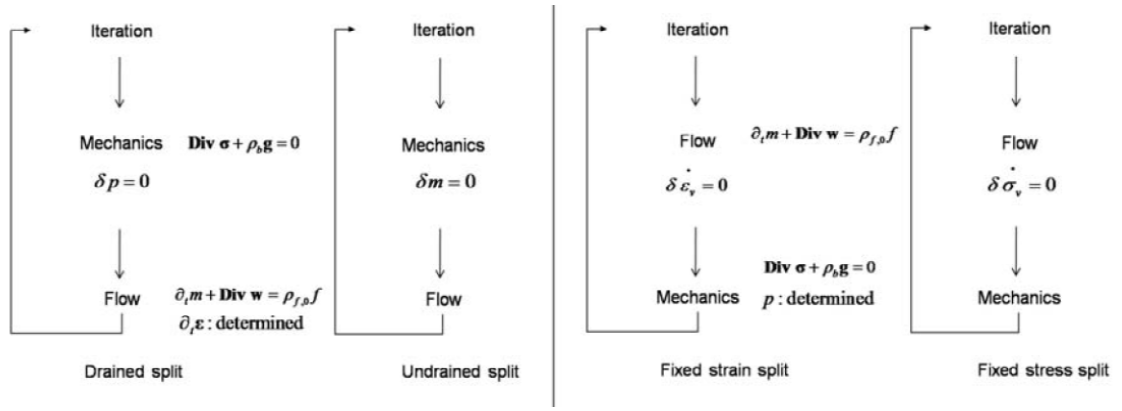

Figure 2-3: Coupling fluid flow and geomechanics: four iterative coupling schemes (Kim, 2010).

As summarized in Tables 2-1 and 2-2, currently in DEAL.II the diffusion equation (step 26) of the single-phase flow and the elastic equation (step 8) are already solved. The available source code of these two problems will be used in this work by and adapted to solve a hydro mechanical coupling using the drained split, undrained split and fixed-stress split.

Recalling now two coupled governing equations in (1.18) and (1.26):

$$\sigma - \sigma_0 = \mathbb{D}^e \mathbb{E} - \mathbb{B}(p - p_0) \tag{2.1}$$

$$\frac{1}{M}\frac{\partial p}{\partial t} + \nabla.\left(-\frac{\mathbb{K}\nabla p}{\mu}\right) = -\mathbb{B} : \frac{\partial \mathbb{E}}{\partial t} \tag{2.2}$$

where σ and σ_0 are the current and initial Cauchy total stress tensor; $\mathbb{D}^e$, $\mathbb{E}$, $\mathbb{B}$ designate respectively the stiffness, strain and Biot tensors; p and p_0 are the current and initial pressure while the hydraulic parameters M, $\mathbb{K}$, μ indicate the Biot modulus, the permeability tensor and the viscosity of the fluid.

As the simplest method to solve sequentially the HM coupling, one can use the drained split in which at each iteration the mechanical equation (2.1) is solved firstly by considering that there is no variation of pore pressure during this calculation. Then the diffusion equation (2.2) are solved in a sequence using the previous solutions of the mechanical problem. This split scheme is simple and quite easy for the implementation but it is conditional convergence, for example in case of the isotropic material this condition $\frac{b^2 M}{K_{dr}} \leq 1$ must be satisfied (K_{dr} is the drained bulk modulus, the readers can refer to Kim et al, 2009 for more details).

To improve the convergence of iterative coupling method, the undrained split and the fixed-stress split are usually proposed. In the undrained split, the mechanical equation (2.1) is

solved firstly but with a modification to satisfy the undrained condition of flux $\delta m = 0$. In case of isotropic material the undrained condition is written:

$$0 = b\delta\varepsilon_v + \frac{1}{M}\delta p \tag{2.3}$$

Substituting equation (2.3) into equation (2.1), the mechanical equation for undrained split can be expressed in form:

$$\sigma - \sigma_0 = \mathbb{D}_{ud}\varepsilon - b\mathbb{I}\left(p - p_0\right) - b^2\mathbb{I}M\varepsilon_v \tag{2.4}$$

in which $\mathbb{D}_{ud} = \mathbb{D}_{dr} + b^2M\mathbb{I}$ with $\mathbb{I}$ the fourth order identity tensor.

After solving the mechanical problem, the diffusion equation (2.2) will be solved normally as in the previous drained split.

Inversely, in the fixed-stress split, the diffusion equation (2.2) will be solved in the first step but a modification is also conducted to satisfy the condition of mean total stress $\delta\dot{\sigma}_v = 0$. Always in case of the isotropic material, the diffusion equation taking into account this last constraint is developed in form (Kim, 2010; Almani et al, 2016):

$$\left(\frac{1}{M} + \frac{b^2}{\lambda}\right)\frac{\partial p}{\partial t} - \nabla.\left(-\frac{\mathbb{K}}{\mu}\nabla p\right) = -b\frac{\partial\varepsilon_v}{\partial t} + \frac{b^2}{\lambda}\frac{\partial p}{\partial t} \tag{2.5}$$

where λ is the first coefficient of Lame and ε_v represents the volumetric strain.

The sequential coupling continues by solving the mechanical problem (Equation 2.1) using the solution of pore pressure obtained from the first step.

2.4 Implementation of sequential hydro-mechanical coupling in DEAL.II

In this part, the sequential hydro-mechanical coupling developed in the context of the finite element method is detailed, including theoretical bases for its implementation in the source code in DEAL.II.

2.4.1 Time and space discretization of governing equations

We present the formulations of time and space discretization of coupled hydro mechanical equations in iterative coupling scheme (drained split, undrained split and fixed-stress split). The 2-dimensional problem is considered in two kinds of material: isotropic material and transversely isotropic material.

The finite element formations of isotropic material are referred to Wan (2002) Jha (2006), Wang (2014), Kim et al (2009, 2011) and Kim (2010) for the drained / undrained split methods and are referred to Almani et al (2016) for the fixed-stress split method. To assign the initial stage (the condition prior to excavation), Mestat (2011) is referred. Equations of the transversely isotropic material are generalized from isotropic material.

a) Mechanical formulations

a1) Drained split and fixed-stress split

The equation (2.1) can be rewritten in the equation (2.6)

$$\nabla.\sigma' - \mathbb{B}\nabla p = 0 \tag{2.6}$$

Using integration by parts, the Eulerian-Lagrangian form (weak form) is

$$\left(\nabla.\sigma' - \mathbb{B}\nabla p, w\right)_{\Omega} = -\left(\varepsilon(w), D_{dr}\varepsilon(u)\right)_{\Omega} + \left(\varepsilon(w), \mathbb{B}p\right)_{\Omega} + \left(w, q\right)_{\partial\Omega} = 0 \tag{2.7}$$

where w is weight function of displacement (u), q is boundary pressure and $\mathbb{D}_{dr}$ is stress-strain tensor (stiffness tensor) in item 1.3.1.

The equation (2.7) can be cast into equation (2.8)

$$\left(\varepsilon(w), \mathbb{D}_{dr}\varepsilon(u)\right)_{\Omega} = \left(\varepsilon(w), \mathbb{B}p\right)_{\Omega} + \left(w, q\right)_{\partial\Omega} \tag{2.8}$$

In finite element method, when the variables are the displacement of nodes $\bar{u}$, the discrete strain vector is expressed by the equation (2.9)

$$\varepsilon = \mathbf{T}\bar{u} \tag{2.9}$$

where displacement vector $\bar{u}$ is a 8x1 vector for quadrilateral finite elements (4 nodes) are used $\left(\bar{u}\right)^T = \left(u_x^1 \quad u_y^1 \quad u_x^2 \quad u_y^2 \quad u_x^3 \quad u_y^3 \quad u_x^4 \quad u_y^4\right)$

$\mathbf{T}$ is the strain interpolation matrix, a 3x4 matrix of vectors, if quadrilateral finite elements are used:

$$\mathbf{T} = \left(T_1 \quad T_2 \quad T_3 \quad T_4\right)$$

where T_a is a 3x2 strain interpolation matrix associated with vertex a in a finite element Ω^e

$$T_j = \begin{pmatrix} \frac{\partial N_a}{\partial x} & 0 \\ 0 & \frac{\partial N_a}{\partial y} \\ \frac{\partial N_a}{\partial y} & \frac{\partial N_a}{\partial x} \end{pmatrix}$$

$$\text{thus } \mathbf{T} = \begin{pmatrix} \frac{\partial N_1}{\partial x} & 0 & \frac{\partial N_2}{\partial x} & 0 & \frac{\partial N_3}{\partial x} & 0 & \frac{\partial N_4}{\partial x} & 0 \\ 0 & \frac{\partial N_1}{\partial y} & 0 & \frac{\partial N_2}{\partial y} & 0 & \frac{\partial N_3}{\partial y} & 0 & \frac{\partial N_4}{\partial y} \\ \frac{\partial N_1}{\partial x} & \frac{\partial N_1}{\partial y} & \frac{\partial N_2}{\partial x} & \frac{\partial N_2}{\partial y} & \frac{\partial N_3}{\partial x} & \frac{\partial N_3}{\partial y} & \frac{\partial N_4}{\partial x} & \frac{\partial N_4}{\partial y} \end{pmatrix} \tag{2.10}$$

Equation (2.8) in matrix form could be written as

$$\mathbf{k}^e u^e = \mathbf{l}^e + \mathbf{f}^e \tag{2.11}$$

where $\mathbf{k}^e = [k_{ab}]$ is locally stiffness matrix of element e. $k_{ab} = e_i^T \int_{\Omega^e} T_a^T \mathbb{D}_{dr} T_b d\Omega e_j$

$\mathbb{D}_{dr}$ is the stress strain tensor,

$1 \le i, j \le n_{sd}$ and $1 \le a, b \le n_{en}$

e_i is the *i*-th Cartesian unit basis vector;

n_{en} is the number of displacement element nodes;

n_{sd} is the number of displacement's degree of freedom;

a,b are the local displacement element node number;

$\mathbf{l}^e$ and $\mathbf{f}^e$ are matrix associated with element e corresponding to the component of pore pressure distributed inside the element or pressure distributed around the element boundary (Neumann boundary).

$\mathbf{l}^e = [l_a]$ and $\mathbf{f}^e = [f_a]$

$$l_a = \int_{\Omega^e} p_e \mathbb{B}_e \nabla \varphi_a d\Omega$$

$$f_a = \int_{\partial\Omega} q \varphi_a d\Omega \text{ for Neumann boundary}$$

φ_a is shape function associated with displacement node *a*.

p_e and $\mathbb{B}_a$ is pore pressure and Biot tensor associated with element e

q is pressure associated with boundary $\partial\Omega$

Finally, globally linear equation for mechanical behaviour in matrix form could be written as

$$\mathbf{K}u = \mathbf{L} + \mathbf{F} \tag{2.12}$$

where $\mathbf{K}$ is globally stiffness matrix and defined by $\mathbf{K} = \mathbb{A}_{e=1}^{n_{el}}(\mathbf{k}^e)$ in which $\mathbb{A}_{e=1}^{n_{el}}$ denotes the finite element assembly operator which assembles the contribution of element e to the global matrix/vector.

$\mathbf{L}$ and $\mathbf{F}$ are matrix defined similarly by $\mathbf{L} = \mathbb{A}_{e=1}^{n_{el}}(\mathbf{l}^e)$ and $\mathbf{F} = \mathbb{A}_{e=1}^{n_{el}}(\mathbf{f}^e)$

- *Stage construction*

For calculating a ground excavation, the initial stage (the condition prior to excavation) is considered to mechanical equation. The equation of mechanics for the drained split or the fixed-stress split is rewritten as in Mestat (2011)

$$\left(\varepsilon(w), \mathbb{D}_{dr}\varepsilon(\delta u)\right)_\Omega = \left(\varepsilon(w), \mathbb{B}p\right)_\Omega + \left(w, q\right)_{\partial\Omega} - \left(\varepsilon(w^0), \mathbb{D}_{dr}\varepsilon(u^0)\right)_\Omega \tag{2.13}$$

where superscript 0 refers to the stage before excavating underground

a2) Undrained split

Similar to the case of drained split, the Eulerian-Lagrangian form (weak form) is

$$\left(\varepsilon(w), \mathbb{D}_{ud}\varepsilon(u)\right)_\Omega = \left(\varepsilon(w), bp\right)_\Omega + \left(w, q\right)_{\partial\Omega} + \left(\varepsilon(w), M\,\mathbb{B}\otimes\mathbb{B} : \mathbb{E}\right)_\Omega \tag{2.14}$$

where $\mathbb{D}_{ud}$ is stress-strain relationship in undrained case $\mathbb{D}_{ud} = \mathbb{D}_{dr} + M\,\mathbb{B}\otimes\mathbb{B}$ (Dormieux et al, 2006).

For isotropic material, $\mathbb{D}_{ud}$ becomes $\mathbb{D}_{ud} = \mathbb{D}_{dr} + b^2 M\,\mathbb{I}$ where $\mathbb{I}$ is the identity tensor.

Similar to drained split, equation (2.14) in matrix form for undrained split becomes to equation (2.15)

$$\mathbf{k}^e u^e = \mathbf{l}^e + \mathbf{f}^e + \mathbf{q}^e \tag{2.15}$$

where $\mathbf{k}^e$ is locally stiff matrix in undrained condition defined similar to equation (2.11) but in this case $k_{ab} = e_i^T \int_{\Omega^e} T_a^T \mathbb{D}_{ud} T_b d\Omega e_j$

$\mathbf{l}^e$ and $\mathbf{f}^e$ is matrix defined similarly in equation (2.11)

$\mathbf{q}^e$ is matrix defined $\mathbf{q}^e = [q_a]$ where $q_a = \int_{\Omega^e} \left(p_e \mathbb{B}_e + M \mathbb{B} \otimes \mathbb{B} : \mathbb{E}_e \right) \nabla \varphi_a d\Omega$

b) Pressure formulations

b1) Drained split and undrained split

The weak form hydraulic equations for isotropic and transversely isotropic media are presented hereafter

For isotropic material the pressure diffusion equation (2.2) is written in discretized implicit Euler form as

$$\frac{p_n - p_{n-1}}{k_n} - M\nabla.\left(\frac{\mathbb{K}}{\mu}\nabla p_n\right) = \left[-bM\frac{(\varepsilon_{v,n} - \varepsilon_{v,n-1})}{k_n}\right] \tag{2.16}$$

with

p_n and p_{n-1} being the pressure at time step n and n-1, respectively,

k_n is the time step, $k_n = t_n - t_{n-1}$,

$\varepsilon_{v,n}$, $\varepsilon_{v,n-1}$ are the volume strain at time step n, n-1, respectively.

K is permeability tensor $K = \begin{bmatrix} \kappa & 0 \\ 0 & \kappa \end{bmatrix}$

κ is the scalar value of permeability.

In space discretization, the weak formulation is expressed by:

$$(p_n, \varphi)_\Omega - (p_{n-1}, \varphi)_\Omega - k_n M (\nabla.\frac{\mathbb{K}}{\mu}\nabla p_n, \varphi)_\Omega = (l_n, \varphi)_\Omega \tag{2.17}$$

where $l_n = bM\frac{(\varepsilon_{v,n} - \varepsilon_{v,n-1})}{k_n}$

Use integrating by parts $(\nabla u, \varphi)_\Omega = (u, \varphi)_{\partial\Omega} - (\nabla\varphi, u)_\Omega$, the equation (2.17) becomes

$$(p_n, \varphi)_\Omega - (p_{n-1}, \varphi)_\Omega - k_n M\left((\frac{\mathbb{K}}{\mu}\nabla p_n, \varphi)_{\partial\Omega} - (\nabla\varphi, \frac{\mathbb{K}}{\mu}\nabla p_n)_\Omega\right) = (l_n, \varphi)_\Omega \tag{2.18}$$

where $(\frac{\mathbb{K}}{\mu}\nabla p_n, \varphi)_{\partial\Omega}$ denotes Neumann boundary conditions. If fluid velocity v is applied in boundary, then $v = \frac{\mathbb{K}}{\mu}\nabla p$, the Neumann boundary become $(\frac{\mathbb{K}}{\mu}\nabla p_n, \varphi)_{\partial\Omega N} = (v, \varphi)_{\partial\Omega N}$. If only Direchlet boundary is applied, the item $(\frac{\mathbb{K}}{\mu}\nabla p_n, \varphi)_{\partial\Omega D}$ will be zero.

Since for isotropic case as assumed here $\mathbb{K} = \kappa\mathbb{I}$ the equation (2.18) can be rewritten into equation (2.19) with κ being the permeability value:

$$(p_n, \varphi)_\Omega - (p_{n-1}, \varphi)_\Omega + k_n M \frac{\kappa}{\mu}(\nabla\varphi, \nabla p_n)_\Omega = (l_n, \varphi)_\Omega + k_n M (v, \varphi)_{\partial\Omega N} \tag{2.19}$$

The matrix form of the diffusion equation (2.19) in discretized form becomes

$$\left(\mathbf{m}^e + k_n \mathbf{a}^e\right) p_n = \mathbf{m}^e p_{n-1} + \mathbf{l}_n^e + \mathbf{f}_n^e \tag{2.20}$$

where $\mathbf{m}^e$ is locally mass matrix of element e: $\mathbf{m}^e = \left[m_{ab}\right]$ with $m_{ab} = \int_\Omega \varphi_a \varphi_b d\Omega$

in which a, b =1,…, n.

n is the number of degree freedom of element e

$\mathbf{a}^e$ is locally Laplace matrix $\mathbf{a}^e = \left[a_{ab}\right]$ with $a_{ab} = M\frac{\kappa}{\mu}\int_{\Omega^e}\left(\nabla\varphi_a\right)^T \nabla\varphi_b d\Omega$

$\mathbf{l}_n^e$ is the component of mechanical effect to pressure in the element e at time step n. $\mathbf{l}_n^e = \left[l_a^e\right]$ with $l_a = \int_\Omega l_n \varphi_a d\Omega$

$\mathbf{f}_n^e$ is the component of velocity effect (Neumann boundary) to pressure in the element e at time step n. $\mathbf{f}_n^e = \left[f_a^e\right]$ with $f_a = k_n M \int_{\partial\Omega} v\varphi_a d\Omega$

Finally, the matrix form of the diffusion equation in discretized form becomes

$$\mathbf{M}p_n = \mathbf{Q} + \mathbf{L} + \mathbf{F} \tag{2.21}$$

where $\mathbf{M}$ is the matrix defined by $\mathbf{M} = \mathbb{A}_{e=1}^{n_{el}}(\mathbf{m}^e + k_n \mathbf{a}^e)$ in which $\mathbb{A}_{e=1}^{n_{el}}$ denotes the finite element assembly operator which assembles the contribution of element e to the global matrix/vector.

$\mathbf{Q}$, $\mathbf{L}$ and $\mathbf{F}$ are matrix defined by $\mathbf{L} = \mathbb{A}_{e=1}^{n_{el}}(\mathbf{m}^e \, \mathrm{p}_{n-1})$, $\mathbf{L} = \mathbb{A}_{e=1}^{n_{el}}(\mathbf{l}^e)$ and $\mathbf{F} = \mathbb{A}_{e=1}^{n_{el}}(\mathbf{f}^e)$

For transversely isotropic material (with material axis coinciding with axis x and y) the pressure diffusion (2.2) is written in time discretization much similarly to the isotropic case

$$\frac{p_n - p_{n-1}}{k_n} - M\nabla.\left(\frac{\mathbb{K}}{\mu}\nabla p_n\right) = \left[-M(b_{xx}\frac{\varepsilon_{n,xx} - \varepsilon_{n-1,xx}}{k_n} + b_{yy}\frac{\varepsilon_{n,yy} - \varepsilon_{n-1,yy}}{k_n})\right] \tag{2.22}$$

where $\mathbb{K}$ is permeability tensor $\mathbb{K} = \begin{bmatrix} \kappa_{xx} & 0 \\ 0 & \kappa_{yy} \end{bmatrix}$

The weak form formulation is then deduced straightforwardly:

$$(p_n - p_{n-1}, \varphi)_\Omega + k_n M(\nabla\varphi, \frac{\mathbb{K}}{\mu}\nabla p_n)_\Omega = (l_n, \varphi) + k_n M(v, \varphi)_{\partial\Omega N} \tag{2.23}$$

where $l_n = M(b_{xx}\frac{\varepsilon_{n,xx} - \varepsilon_{n-1,xx}}{k_n} + b_{yy}\frac{\varepsilon_{n,yy} - \varepsilon_{n-1,yy}}{k_n})$

In the matrix form, these equations are written as

$$\left(\mathbf{m}^e + k_n \mathbf{a}^e\right) p_n = \mathbf{m}^e p_{n-1} + \mathbf{l}_n^e + \mathbf{f}_n^e \tag{2.24}$$

where $\mathbf{m}^e$, $\mathbf{l}_n^e$ and $\mathbf{f}_n^e$ are similar to the equation (2.20) and

$\mathbf{a}^e$ is locally Laplace matrix, in this case, $\mathbf{a}^e = [a_{ab}]$ with $a_{ab} = M\int_{\Omega^e}(\nabla\varphi_a)^T\frac{\mathbb{K}}{\mu}\nabla\varphi_b d\Omega$

b2) Fixed-stress split

For isotropic material the diffusion equation (2.5), for this splitting scheme could be written in times implicit form as

$$\frac{p_n - p_{n-1}}{k_n} - \frac{1}{\left(\frac{1}{M} + \frac{b^2}{\lambda}\right)}\nabla.\left(\frac{\mathbb{K}}{\mu}\nabla p_n\right) = \left[-\frac{b}{\left(\frac{1}{M} + \frac{b^2}{\lambda}\right)}\frac{(\varepsilon_{v,n} - \varepsilon_{v,n-1})}{k_n}\right] + \frac{b^2}{\lambda\left(\frac{1}{M} + \frac{b^2}{\lambda}\right)}\frac{p_n^k - p_{n-1}}{k_n} \tag{2.25}$$

where λ is Lame's first parameter

p_n^k is the pressure at time step n and iterative step k

In space discretization, the fixed-stress split equation of isotropic material becomes:

$$\left(p_n - p_{n-1}, \varphi\right)_\Omega + \frac{k_n}{\left(\frac{1}{M} + \frac{b^2}{\lambda}\right)}(\nabla\varphi, \frac{\mathbb{K}}{\mu}\nabla p_n)_\Omega = \left(f_n, \varphi\right)_\Omega + \frac{k_n}{\left(\frac{1}{M} + \frac{b^2}{\lambda}\right)}(v, \varphi)_{\partial\Omega N} \tag{2.26}$$

where $l_n = \frac{b}{\left(\frac{1}{M} + \frac{b^2}{\lambda}\right)}\frac{(\varepsilon_{v,n} - \varepsilon_{v,n-1})}{k_n} + \frac{b^2}{\lambda\left(\frac{1}{M} + \frac{b^2}{\lambda}\right)}\frac{p_n^k - p_{n-1}}{k_n}$

The matrix form becomes finally:

$$\left(\mathbf{m}^e + k_n\mathbf{a}^e\right)p_n = \mathbf{m}^e p_{n-1} + \mathbf{l}_n^e + \mathbf{f}_n^e \tag{2.27}$$

where $\mathbf{m}^e$, $\mathbf{l}_n^e$ and $\mathbf{f}_n^e$ are similar to the equation (2.20) and

$\mathbf{a}^e$ is locally Laplace matrix, in this case, $\mathbf{a}^e = \left[a_{ab}\right]$ with

$$a_{ab} = \frac{1}{\left(\frac{1}{M} + \frac{b^2}{\lambda}\right)}\int_{\Omega^e}\left(\nabla\varphi_a\right)^T\frac{\mathbb{K}}{\mu}\nabla\varphi_b d\Omega$$

For transversely isotropic material (with material axis coinciding with axes x and y) the diffusion equation for fixed-stress split is written in following form

$$\left(\frac{1}{M} + \frac{b_{xx}^2}{E_{xx}} + \frac{b_{yy}^2}{E_{yy}}\right)\frac{\partial p}{\partial t} + \nabla.(-\frac{\mathbb{K}}{\mu}\nabla p) = -(b_{xx}\frac{\partial\varepsilon_{xx}}{\partial t} + b_{yy}\frac{\partial\varepsilon_{yy}}{\partial t}) + \left(\frac{b_{xx}^2}{E_{xx}} + \frac{b_{yy}^2}{E_{yy}}\right)\frac{\partial p}{\partial t} \tag{2.28}$$

The time-discretized diffusion equation is then written

$$\frac{p_n - p_{n-1}}{k_n} + \frac{1}{\left(\frac{1}{M} + \frac{b_{xx}^2}{E_{xx}} + \frac{b_{yy}^2}{E_{yy}}\right)}\nabla.\left(\frac{\mathbb{K}}{\mu}\nabla p_n\right) = \left[-\frac{(b_{xx}\frac{\varepsilon_{n,xx} - \varepsilon_{n-1,xx}}{k_n} + b_{yy}\frac{\varepsilon_{n,yy} - \varepsilon_{n-1,yy}}{k_n})}{\left(\frac{1}{\frac{b_{xx}^2}{E_{xx}} + \frac{b_{yy}^2}{E_{yy}}}\right)\left(\frac{1}{M} + \frac{b_{xx}^2}{E_{xx}} + \frac{b_{yy}^2}{E_{yy}}\right)}\right] + \frac{\left(\frac{b_{xx}^2}{E_{xx}} + \frac{b_{yy}^2}{E_{yy}}\right)}{\left(\frac{1}{M} + \frac{b_{xx}^2}{E_{xx}} + \frac{b_{yy}^2}{E_{yy}}\right)}\frac{p_n^k - p_{n-1}}{k_n} \tag{2.29}$$

where p_n^k is the pressure at time step n and iterative step k

Spatial discretization of this equation leads, for the fixed-stress split equation of transversely isotropic material, to

$$\left(p_n - p_{n-1}, \varphi\right)_\Omega + \frac{k_n}{\left(\frac{1}{M} + \frac{b_{xx}^2}{E_{xx}} + \frac{b_{yy}^2}{E_{yy}}\right)}\left(\nabla\varphi, \frac{\mathbb{K}}{\mu}\nabla p_n\right) = \left(l_n, \varphi\right)_\Omega + \frac{k_n}{\left(\frac{1}{M} + \frac{b_{xx}^2}{E_{xx}} + \frac{b_{yy}^2}{E_{yy}}\right)}\left(v, \varphi\right)_{\partial\Omega N} \tag{2.30}$$

where $l_n = \dfrac{\left(b_{xx}\dfrac{\varepsilon_{n,xx} - \varepsilon_{n-1,xx}}{k_n} + b_{yy}\dfrac{\varepsilon_{n,yy} - \varepsilon_{n-1,yy}}{k_n}\right)}{\left(\frac{1}{M} + \frac{b_{xx}^2}{E_{xx}} + \frac{b_{yy}^2}{E_{yy}}\right)} + \dfrac{\left(\frac{b_{xx}^2}{E_{xx}} + \frac{b_{yy}^2}{E_{yy}}\right)}{\left(\frac{1}{M} + \frac{b_{xx}^2}{E_{xx}} + \frac{b_{yy}^2}{E_{yy}}\right)}\dfrac{p_n^k - p_{n-1}}{k_n}$

The matrix form of this last equation is written as below:

$$\left(\mathbf{m}^e + k_n\mathbf{a}^e\right)p_n = \mathbf{m}^e p_{n-1} + \mathbf{l}_n^e + \mathbf{f}_n^e \tag{2.31}$$

where $\mathbf{m}^e$, $\mathbf{l}_n^e$ and $\mathbf{f}_n^e$ are similar to the equation (2.20) and

$\mathbf{a}^e$ is locally Laplace matrix, in this case, $\mathbf{a}^e = \left[a_{ab}\right]$ with

$$a_{ab} = \frac{1}{\left(\frac{1}{M} + \frac{b_{xx}^2}{E_{xx}} + \frac{b_{yy}^2}{E_{yy}}\right)}\int_{\Omega^e}\left(\nabla\varphi_a\right)^T\frac{\mathbb{K}}{\mu}\nabla\varphi_b d\Omega$$

2.4.2 Algorithm and implementation in DEAL.II

The algorithms of drained, undrained and fixed-stress split are presented in the Figure 2-4. Note that for the fixed-stress split, the order of mechanical simulation and pressure simulation has changed: pressure simulation first and mechanical simulation after that.

0. Calculation of initial parameters: time step spacing $k_n = t_n - t_{n-1}$, etc..

1. Initialization of the starting time: $p_0 = p_{ini}$ and $u_0 = u_{ini}$

2. At time step, n (n is started from 1)

a) At iterative step 0: assign $p_n^{(0)} = p_{n-1}$,

b) At iterative step k (k is started from 1)

- Mechanical simulation

+ Governing equation is the equation (2.1) for drained & fixed-stress splits and the equation (2.4) for undrained split

+ Input data is the pressure of the previous iterative step $p_n^{(k-1)}$

+ Results are the displacement $u_n^{(k)}$ and the volumetric strain $\varepsilon_{v,n}^{(k)}$

- Pressure simulation

+ Governing equation is the equation (2.2) for drained & undrained splits and is equation (2.5) for fixed-stress split

+ Input data is volumetric strain of the current iterative step $\varepsilon_{v,n}^{(k)}$ and the pressure of the previous time step p_{n-1}

+ Results is the pressure $p_n^{(k)}$

c) Check for the convergence of both results $u_n^{(k)}$ and $p_n^{(k)}$ by L^2 Error Norm

Criteria: $\frac{\left\|u_n^{(k)} - u_n^{(k-1)}\right\|}{\left\|u_n^{(k)}\right\|} \leq TOL_u$ and $\frac{\left\|p_n^{(k)} - p_n^{(k-1)}\right\|}{\left\|p_n^{(k)}\right\|} \leq TOL_p$

If the criteria is NO, go to step 2.b with iterative step $k+1$

If the criteria is YES, end of iterative step and update $u_n = u_n^{(k)}$ and $p_n = p_n^{(k)}$

3. If n < total time step required, go to item 2 with time step n

If n = total time step required, end of time step

Figure 2-4: Algorithm of iterative coupling: drained, undrained and fixed-stress split

Legends:

t_n and t_{n-1} are the interval calculated time at the step n and $n-1$, respectively.

$p_n^{(k-1)}$ denotes pressure value at the iterative step $k-1$ of the time step n

p_{ini} and u_{ini} are the initial pressure and initial displacement of simulation domain.

TOL_u and TOL_p are the required tolerance.

The structure of the hydro mechanical coupling code is presented in the Fig 2-5. Six parts are in the code including MESH, MATERIALS, INITIAL CONDITION, BOUNDARY CONDITIONS, CALCULATION and POST-PROCESSING. The mesh of simulation is inputted from an ".inp" file which can be generated by another software or by DEAL.II. Materials are inputted through a text file with the strictly form presented in Appendix D. Two kinds of material which can be inputted into the code are isotropic and transversely isotropic. Initial conditions can be default if the initial stresses are zero or by calculating a balance state to get the initial condition, if the initial stresses are not zero. Boundary condition of mechanics and hydraulic are controlled separately by Dirichlet boundary or by Neumann boundary. The code can simulate the mechanical problem only, the hydraulic only or a coupled hydro mechanical problem. For hydraulic calculation, transient state or steady state can run into the code in according the purpose of simulation. The last part is the post processing, in which all information is post processed, for example the section which we want to output the result, etc…, is controlled by a text file.

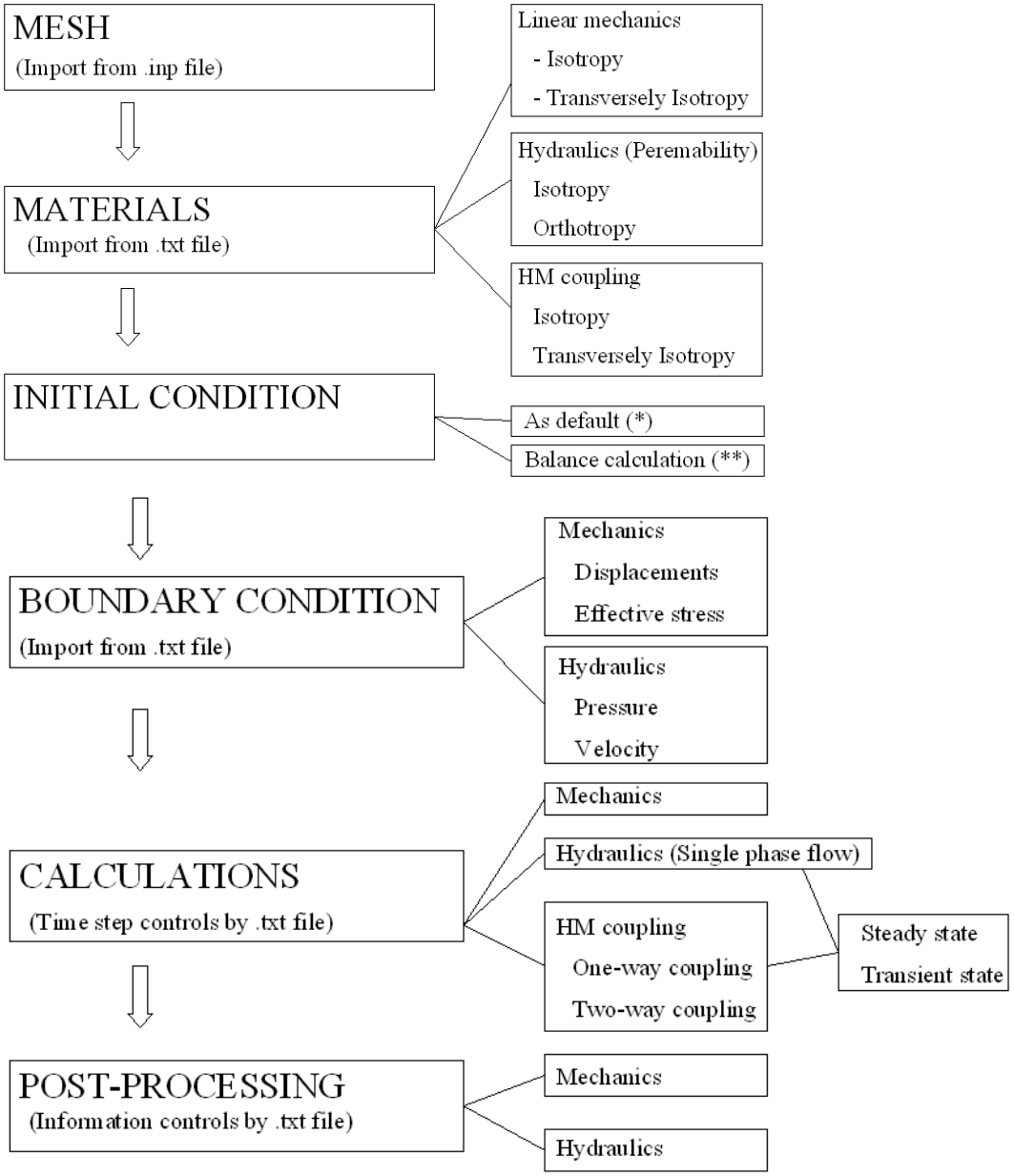

Figure 2-5: Structure of hydro mechanical coupling code.

Legends (*) Default initial condition is state which initial pressure can be inputted directly while initial stresses need to be zero

(**) Balance calculation to get initial condition is the state which initial stresses are not zero.

2.5 Validations

Two problems are selected to validate the coupling of hydro mechanical calculation. One is the Mandel's problem (Mandel, 1953) in transversely isotropic material and another one is tunnel excavation problem (Torres and Zhao, 2009). The Mandel's problem is used to validate the coupling of hydro mechanical processing to the code with the transient state, while the tunnel excavation problem is used to validate the assignment of initial condition to the code as well as transient process of water drained out of tunnel.

2.5.1 Mandel's problem in transversely isotropic materials

The classical case of Mandel's original solution, in which the fluid and the soil particles are incompressible, is rewritten in Verruijt (1963). Later in the more general case, with compressible fluid and soil particles, the problem is presented by Cheng and Detourney (1988). Abousleiman et al, (1996) has developed a solution of Mandel's problem into transversely isotropic material (Appendix B).

The geometry of Mandel's problem in anisotropic case sketched in Fig 2-6 involves an infinitely long rectangular specimen (0.2m x 0.2m) sandwiched at the top and the bottom by two rigid frictionless plates. The lateral sides are free from normal, shear stress, and pore pressure. At t = 0, a force of 2F is applied to the rigid plates. The parameters of porous media are selected as in the Abousleiman et al, (1996) and summarized in the table 2-4. One fourth of the specimen is carried out in the code of hydro mechanical coupling and compared to analytical solution (Abousleiman et al, 1996). Three items are compared; the first one is pressure distribution at the section y=0 in transient state (section 1-1); the second and third ones are the x-displacement at the section y=0 (section 1-1) and the y-displacement at the section x=0 (section 2-2). The second and the third ones are only comparison at time of 1000s because the variation of displacement is in small interval transient states.

The pressure distribution is in Figure 2-7 and the comparison of pressure at the section 1-1 between numerical result (the developed code in DEAL.II) and analytical result at transient state (100s, 1000s, 2000s, 3000s, 4000s) is the Figure 2-8. The L^2 Error Norm $\frac{\left\| p_n^{(numerical)} - p_n^{(analytical)} \right\|}{\left\| p_n^{(analytical)} \right\|}$ of difference between analytical and numerical results is less than 1%

The displacements in the x-direction of the section 1-1 and in the y-direction of the section 2-2 are compared to analytical solution in the Figure 2-9.

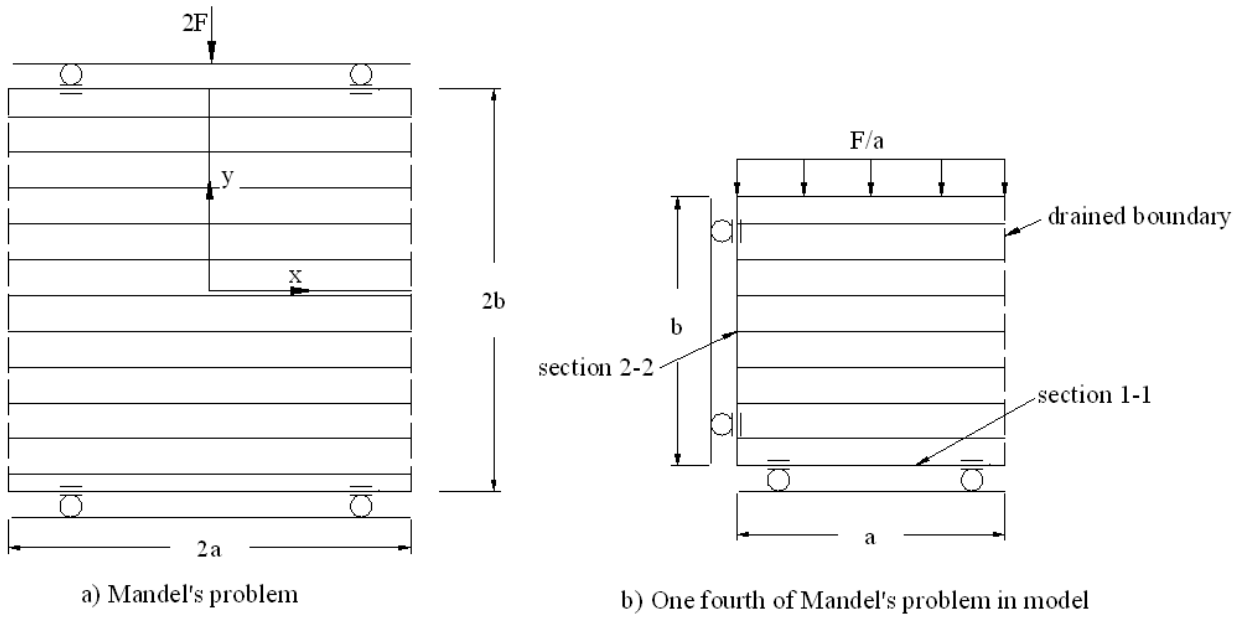

Figure 2-6: Sketch of (a) Mandel's problem and (b) One fourth of Mandel's problem in model

Symbol	Name	Value	Unit
b_x	Biot coefficient	0.733	
b_y	Biot coefficient	0.749	
E_x	Young's modulus	20 600	MPa
E_y	Young's modulus	17 300	MPa
ν_{zx}	Poisson ratio	0.189	
ν_{yx}	Poisson ratio	0.246	
G_{xy}	Shear modulus	7 230	MPa
M	Biot modulus	15 800	MPa
ϕ	Reservoir porosity	0.4	
K_{xx}	Reservoir permeability	10^{-7}	Darcy
K_{yy}	Reservoir permeability	$2*10^{-8}$	Darcy
μ	Viscosity of water	10^{-6}	kPa.s
q	Applying total pressure	10	MPa

Table 2-3 Parameters of Mandel problem in transversely isotropic material

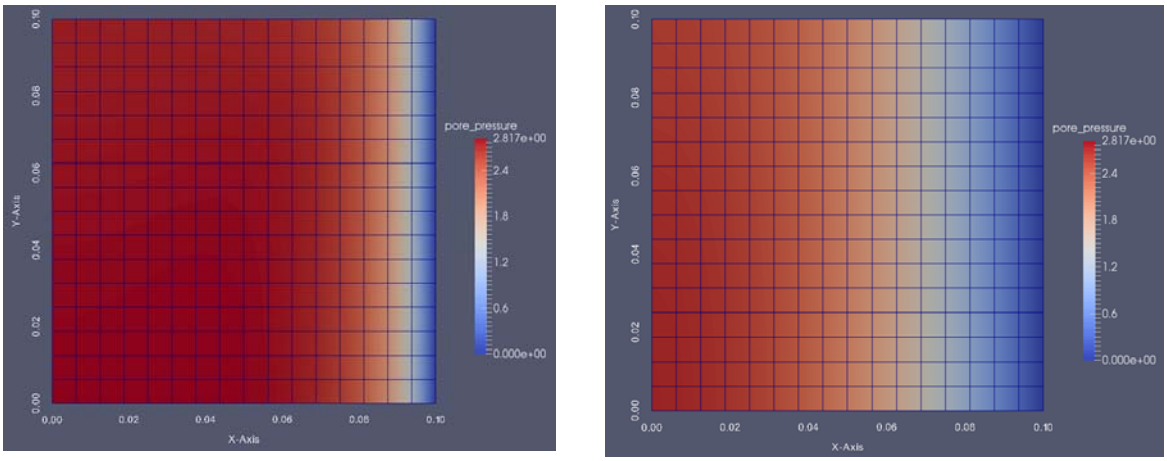

a) At 100s

b) At 1000s

Figure 2-7: The pressure distribution in specimen at interval state (100s, 1000s)

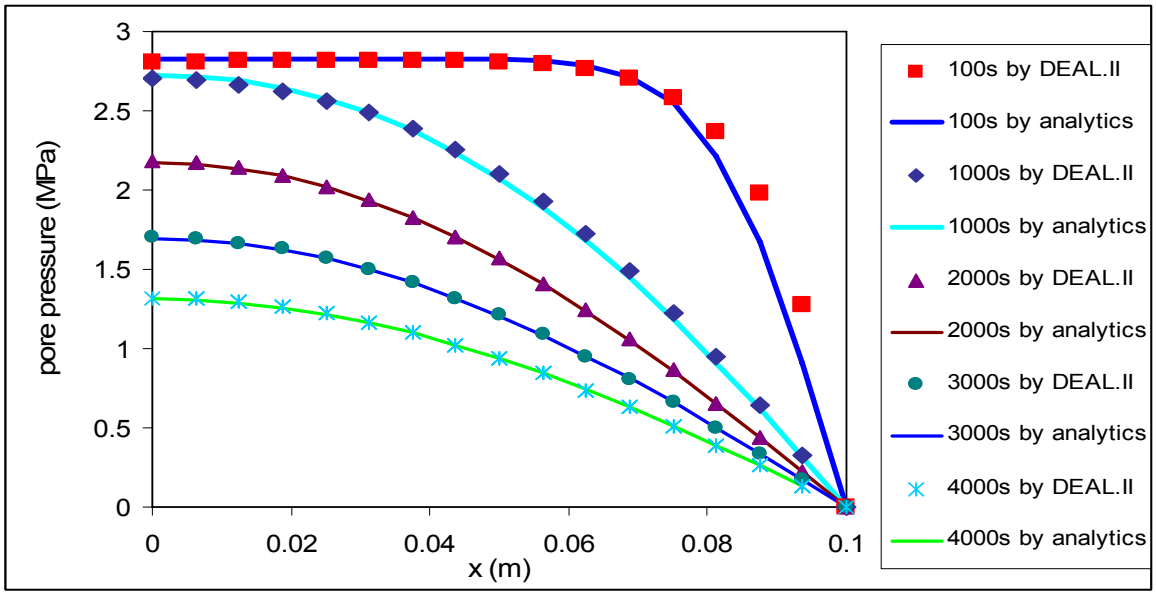

Figure 2-8: Comparison of pore pressure at section y = 0.0 m

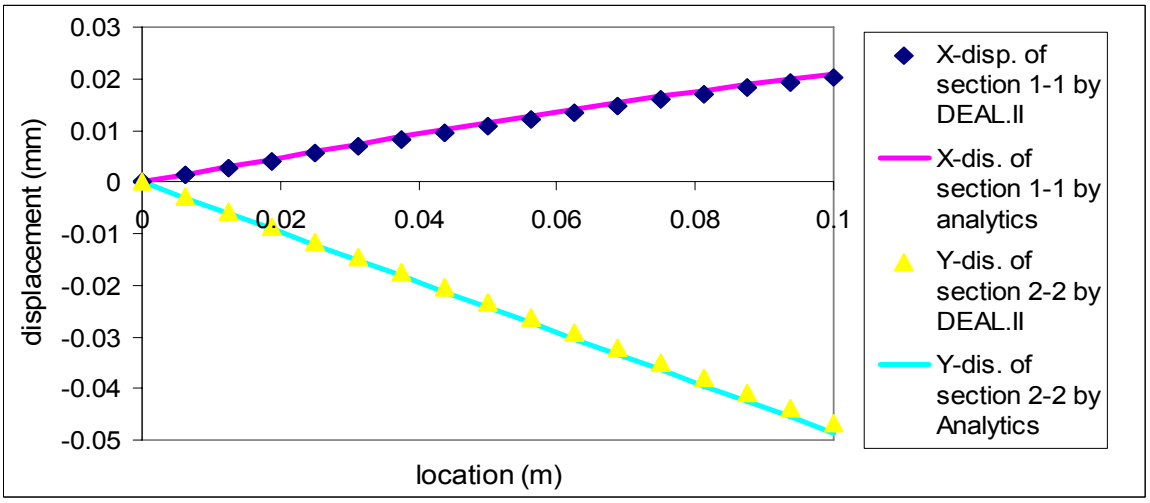

Figure 2-9: Comparison of x-displacements at section 1-1 and the y-displacement at section 2-2 at time of 1000s

2.5.2 Tunnel excavation problem in isotropic and transversely isotropic porous medium

In this part, the developed HM coupling module in DEAL.II will be used to simulate the behaviour of deep tunnel excavated in the poro-elastic media. The obtained results will be compared with some referent results which allow to validate our developed code. For this purpose, two examples are considered: the first example presents the tunnel excavated in an isotropic porous medium that the available analytical solutions provided by Torres and Zhao (2009) at steady state flow is used as the referent solution (Appendix B). The other studied example is the excavated tunnel in the transversely isotropic porous medium taking into account the transient fluid flow. Our results will be compared with the ones conducted from the commercial code FLAC3D (Itasca, 2006).

a) Deep tunnel in isotropic porous medium

The problem to be validated is represented in Figure 2-10. A section of cylindrical tunnel of radius r=1.0m is excavated in an elastic porous media. Symmetry conditions for geometry and loading will be assumed (i.e., gravity will be disregarded), so the problem in Figure 2-10 is representative of the case of a deep tunnel excavated in elastic ground subject to uniform initial stresses.

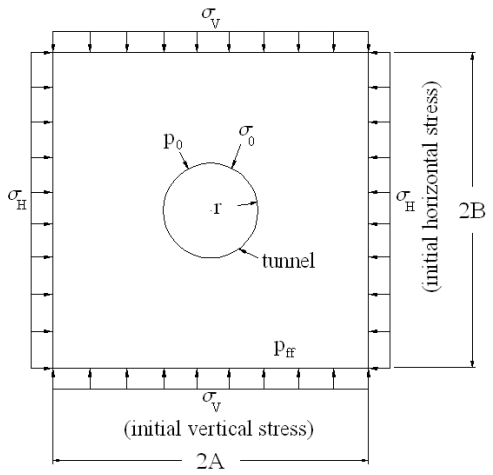

Figure 2-10: The sketch of tunnel excavation problem.

Prior to excavation, the total stresses in the medium are uniformed and equal to $\sigma_V = \sigma_H = -12.5MPa$ (note here that the compressional stress takes the negative value, the sign convention adopted throughout this work) and the pore pressures in the ground are also uniformed and equal to $p_{ff} = 4.7MPa$. The tunnel is then excavated without support. We assume that the calculated area of simulation (2A x 2B = 48m x 48m) is large enough for the tunnel radius in which the pressure at boundary is kept constant of the far-field value p_{ff} in both analytical solution (Torres and Zhao, 2009) and numerical simulation. Note that the analytical solution obtained only in the stead flow regime in which the radius of pore pressure distribution is prior determined, thus in this first example, the numerical simulation is also

done in the same condition. Two boundary conditions around the tunnel are considered which correspond to the undrained condition (the pressure around the tunnel p_0 is kept as the initial value 4.7 MPa and $\sigma_0 = 0$) and the drained condition (the pressure around the tunnel p_0 is down to 0 MPa and $\sigma_0 = 0$).

One fourth of tunnel (A=24m and B=24m) is used for numerical calculation. Parameters of medium are in the table 2-6. The steady state which the pore pressure is distributed around radius of 12m (after about 15 years) is obtained to compare with analytical result (Torres, 2009) (Appendix B). Two stages of running code are presented below:

- The first stage is to establish the initial condition. The initial effective stresses in two directions are $\sigma_V^{'} = \sigma_V + bp$ =-12.5+4.7=-7.8 MPa and $\sigma_H^{'} = \sigma_H + bp$ =-12.5+4.7=-7.8 MPa. The results of assigning the initial effective stresses and pressure are presented in Figure 2-11

- The second stage is to calculate the displacement, pressure, radial effective stress around the tunnel. The result of radial displacement distribution around the tunnel is shown in Figure 2-12 corresponding to the steady state (after about 15years; note that the results after 1 year and 10 years are added for reference of the steady state). The comparisons of radial displacement, radial effective stress and pressure around the tunnel are presented in Figure 2-13 and 2-14. A very good agreement between the analytical and numerical results can be stated which demonstrated the correctness of our code in the steady state flow condition of the isotropic porous medium.

Symbol	Name	Value	Unit
b	Biot's coefficient	1	
E	Young's modulus	4 000	MPa
ν	Poisson's ratio	0.3	
M	Biot' modulus	6 000	MPa
K	Porous media permeability	1.33×10^{-20}	m^2
μ	Viscosity of water	10^{-3}	Pa.s

Table 2-4 Parameters of tunnel excavation problem in isotropic material

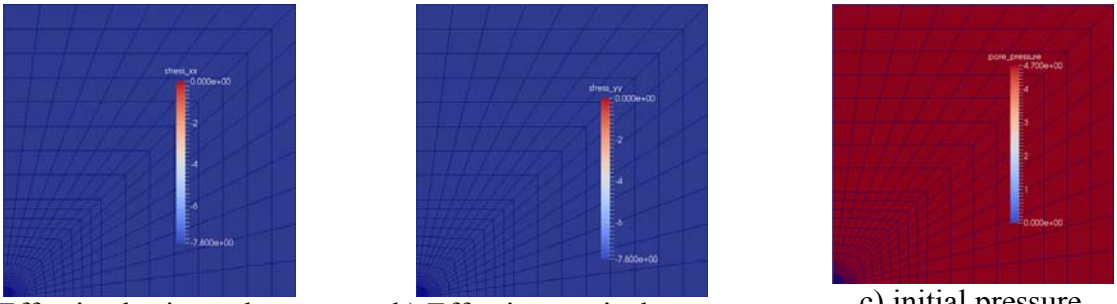

a) Effective horizontal stress b) Effective vertical stress c) initial pressure

Figure 2-11: The resuts of establishing initial effective stress in two directions

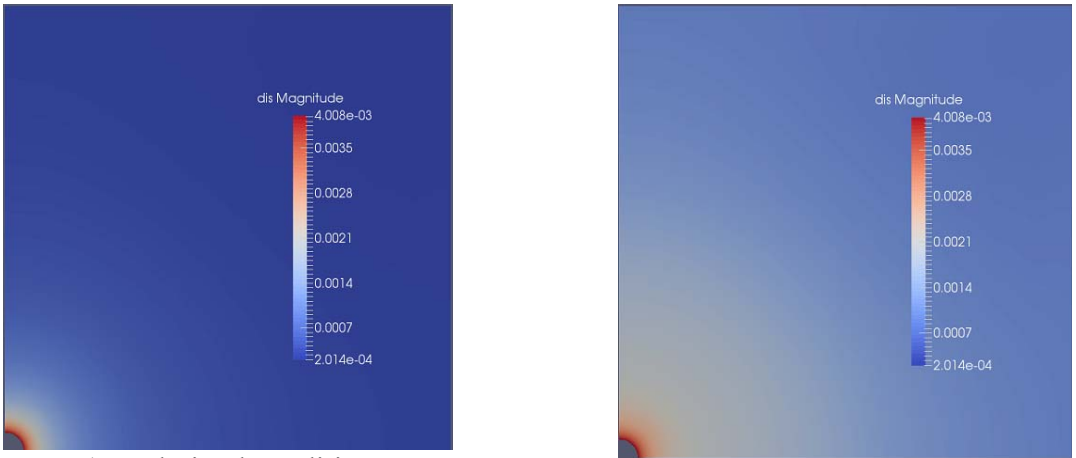

a) Undrained condition b) Drained condition

Figure 2-12: The resut of radial displacement

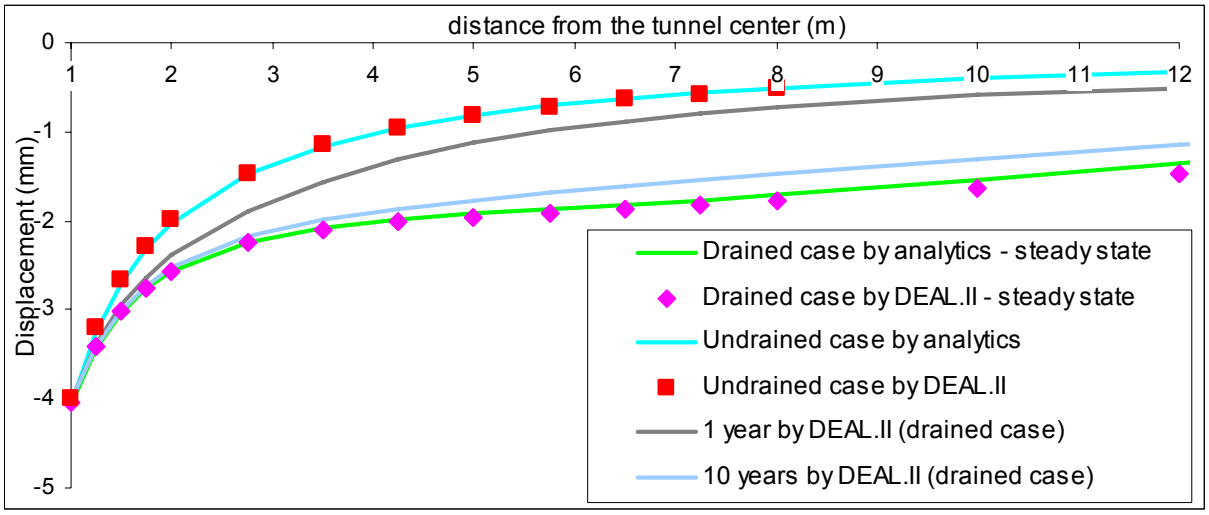

Figure 2-13: A comparison of radial displacement around tunnel

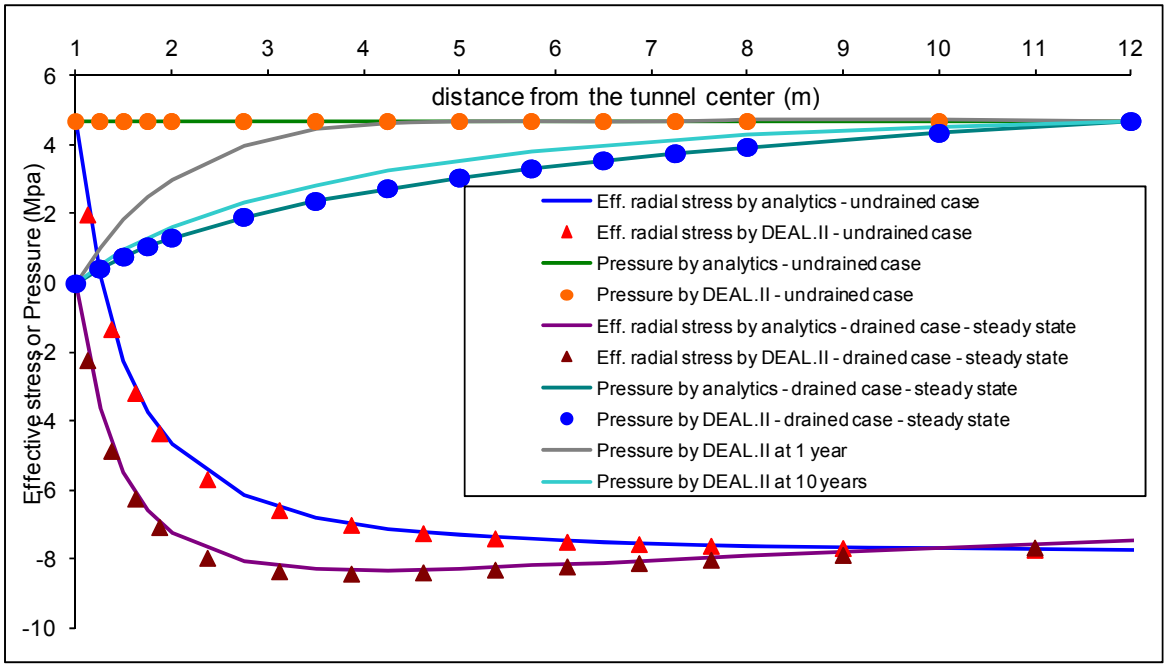

Figure 2-14: A comparison of radial effective stress and pressure of undrained case and drained condition

b) Deep tunnel in transversely isotropic porous medium

We consider in this part the deep tunnel excavated in a transversely isotropic porous medium. The simulation is carried out in the transient state of fluid flow and our obtained results by DEAL.II will be compared with the result furnished from the commercial code Flac3D (Itasca, 2006).

The initial condition, boundary conditions and geometry are similar as the previous problem in which initial stress $\sigma_V = \sigma_H = -12.5MPa$ (negative value of total stress denotes for compression), initial pore pressure $p_{ff} = 4.7Mpa$. Similarly, due to the symmetric of the problem only one-fourth of the geometry is used to model the tunnel of 1m of radius. All the necessary parameters of the transversely poro-elastic of the porous medium is summarized in table 2-5.

As the first results, in Figure 2-15 are highlighted the isovalues of the pore pressure and displacement around the tunnel taken at the instant of 1 hour after the excavation. A quite similar results can be observed from the isovalues. Furthers, in Figure 2-16 are illustrated the results of pore pressure and effective radials stress following the horizontal cut (Ox axis) and vertical cut (Oy direction) at the center of tunnel at different instants of 1 hour, 1day, 1 month, 1 year and 5 years after the excavation. These results are obtained from our developed HM module in DEAL.II and Flac3D. It shows that our results agree very well with ones conducted in Flac3D which demonstrated the accuracy of our developed code.

Symbol	Name	Value	Unit
$b_x=b_y$	Biot's coefficient	0.6	
E_x	Young's modulus in x-direction	5 600	MPa
E_y	Young's modulus in y-direction	4 000	MPa
ν_{xz}	Poisson's ratio	0.3	
ν_{yx}	Poisson's ratio	0.142	
G_{xy}	Shear modulus	1 600	MPa
M	Biot' modulus	8 676	MPa
K_{xx}	horizontal permeability	$4.0x10^{-20}$	m^2
K_{yy}	vertical permeability	$1.33x10^{-20}$	m^2

Table 2-5 Parameters of tunnel excavation problem in transversely isotropic material

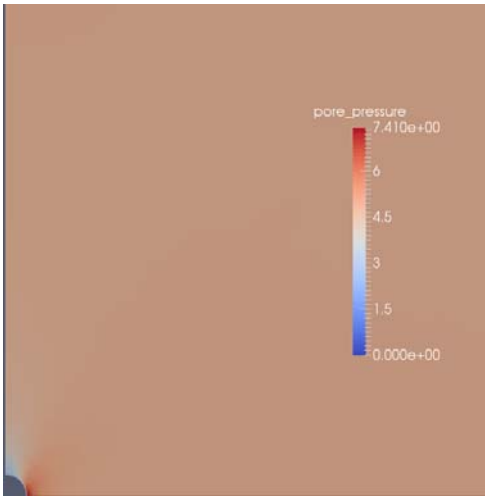

a) Pore pressure by DEAL.II

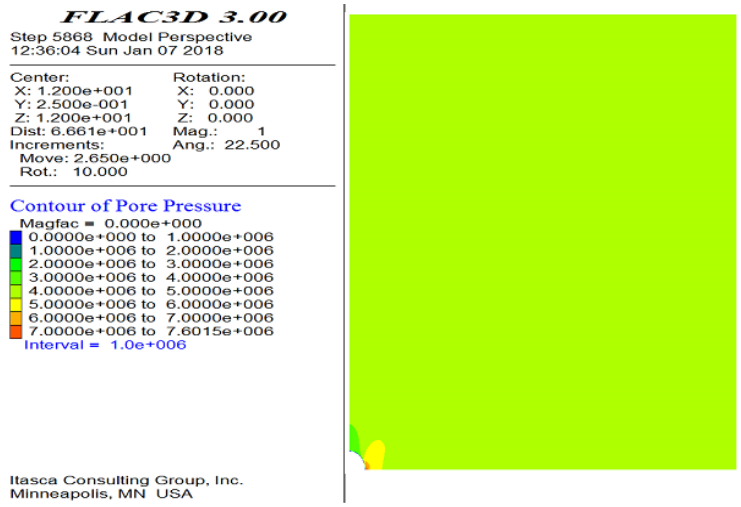

b) Pore pressure by Flac3D

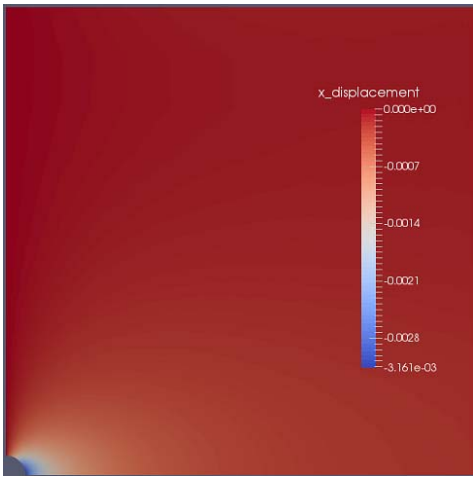

c) x-displacement by DEAL.II

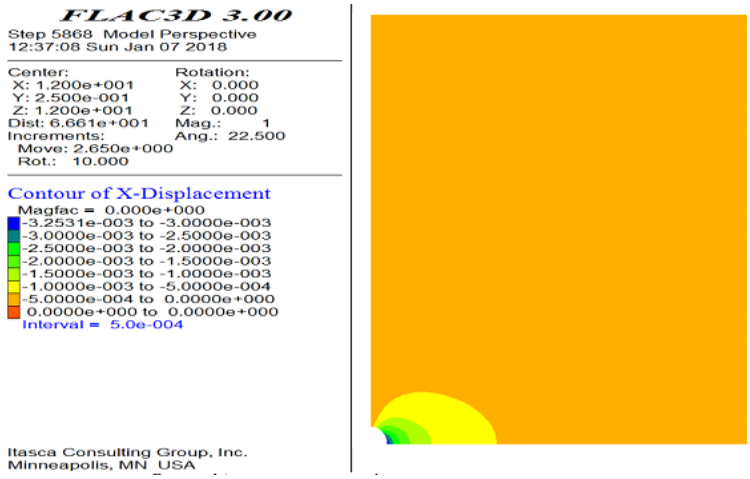

d) x-displacement by Flac3D

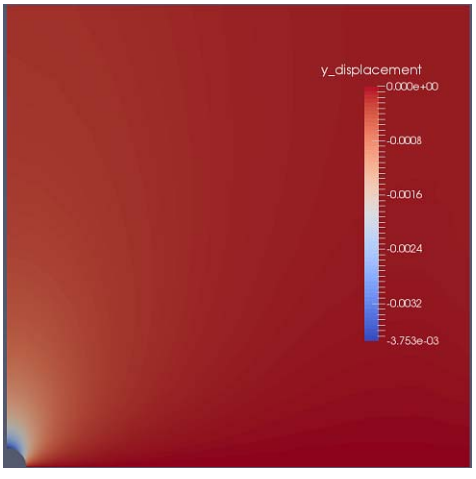

e) y-displacement by DEAL.II

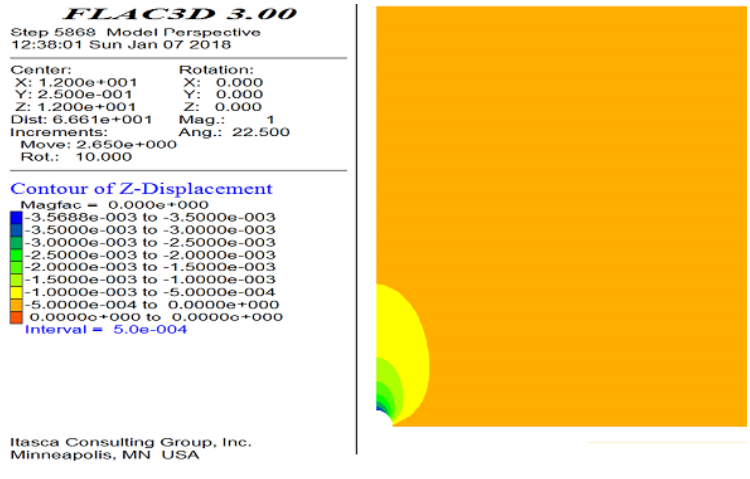

f) y-displacement by Flac3D

Figure 2-15: Isovalue of pore pressure and displacement: left by the developed code (DEAL.II) and right by Flac3D

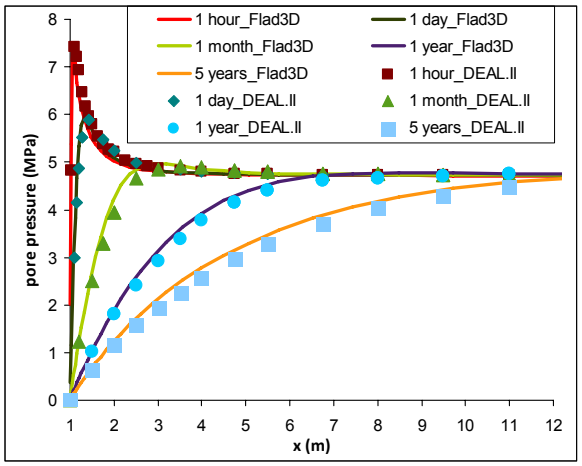

a) Pore pressure of x-axis

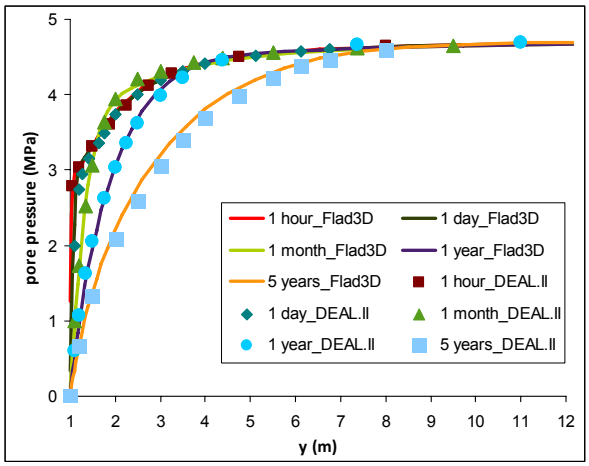

b) Pore pressure of y-axis

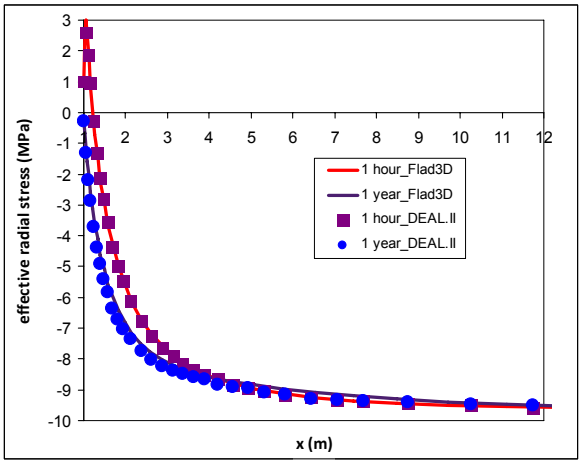

c) effective radial stress of x-axis

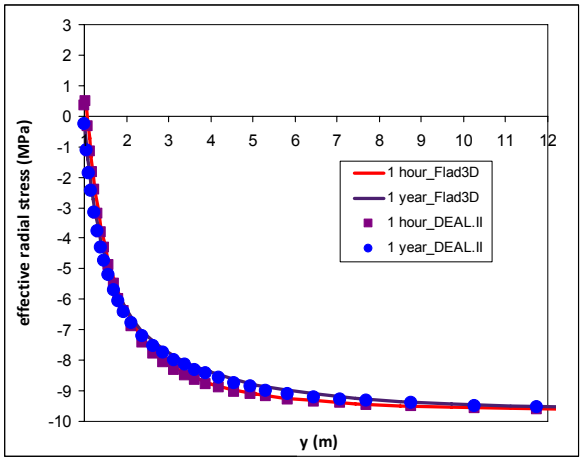

d) effective radial stress of y-axis

Figure 2-16: Pore pressure, effective radial stress at two sections: x-axis (left) and y-axis (ritght)

2.6 Summary

In this chapter, we developed a code in the frameworks of hydro mechanical coupling in which four mains item were done:

- Expand the two current steps of DEAL.II (step 26 for diffusion equation and step 8 for linear mechanical equation) for isotropic material into transversely isotropic material. Variety initial conditions were added: as default or by balance calculation.

- Couple the two above steps (step 26 and step 8) into hydro mechanical coupling calculation with two kinds of coupling: one-way coupling (H->M) and two-way coupling (H<->M).

- Control all input data (mesh, materials, boundary conditions, time step calculation, post-processing, etc…) by txt file outside of code body. Hence, it helps user easy to run the code.

- Validate the code with the known analytical solutions and show that the code runs correctly.

CHAPTER 3: FRACTURE MODELING IN POROUS MEDIUM: EMBEDDED FRACTURE CONTINUUM APPROACH

3.1. Introduction

Fractured media modeling is usually conducted through two main approaches such as the continuum and discontinuum approach (Sahimi, 2011; Min and Jing, 2003; Min et al 2004a,b; Jaeger, Cook & Zimmerman, 2007; Marmier 2007; Botros et al., 2008; Rutqvist et al., 2013; Lei 2016). In the former approach, the fractured medium is replaced by an equivalent continuum medium whose properties are derived from the upscaling procedure by using a homogenization technique. Thus, for this latter approach, the effect of fractures is implicitly accounted for in the equivalent constitutive model that can be described by the principles of continuum mechanics. This approach has the advantage for solving problems of large scales with the high densities of fractures but its results may be sensitive to the domain's size especially when the studied domain smaller than the representative elementary volume (Rutqvist et al., 2013). Otherwise, the homogenization-based continuum model may not take into account the connectivity effect of fractures, the effect of clustering and spatial distribution of fractures or the individual characteristics of a fracture since these characteristics are, at best, taken into account through some statistical features of all crack sets.

In the second approach, the fractured medium is represented as an assemblage of blocks (discrete elements) bounded by a number of intersecting discontinuities (Sahimi, 2011; Min and Jing, 2003; Min et al 2004a,b; Jiang & Younis, 2015; Lei 2016). The overall behaviour of the fractured medium is mainly affected by the interactions between the matrix blocks and fractures (interface between blocks). Even if this approach can better investigate the behaviour of fractured medium at small scale, it can be very expensive on computer memory and time simulation particularly for the problem at large scale. It is the principal reason that this approach has not been widely used in the industry for field-scale reservoir simulation.

To overcome the limitation as well as to take advantage of these two-mentioned approaches, another method which borrows the concept of continuum models and also incorporates the effect of fractures explicitly was introduced. In the literature, it could be known as the "fracture continuum approach" (Svensson, 2001; McKenna & Reeves, 2006; Reeves et al., 2008a,b; Botros et al., 2008; Hao et al., 2012; Kalinina et al., 2014), "fracture-cell model" (Sakhaee-Pour & Wheeler, 2016; Gong, 2016) or "embedded discrete fracture model" (Lee et al., 2010; Li & Lee 2008; Moinfar 2013; Shakiba, 2014; Xu 2015; Yan et al. 2016). The common point of these studies which represents also the principal idea of this kind of

approach lies on the concept of fracture cell which represents the grid cell of the discretized medium that are intersected by one or many fractures in the medium. Each fracture cell presents a porous medium that has their own properties calculated from the contributed properties of intact matrix and fractures and hence the behaviour of fracture cell can be different with respect to the intact matrix. This approach was applied with success particularly to study the flow problem (Svensson, 2001; McKenna & Reeves, 2006; Reeves et al., 2008; Botros et al., 2008; Sakhaee-Pour & Wheeler, 2016; Gong, 2016) or coupled flow and heat transfer process (Hao et al., 2012; Kalinina et al., 2014) in the fractured reservoir. Some applications were recently conducted for the coupled hydro-mechanical problem (Moinfar, 2013; Moinfar et al., 2013; Figueiredo et al., 2015; 2017).

In this work, this last approach, call hereafter as the embedded fracture continuum approach (EFC) is chosen to study the couple hydro-mechanical behaviour of the fractured porous media. The structure of this chapter is organized as follows. Following this introduction, we will detail the fracture cell concept and its implementation in the code DEAL.II. Next the question of how to determine the equivalent (poro-elastic and hydraulic) properties of fracture cell is addressed. Finally, some verification tests that aim to validate the implementation of the embedded fracture continuum approach in the code cloture the chapter.

3.2. Implementation of embedded fracture continuum approach in DEAL.II

The principal idea of the embedded fracture continuum approach lies on the concept of fracture cell and its properties by taking into account the contribution of the embedded fracture in the cell. We recall that a fracture cell as defined in the literature (Svensson, 2001; McKenna & Reeves, 2006; Reeves et al., 2008; Botros et al., 2008; Sakhaee-Pour & Wheeler, 2016; Gong, 2016) represents a grid cell (continuum homogenous media) that is intersected at least by one fracture. Otherwise to distinguish from the fracture cell we call the grid cells that are not intersected by any fracture as matrix cell as illustrated in Figure 3-1. The matrix cell represents a porous media (porous matrix) and hence it has the physical properties of this porous matrix. Due to the presence of fracture, the properties of fracture cell which are no longer ones of the porous matrix will be determined as properties of an equivalent porous medium which will be detailed in the next section.

Based on the fracture-cell concept, the simple mesh such as the Cartesian mesh will be used in the embedded fracture continuum approach. However, in some previous works (Svensson, 2001; McKenna & Reeves, 2006; Reeves et al., 2008; Botros et al., 2008; Moinfar, 2013; Moinfar et al., 2013; Sakhaee-Pour & Wheeler, 2016; Gong, 2016; Figueiredo et al., 2015; 2017) it shown that a quite fine mesh is usually required to satisfy the computational error

tolerance and to fit at some acceptable levels the real geometry of fractures. This could lead to very heavy numerical calculation. In order to satisfy the exigencies of the tolerated numerical error, and minimize the number of degree of freedom (D.O.F) of numerical models in many cases one use some local mesh refining strategies (a global refinement would lead to a great number of D.O.F). For this aim, in this work, a local refinement technique based on the hanging node method is used.

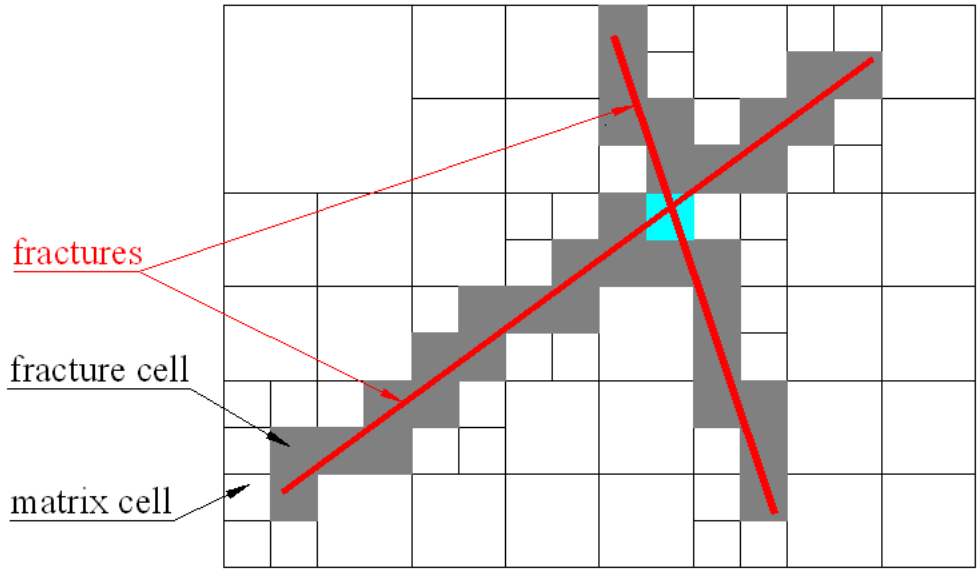

Figure 3-1: Sketch of fracture-cell and matrix cell concept with hanging nodes obtained from the local refinement of mesh.

Local refinement using the hanging node in DEAL II

It is well known that there are three basic approaches available for the refinement of mesh (Karlsson, 2012). The first approach is h-adaptivity in which the mesh connectivity is changed and refined by adding points, thus reducing the size of the cell. The second approach is p-adaptivity which is obtained by increasing or decreasing the order of accuracy of the underlying numerical scheme, thus the mesh connectivity is remained in this second method. The last approach is r-adaptivity in which both the mesh connectivity and order of accuracy are kept constant but the points are repositioned to minimize the computational error. In numerical practice, h-adaptivity is the most common used scheme and is known as adaptive mesh refinement. For example, we want to get more accuracy of results at the point “A” by refinement technique (Figure 3-2a). Numerous refined nodes need to be added if h-adaptivity is used. Hence, the total degree of freedoms is increase rapidly (Figure 3-2b). The number of nodes is remained for other methods, but the polynomial degree (p) is increase in p-adaptivtiy and reposition of nodes is required in r-adaptivity (Figure 3-2c,d).

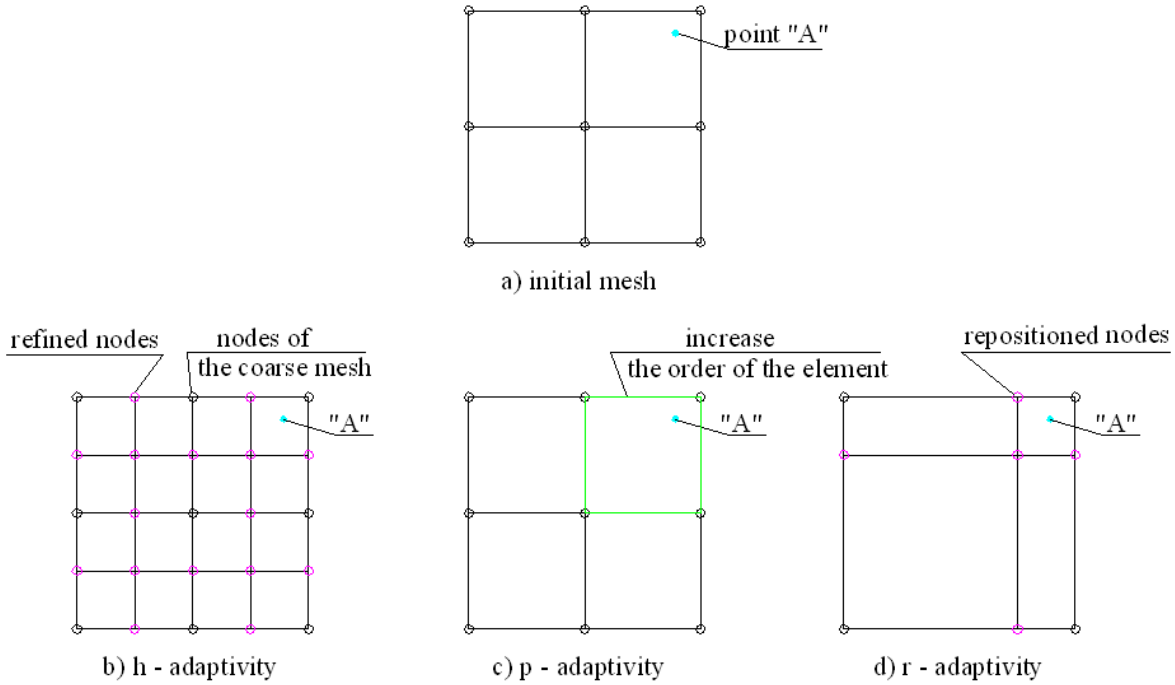

Figure 3-2. Three approaches for mesh refinement: h-adaptivity, p-adaptivity and r-adaptivity

In DEAL.II the adaptive mesh refinement (called also as local refinement of mesh) is based on the hanging node technique (Rheinboldt and Mesztenyi, 1980; Demkowicz et al., 1989; Bornemann et al., 1993; Bangerth and Kanschat, 1999; Bangerth et al., 2007; Heister, 2011 and Karlsson, 2012). This adaptive meshing refinement is the one of the original goals developed in DEAL.II (Bangerth and Kanschat, 1999; Bangerth et al, 2007). Otherwise, when performing an adaptive mesh refinement, we usually distinct two kinds of refinement: isotropic and anisotropic refinement (Karlsson, 2012). In isotropic mesh refinement, the mesh is refined in all directions (for example one quadrilateral is split into four quadrilaterals) while anisotropic mesh is refined in only one direction (a quadrilateral gets split into two following one direction). Isotropic mesh refinement is provided in DEAL.II

The notion of hanging nodes is used to represent the irregular nodes. If one cell is refined while its neighbor is not refined, the face between the two cells has an irregular point. We recalled the definition of regular and irregular point by Demkowicz et al (1989) in which a point is called regular if it constitutes a vertex (corner) for each of the neighboring cells; otherwise it is irregular. In two-dimensional meshes, the index of irregularity is the maximum number of irregular nodes on an element face: for example, meshes which has the index of irregularity equaled to one are called 1-irregular meshes. In this case, the point connecting the neighbor and the two refined cells is called a “hanging node” (Karlsson, 2012). An example of a hanging node in 2D is sketched in Figure 3-3 in which point 8, 9 are hanging nodes. The 1-irregular meshes were proposed and implemented in DEAL.II.

Corresponding to the local refinement using the hanging node technique, triangulation objects in DEAL II do not only store the respective finest cells but also their (now inactive) ancestors. As consequence, a triangulation has information of a collection of trees, where the cells of the coarsest mesh form the roots and children branch of their parent cells. DEAL.II supports regular (bisection) refinement of cells, leading to 2, 4, or 8 children per cell in 1D, 2D, and 3D, respectively (Bangerth et al., 2007). Thus, the cells in DEAL.II can be formed binary trees, quad-trees, or oct-trees, respectively. A simple example of an adaptively refined 2D mesh along with its tree of cells is shown in Figure 3-4. Such triangulation can be read from a file (with different accepted formats in DEAL.II) or can be started from a coarse mesh which will be refined recursively (global refinement or local refinement) by users (Bangerth and Rannacher, 2003).

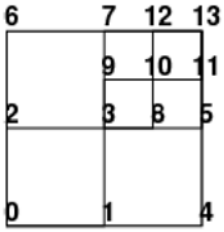

Figure 3-3. An example of global enumerations of degrees of freedom on the mesh for Q1 elements with each node has one degree of freedom (Bangerth and Kanschat, 1999)

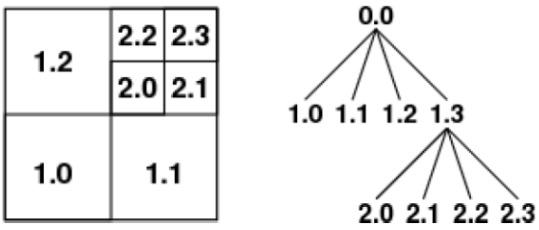

Figure 3-4. A simple two-dimensional mesh with cells number based on their refinement level and index within a level (left) and the corresponding quad-tree of cells (right) (Bangerth and Kanschat, 1999)

One of the most important point in the local refinement is to ensure the consistency the finite element functions between the refined and the coarse part of the mesh. The most common technique is the transition elements (Bornemann et al 1993) which are however complicated or impossible to construct for all-quadrilateral and all-hexahedral meshes in the 3D case (Bangerth and Kanschat, 1999; Bangerth et al, 2007). Instead, in DEAL.II the adopted technique based on hanging nodes ensures this consistency by using the additional constraints in the linear system (Rheinboldt and Mesztenyi, 1980). Such constraints will be computed for all faces with hanging nodes and all conforming finite element spaces and then they will be gathered into a system of constraints represented by constraint matrix (see details in Bangerth et al, 2007). As an example, let's consider the cell mesh presented in Figure 3-4 in the

context of classical Laplacian problem when each node has one degree of freedom. The finite element function written in this cell is (Bangerth et al, 2007):

$$u_h(x) = \sum_{i=0}^{13} U_i \varphi(x) \tag{3.1}$$

where

x is the point in the cell,

U_i is the degree of freedom (numbering from 0 to 13 as shown in Figure 3-3),

$\varphi(x)$ is the interpolation function

The consistency of structure is ensured by using the following constraint equations at two nodes 8 and 9.

$$U_8 = \frac{1}{2}U_3 + \frac{1}{2}U_5 \quad \text{and} \quad U_9 = \frac{1}{2}U_3 + \frac{1}{2}U_7 \tag{3.2}$$

Such constraints need to be computed for all faces with hanging nodes and all conforming finite element spaces also. Then, they can be combined into a system $\mathbf{CU=0}$ of constraints.

In case of no hanging node in the system, all components of matrix $\mathbf{C}$ should be zero. On other hand, in case of there are some hanging nodes, for the simple example above, the matrix $\mathbf{C}$ should have the components corresponding to the D.O.F of these hanging nodes. In this case, the matrix $\mathbf{C}$ would have the form:

$$\mathbf{C} = \begin{pmatrix} 0 & 0 & 0 & -1/2 & 0 & -1/2 & 0 & 0 & 1 & 0 & 0 & 0 & 0 & 0 \\ 0 & 0 & 0 & -1/2 & 0 & 0 & 0 & -1/2 & 0 & 1 & 0 & 0 & 0 & 0 \end{pmatrix} \tag{3.3}$$

Note: the equation (3.3) shows only the two rows 8 and 9 of the constraint matrix $\mathbf{C}$

Workflow to model explicitly fractures in the porous medium

With all above fracture-cell, matric cell concept and hanging node technique to refine locally the mesh, we can extend easily the hydro-mechanical code in DEAL.II as developed in chapter 2 to model explicitly the embedded fractures in the porous medium. Concretely, each matrix cell or fracture-cell in our model now represent a porous medium. For the sake of clarity, in Figure 3-6 is resumed our procedure to model fracture based on of the embedded fracture continuum approach in DEAL.II. In detail, from the global coarse mesh which can be imported from a text file (for example an ".inp" file), the fracture network will be explicitly defined in the model. Then another input text file (.txt file) including all necessary geometric information of fractures like the center, length, width and oriented angle is imported defining characteristics of each crack/fracture. All cells intersected by the fractures netwok will be found automatically and then the local refinement is applied to refine these cells around

fractures while the level of local refinement is controlled by users. Figure 3-5 shows as an example an embedded fracture which can be modeled with the differential level of local refinement. Based on the properties of the matrix and fracture, the equivalent properties of fracture-cell are calculated and distributed to each fracture-cell.

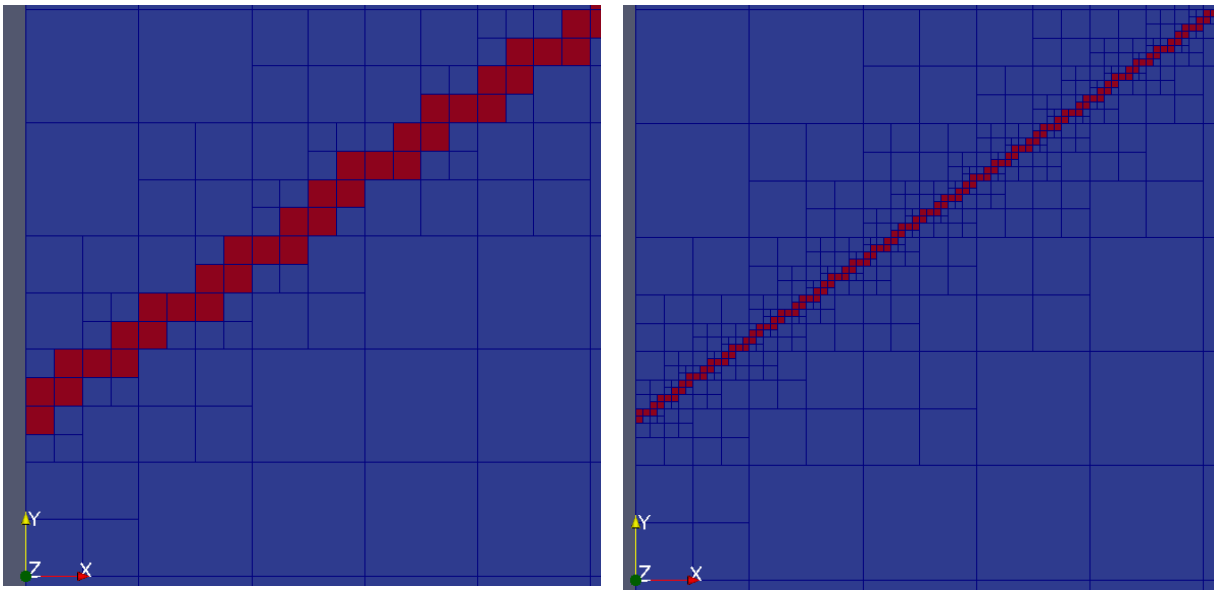

Figure 3-5: Fracture-cell elements with the differential level of local refinement: two times of local refinement (on the left) and four times of local refinement (on the right) with respect to the global mesh.

Note: red elements denote fracture-cell elements and blue elements denote matrix elements.

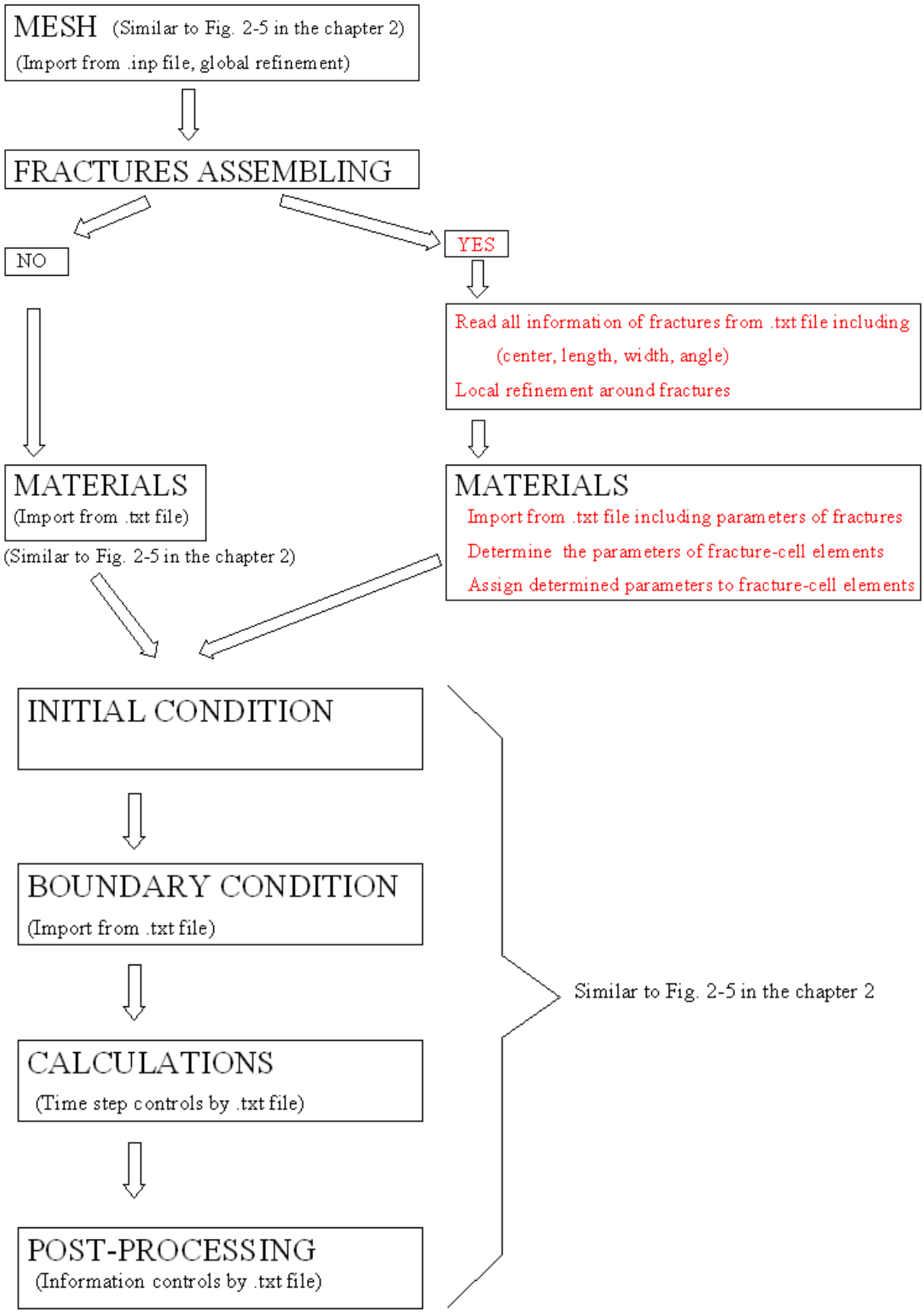

Figure 3-6: Structure of assembling fractures into the hydro mechanical coupling code.

3.3. Determination of the equivalent properties of fracture cell

In this part, the determination of the equivalent poro-elastic and hydraulic properties of the fracture cell will be presented. In general, we distinguish two types of fracture-cell: type I represents the cell intersected by only one fracture while type II gather all fracture-cells intersected by multiple fractures (more than one fracture) as indicated in figure (3-6).

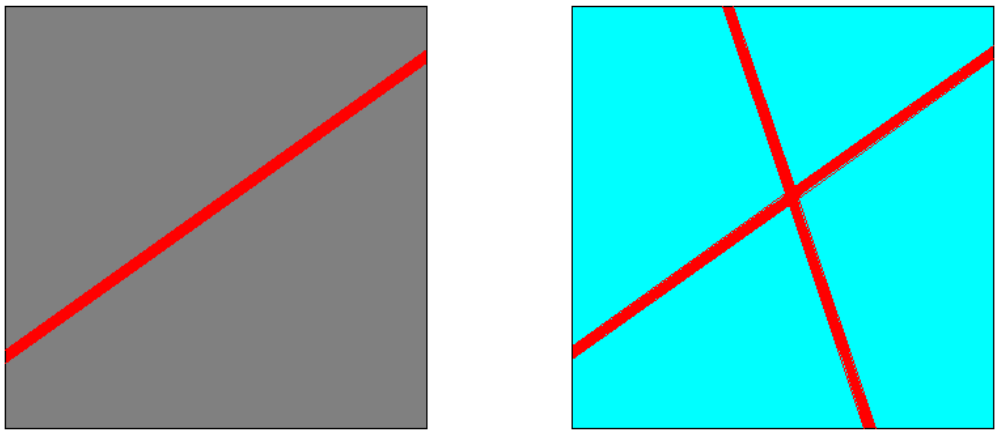

(a) (b)

Figure 3-7 Two types of fracture cells: type I represents cell intersected by only one fracture (a) and type II indicates cell intersected by more than one fracture (b).

3.3.1. Equivalent poro-elastic properties of fracture cell

Equivalent poro-elastic based on micromechanical solution

In the literature, some scholars (Rutqvist et al., 2013; Figueiredo et al., 2015) attempt to determine the equivalent properties of fracture-cell by using the micromechanical solution. As for instance, in their study (Rutqvist et al., 2013) divided the fractured domain into different elements and they used the Oda's crack tensor theory to calculate the upscaled properties for each element. By comparing the results with the alternative DFN models, a reasonably good agreement was observed by these authors. However, the authors pointed out that some difficulties can be encountered in this approach based on the Oda's crack tensor when the size of element becomes small or/and only one or a few fractures intersect the element. Recently, Figueiredo and collaborators (Figueiredo et al., 2015, Figueiredo et al., 2017) propose to determine the Young's modulus of the elements intersected by a fracture from the following equation:

$$\frac{1}{E^{fc}} = \frac{1}{E_m} + \frac{1}{k_n h} \tag{3.4}$$

where E_m, k_n and h indicate respectively the Young's modulus of intact matrix, the normal stiffness of fracture and the element size.

In effect, this formula is extracted from the solution of the joint model as detailed below. It is important to note that in their works, Figueiredo and co-authors (Figueiredo et al., 2015, Figueiredo et al., 2017) assumed that the equivalent properties are isotropic and homogeneous for all fracture cells. However, the determination of other equivalent poroelastic properties like the Biot coefficient and Biot's modulus was not discussed in the above-mentioned reference. To validate the proposed solution, Figueiredo and co-authors (Figueiredo et al., 2015, Figueiredo et al., 2017) compared their numerical results with the analytical solution in a simple case of one vertical and completely open fracture. The difference of stress concentration near the fracture smaller than 5% was observed following these authors.

Although that the application of the micromechanical solution on determining the equivalent properties of the fracture-cell is questionable, particularly for small cell which usually violates the condition of the existence of a representative elementary volume (REV), we can state however its efficiency as demonstrated in the above-mentioned works. While the micromechanical approach based on the Oda's crack tensor is a good choice for the medium with high density of fractures embedded in a quite large fracture-cell, the joint model seems to be more appropriate for small cell with only one or few fractures intersected the element. This observation is consistence with the discussion of (Maghous et al. 2011) who studied the poroelastic behaviour of jointed rock by using micromechanics approach. Following these authors, the homogenization techniques based on the well-known Eshelby's theory (Eshelby 1957) can be used for short joints as a limiting situation of embedded ellipsoidal inclusions (known as cracked medium) while for the long joints cross-cutting the REV, the joint model is suggested.

In this work, because the fracture cell's size conducted in our work will be small (by using the hanging node technique to refine mesh) and each cell can be intersected with only one or few fractures, the joint model will be chosen. The detail about this type of model was largely discussed in the literature (see Maghous et al. 2011 and different references cited therein), hence in what it follows, only some important results of this model will be captured. Otherwise, in our study, we assume that all the joints have the same Biot coefficient (which is equal to 1) while the Biot modulus of fracture is very large, thus the overall poro-elastic properties of the jointed medium can be written as follow (Maghous et al. 2011):

$$
\begin{aligned}
&\mathbb{S}^{\hom} = \mathbb{S}^{m} + \sum_{i} \mathbb{S}^{i};\\
&\mathbb{S}^{i} = \frac{1}{d_i.k_n^i}\underline{n}_i \otimes \underline{n}_i \otimes \underline{n}_i \otimes \underline{n}_i + \frac{1}{d_i.k_t^i}\underline{t}_i \overset{s}{\otimes} \underline{n}_i \otimes \underline{t}_i \overset{s}{\otimes} \underline{n}_i + \frac{1}{d_i.k_t^i}\underline{t}_i' \overset{s}{\otimes} \underline{n}_i \otimes \underline{t}_i' \overset{s}{\otimes} \underline{n}_i;\\
&\mathbb{B}^{\hom} = \mathbb{I} : (\mathbb{I} - \mathbb{S}^{m} : (\mathbb{S}^{\hom})^{-1});\\
&\frac{1}{M^{\hom}} = \mathbb{I} : \mathbb{S}^{m} : \mathbb{B}^{\hom};
\end{aligned}
\tag{3.5}
$$

where $\mathbb{S}^{\hom}$, $\mathbb{S}^{m}$, $\mathbb{S}^{i}$ are respectively the compliance tensor of the overall medium, intact matrix and i^{th} joint family; $k_n^{\,i}$ and $k_t^{\,i}$ designate the normal and shear stiffness while $\underline{n}_i$, $\underline{t}_i$ and $\underline{t}_i'$ indicate the unit normal and tangential vectors and the parameter d_i is the spacing of the i^{th} joint set.

We consider now as the simplest case a fracture-cell intersected by one horizontal fracture (the normal vector of the fracture is parallel to the vertical axis $\underline{n}=\underline{e}_3$). Supposing that the isotropic intact matrix is characterized by the elastic modulus (E_m,ν_m and $G_m = E_m/(2(\nu_m+1))$, we can deduce without difficulty from equation (3.5) the equivalent poro-elastic properties of the fracture cell which belong to the transversely isotropic material class:

$$
\begin{aligned}
&E_1^{fc} = E_2^{fc} = E_m;\\
&\frac{1}{E_3^{fc}} = \frac{1}{E_m} + \frac{1}{k_n d};\\
&\nu_{12}^{fc} = \nu_m;\\
&\frac{1}{\nu_{31}^{fc}} = \frac{1}{\nu_m}(1 + \frac{E_m}{k_n d});\\
&\frac{1}{G_{23}^{fc}} = \frac{1}{G_m} + \frac{1}{k_t d};\\
&b_1^{fc} = b_2^{fc} = \frac{\nu_m E_m}{E_m(1-\nu_m) + k_n d(1-2\nu_m)(1+\nu_m)};\\
&b_3^{fc} = \frac{(1-\nu_m)E_m}{E_m(1-\nu_m) + k_n d(1-2\nu_m)(1+\nu_m)};\\
&M^{fc} = k_n d + \frac{(1-\nu_m)E_m}{(1-2\nu_m)(1+\nu_m)};
\end{aligned}
\tag{3.6}
$$

For the more general case of the fracture-cell intersected by an inclined fracture (fracture cell *type I*) as shown in Figure 3-8**,** its equivalent properties in the global reference ($\underline{e}_1, \underline{e}_2, \underline{e}_3$) can be determined from ones calculated in the local coordinate system associated with the fracture ($\underline{n}$, $\underline{t}$, $\underline{t}'$) by rotating an angle θ (with $\theta \in [0, \pi]$) around the horizontal axis $\underline{e}_1$. Note that in the local reference ($\underline{n}$, $\underline{t}$, $\underline{t}'$), the equivalent poroelastic of fracture cell are calculated directly from ones obtained in the case of horizontal fracture (equation 3.6). The difference lies only on the spacing parameter d which is equal to the element size of element ($d=h$) in the case of horizontal fracture while for the inclined fracture it is calculated as:

$$
d = \begin{cases} h.|\cos\theta| & if \quad \theta \in [0, \pi/4] \cup [3\pi/4, \pi] \\ h.\sin\theta & if \quad \theta \in [\pi/4, 3\pi/4] \end{cases}
\tag{3.7}
$$

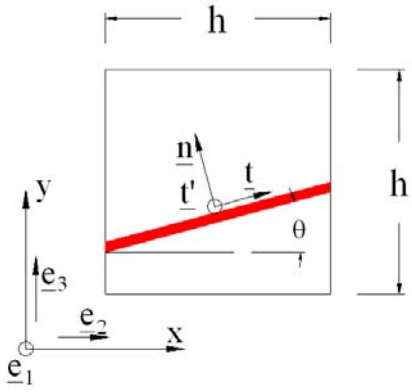

Figure 3-8: fracture-cell intersected by an inclined fracture which is characterized by an inclination angle θ ($\theta \in [0, \pi]$).

Then by rotating an angle θ around the horizontal axis $\underline{e}_1$, the equivalent poro-elastic properties of the fracture-cell intersected by inclined fracture in the global reference ($\underline{e}_1, \underline{e}_2, \underline{e}_3$) become anisotropic with the stiffness tensor (inverse of the compliance tensor) and Biot tensor written in the matrix form as follow:

$$\mathbb{C}^{fc} = \begin{pmatrix} C_{11} & C_{12} & C_{13} & C_{14} & 0 & 0 \\ C_{12} & C_{22} & C_{23} & C_{24} & 0 & 0 \\ C_{13} & C_{23} & C_{33} & C_{34} & 0 & 0 \\ C_{14} & C_{24} & C_{34} & C_{44} & 0 & 0 \\ 0 & 0 & 0 & 0 & C_{55} & C_{56} \\ 0 & 0 & 0 & 0 & C_{56} & C_{66} \end{pmatrix}; \quad \mathbb{B}^{fc} = \begin{pmatrix} b_{11} & 0 & 0 \\ 0 & b_{22} & b_{23} \\ 0 & b_{23} & b_{33} \end{pmatrix}; \tag{3.8}$$

The non-zero components of the compliance tensor, Biot tensor as well as the Biot modulus of the fracture-cell which are function of the elastic modulus (E_m, ν_m) of intact matrix, the mechanical properties (k_n, k_t) of fracture and the inclination angle θ are written in the global coordinate system ($\underline{e}_1, \underline{e}_2, \underline{e}_3$) as:

$$
\begin{aligned}
&S_{11}^{fc}=\frac{1}{E_m};S_{12}^{fc}=S_{21}^{fc}=S_{13}^{fc}=S_{31}^{fc}=-\frac{\nu_m}{E_m};\\
&S_{22}^{fc}=\frac{1}{E_m}+\frac{\cos^2\theta.\sin^2\theta}{k_t.d}+\frac{\sin^4\theta}{k_n.d};S_{23}^{fc}=-\frac{\nu_m}{E_m}-\frac{(k_n-k_t)\cos^2\theta.\sin^2\theta}{k_n.k_t.d};\\
&S_{24}^{fc}=\frac{\sin 2\theta(k_t+(k_n-k_t)\cos 2\theta)}{4k_n.k_t.d};S_{33}^{fc}=\frac{1}{E_m}+\frac{\cos^2\theta.\sin^2\theta}{k_t.d}+\frac{\cos^4\theta}{k_n.d};\\
&S_{34}^{fc}=\frac{\sin 2\theta(k_t-(k_n-k_t)\cos 2\theta)}{4k_n.k_t.d};\\
&S_{44}^{fc}=\frac{E_m(k_n+k_t)+4k_n.k_t.d(1+\nu_m)+E_m(k_n-k_t)\cos 4\theta}{8E_m.k_n.k_t.d};\\
&S_{55}^{fc}=\frac{1}{4}(\frac{1}{G_m}+\frac{\cos^2\theta}{k_t.d});S_{56}^{fc}=\frac{\sin 2\theta}{8k_t.d};S_{66}^{fc}=\frac{1}{4}(\frac{1}{G_m}+\frac{\sin^2\theta}{k_t.d});\\
&b_{11}^{fc}=\frac{\nu_m E_m}{E_m(1-\nu_m)+k_n.d(1-2\nu_m)(1+\nu_m)};\\
&b_{22}^{fc}=\frac{1}{2}\frac{E_m(1-(1-2\nu_m)\cos 2\theta)}{E_m(1-\nu_m)+k_n.d(1-2\nu_m)(1+\nu_m)};\\
&b_{23}^{fc}=\frac{1}{2}\frac{E_m(1-2\nu_m)\sin 2\theta}{E_m(1-\nu_m)+k_n.d(1-2\nu_m)(1+\nu_m)};\\
&b_{33}^{fc}=\frac{1}{2}\frac{E_m(1+(1-2\nu_m)\cos 2\theta)}{E_m(1-\nu_m)+k_n.d(1-2\nu_m)(1+\nu_m)};\\
&M^{fc}=k_n.d+\frac{E_m(1-\nu_m)}{(1-2\nu_m)(1+\nu_m)};
\end{aligned}
\tag{3.9}
$$

For the fracture-cell intersected by multiple fractures (fracture cell *type II*), its equivalent poro-elastic properties using the solution of joint model (equation 3.5) own the same anisotropic characteristic as case of *type I*. Similarly, for fracture cell *type II,* its compliance tensor, Biot tensor and Biot modulus depend on the elastic modulus (E_m, ν_m) of intact matrix, the mechanical properties (k_n^i, k_t^i) as well as the corresponding inclination angle θ_i^i of each fracture *i* that intersect the cell.

Masonry model

The joint model as presented previously is largely used in the literature to model crack/fracture or default owing a small aperture with respect to the large size of the studied domain. It means that in our context, the width of fracture (w) is small with respect to the size h of fracture cell. However, if the fracture's aperture is comparable with the size of cell, the simplified solution of joint model is not adequate. In this latter case, the solution using in the masonry model (see for example Rekik and Lebon, 2012 and references cited therein) may be more appropriate. Following that, the effective transversely isotropic properties coinciding to vertical direction $\underline{e}_3$ (see Appendix A of Rekik and Lebon, 2012) of the stratified brick/mortar (see Figure 3-9) can be deduced as follows:

(3.10)

$$E_1^{\hom} = E_2^{\hom} = \frac{[E_f w(\nu_m - 1) + E_m(h-w)(\nu_f - 1)][E_f w(\nu_m + 1) + E_m(h-w)(\nu_f + 1)]}{h[E_f w(\nu_m - 1)(\nu_m + 1) + E_m(h-w)(\nu_f - 1)(\nu_f + 1)]};$$

$$E_3^{\hom} = \left\{ \frac{(h-w)w\left[E_f^2(\nu_m + 1)(2\nu_m - 1) + E_m^2(\nu_f + 1)(2\nu_f - 1)\right]}{E_m E_f h\left[E_f w(\nu_m - 1) + E_m(h-w)(\nu_f - 1)\right]} \right.$$

$$\left. + \frac{h^2(\nu_f - 1) - 2h.w(2\nu_m\nu_f + \nu_f - 1) + w^2(4\nu_m\nu_f + \nu_m + \nu_f - 2)}{h\left[E_f w(\nu_m - 1) + E_m(h-w)(\nu_f - 1)\right]} \right\}^{-1};$$

$$\nu_{12}^{\hom} = \nu_{21}^{\hom} = \frac{E_f w(\nu_m - 1)(\nu_m + 1)\nu_f + E_m(h-w)(\nu_f - 1)(\nu_f + 1)\nu_m}{E_f w(\nu_m - 1)(\nu_m + 1) + E_m(h-w)(\nu_f - 1)(\nu_f + 1)};$$

$$\nu_{31}^{\hom} = \nu_{32}^{\hom} = \left\{ \frac{(h-w)w\left[E_f^2(\nu_m + 1)(2\nu_m - 1) + E_m^2(\nu_f + 1)(2\nu_f - 1)\right]}{E_m E_f h\left[w(\nu_m - \nu_f) + h\nu_m(\nu_f - 1)\right]} \right.$$

$$\left. + \frac{h^2(\nu_f - 1) - 2h.w(2\nu_m\nu_f + \nu_f - 1) + w^2(4\nu_m\nu_f + \nu_m + \nu_f - 2)}{h\left[w(\nu_m - \nu_f) + h\nu_m(\nu_f - 1)\right]} \right\}^{-1};$$

$$G_{23}^{\hom} = \left(\frac{h-w}{h.G_m} + \frac{w}{h.G_f} \right)^{-1};$$

Where E_m, ν_m, G_m (and E_f, ν_f, G_f) are the Young's modulus, Poisson's ratio and shear modulus of brick (corresponding mortar).

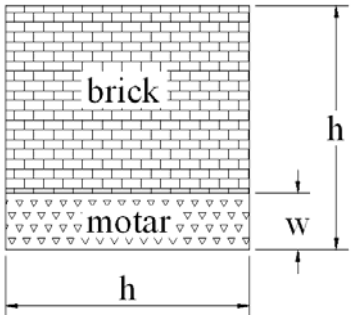

Figure 3-9: Masonry stratified brick/mortar model: the equivalent properties of the homogenized medium are calculated from the properties of brick and mortar (Rekik and Lebon, 2012)

Application in our study, brick represents the intact matrix while mortar can be considered as the fracture. Note that, for the fracture of width w we have the following relationships between the Young's modulus, Poisson's ratio, shear modulus (E_f, ν_f, G_f) and the normal and shear stiffness of joint (k_n, k_t) as follows:

$$E_f = \frac{(3k_n - 4k_t)k_t w}{k_n - k_t}; \nu_f = \frac{k_n - 2k_t}{2(k_n - k_t)}; G_f = w.k_t \tag{3.11}$$

Thus from the equations (3.10) and (3.11) we obtain the equivalent mechanical properties of fracture-cell as function of the mechanical properties of intact matrix (E_m, ν_m, G_m), normal and shear stiffness (k_n, k_t) of joint, fracture's aperture w and cell size h. Knowing the compliance tensors of matrix and of the overall medium, the coupling hydro-mechanical properties (Biot coefficients and Biot modulus) can be then calculated using the formula presented in equation

(3.5). Particularly, as a limit case, by taking $w \rightarrow 0$ the solution of the masonry model reduces to the well-known solution of joint model (equation 3.6).

Isotropic approximations of the equivalent poro-elastic properties of fracture-cell

As mentioned above, in their work Figueiredo and co-authors (Figueiredo et al., 2015, Figueiredo et al., 2017) considered that the Young's modulus of all fracture cells in the whole medium have the same elastic modulus as one determined in the fracture cell intersected by a horizontal fracture:

$$E_{iso}^{fc} = E_{fc3}; \nu_{iso}^{fc} = \nu_m; \tag{3.12}$$

with E_{fc3} is defined in equation (3.6).

Thus, in these last works they do not distinguish fracture cells intersected by one or many fractures. Otherwise, this approximation is applicable only for fractures owing the same mechanical properties.

In this work, other approximations will be considered. We can mention for example the isotropic approximation of an anisotropic tensor $\mathbb{C}_{ani}$ proposed in (Bornert, Bretheau & Gilormini, 2001) by taking the following projection:

$$\begin{aligned} &\mathbb{C}_{iso} = 3k_{iso}\mathbb{J} + 2\mu_{iso}\mathbb{K}; \\ &k_{iso} = \frac{\mathbb{J}:\mathbb{C}_{ani}}{3}; \mu_{iso} = \frac{\mathbb{K}:\mathbb{C}_{ani}}{10}; \end{aligned} \tag{3.13}$$

with the tensors $\mathbb{J}; \mathbb{K}$ are defined as:

$$\mathbb{J} = \frac{1}{3}\mathbb{I} \otimes \mathbb{I}; \ \mathbb{K} = \mathbb{I} - \mathbb{J}; \tag{3.14}$$

Application to our case for an anisotropic tensor $\mathbb{C}^{fc}$ (see equation 3.8), the isotropic elastic modulus of the fracture cell is approximated as:

$$\begin{aligned} &E_{iso}^{fc} = \frac{9k_{iso}^{fc}.\mu_{iso}^{fc}}{3k_{iso}^{fc} + \mu_{iso}^{fc}}; \nu_{fc}^{iso} = \frac{3k_{iso}^{fc} - 2\mu_{iso}^{fc}}{2(3k_{iso}^{fc} + \mu_{iso}^{fc})}; \\ &k_{iso}^{fc} = \frac{C_{11} + 2C_{12} + 2C_{13} + C_{22} + 2C_{23} + C_{33}}{9}; \\ &\mu_{iso}^{fc} = \frac{2C_{11} - 2C_{12} - 2C_{13} + 2C_{22} - 2C_{23} + 2C_{33} + 3C_{44} + 3C_{55} + 3C_{66}}{30}; \end{aligned} \tag{3.15}$$

The corresponding Biot coefficient and Biot modulus can be obtained as function of the isotropic elastic modulus of intact matrix and ones of fracture-cell as follow:

$$
\begin{aligned}
&b_{iso}^{fc} = 1 - \frac{E_{iso}^{fc}(1-2\nu_m)}{E_m(1-2\nu_{iso}^{fc})};\\
&\frac{1}{M_{iso}^{fc}} = \frac{3(1-2\nu_m)b_{iso}^{fc}}{E_m};
\end{aligned}
\tag{3.16}
$$

The formula present in equation (3.12) can be used for both types of fracture cells and the contribution of different families of fracture owing different mechanical properties is accounted for in this approximation.

Another isotropic approximation is proposed in this work. Following that we consider the Young's modulus and Poisson's ratio of fracture cells intersected by the same inclined fracture (fracture cell type I) as:

$$
\begin{aligned}
&E_{iso}^{fc} = \begin{cases} \dfrac{1}{S_{22}} = \left(\dfrac{1}{E_m} + \dfrac{\cos^2\theta.\sin^2\theta}{k_t.d} + \dfrac{\cos^4\theta}{k_n.d}\right)^{-1}, & if \quad \theta \in [0,\pi/4] \cup [3\pi/4,\pi] \\ \dfrac{1}{S_{11}} = \left(\dfrac{1}{E_m} + \dfrac{\cos^2\theta.\sin^2\theta}{k_t.d} + \dfrac{\sin^4\theta}{k_n.d}\right)^{-1}, & if \quad \theta \in [\pi/4,3\pi/4] \end{cases}\\
&\nu_{iso}^{fc} = \nu_m;
\end{aligned}
\tag{3.17}
$$

While for the fracture cells of type II (cell intersected by multiple fractures), we can take the general formula:

$$
\begin{aligned}
&E_{iso}^{fc} = \left(\frac{1}{E_m} + \sum_i \left(\frac{\cos^2\theta_i.\sin^2\theta_i}{k_t^i.d_i} + \frac{\cos^4\theta_i}{k_n^i.d_i}\right) + \sum_j \left(\frac{\cos^2\theta_j.\sin^2\theta_j}{k_t^j.d_j} + \frac{\sin^4\theta_j}{k_n^j.d_j}\right)\right)^{-1};\\
&\nu_{iso}^{fc} = \nu_m;\\
&\text{if } \theta_i \in [0,\pi/4] \cup [3\pi/4,\pi]; \text{ and if } \theta_j \in [\pi/4,3\pi/4]
\end{aligned}
\tag{3.18}
$$

To distinguish with this latter isotropic approximation, we call hereafter the approximations proposed in equations (3.12) and (3.15) as Figueiredo and Bornert isotropic approximations respectively

Transversely isotropic approximations of the equivalent poro-elastic properties of fracture cell

Another type of approximation was also conducted in this work when we approximate the anisotropic stiffness tensor $\mathbb{C}^{fc}$ of fracture cell as a transversely isotropic with the vertical symmetric axis (noted as VTI medium). As the first approximation, we can take the following projection:

$$
\begin{aligned}
&\mathbb{C}_{IsoTra}^{fc} = (\mathbb{E}^1 : \mathbb{C}_{ani}^{fc})\mathbb{E}^1 + (\mathbb{E}^2 : \mathbb{C}_{ani}^{fc})\mathbb{E}^2 + \frac{1}{2}(\mathbb{E}^3 : \mathbb{C}_{ani}^{fc})\mathbb{E}^3 + \frac{1}{2}(\mathbb{E}^4 : \mathbb{C}_{ani}^{fc})\mathbb{E}^4 +\\
&+\frac{1}{2}(\mathbb{E}^6 : \mathbb{C}_{ani}^{fc})\mathbb{E}^5 + \frac{1}{2}(\mathbb{E}^5 : \mathbb{C}_{ani}^{fc})\mathbb{E}^6;
\end{aligned}
\tag{3.19}
$$

where $\mathbb{E}^1; \mathbb{E}^2; \mathbb{E}^3; \mathbb{E}^4; \mathbb{E}^5; \mathbb{E}^6$ is the well-known transversely isotropic base of Walpole (Walpole 1979) which are defined in Appendix C.

The development shows that the five independent parameters of the approximated VTI fracture cell can be calculated from thirteen parameters of the anisotropic tensor C_{ij}^{fc} (see equation 3.8) as follows:

$$
\begin{aligned}
&E_1^{fc} = E_2^{fc} = \frac{((C_{11}^{fc}+C_{23}^{fc})^2-(C_{11}^{fc}+2C_{12}^{fc}+C_{22}^{fc})C_{33}^{fc})(C_{11}^{fc}-2C_{12}^{fc}+C_{22}^{fc}+2C_{66}^{fc})}{9};\\
&E_3^{fc} = C_{33}^{fc} - \frac{(C_{13}^{fc}+C_{23}^{fc})^2}{C_{11}^{fc}+2C_{12}^{fc}+C_{22}^{fc}};\\
&G_{13}^{fc} = G_{23}^{fc} = \frac{C_{44}^{fc}+C_{55}^{fc}}{4};\\
&\nu_{12}^{fc} = \nu_{21}^{fc} = \frac{2(C_{13}^{fc}+C_{23}^{fc})^2 - C_{33}^{fc}(C_{11}^{fc}+6C_{12}^{fc}+C_{22}^{fc}-2C_{66}^{fc})}{2(C_{13}^{fc}+C_{23}^{fc})^2 - C_{33}^{fc}(3C_{11}^{fc}+2C_{12}^{fc}+3C_{22}^{fc}+2C_{66}^{fc})};\\
&\nu_{31}^{fc} = \nu_{32}^{fc} = \frac{C_{13}^{fc}+C_{23}^{fc}}{C_{11}^{fc}+2C_{12}^{fc}+C_{22}^{fc}};
\end{aligned}
\tag{3.20}
$$

Analogically, we can determine easily the Biot coefficients and Biot modulus from these five parameters of the VTI fracture cell:

$$
\begin{aligned}
&b_1^{fc} = b_2^{fc} = \frac{E_m E_3^{fc}(\nu_{12}^{fc}-1) + E_1^{fc}\left[E_3^{fc}(1+\nu_{31}^{fc})(1-2\nu_m) + 2E_m(\nu_{31}^{fc})^2\right]}{2E_m E_1^{fc}(\nu_{31}^{fc})^2 + E_m E_3^{fc}(\nu_{12}^{fc}-1)};\\
&b_3^{fc} = \frac{2E_1^{fc}\nu_{31}^{fc}[E_m\nu_{31}^{fc} + E_3^{fc}(1-2\nu_m)] + E_3^{fc}(1-\nu_{12}^{fc})[E_3^{fc}(1-2\nu_m) - E_m]}{2E_m E_1^{fc}(\nu_{31}^{fc})^2 + E_m E_3^{fc}(\nu_{12}^{fc}-1)};\\
&\frac{1}{M_{fc}} = \frac{(2b_1^{fc}+b_3^{fc})(1-2\nu_m)}{E_m};
\end{aligned}
\tag{3.21}
$$

The second approximation that will be proposed in this work by replacing the five independent parameters of the VTI fracture cell in equation (3.20) by:

$$
\begin{aligned}
&E_1^{fc} = E_2^{fc} = \left(\frac{1}{E_m} + \frac{\cos^2\theta.\sin^2\theta}{k_t.d} + \frac{\sin^4\theta}{k_n.d}\right)^{-1};\\
&E_3^{fc} = \left(\frac{1}{E_m} + \frac{\cos^2\theta.\sin^2\theta}{k_t.d} + \frac{\cos^4\theta}{k_n.d}\right)^{-1};\\
&G_{13}^{fc} = G_{23}^{fc} = \frac{2E_m.k_n.k_t.d}{E_m(k_n+k_t) + 4k_n.k_t.d(1+\nu_m) + E_m(k_n-k_t)\cos 4\theta};\\
&\nu_{12}^{fc} = \nu_{21}^{fc} = \frac{E_1^{fc}\nu_m}{E_m};\\
&\nu_{31}^{fc} = \nu_{32}^{fc} = E_3^{fc}\left(\frac{\nu_m}{E_m} + \frac{(k_n-k_t)\cos^2\theta.\sin^2\theta}{k_n.k_t.d}\right);
\end{aligned}
\tag{3.22}
$$

Hereafter the first VTI approximation (equation 3.20) will be called as Walpole VTI approximation (due to the fact that it is done by using the projection conducted on the Walpole's base) to distinguish with the second VTI approximation (equation 3.22).

3.3.2. Equivalent permeability of fracture cell

The determination of the equivalent permeability of the fracture-cell has been discussed in a lot of work since several decades (Parsons, 1966; Nelson 2001; Sarkar et al. 2004; Reeves et al., 2008; Botros et al. 2008; Sakhaee-Pour && Wheeler, 2016). In general, all studies based on the hypothesis that the flow in the fractured element is principally conducted through the fracture inside the domain by considering that the permeability of intact matrix is negligible with respect to the permeability of fracture. Note that it is largely accepted that the permeability of the fracture K_f is calculated from the fracture's width w. In the 2D case, flow in fracture is assumed to be laminar between two infinite parallel smooth plates, thus the permeability K_f is defined as follow (Kranz et al. 1979; Witherspoon et al., 1980):

$$K_f = \frac{w^2}{12} \tag{3.23}$$

We consider now a square fracture-cell (of size h) intersected by a inclined fracture (of width w) characterized by the inclination angle θ. On its lateral boundaries, the fracture cell is imposed respectively a constant pressure p_1 on the left and p_2 on the right while the top and bottom sides of the cell are considered to be impermeable.

Knowing the pressure at two ends of the fracture, the flux flow through the length l of fracture is:

$$q_l = K_f w \frac{p_1 - p_2}{l} \tag{3.24}$$

Hence it is not difficult to calculate the flux in the horizontal direction q_x by taking into account the fact that $l=h/\cos(\theta)$:

$$q_x = K_f w \frac{p_1 - p_2}{l} \cos(\theta) = K_f w \frac{p_1 - p_2}{h} \cos^2(\theta) \tag{3.25}$$

Similarly, the flux $q_{x,fc}$ flow through fracture-cell element is determined as:

$$q_{x,fc} = K_{fc}^x h \frac{p_1 - p_2}{h} \tag{3.26}$$

By neglecting the flow in matrix (permeability of matrix is small with respect to the permeability of fracture), the flux flow through fracture-cell must be equal to one through the fracture ($q_x = q_{x,fc}$), thus from two equations (3.25) and (3.26) we can deduce:

$$K_{fc}^x = K_{fc}^y = K_{fc}^{iso} = \left\{ \begin{array}{l} K_f \frac{w}{h} \cos^2(\theta) \quad \text{if } \theta \in [0, \pi/4] \cup [3\pi/4, \pi] \\ K_f \frac{w}{h} \sin^2(\theta) \quad \text{if } \theta \in [\pi/4, 3\pi/4] \end{array} \right\} \tag{3.27}$$

As the particular case, if fracture is horizontal (θ=0), the permeability of fracture-cell is simplified to:

$$K_{fc}^{x} = K_f \frac{w}{h} \tag{3.28}$$

The obtained result in equations (3.25) and (3.27) mean that if a fracture is inclined with respect to the axis of pressure gradient, it will work as a horizontal fracture with the permeability of fracture which is corrected by a factor $\cos^2(\theta)$. This result is largely adopted in standard reservoir engineering (Parsons 1966; Nelson 2001; Sakhaee-Pour & Wheeler, 2016). Otherwise, the permeability of fracture cell is calculated from this corrected permeability by multiplying the ratio of fracture's width and cell size (w/h).

Note however that some other corrected parameters were introduced in the literature. For example, (Sarkar et al., 2004) proposed the correction factor $\cos(\theta)$ instead of $\cos^2(\theta)$ based on a backed numerical analysis. In other contributions (Reeves et al., 2008; Botros et al. 2008) the authors introduce the correction factor as $\left(|\sin(\theta)| + |\cos(\theta)|\right)$.

In this work, the formulae presented in equation (3.27) will be used to determine the equivalent permeability of fracture cell of *type I*. More precisely, for the sake of simplicity, we assume that all fracture cell intersected by the same fracture owe the same isotropic permeability which is calculated from equation (3.27).

For the fracture cell type II, the presence of multiple fractures is added up meaning that:

$$K_{iso}^{fc} = \frac{1}{h}\sum_i K_f^i.w_i.\cos^2(\theta_i) + \frac{1}{h}\sum_j K_f^j.w_j.\sin^2(\theta_j)$$
$$\text{if } \theta_i \in [0, \pi/4] \cup [3\pi/4, \pi]; \text{ and if } \theta_j \in [\pi/4, 3\pi/4] \tag{3.29}$$

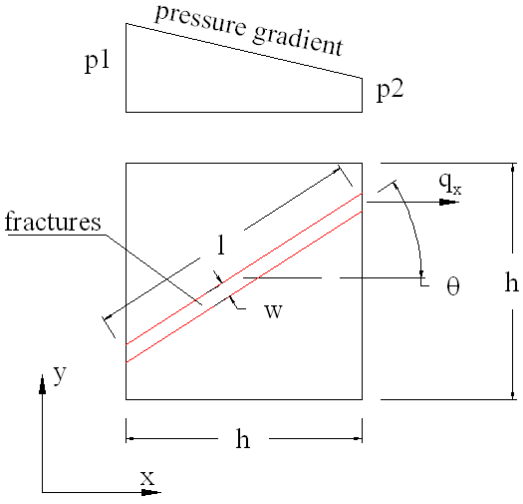

Figure 3-10 Flux through fracture-cell element intersected by one fracture.

3.4. Verification tests

In this section, some numerical tests will be conducted to verify the accuracy of the EFC approach. In the first stage, two examples which represent correspondingly the purely mechanical and purely hydraulic problems are considered which aim to investigate the convergence solution of EFC with respect to the fracture-cell size as well as to verify the correctness of different approximations of the equivalents properties of fracture-cell. For the first purpose, the size of fracture-cell will be gradually decreased by using the local refinement of mesh based on the hanging node technique. For the second purpose, we will compare the results obtained from different approximations with ones obtained from the referent numerical simulation based on the conformed mesh. Finally, the coupling hydro-mechanical problem will also be considered in the third example which allows to cloture the validation process.

3.4.1 Purely mechanical test

We consider in this first example an elastic medium with dimension L=1.0m of width and H=1.25m in height as shown in Figure 3-11. The medium is intersected by a fracture with 0.13mm of width which could be inclined with respect to the horizontal axis an angle ϕ. Due to the symmetric reason, we consider only the inclination angle ϕ varying from 0° to 45° (with interval 5° for each case of study). The elastic properties of the isotropic medium consist of Young's modulus E_m=84.6 (GPa) and Poisson ratio ν=0.24 while the normal and shear stiffness of the fracture are respectively k_n=434 (GPa/m) and k_t=86.8 (GPa/m). These parameters referred from the Sellafield (UK) site (Nirex 1997a, 1997b) which will be presented in detail in the next chapter. The limit conditions of the considered model consist of applying a normal stress 24.46 MPa on top boundary while the displacement is fixed on the bottom boundary. For the comparison and validation purpose, a controlled point "A" located on the middle of the top boundary is chosen whose vertical displacement will be determined and compared in different studied cases and with referent results.

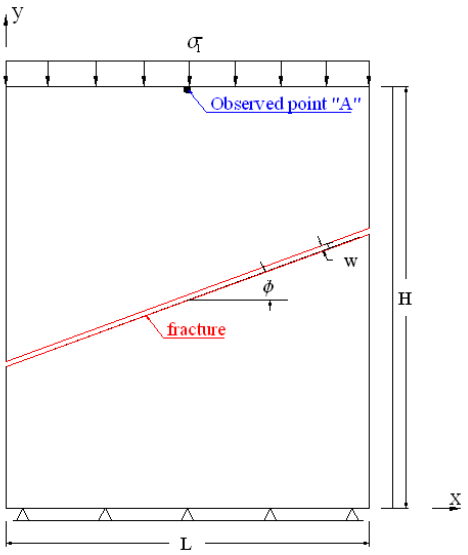

Figure 3-11: Sketch of the purely mechanical test

In the first stage, we investigate the influence of the fracture-cell size on the obtained results by changing the local refinement level. More precisely, as introduced in the previous section, a text file which contains the mesh information including geometry, boundary identify, material identify is provided. Mesh generated directly from the text file is the root mesh (Figure 3-12a) known also as global refinement of the mesh to distinguish with local refinement of the mesh around the fracture. In Figure 3-12 (a,b) we present two cases of global refinement of the mesh with the corresponding level of refinement N=2 and N=4 to define an inclined fracture. This means that the global square cell size equal respectively to $\Delta=L/2^2$ and $\Delta=L/2^4$. No local refinement was conducted in these cases meaning also that the fracture cell size equal to the global cell size $h=\Delta$. Respectively in Figure 3-12(c-f) are presented the inclined fracture which is now modeled by using the local refinement of the mesh with different level of refinement N=5 to N=8. In these last cases, the global mesh size is maintained at $\Delta=L/2^4$ while the fracture cell size is decreased respectively from $h= L/2^5$ to $h= L/2^8$. Thus, by comparing with the global mesh, the fracture cell size equal to $\Delta/2$ (N=4) and to $\Delta/16$ (N=8) while regarding with the fracture aperture w this cell size ranges from $478w$ to $30w$. Figure 3-13 is highlighted the model of fracture using the local refinement with N=9 as well as a zoom around the fracture. Then for the illustration purpose in Figure 3-14 we present the model of the fractured medium by considering different inclination angle (from 0° to 45°) and in all these cases the size of the global cell and fracture cell are fixed at $\Delta=L/2^4$ and $h= L/2^7$ (or corresponding to the case N=7 and $h=\Delta/8$). We note also that corresponding to the variation of inclination angle, the number of fracture-cell mesh increase from 992 for horizontal fracture to 1328 for fracture oriented at 45°. In what it follows, we clarify that in all our verification tests, the root mesh size is fixed at $\Delta=L/2^4$.

In Figure 3-15 are presented the vertical displacement of the controlled point A calculated with different level of local refinement of the mesh N to model the fracture. The calculations were conducted with five approximations of the equivalent elastic properties of fracture-cell which consists of three isotropic approximations (Figueiredo, Bornert and isotropic approximation proposed in this work) and two transversely isotropic approximations (Walpole approximation and our proposed transversely isotropic approximation). In general, we can state that the vertical displacement of the controlled point decreases with respect to the local refinement level (N). This decrease is most pronounced for the case of inclined fracture at 45° and it seems to be more slightly when the inclination angle decreases. Concretely, a maximum variation about 6% between N=4 and N=9 can be noted for the Bornert approximation while with the two other isotropic approximations it is about 4%. Concerning the transversely isotropic approximation, it is shown that the maximum variation is more important with about 20% and 10% for the Walpole approximation and our proposed approximation, respectively. From this test, we can remark that for all isotropic approximations, at the local refinement level N=7 the result attaints its asymptote (no significant difference can be observed between N=7 and N=9 illustrating the variation is smaller than 1%). However, for the transversely isotropic approximations, it seems that the more important level of local refinement is required when the results converge at N=8.

In the second stage of this purely mechanical test, we compare our results with ones obtained from the simulation conducted on the commercial code Flac3D (Itasca, 2006). In this last numerical simulation, the same geometric model, boundary conditions and material as the previously presented model are used. The principal difference lies on the way to model fracture when in Flac3D code, fracture is represented by interface elements (see Figure 3-16). To simulate the 2D plane strain condition as one conducted in DEAL.II, the model thickness in Flac3D is chosen small (0.1mm) while the uniform mesh with size about 7.81mm, which is equivalent to $L/2^7$, is considered. In Figure 3-17 are highlighted the displacement of the controlled point calculated from five approximations model and from Flac3D. The first observation is concerned to the results obtained from the Bornert isotropic approximation: no variation of displacement with respect to the inclination angle of fracture can be stated and these results seem very far from the results of Flac3D which is confirmed by an important relative error (from 14% to 25%) as shown in Figure 3-18. A quite similar comment can be attributed to the results calculated from the Walpole transversely isotropic approximation while at only small inclination angle, the results of this latter approximation method is near the referent results of Flac3D. From the inclination angle 30° the results calculated from the Bornert isotropic and Walpole transversely isotropic approximations are quite analog. The Figueiredo isotropic approximation presents a higher accuracy, with differences to Flac3D calculs inferior to 5% for the inclination angle ranging from 0° to 20° attaining 8% at for

higher inclination angle (maximum difference for an angle of about 35°). With the same range of inclination angle from 0° to 20°, the most concordance with the results of Flac3D is ones obtained from the transversely isotropic approximation proposed in this work (the relative error is inferior to 3%). However, the discrepancy of this latter approximation with the referent results is much more pronounced with the increase of the inclination angle when it can reach about 16% at inclination angle 45°. The most interesting results reserves to ones of the isotropic approximation proposed in this work. For all considered cases of inclined fracture, the difference between this last approximation method and the Flac3D simulation is smaller than 3% when the displacement curve of the controlled point match quite well with the reference result. Finally, for the illustration purpose, in Figure 3-19 are captured the isovalues of vertical displacement in the whole model with inclined fracture of 30°. These isovalues are obtained from Flac3D and EFC method by using our proposed isotropic approximation and a quite similitude can be state from these results.

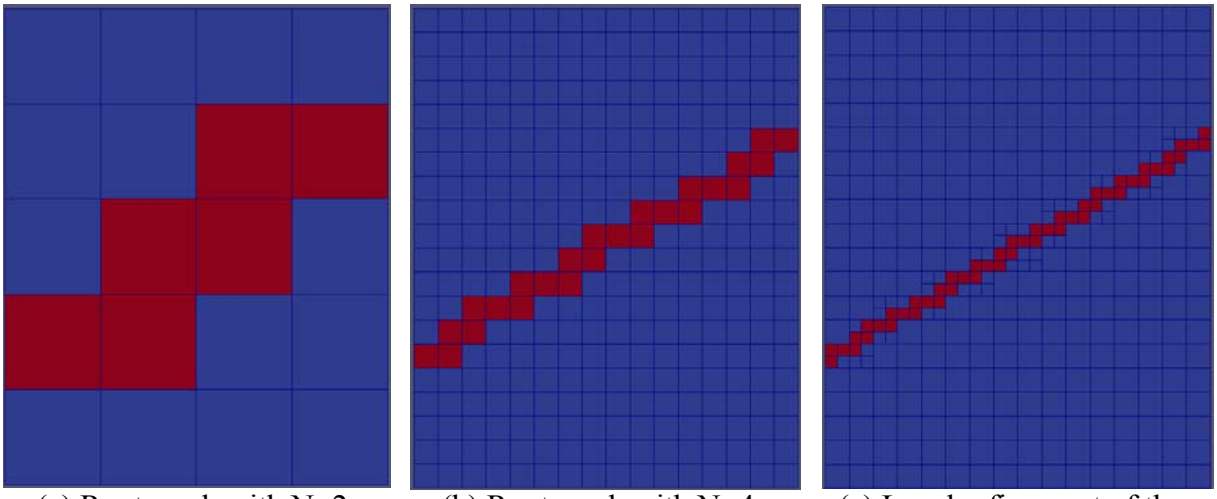

(a) Root mesh with N=2 (b) Root mesh with N=4 (c) Local refinement of the mesh with N=5

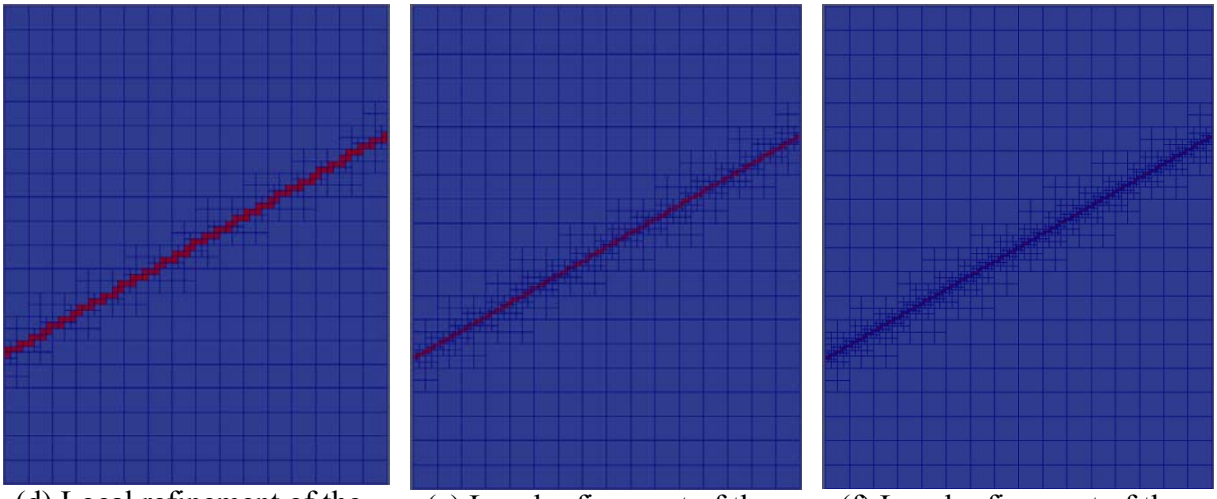

(d) Local refinement of the mesh with N=6 (e) Local refinement of the mesh with N=7 (f) Local refinement of the mesh with N=8

Figure 3-12: modeling of fracture oriented 30° by using: root mesh (global refinement of the mesh) with N=2 (a) and N=4 (b); local refinement of the mesh with N=5 (c), N=6 (d), N=7 (e) and N=8 (f).

Note: red elements denote fracture-cell elements and green elements denote matrix elements.

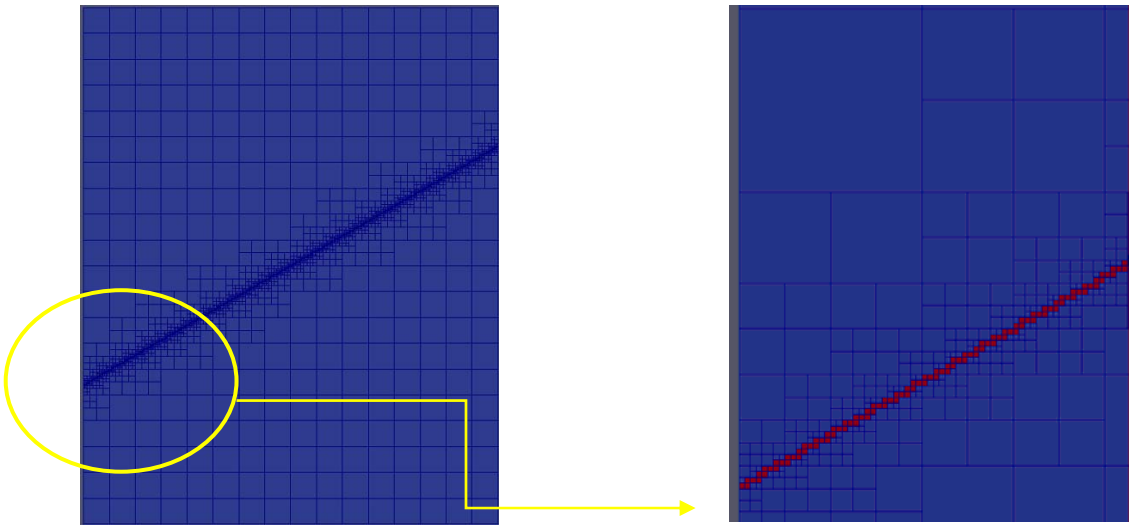

Figure 3-13: modeling of fracture oriented 30° by using local refinement of the mesh N=9 (left) and a zoom around fracture (right).

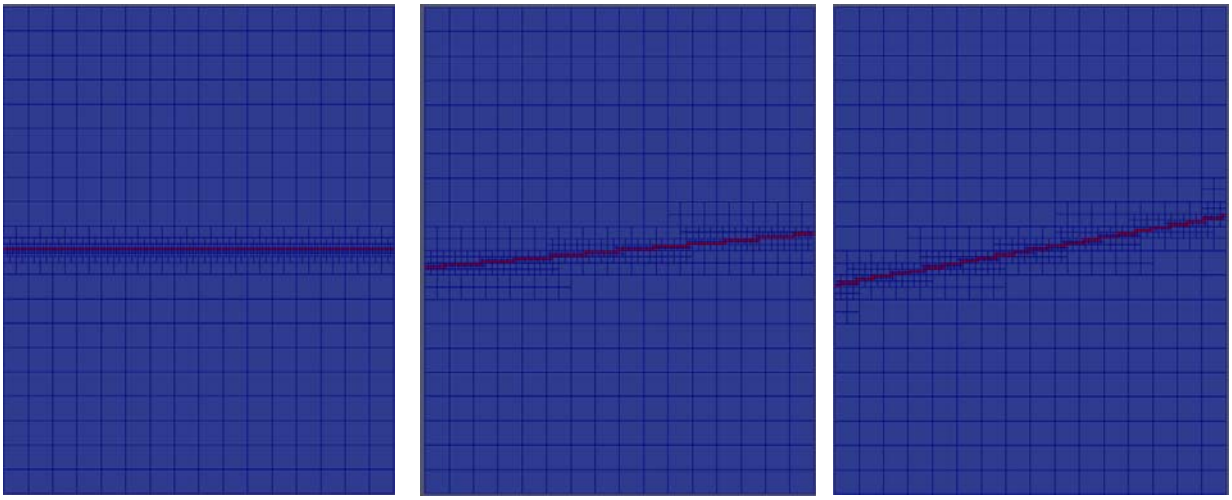

(a) 0 degree (b) 5 degree (c) 10 degree

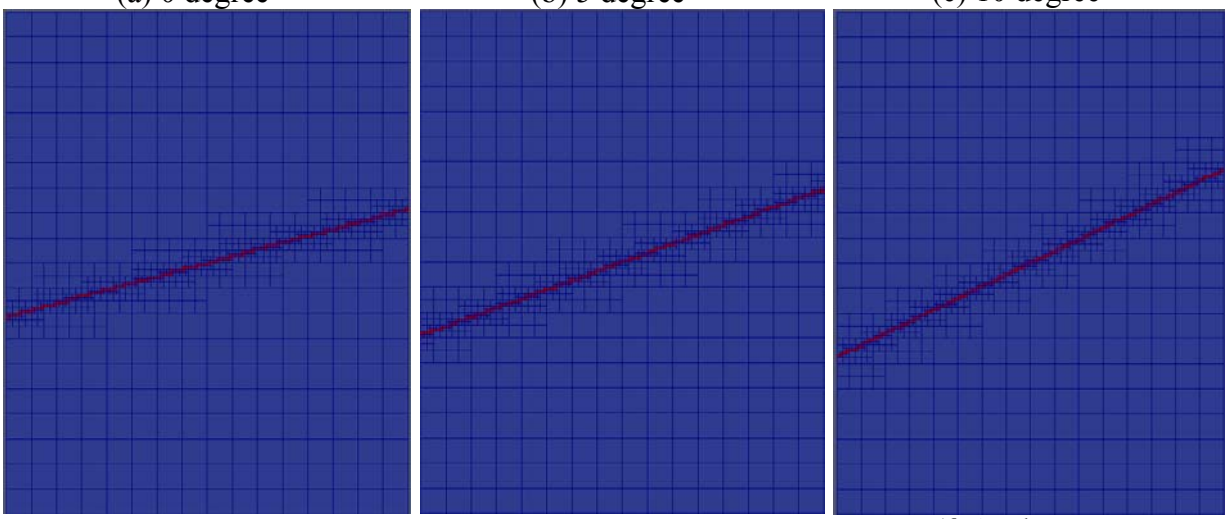

(d) 15 degree (e) 20 degree (f) 25 degree

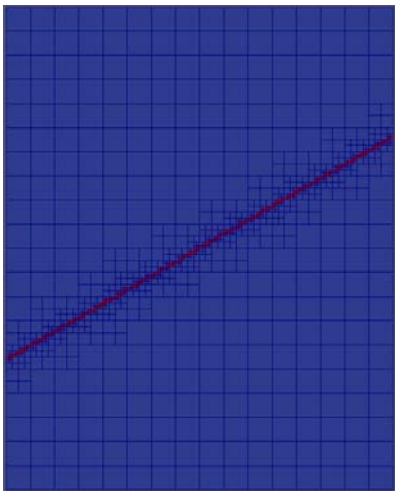

(g) 30 degree

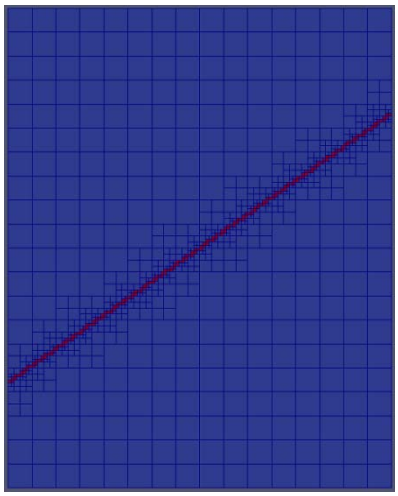

(h) 35 degree

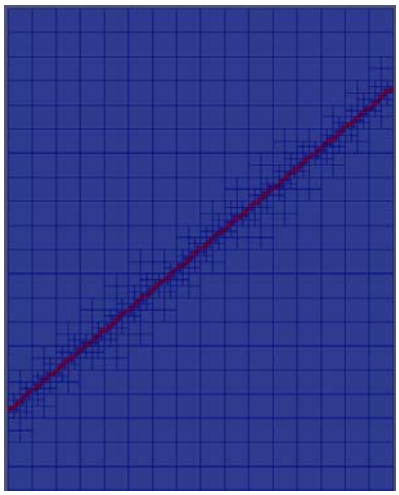

(i) 40 degree

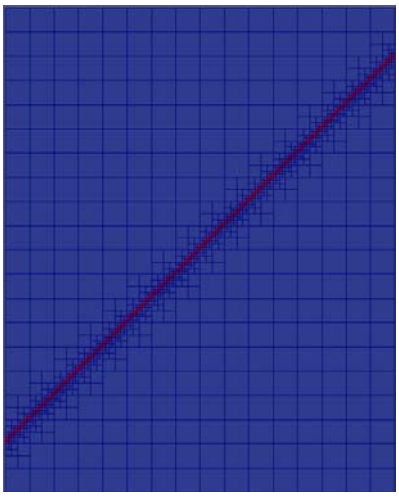

(k) 45 degree

Figure 3-14: modeling of inclined fracture (with inclined angle varies from 0 degree to 45 degree) by using the local refinement of the mesh N=7.

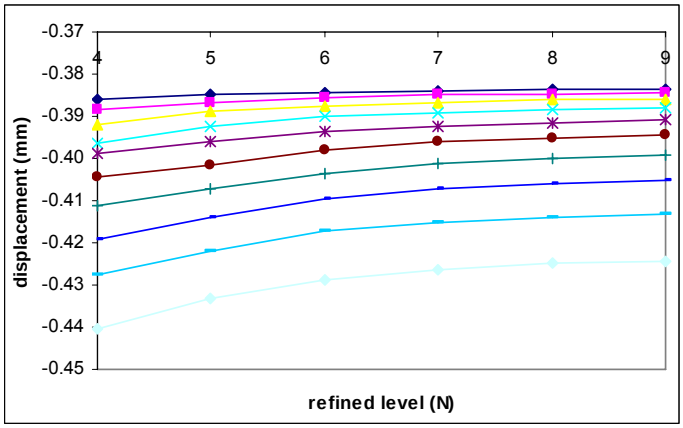

(a) Figueiredo isotropic approximation

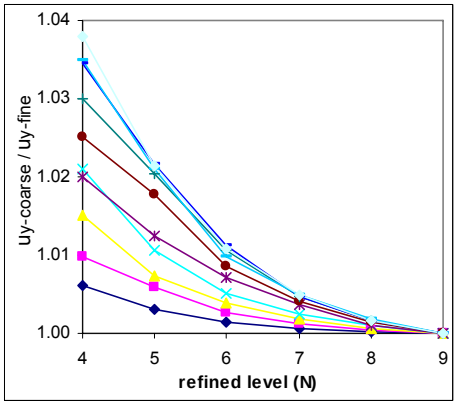

(b)

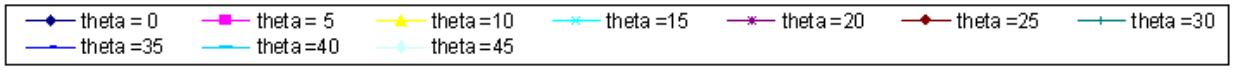

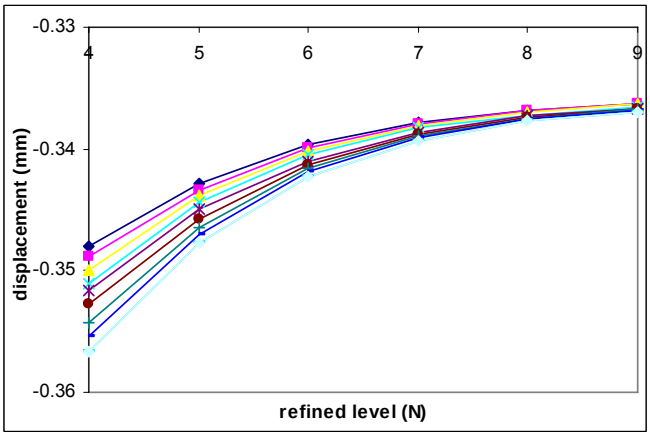

(c) Bornert isotropisation approximation

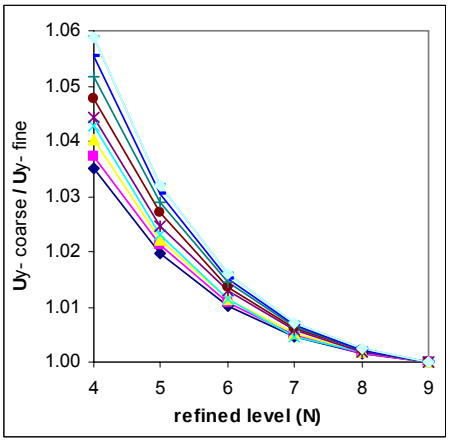

(d)

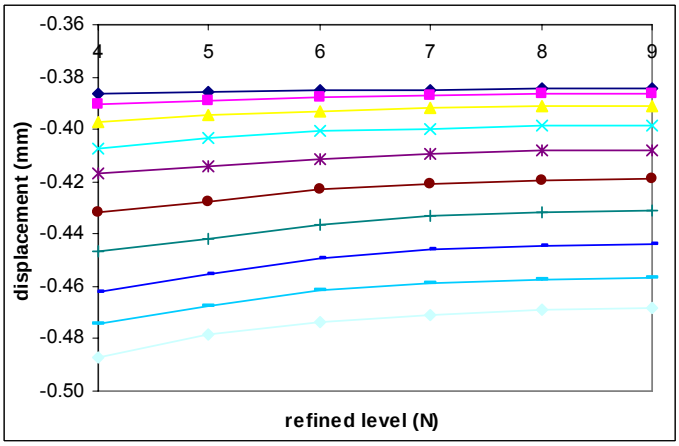

(e) our proposed isotropic approximation

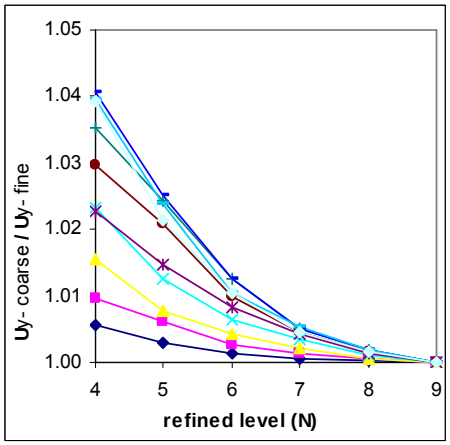

(f)

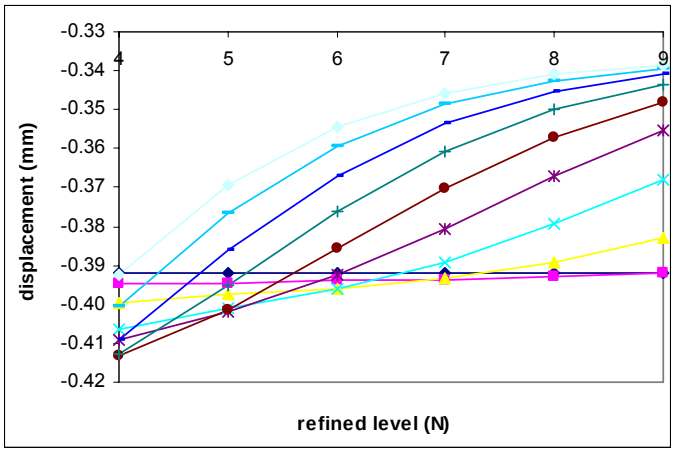

(g) Walpole transversely isotropisation approximation

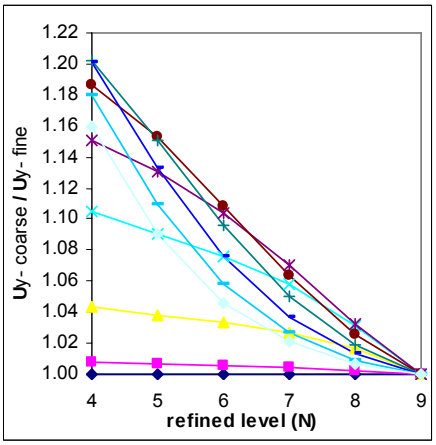

(h)

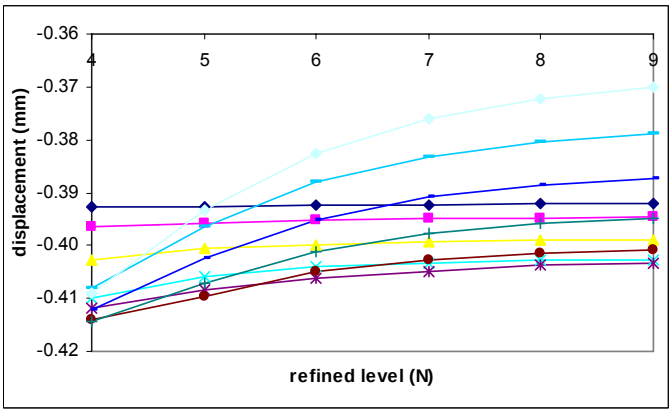

(k) our proposed transversely isotropic approximation

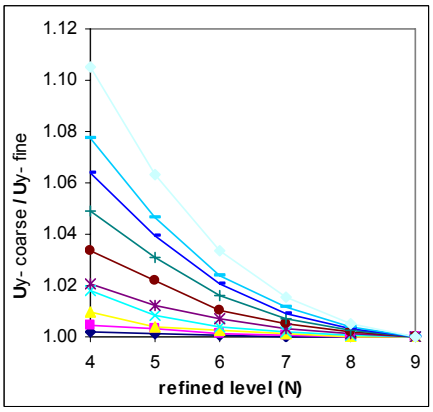

(l)

Figure 3-15: Vertical displacement (on the left) and the ratio U_y-coarse / U_y-fine at the controlled point "A" between coarse fracture-cell size and finest fracture-cell size (on the right) by different approximations: (a,b) Figueiredo approximation, (c,d) Bornert isotropisation approximation, (e,f) our proposed isotropic approximation, (g,h) Walpole transversely isotropisation approximation, and (k,l) our proposed transversely isotropic approximation.

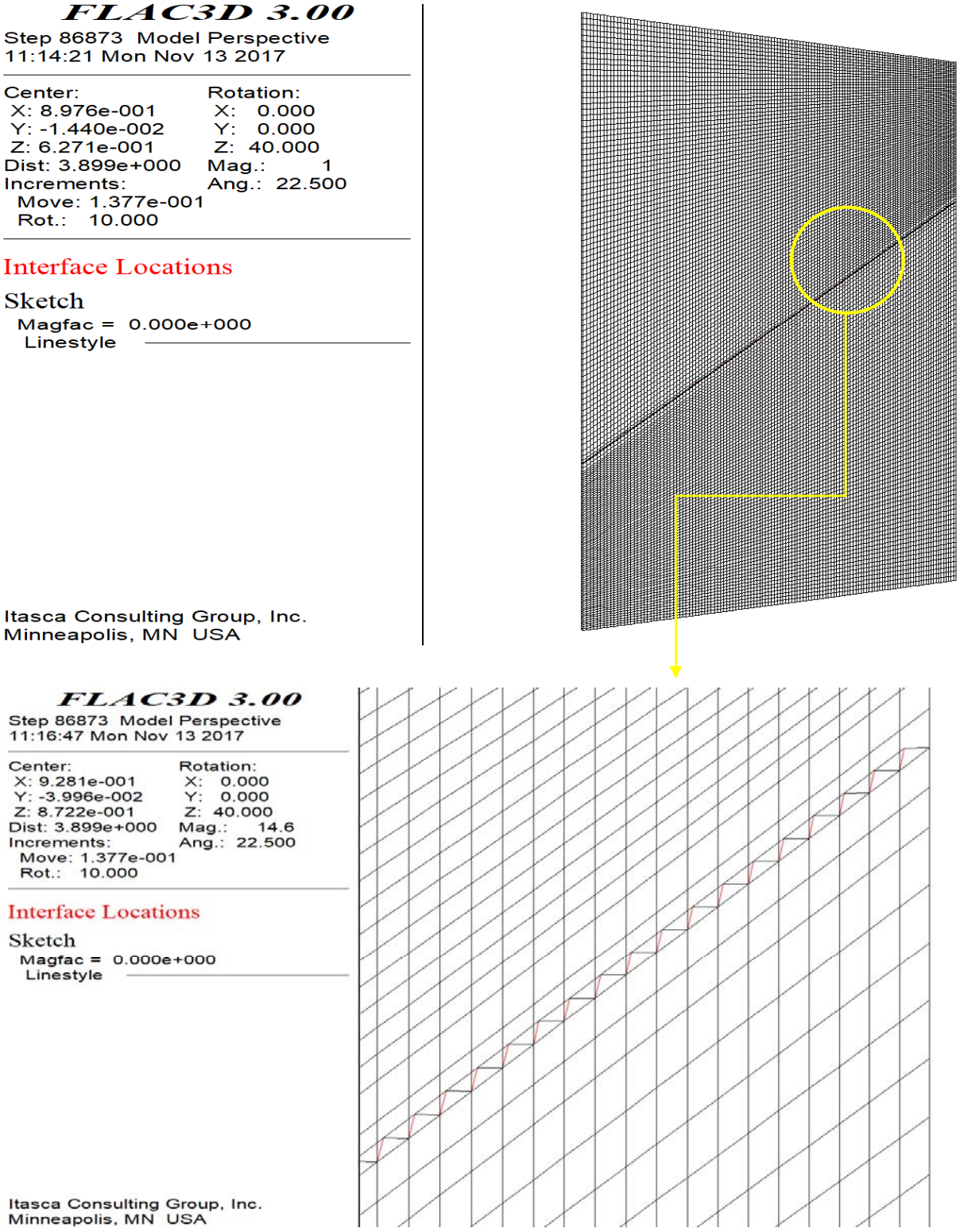

Figure 3-16: Geometric model conducted in the Flac3D code by using the interface elements to model fracture (top) and a zoom around fracture (bottom)

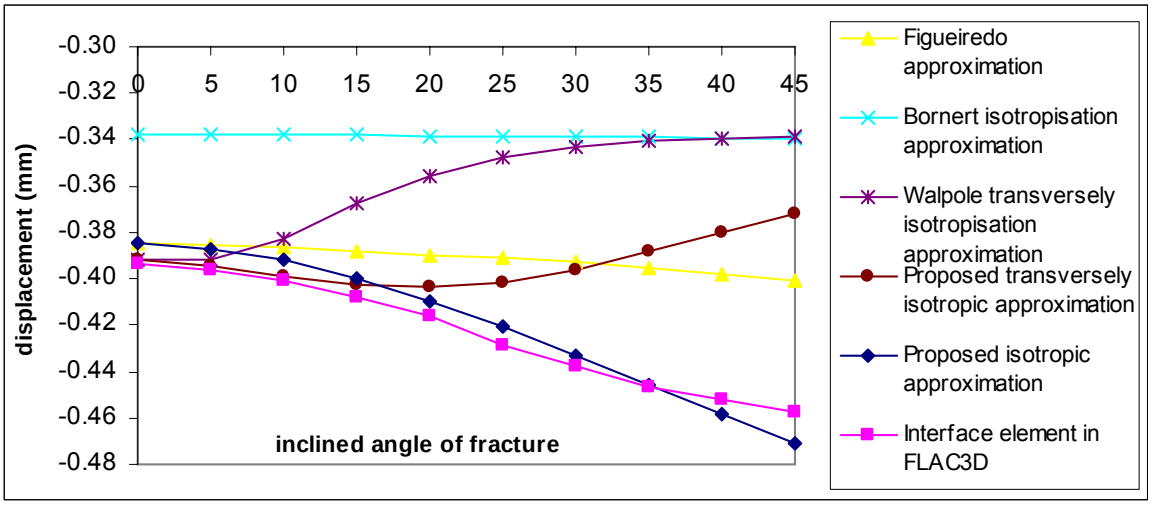

Figure 3-17: Vertical displacement at the controlled point A obtained: from the embedded fracture continuum approach by using different approximations of the equivalent properties of fracture-cell and from Flac3D using the interface elements.

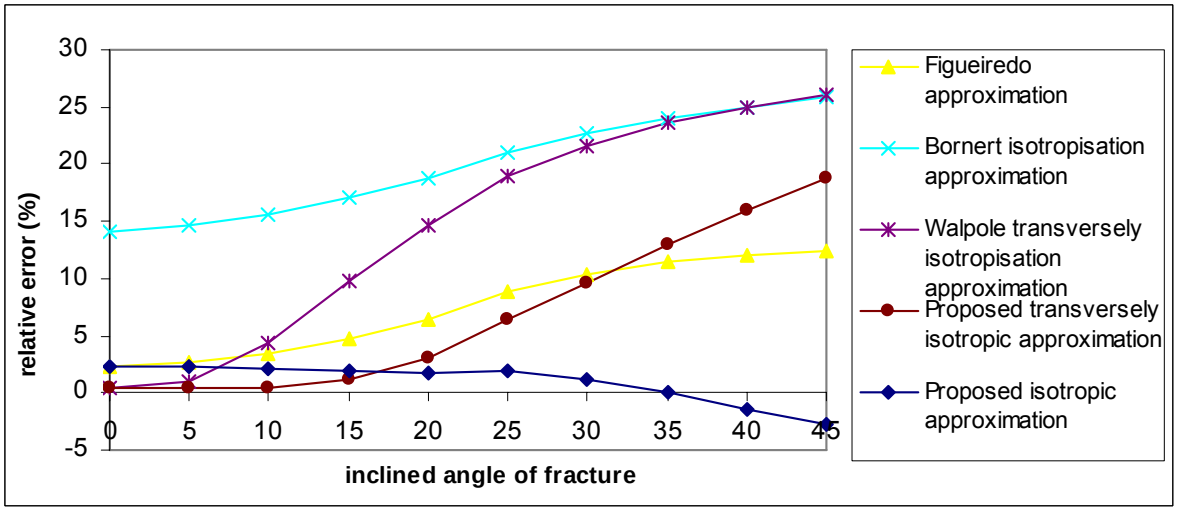

Figure 3-18: Comparison of the displacement at the controlled point A obtained: from the embedded fracture continuum approach by using different approximations of the equivalent properties of fracture-cell with the result calculated from Flac3D using the interface elements.

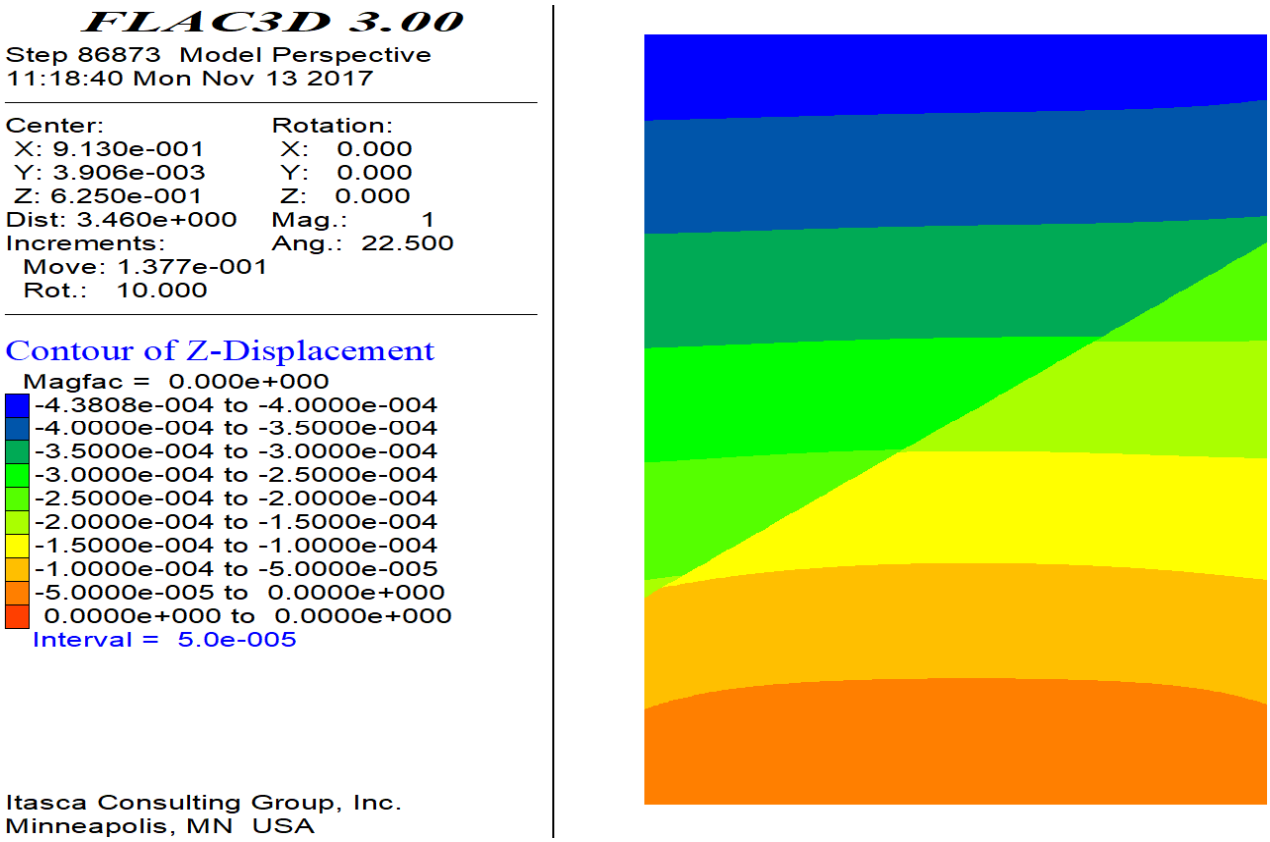

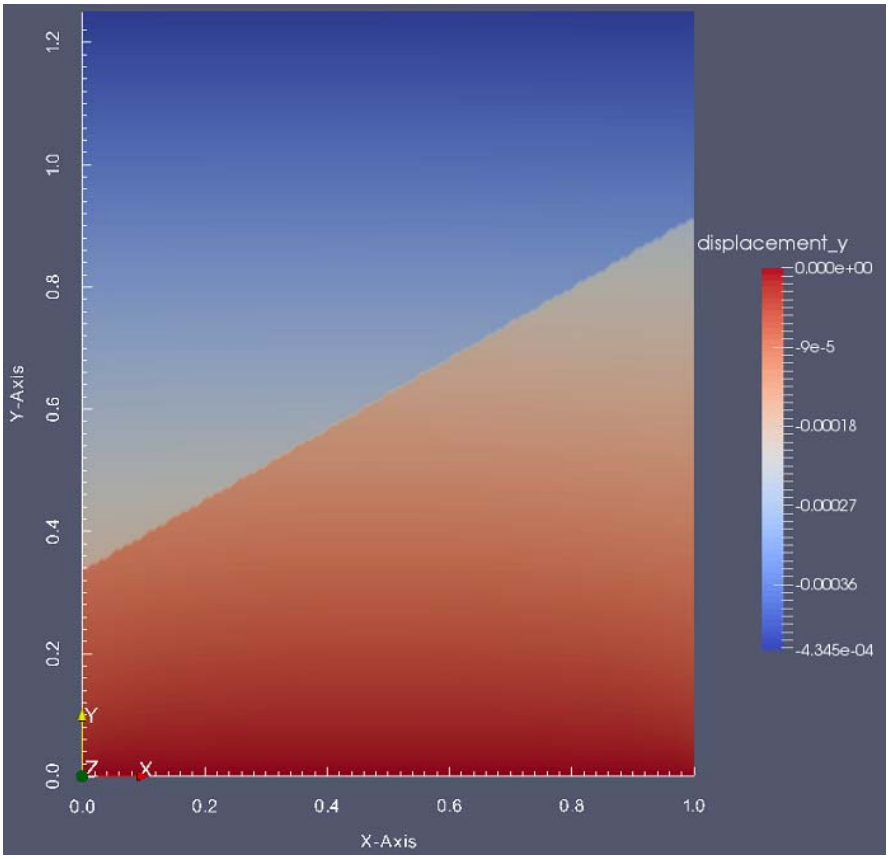

Figure 3-19: isovalue of vertical displacement obtained from FLAC3D (fracture modeled as interface elements) (top) and from Deal II by using EFC method with our proposed isotropic approximation (bottom). In these figure the inclined fracture of 30 degree is considered.

3.4.2 Purely hydraulic test

In this second test, the same geometric model as the previous example is used but the matrix is now porous characterizing by a hydraulic permeability (see Figure 3-20). Otherwise, for the validation purpose, we intend to compare the results obtained from the EFC approach (fracture-cell model) with ones determined from the other numerical simulation based on the conform mesh. More precisely, in this latter simulation the fracture will be modeled explicitly with his real width and the used mesh conform with the geometry of fracture (see Figure 3-22). For the sake of simplicity, the fracture aperture in this study is assumed to be equal to $w=1mm$. Corresponding to this aperture, the permeability of fracture calculated from Poisseuille's law is $K_f=w^2/12=8.33\ x\ 10^{-8}$ (m^2). The permeability of the porous medium referred from the Sellafield (UK) site (Namdari, 2016) is about 2.4 x 10^{-15}(m^2) which seems to be neglected with respect to the permeability of fracture. The viscosity and compressibility of fluid are 0.001(Pa.s) and 5.0×10^{-10} (Pa^{-1}), respectively. Note that the permeability of fracture cell is supposed to be isotropic and calculated from the permeability of fracture following equation (3.27). As shown in Figure 3-20 the top and bottom boundaries of the model are considered to be impermeable, while a constant gradient pressure is imposed on two lateral boundaries by applying the pressure P1=10(MPa) on the left and P2=0 (MPa) on the right of the model.

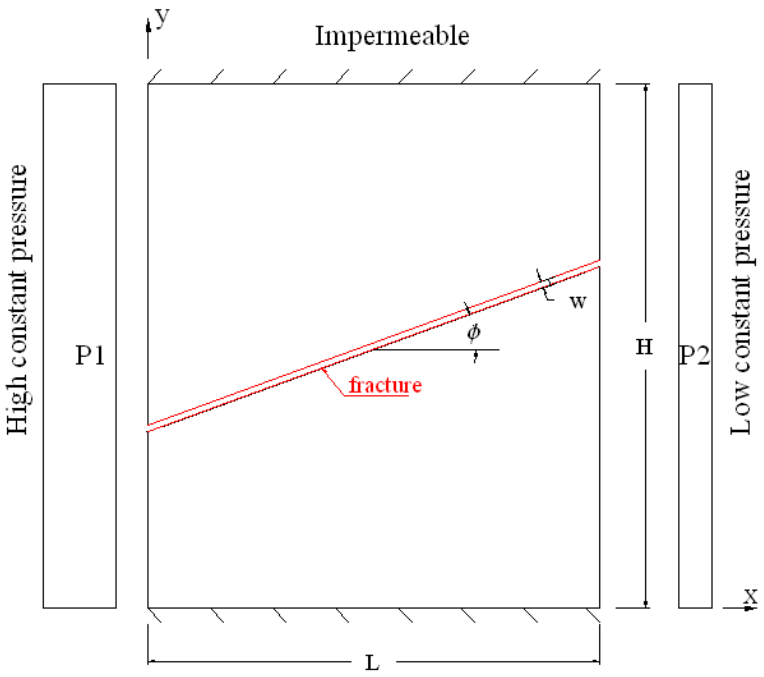

Figure 3-20: Geometry and boundary conditions of the purely hydraulic test

Similar to the previous mechanical test, in the first stage, we will investigate the convergence of EFC approach by modeling the fracture with different local refinement level which induces different values of fracture-cell size. For the comparison purpose, we will calculate only the horizontal fluid flux q_x passing though the medium. By changing the local refinement level from N=4 to N=9 to model the fracture, the respective ratio of fracture-cell size and fracture aperture ranges from *h/w*=62.5 to *h/w*=4.

The results of fluid flux q_x calculated from different study cases of inclined fracture are illustrated in Figure 3-21a. Otherwise in Figure 3-21b, we present the relative difference between the fluid flux calculated at each level of refinement (N) with respect one calculated at the level N=9. The Figure 3-21b shows a difference about 4% at N=4 for the fracture inclined 45° which reduces to about 1% at N=6. Moreover, it can be stated that from the local refinement level N=7 the results seem converge when the difference is negligible (difference is inferior to 0.5% for all inclination angle of fracture as shown in Figure 3-21b).

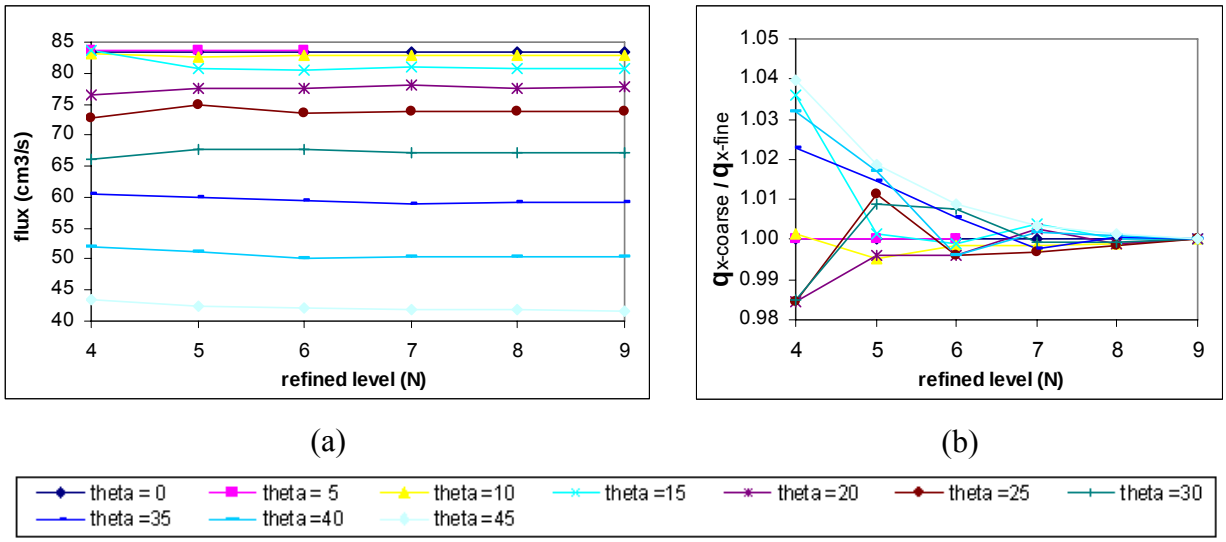

Figure 3-21: (a) flux going through fracture and (b) relative difference q_x-coarse$/q_x$-fine between coarse fracture-cell size and fine fracture-cell size.

In the second stage, we compare the results calculated from the EFC approach with the results conducted from the conform-mesh simulation. In this latter calculation, the explicit fracture (with 1mm of width) is modeled by fine meshes which conform to the geometry of fracture. In Figure 3-22 are illustrated the geometric model of the conform-mesh simulation with different inclined fracture (from 0° to 45°). In Figure 3-23 are presented the curve of fluid flux q_x as function of inclination angle calculated from the EFC method and conform-mesh model. Two curves seem match quite well when the highest relative error $\left(q_x^{\text{fracture\_cell}} - q_x^{\text{conformed\_mesh}}\right)/q_x^{\text{conformed\_mesh}}$ is less than 5%.

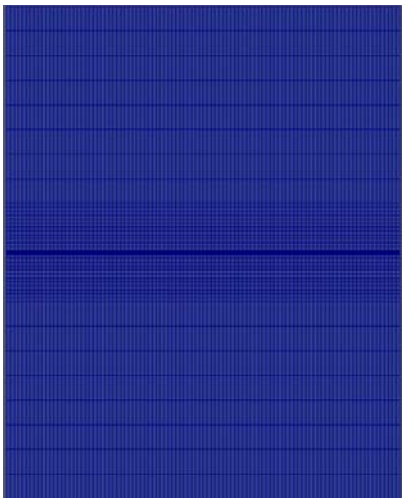

(a) 0 degree

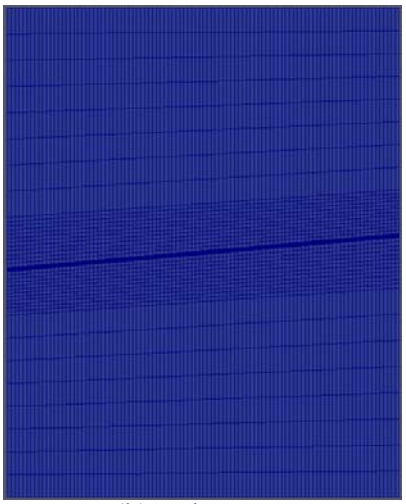

(b) 5 degree

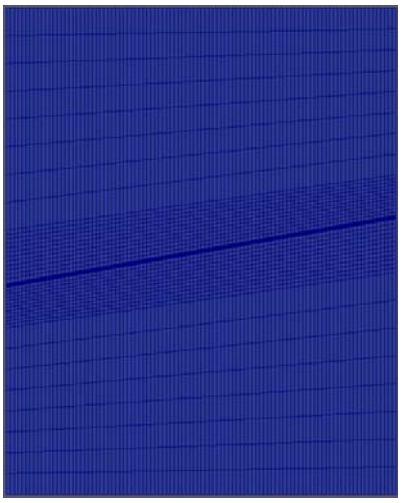

(c) 10 degree

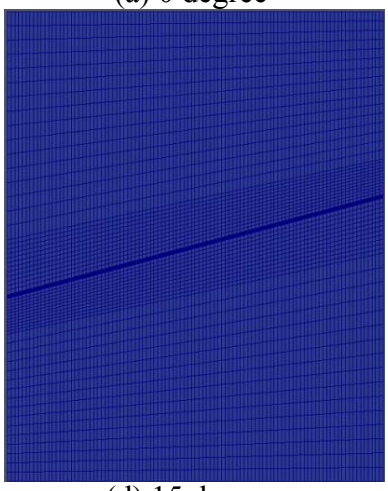

(d) 15 degree

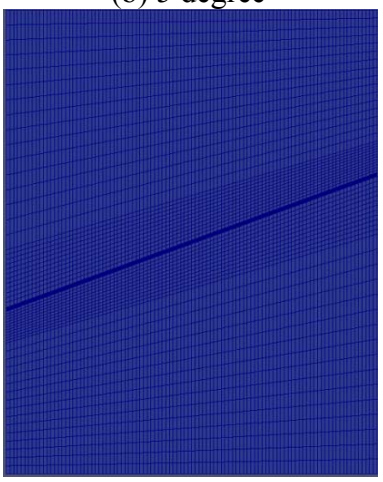

(e) 20 degree

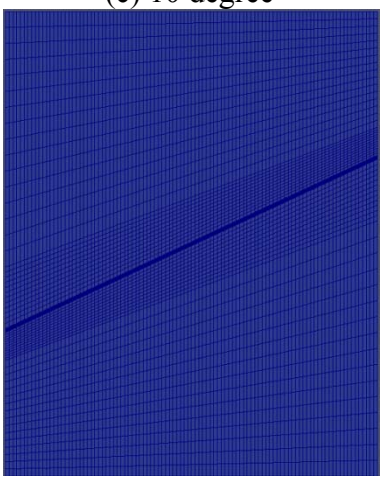

(f) 25 degree

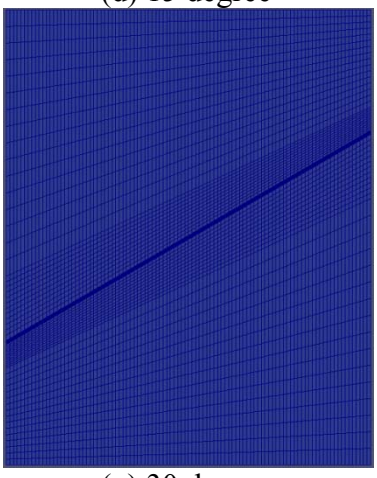

(g) 30 degree

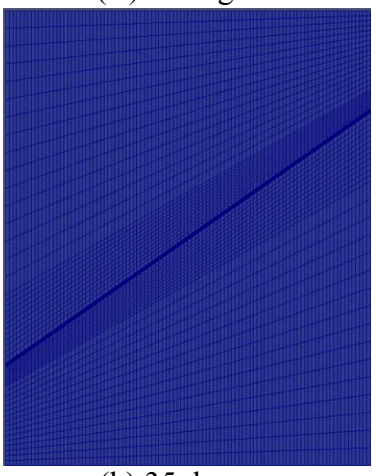

(h) 35 degree

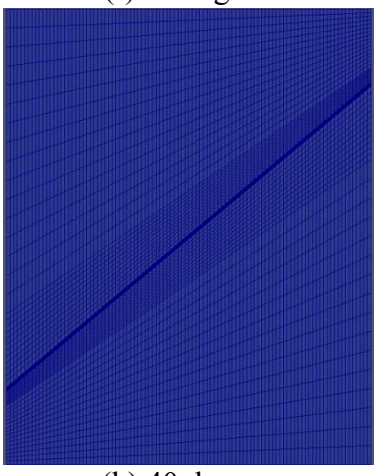

(k) 40 degree

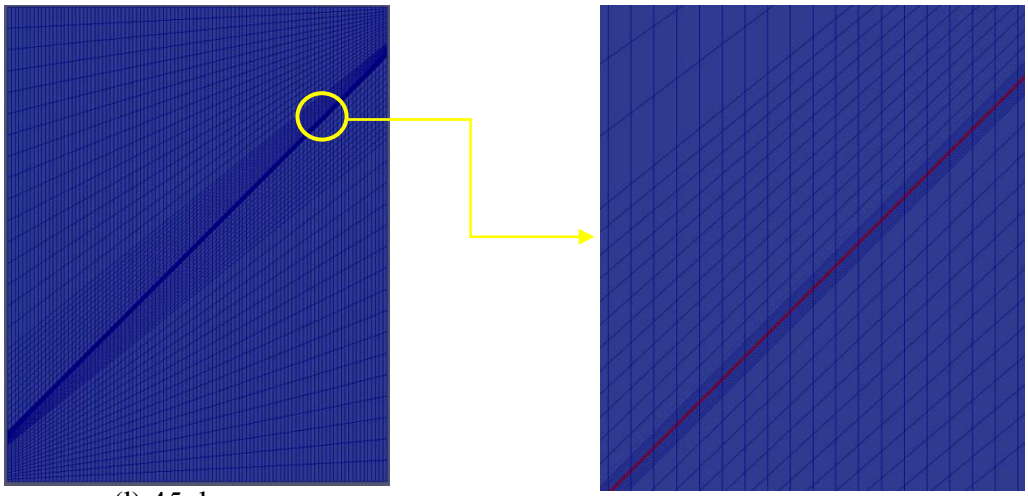

(l) 45 degree (m) a zoom around fracture

Figure 3-22: conformed explicit fracture mesh for fracture oriented from 0 degree to 45 degree.

(Note: red elements denote fracture elements and green elements denote matrix elements).

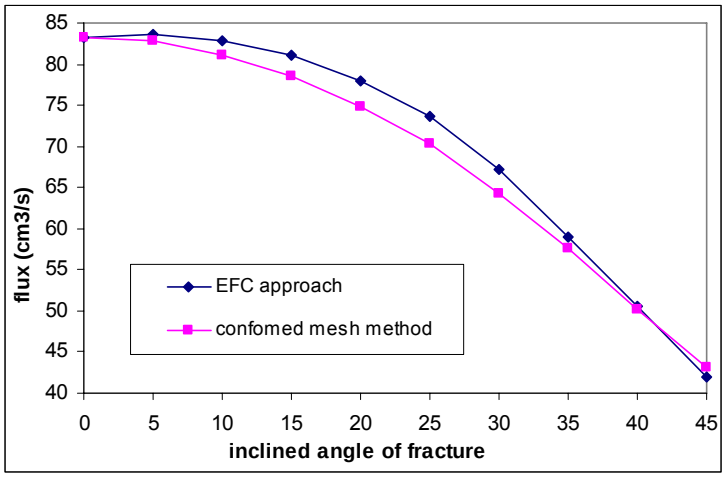

Figure 3-23: flux going through the medium in EFC approach and conformed mesh method.

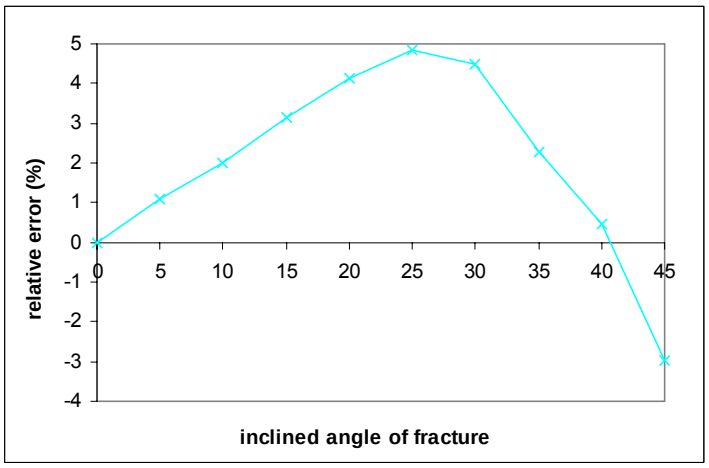

Figure 3-24: relative error (%) of flux going through the medium between EFC approach and conformed mesh method.

3.4.3 Coupled HM test

As the last verification test, we consider the problem in the context of the hydro-mechanical coupling. The same geometry, mechanical properties as well as hydraulic properties of the porous matrix as the two previous examples are used. Concretely, the properties of the porous medium are characterized by Young's modulus E_m=84.6 (GPa), Poisson ratio ν=0.24 and permeability 2.4 x 10^{-15}(m^2). In addition, the two HM coupling parameters of the porous matrix which are respectively the Biot coefficient b=0.8 and Biot modulus M=20.8(GPa) are also referred from the Sellafield (UK) site as summarized in Table 3-1. Regarding with the fracture, a shorter fracture (l=0.6m) which lies in the middle and does not cross-cutting the boundary of the medium is considered (Figure 3-25). Nevertheless, the aperture w=1mm and the properties of the fracture such as normal and shear stiffness k_n=434 (GPa/m) and k_t=86.8 (GPa/m) and the permeability $K_f=w^2/12=8.33 \times 10^{-8}$ (m^2) are maintained. In the first stage, the saturated domain which is fixed on the left, right and bottom boundaries is assumed to be sealed. Corresponding to an applied uniaxial stress σ_1=24.46 MPa on top boundary (which is impermeable), an excess pore pressure in the medium up to 3.54 MPa is induced. In the next stage, the top boundary is opened which allows water to drain out of the medium while the uniaxial stress of 24.46 MPa is maintained (Figure 3-25). As shown in Figure 3-25, two controlled points "A" and "B" located at (0.5m, 1.25m) and (1.0m, 0.0m) respectively as well as a cutting-section "CC" at x = 0.5m are selected to observe the results during this second transient stage. For the validation purpose, the similar scenario as in the hydraulic test is used when we will compare the results obtained from EFC approach (shown in Figure 3-26) with ones calculated from the conform-mesh simulation. In the conform-mesh simulation, the elastic parameters of fractures are obtained from equation (3.11) while the Biot's coefficient and Biot modulus are taken as $b_f = 1;\ M_f = \frac{1}{c_f}$ with c_f is the fluid compressibility.

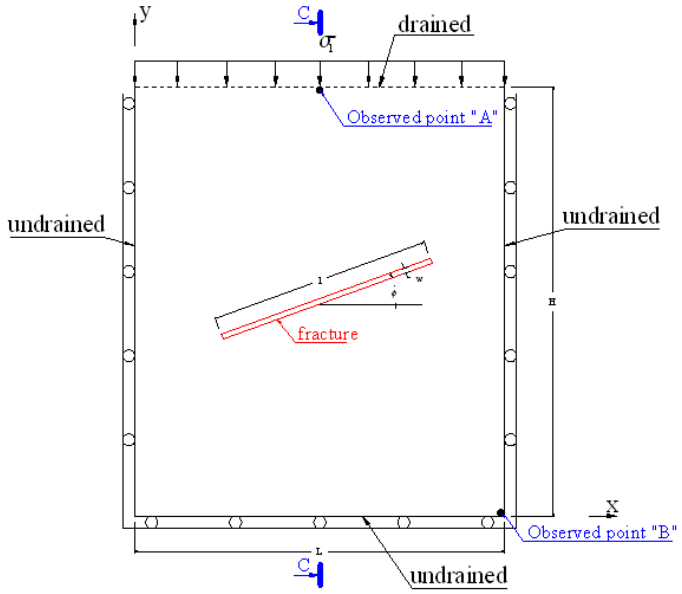

Figure 3-25: Sketch of hydro mechanical test

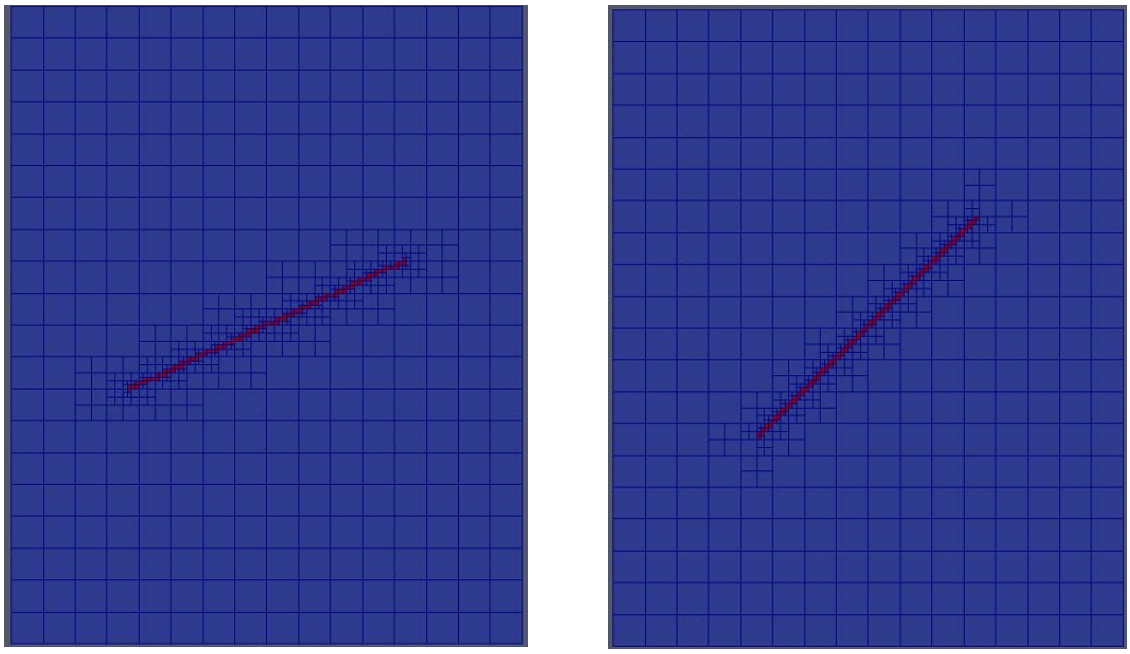

(a) 25 degree (b) 45 degree

Figure 3-26: EFC approach to model the hydro-mechanical problem with fracture oriented: 25 degrees (a) and 45 degrees (b) in the porous medium.

Note: red elements denote fracture-cell elements and green elements denote matrix elements.

Matrix (porous medium)	Young's modulus E_m (GPa)	84.6
	Poisson ratio ν_m	0.24
	Biot coefficient	0.8
	Biot modulus (GPa)	20.8
	Permeability (m2)	$2.4*10^{-15}$

Table 3-1: Poromechanical properties of porous medium (matrix)

To simplify the presentation, in this test, only the equivalent mechanical properties of fracture-cell calculated from our proposed isotropic approximation (equations 3.17) are used while the permeability and coupling HM properties are determined respectively from equations (3.27) and (3.16). Moreover, the local refinement level N=7 will be used. The results obtained from the two previous examples can explain our choices here when at N=7 both the purely mechanical and hydraulic results seem converge while our proposed isotropic approximation matches the best with the reference results. Otherwise, the observation from the previous tests also highlights that the maximum difference between the EFC approach and the referent simulation are usually stated at the inclination angle of 25° and 45°, thus in this last test the simulation is carried out with only these two inclination angles of fracture.

In Figures 3-26 and 3-27 are illustrated respectively the variation of vertical displacement of point “A” and of excess pore pressure at point “B” versus elapsed time. As expected, the decrease of the excess pore pressure (because water drains out at the top boundary) induces an increase of effective stress which explains the increase as well of the displacement in the medium as function of time. This well-known consolidation phenomenon in porous medium has been described since long-time as the Mandel–Cryer effect (Mandel, 1953; Cryer, 1963, Abousleiman et al, 1996). By comparing the results of two approaches (EFC and conform-mesh method) a good agreement can be observed when the relative error is smaller than 3% for all transient calculation instants (see Figure 3-29). The accordance of the results is also illustrated in Figure 3-42 and 3-32 in which are presented the distribution of pore pressure following the vertical “CC” at different instants (1s, 10s, 20s) of fluid diffusion for both cases of inclined fracture. Finally, as an illustration, in Figures 3-31 and 3-32 are captured the iso-values of the pore pressed and vertical displacement in the whole medium at instant t=10s. The results calculated from two approaches (EFC and conform-mesh) for two inclination angles of fracture (θ=25° and θ=45°) show the very similar distribution of pressure and displacement in the model.

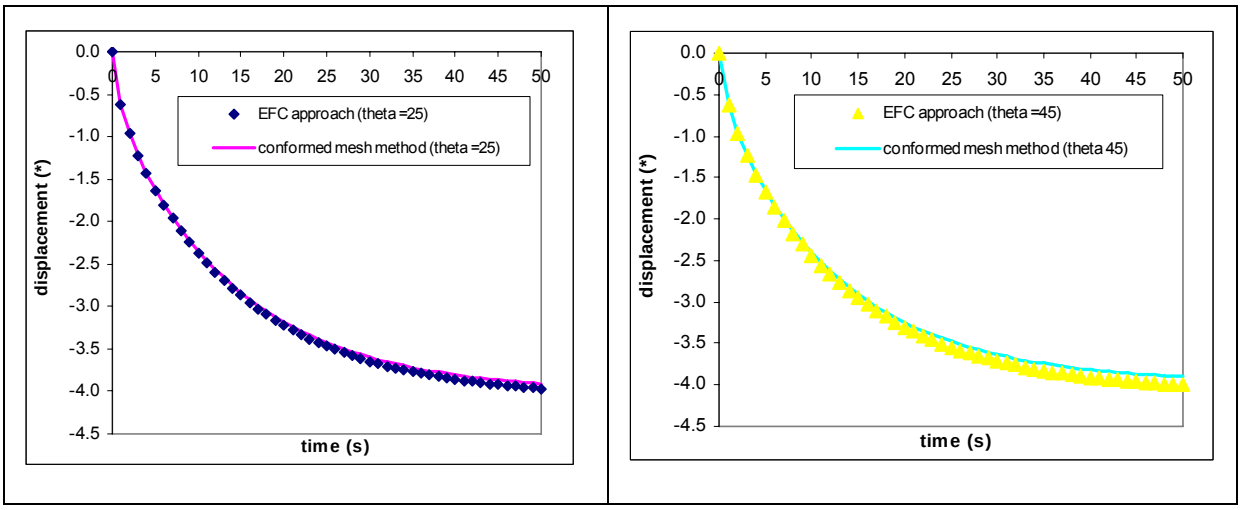

Figure 3-27: vertical displacement at point "A" versus elapsed time for fracture oriented 25 degrees (left) and 45 degrees (right).

(*) values in vertical axis are displacement $*10^5$ (m)

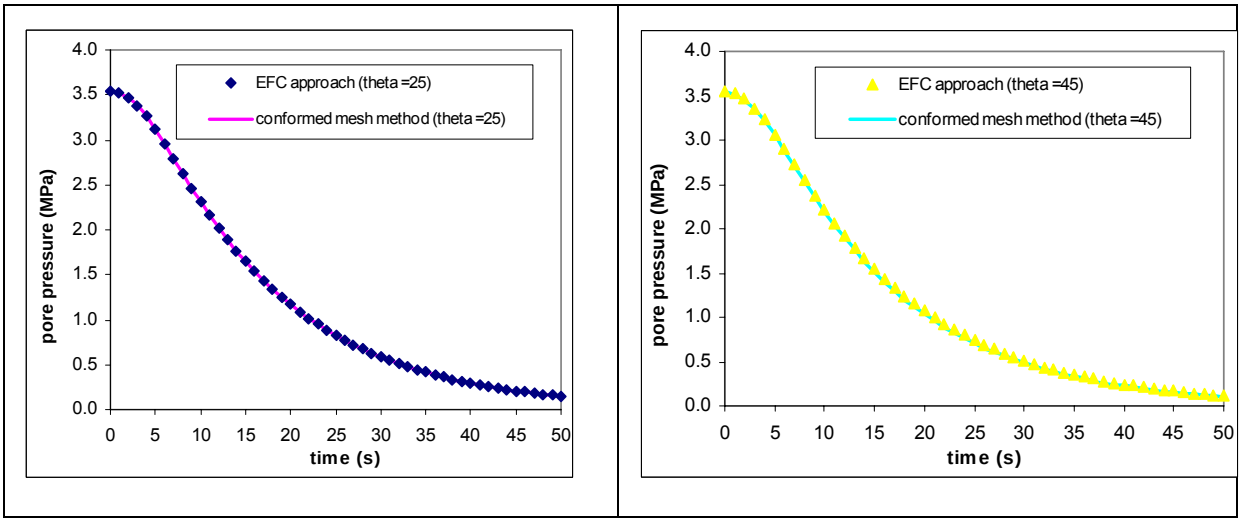

Figure 3-28: pore pressure at point "B" versus elapsed time for fracture oriented 25 degrees (left) and 45 degrees (right).

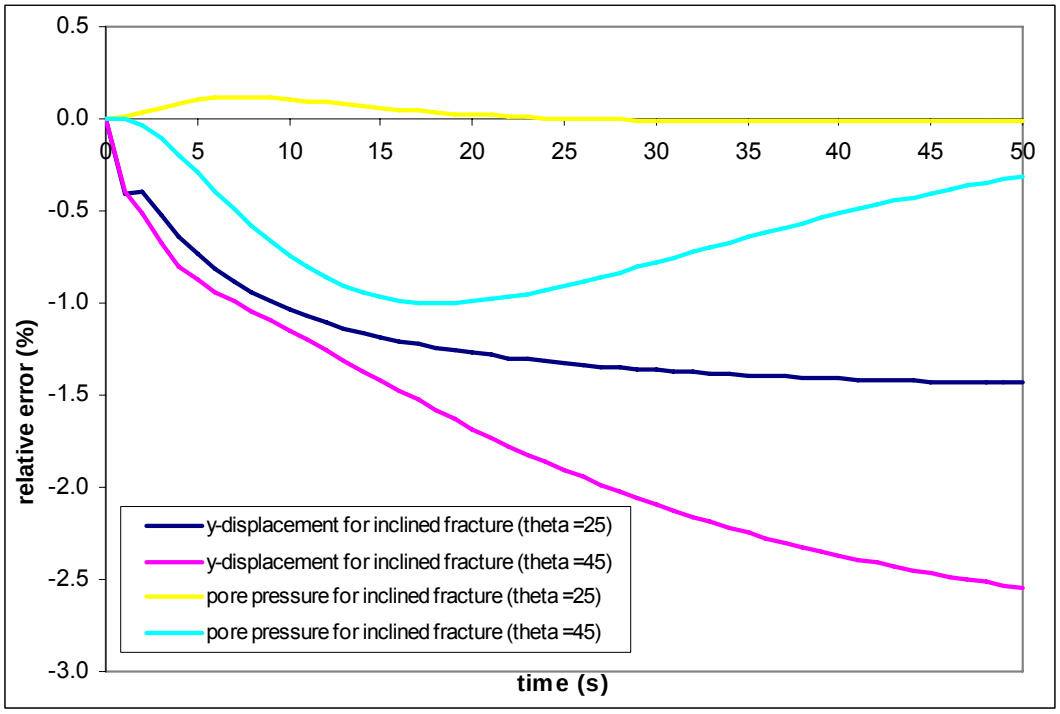

Figure 3-29: relative error (%) of vertical displacement at point "A" and of pore pressure at point "B" between the two approaches (EFC and conform-mesh method).

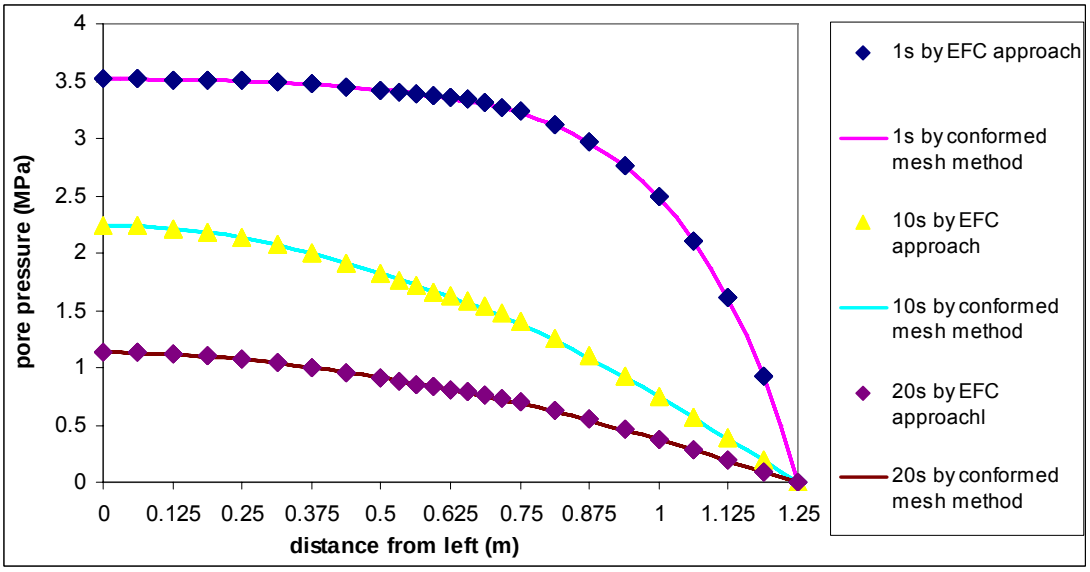

Figure 3-40: Distribution of pore pressure following the vertical cut "CC" at different instants (case of inclined fracture 25°).

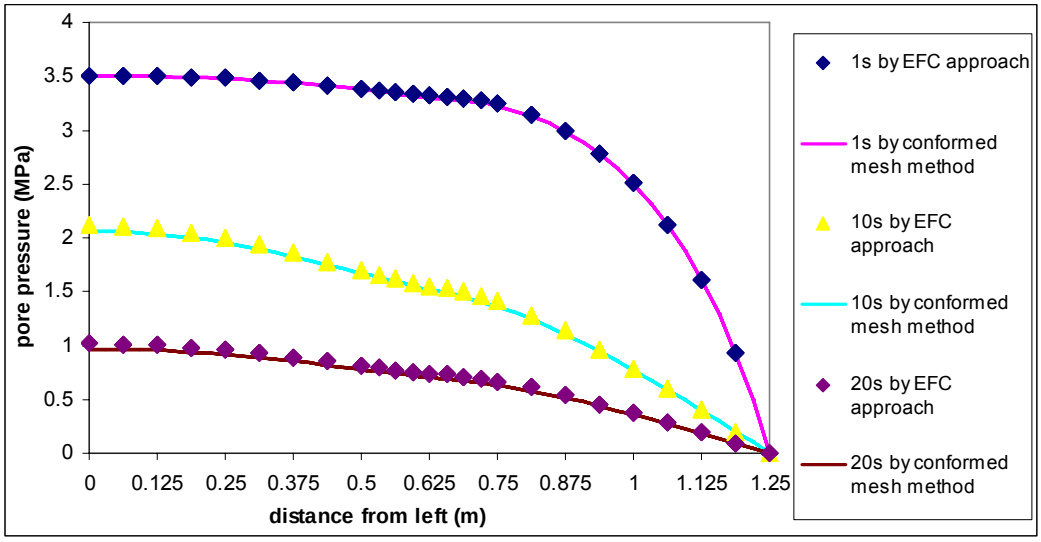

Figure 3-41: Distribution of pore pressure following the vertical cut "CC" at different instants (case of inclined fracture 45°).

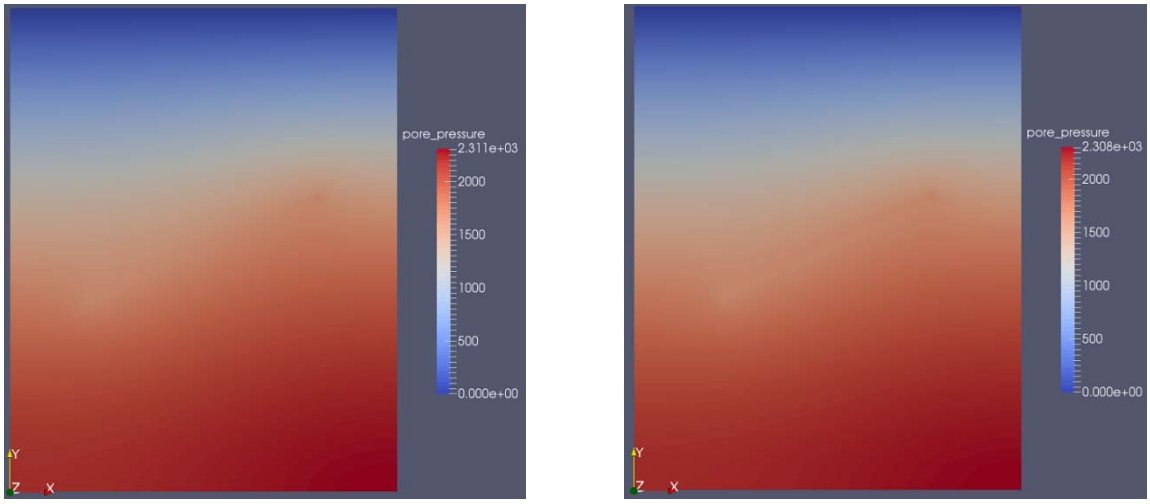

(a) Conformed-mesh method (θ=25°) (b) EFC approach (θ=25°)

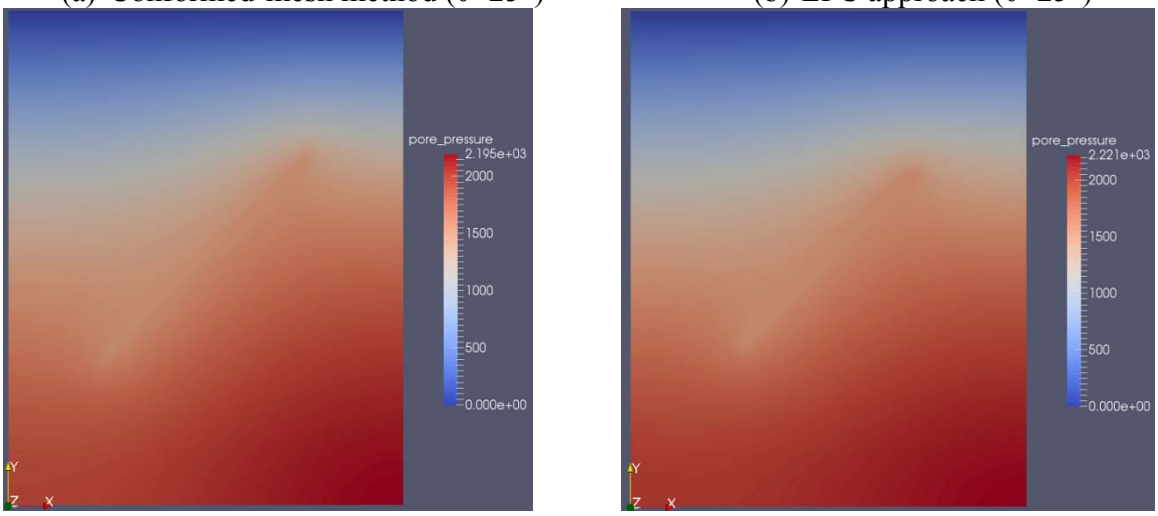

(c) Conform-mesh method (θ=45°) (d) EFC approach (θ=45°)

Figure 3-42: Distribution of pore pressure in the medium at instant 10s obtained from conform-mesh simulation (a,c) and EFC approach (b,d).

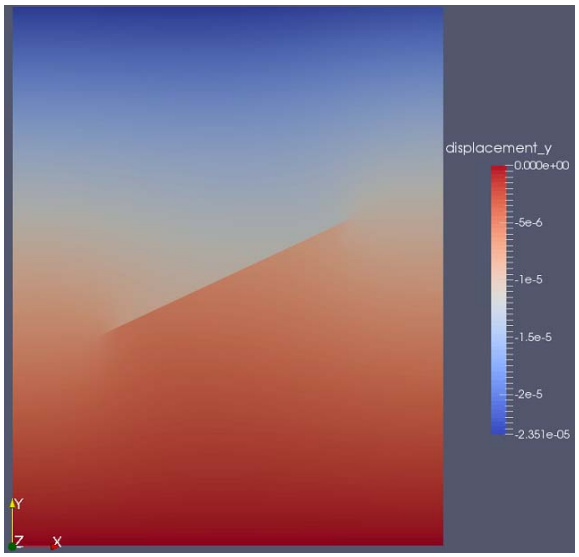

(a) Conform-mesh method (θ=25°)

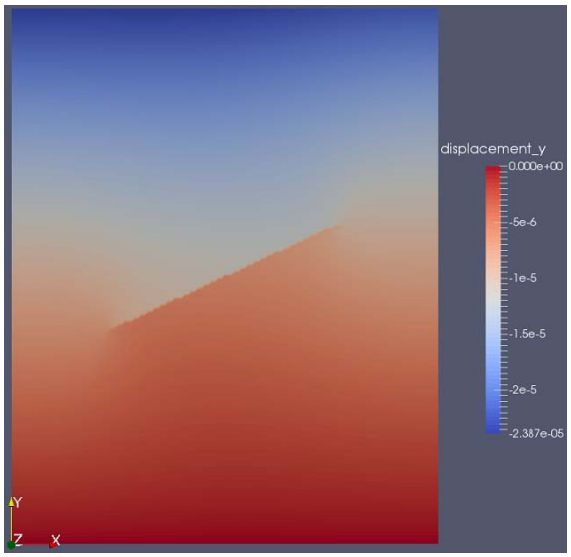

(b) EFC approach (θ=25°)

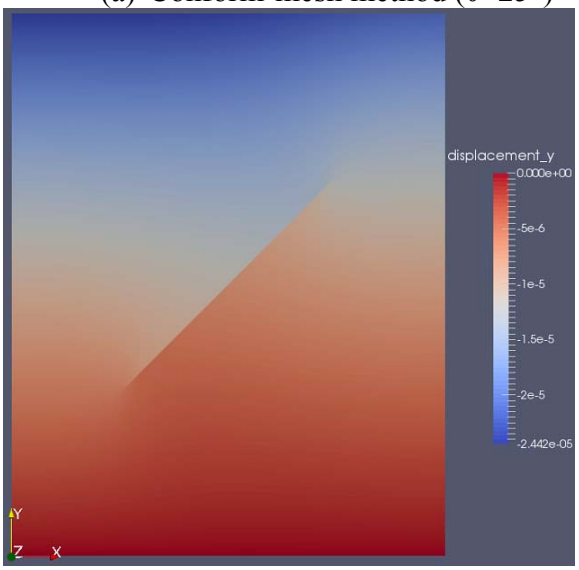

(c) Conform-mesh method (θ=45°)

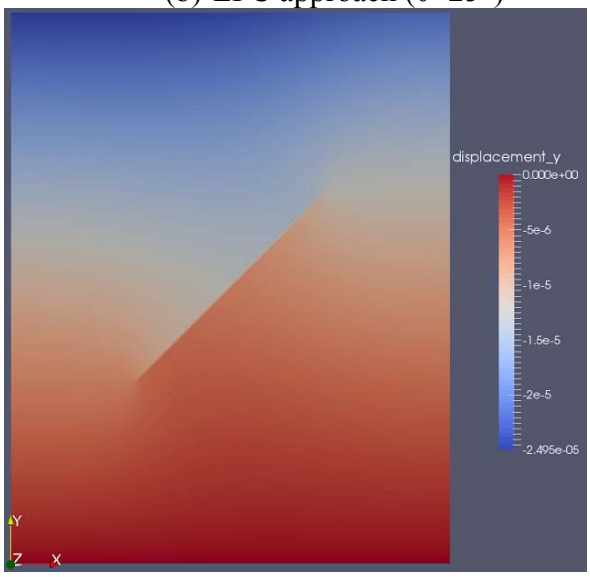

(d) EFC approach (θ=45°)

Figure 3-43: vertical displacement in the medium at instant 10s obtained from conform-mesh simulation (a,c) and EFC approach (b,d).

3.4 Summary.

In this chapter, an approach called embedded fracture continuum approach (EFCA) is presented to model explicitly the fracture network in the porous medium. This approach takes advantages of the two well-known continuum and discontinuum approaches when it could borrow the concept of continuum models while fracture effect can be incorporated explicitly. The principal idea of this approach lies on the utilization of fracture-cell concept which represents an equivalent porous medium. The determination of the properties of this last medium by accounting for the contribution of fracture embedded in the element-cell intersected by this fracture is a primordial task of this approach. In the present work, based on the theory of joint model we highlighted that the equivalent properties of the fracture-cell are anisotropic. Some approximations by assuming that equivalent properties of the fracture-cell

are isotropic or transversely isotropic are then presented. The implementation of the EFC approach in DEAL.II is detailed and we emphasize the utility of the local refinement technique by using the hanging node to model the fracture in our approach. Then through some verifications tests, we investigate the correctness of the EFC approach and different approximations. The results show that the accuracy of the EFC depends on the fracture-cell size which can be controlled through the local refinement level. At a required refinement level, the comparison with the referent results conducted from the conform-mesh method highlight a good agreement when the isotropic approximation proposed in this work is used. In the next chapter, this approach based on the isotropic approximation and the hanging node technique will be applied to simulate the hydro-mechanical behaviour in a real fractured reservoir.

CHAPTER 4: APPLICATION OF EFC APROACH ON THE MODELING OF FRACTURED ROCK MASSES IN REAL FIELD

4.1 Introduction

This chapter is devoted to demonstrate the capabilities of EFC approach and developed software in modeling the behaviour of fractured rock masses at industrial scale. Basically, two problems are treated: (1) determination of the effective mechanical and hydraulic properties of the fractured rock masses, (2) effects of hydro mechanical coupling and of double-permeability in well production.

For the first problem the well-known Sellafield site was selected to get fracture information as well as material properties of matrix and fractures. This choice is mainly orientated form the plenitude of public information from United Kingdom Nirex Limited as part of the second Bench Mark Test (BMT2) of the international collaborative program DECOVALEX III (Nirex 1997a, 1997b). The information of the site is well organized and classified and there is a number of studies performed by some former authors such as Blum et al (2003, 2005), Min and Jing (2003) Min et al (2004a, 2004b, 2005), Anderson et al (2005), Marmier (2007), Baghbanan (2008). These works served firstly for a cross checking of properties and crack geometry during the phase of crack network generation and secondly as a base for comparison with results of this work. Based on overall fracture information of Sellafield site such as fracture density, law distribution of length, orientation and location of fractures, the fracture network generation was performed using the procedure developed during this work. For generation of the fracture network the information of each fracture such as fracture center, fracture length, fracture aperture and fracture orientation must be prior provided. The effective mechanical properties as well as effective permeability of fractured rock mass are then deduced from EFC approach and by explicitly use of a number of fractures. As compared to the former studies form Min and Jing (2003), Min et al (2004b) the fundamental difference in present study is the consideration of the contribution of the matrix permeability in the overall effective permeability, not to talk about effective mechanical properties.

For the second application (2), a fractured reservoir should be considered in order to demonstrate the double-permeability and double porosity effect. For simplicity, and in order to take advantage from information on fractures geometry and properties of already described Sellafield site, information very often confidential for real reservoirs, we considered an hypothetical reservoir, with crack geometry as that of Sellafield, but with a much higher matrix porosity, characteristic of reservoir rocks.

Since in large scale simulation the hydromechanical behaviour of the rock masses is thought to be dominated by behaviour of few large fractures, for this problem only long fractures with big opening are explicitly modeled. Production rate and cumulative production of a reservoir are estimated using single-phase flow approach. Taking advantage from EFC approach developed in this study, the local closure of fracture in response to the decrease of the fluid pressure in fracture, as proposed in Bandis et al. (1983) and Barton et al. (1985) is modeled and the subsequent effects on production rate and elapsed time are evaluated

4.2 Real field data used in the modeling

In this part, the data used for the modeling taken from the real field (Sellafield site in UK) will be briefly synthetized. It consists of all necessary data about the fractures such as length, orientation, location as well as fractures' aperture which will be used as the input data for the generation of the discrete fractures network (DFN) in our modeling. The abundancy of information about this site explain our motivation to consider its modeling. In fact, geotechnical data (among others) of the site is available in the literature thanks to the investigation program performed by United Kingdom Nirex Limited (Nirex 1997a,1997b). Part of this information is provided as input data for Bench Mark Test (BMT2) of the international collaborative program DECOVALEX III (Blum et al., 2003, 2005; Min and Jing, 2003; Min et al., 2004a, 2004b, 2005; Eloranta 2000; Anderson et al., 2005, Marmier 2007, Baghbanan 2008). The site was studied in respect with the nuclear waste disposals in the earlier nineties.

4.2.1 Fracture trace lengths

Analysis of the fracture data for the repository host rock in the Sellafied site indicates that a power-law fracture length distribution can describe the fracture network geometry (Blum et al, 2003, 2005; Min and Jing, 2003; Min et al, 2004a, 2004b, 2005; Anderson et al, 2005; Marmier, 2007; Baghbanan, 2008). The power-law distribution of the fracture length is given by the following equation:

$$N_F = C.L^{-D} \tag{4.1}$$

where N_F is the number of fractures (with fracture length greater than the length L) per unit area; C is the constant density and D is the fractal dimension.

Using this Eq. (4.1), we can calculate number of fracture in a range of fracture length (L_a , L_b) as:

$$N_F^{ab} = C\left(L_a^{-D} - L_b^{-D}\right) \tag{4.2}$$

The parameters C and D can be chosen depending on the intensity of fractures of the site. This intensity is not uniform and schematically three zones with density from low to high are distinguished. Correspondingly, the following values are proposed for these two parameters of crack length distribution (Blum et al, 2003, 2005; Min and Jing, 2003; Min et al, 2004a, 2004b, 2005; Anderson et al, 2005; Marmier, 2007; Baghbanan, 2008; Nirex, 1997a, 1997b): C=1.2 and D=2.0 for low-density zone; C=2.17 and D=2.08 for median-density crack zone and C=4.0 and D=2.2 for high-density crack zone (see Table 4.1). With these fractal dimensions, more than 95% of fractures have trace lengths less than 2m (Baghbanan, 2008), and the calculated mean trace length is about 0.92 m (Nirex, 1997a; Nirex, 1997b). For illustration purpose, in Figure 4-1 are presented these power-law distributions for fracture length with three cases of fractures density. The figure is taken from Nirex report (1997b) as shown in Figure 4-1a and replotted in this work using the parameters C and D as mentioned above (Figure 4-1b).

Otherwise, as described in the many contributions (Blum et al, 2003, 2005; Min and Jing, 2003; Min et al, 2004a, 2004b, 2005; Anderson et al, 2005; Marmier, 2007; Baghbanan, 2008; Nirex, 1997a, 1997b), only fractures greater than 0.5 m of length were recorded in the site investigation and this is why the fractures length from 0.5m to 250m are usually chosen as the minimum cut-off length and the maximum cut-off length of the power-law (Blum et al, 2003, 2005; Min and Jing, 2003; Min et al, 2004a, 2004b, 2005). The corresponding fracture intensity P_{20} (defined as the number of fractures per meter square) 4.8, 9.19 and 18.3 were determined for the low, median and high crack density zones, respectively. Another fracture intensity known as the total trace length per meter square (the parameter P_{21}) were calculated by UoB/NIREX teams University of Birmingham/Nirex (UK) (Anderson et al, 2005) with the corresponding values 4.85, 8.92 and 16.91 for zones with low, medium and high crack density.

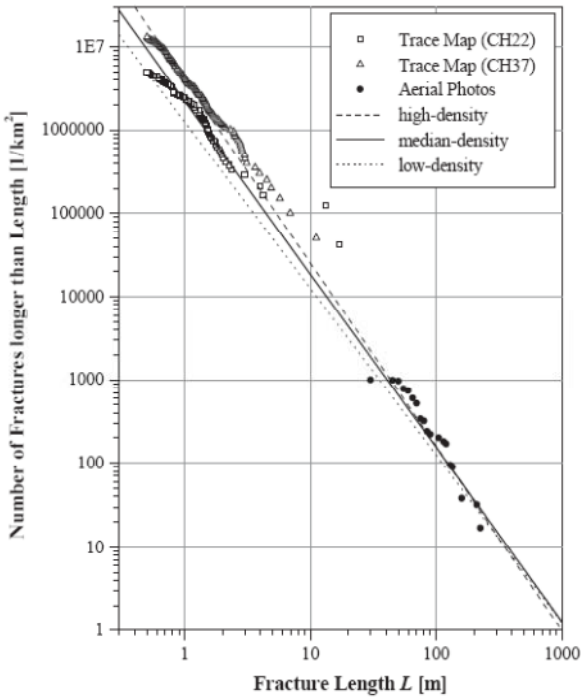

(a) from Nirex, 1997b

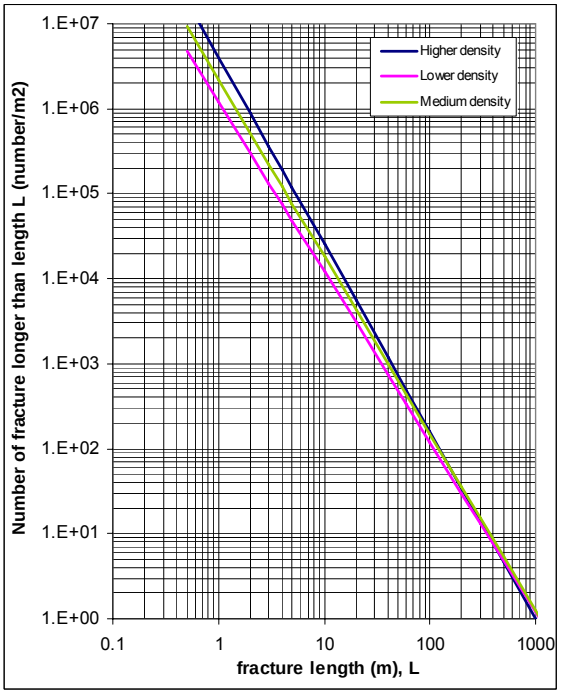

(b) from parameters in the table 4-1

Figure 4-1 Power law distribution of fracture length in the Sellafied site from the Nirex report (1997b) (a) and reploted in this work using the proposed parameters C and D (b).

Cases	C	D	P_{20}	P_{21} (m/m2)
Low-density	1.20	2.00	4.80	4.85
Medium-density	2.17	2.08	9.19	8.92
High-density	4.00	2.20	18.38	16.91

Table 4-1 Parameters for fracture length of the Sellafied site (Nirex, 1997a, 1997b, Blum, 2003; Andeson et al, 2005).

4.2.2 Orientations of fractures

As commonly assumed in DFN modeling, the orientations of fractures in Sellafied site seem to follow a Fisher distribution (Nirex, 1997a, 1997b; Eloranta, 2000; Blum et al, 2003, 2005; Min and Jing, 2003; Min et al, 2004a, 2004b, 2005; Anderson et al, 2005; Marmier, 2007; Baghbanan, 2008). It was pointed out that in this site there are four principal sets of fracture as resumed in table (4.2). The probability of the fracture with the direction angle θ that deviates from the mean orientation angle of a fracture set is calculated as follow (Baghbanan, 2008):

$$\mathrm{P}(\theta) = \frac{e^{K} - e^{K\cos(\theta)}}{e^{K} - e^{-K}} \qquad (4.3)$$

where *K* is the Fisher constant, which is assigned for each fracture set according to Table 4.2 (Nirex, 1997a; Nirex, 1997b).

Joint Set	Dip/Dip direction (degree)	Fisher constant (*K*)	Max/Min Spacing (m)	Mean Spacing (m)
1	8/145	5.9	5.35/0	0.29
2	88/148	9.0	2.21/0	0.26
3	76/21	10.0	2.01/0	0.28
4	69/87	10.0	3.54/0	0.31

Table 4-2: Parameters used for fracture orientation of the Sellafied site (Nirex, 1997a; Nirex, 1997b; Eloranta, 2000)

4.2.3 Location of the fractures

Concerning the location of fractures (i.e, the spatial distribution of their centres), a Poisson distribution has been largely assumed for the fracture midpoints (Min and Jing, 2003; Min et al, 2004a, 2004b, 2005; Anderson et al, 2005; Baghbanan, 2008). In a DFN approach of crack geometry modeling, the locations of fracture centers are generated by generating random numbers based on a recursive algorithm. If the generation space is defined in terms of two coordinate ranges ($x_{\min}, x_{\max}$) and ($y_{\min}, y_{\max}$) along a local set of Cartesian axes, one can generate midpoint coordinates (x_i and y_i) of every fracture through the following equations (Baghbanan, 2008):

$$\begin{aligned} x_i &= x_{\min} + R_{x,i}(x_{\max} - x_{\min}) \\ y_i &= y_{\min} + R_{y,i}(\mathrm{y}_{\max} - y_{\min}) \end{aligned} \tag{4.4}$$

where $R_{x,i}$, $R_{\mathrm{y},i}$ are number in the range [0,1]

4.2.4 Aperture of fractures

In general, by definition, the apparent aperture of fracture is the distance between the two surfaces of the fracture. However, depending on the real applications, one distinguishes the hydraulic aperture which is back-calculated using cubic law equation from laboratory test results of flow rates (Ge, 1997), and mechanical aperture when one considers the problem of applied stress acting normal to the mean fracture plane (Renshaw, 1995). In this study, the term “aperture” means the hydraulic aperture unless specifically stated and the validity of cubic law for laminar fluid flow through fractures is also assumed.

Studying the correlation between fracture aperture and trace length, Baghbanan (2008) showed that the fracture aperture in Sellafield site can vary from 1 to 200 µm and the lognormal distribution was proposed (see Figure 4-2). Blum et al. (2004) indicated that the mean hydraulic apertures ranged between 0.3µm and 180.7µm depending on the mechanical properties and the applied stresses state. However, to simplify the implementation, the initial fracture aperture usually is assumed as being uniform. The value chosen of this uniform aperture is however disperse: for example, in Min et al. (2004a ,2004b) it was taken 30µm or 65µm; while in other works it was: 65µm or 200µm in Baghbanan (2008), 85µm in Namdari et al. (2016) or 130.7µm in Blum et al. (2003). This difference comes from the different critical normal stress (corresponding to different depth of given samples) as reported by Nirex (1997c). In Min et al. (2004a) the initial aperture 65 µm was chosen corresponding to the normal stress 30 MPa.

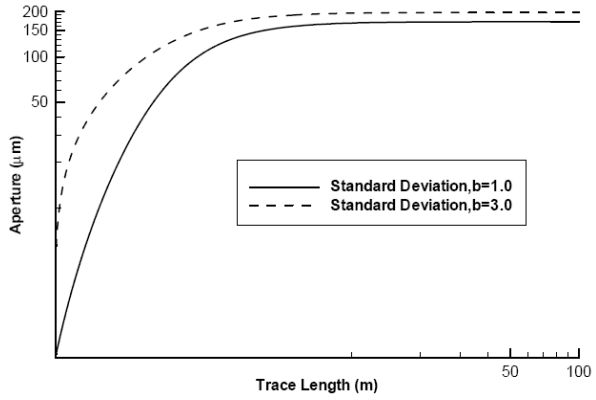

Figure 4-2: Fracture aperture versus trace length for different values of standard deviation (Baghbanan, 2008)

4.2.5 Mechanical properties of rock and fractures

For the modeling, the mechanical properties of the rock matrix and of fractures is crucial. In this work, the mechanical properties of rock matrix (intact rock), assumed isotropic as resumed in Table 4-3 are taken from Nirex reports (1997a, 1997b) which are as well represented by various authors such as Eloranta, 2000; Blum et al. 2003, 2005; Min and Jing 2003; Min et al. 2004a, 2004b, 2005; Anderson et al. 2005; Marmier 2007; Baghbanan, 2008. Concerning the mechanical properties of joints, the normal and shear modulus (k_n=434GPa/m, k_s=86.6GPa/m) are reported in these last works which are also chosen in our modeling.

Rock matrix	Bulk density ρ [kg/m3]	2750
	Young's modulus E_{block} [GPa]	84
	Poisson ratio ν	0.24
Fractures	Joint normal stiffness k_n [GPa/m]	434
	Joint shear stiffness k_s [GPa/m]	86.8

Table 4-3: Parameters used for rock matrix and fractures

4.2.6 Initial stresses

To complete this synthetic part, we note that the in-situ stress field (MPa) is described by the following equations (Nirex 1997c):

$$\sigma_V = 0.0294D + 0.26622$$
$$\sigma_H = 0.03113D + 1.88747 \quad (4.5)$$

where σ_V is vertical stress, σ_H is horizontal stress and D is depth below ground level [m].

In this study, we consider that the center of the studied domain lies at the depth 725m from the ground surface, thus $\sigma_V = 18.35$ MPa and $\sigma_H = 24.46$ MPa from the Eq. (4.6).

4.3 Generation of the discrete fractures network

The synthetized data as presented in the previous part will be used as input for the generation of the fractures network. For the clarity of the purpose, the methodology to generate DFN realizations is detailed in following steps as below:

Step 0: Read the input of different fractures network's parameters including the fractal dimensions (C, D), the Fisher constant (K) of different principal sets of fractures and the dimension of the geometrical model (A).

Step 1: Calculate the number of fractures to be generate from each class of fractures length [l_a , l_b] based on the power law distribution (Eq. 4.2). The corresponding mean value of fracture length of each class is $l_{ab} = \frac{l_a + l_b}{2}$. Then the total number of fractures in the model can be evaluated.

Step 2: Corresponding to each principal fracture set, determine the number of fracture in each angle interval [θ_a , θ_b] by using the Fisher distribution (Eq. 4.3). The mean value of fracture angle is taken as $\theta_{ab} = \frac{\theta_a + \theta_b}{2}$ will be then stored in a list.

Step 3: Using the Poisson distribution (Eq. 4.4), another list of the center coordinates of all fractures is generated.

Step 4: Distribute three parameters (length, angle, and center) for each fracture.

With each fracture length l_{ab} in step 2 (we begin fracture generation from the longest to the shortest fracture), its location and orientation are randomly taken from the list of orientation angle (step 2) and list of center coordinates (step 3). With the chosen position of the fracture center, if 20% (*) of fracture length is outside of the domain, this last center is suppressed and another center is generated following the same steps.

Step 5: Adjust the fracture length and the fracture center.

The fracture length and the fracture center will be adjusted to keep the difference of total trace length of fractures between the model and the input data be less than 5%. $\left(\frac{\left| p_{21} A - L^* \right|}{p_{21} A} < 5\% \right)$

where L^* is the total trace length of fractures in the model, p_{21} is fracture intensity (taken from the table 4-1), A is the area of representative element volume.

The fracture length will be increased or reduced by factor k in the equation $l_{ab}^{adjust} = k l_{ab}$

where $k = \frac{p_{21} A}{L^*} = \frac{p_{21} A}{\sum_{1}^{N} l_{ab}^*}$ with l_{ab}^* is the trace length of fracture before adjustment.

From the result of fracture adjustment, fracture center will be updated.

The output of DFN (center, length, orientation, total trace length) will be saved in a text file which will be imported in DEAL II for the simulations. Note that at the end of this step, the DFN is successfully generated which takes into account all the dead-end fractures as well as isolated fractures.

Step 6: Eliminate dead-ends and isolated fractures (**).

- step 6a: For each fracture, its intersection with the boundaries and other fractures will be counted. If number of intersection points is less than 2, this fracture will be deleted.

- step 6b: If the number of intersections is more than 2, this fracture is adjusted to the maximum distance of its intersection points. Fracture center and fracture length are then updated. We call this process is “cutting fracture”.

- step 6c: Eliminate isolated fractures. To this end, in the first stage we define four boundaries as four interconnected fractures while all the other fractures (obtained from the previous step

6b) are set as isolated fractures. We check in the second stage that if there is an isolated fracture which connects to an interconnected fracture. If it is the case, the status of this former fracture will be changed and it is classified to the interconnected fracture class. This step will be repeated and finished only if there is any isolated fracture changing its status.

-Step 6d: Output the information of all interconnected fractures to another text file which can be imported in DEAL II to model the DFN without dead-end and isolated fractures.

(*) The proposed value of 20% is tentative value. In reality, the total trace length of all fractures (the P_{21}) may approach the required value if this tentative value (20%) is reduced but our results show that the procedure to re-find the new center of fracture can become much more expensive in this case.

(**) Generally, natural fracture systems comprise a network of conductive fracture segments, which at both endpoints connect to either the conductive network or to the domain boundary, and a number of non-conductive fracture segments, which connect only at one end-point (see Figure 4-3). We refer to these non-conductive segments as "dead-ends" (Birkholzer and Karasaki, 1996). As a matter of fact these dead-ends segments need not to be suppressed in EFC we developed and some analyses further on in this study they are kept. But, in works performed by other authors that used DFN approach on this site, these dead-ends could not be managed. In order to compare our results with results of these authors we added this last elimination of dead-ends in some of our analyses. When this happened, it is explicitely indicated in the text.

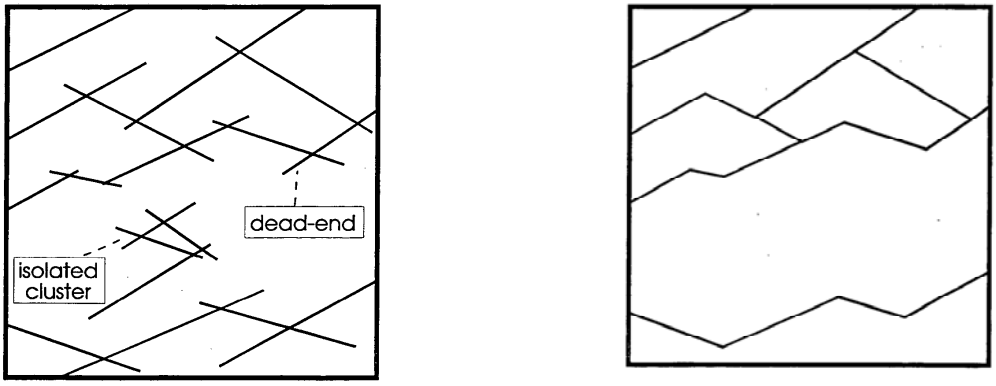

Figure 4-3. DFN with dead-end and isolated fractures (a), DFN without dead-end and isolated fractures (b) (Birkholzer and Karasaki, 1996).

4.4 Representative elementary volume (REV) of the fractured rock mass

The DFN generation process is used to construct the REV of the fractured medium (Sellafield site) through which the effective hydro-mechanical properties can be calculated using the numerical upscaling method. In the literature, this subject was discussed in different

contributions, mainly based on the discontinuum approach. For example, in their works, Min and his collaborators (Min and Jing 2003, Min et al 2004a) used the UDEC code to investigate the existence and the size of REV. Study was conducted on a square model with the size varying from 0.25m x 0.25m to 8m x 8m. Considering the purely mechanical problem, these authors showed that for this fractured rock mass, the REV exist and its size can be chosen from 2m to 6m with the coefficient of variation is from 10% to 5%, respectively. The coefficient of variation is defined as the ratio of standard deviation over the mean value (Min et al, 2004a). The same observation REV size was obtained for the hydraulic problem of this fractured rock. More precisely, in their work Min et al. (2004a) proposed that the REV size for the effective permeability can be taken from 2 m to 8m with the coefficient of variation is 30%, 20% and 10% corresponding to REV of 2m, 5m and 8m, respectively. From these discussions, it seems that a REV with the smallest size about 2m (corresponding about two times of the mean length of the DFN in Sellafield site) can be chosen to calculate the effective mechanical properties as well as the effective permeability of this fractured rock mass.

Below, we present an example of the DFN generated for a REV with 2m of size. Firstly, in Table 4-4 and 4-5 are detailed the number of fractures for each length group and orientation group as well as the total number of fracture corresponding to the high-density crack zone of fracture distributed in the area of the VER (P_{20}=18.38 as shown in Table 4-1 and hence the total number of fracture $N = p_{20}\,\mathrm{A} = 73$ fractures). The distribution of fractures for each group respects the theoretical power law distribution as showed in figure 4-4 and 4-5. Note here that the fractures are generated in the horizontal plane Oxy with the x-axis represents the North direction. Figure 4-6 illustrates the results of step 4 (draft sample), step 5 (sample with dead-end and isolated fractures) and step 6 (sample without dead-end fractures).

Length arrange		Number
la	lb	
0.5	0.55	14
0.55	0.6	10
0.6	0.65	8
0.65	0.7	6
0.7	0.8	9
0.8	0.9	6
0.9	1	4

Length arrange		Number
la	lb	
1	1.2	5
1.2	1.4	3
1.4	1.6	2
1.6	1.8	1
1.8	2	1
2	2.83 (*)	4
Total		73

Table 4-4: Number of fractures distributed in each group of fracture length (result of step 1)

(*) 2.83m is the maximum trace length which could be obtained in the VER with 2m of size ($2\sqrt{2} = 2.83m$)

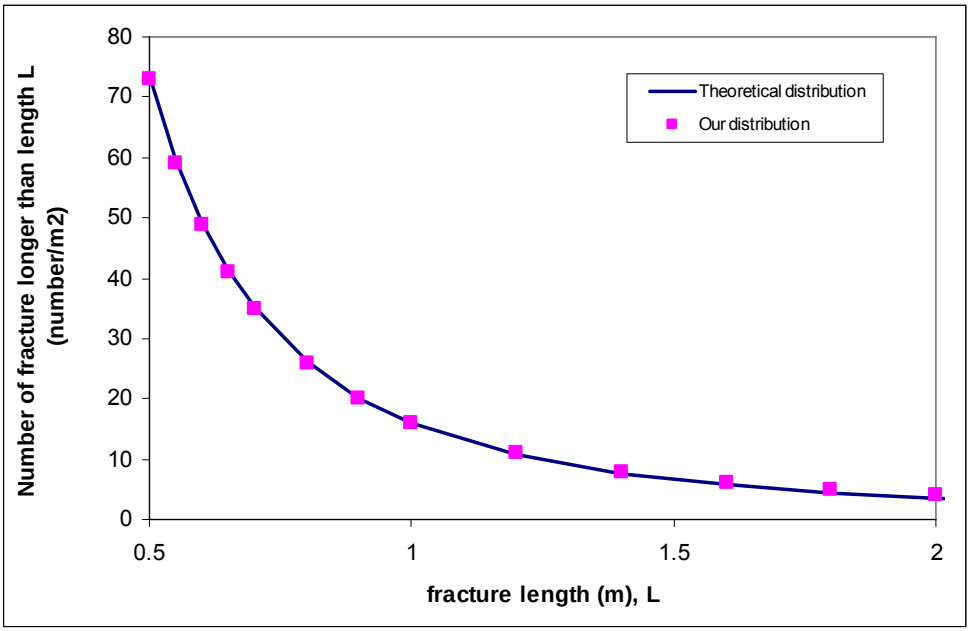

Figure 4-4: Number of fracture versus fracture length (following the theoretical power law distribution)

Angle to x direction		N° of principal fractures set				Total fractures
theta(a)	theta(b)	1	2	3	4	
-5	5	2	2	3	0	7
5	15	1	1	3	0	5
15	25	1	0	1	0	2
25	35	0	0	2	0	2
35	45	0	0	3	1	4
45	55	0	0	2	1	3
55	65	0	0	1	2	3
65	75	0	0	0	3	3
75	85	0	0	0	2	2
85	95	1	0	0	1	2
95	105	1	1	0	3	5
105	115	2	1	0	3	6
115	125	2	2	0	2	6
125	135	2	3	0	1	6
135	145	1	2	0	0	3
145	155	1	1	0	0	2
155	165	2	2	1	0	5
165	175	2	3	2	0	7
Total		18	18	18	19	73

Table 4-5: Number of fractures distributed in each group of fracture orientation (result of step 2)

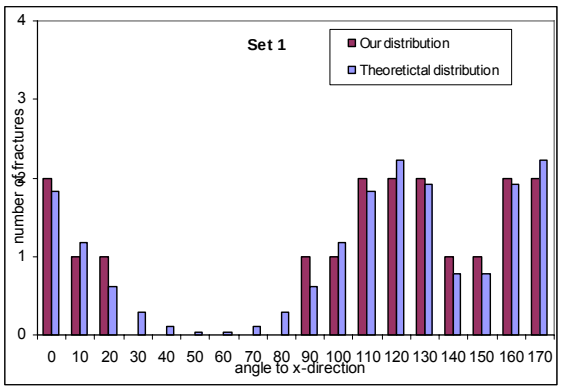

(a)

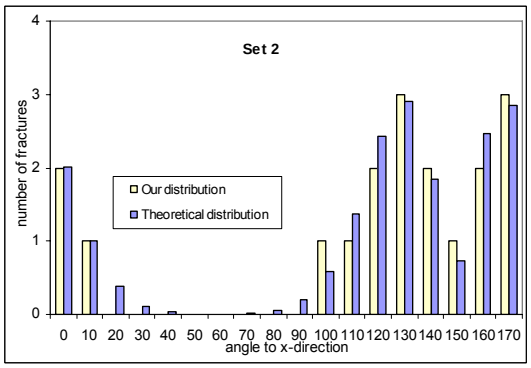

(b)

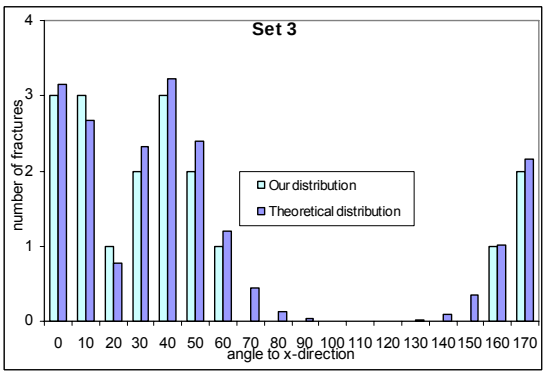

(c)

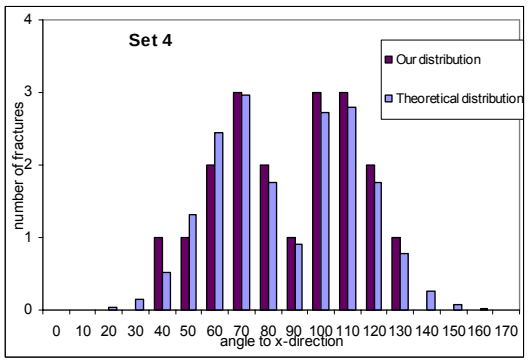

(d)

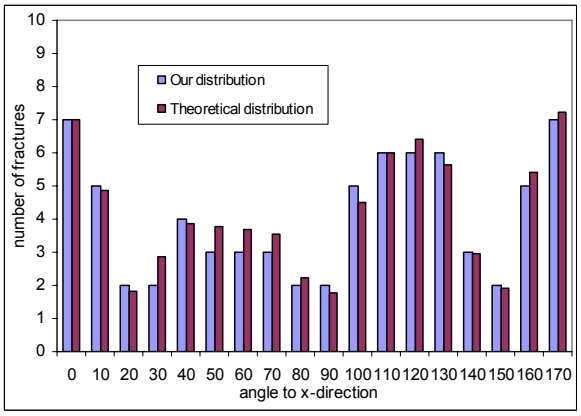

(e)

Figure 4-5: Number of fracture versus the direction angle corresponding to four principal fracture sets (a,b,c,d) and total fracture distribution (e).

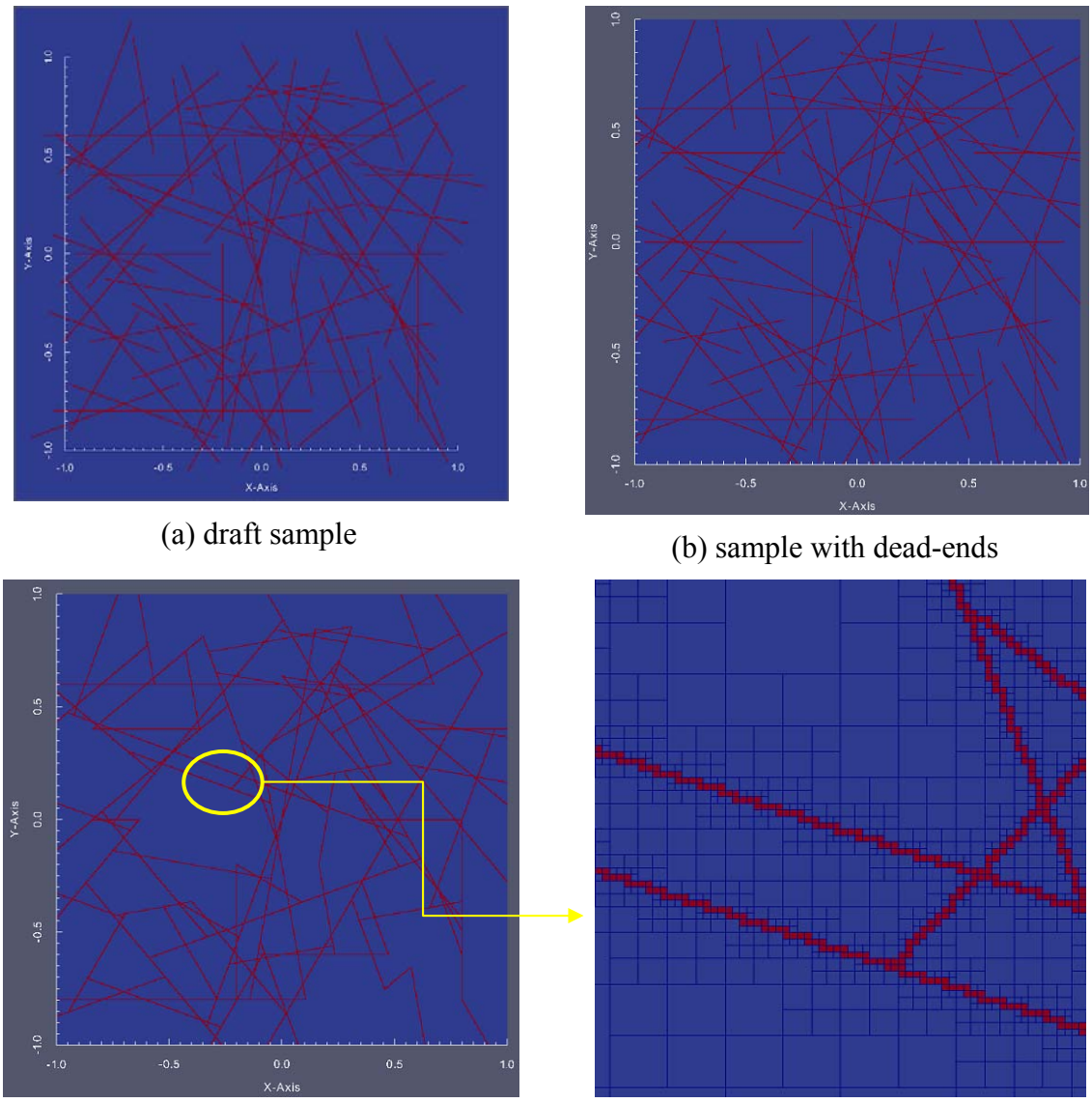

(a) draft sample

(b) sample with dead-ends

(c) sample without dead-ends

(d) a zoom around fractures

Figure 4-6: The DFN genration process: (a) draft sample (result of step 4), (b) sample after adjustment (result of step 5), (c) sample without dead-end (result of step 6) and (d) a zoom around fractures.

4.5 Determination of the effective elastic properties and permeability of fractured rock masses in Sellafield site

4.5.1 Methodology for the determination of the effective elastic properties

The determination of the effective elastic properties of fractured rock masses in Sellafield site was carried out in the work of Min and Jing (2003) based on the distinct element method implemented in the UDEC code. In this study, the dead-end fractures and isolated fractures were not considered in the DFN. However, Yang et al (2014) by using the finite element method to study another type of fractured rock highlighted that ignoring the dead-end and isolated fractures can cause change of stress distribution and may leads to wrong results.

In this work, this topic will be reconsidered by using our developed EFC approach. Similar to the previous works, the effective elastic properties of fractured rock masses in Sellafield site will be investigated by using the 2D plane strain analysis. In this condition, the linear elastic behaviour of a general anisotropic media is given by

$$\varepsilon_{mn} = S_{mnpq}\sigma_{pq} \tag{4.7}$$

in which the matrix form gives (see Min and Jing, 2003; Yang et al, 2014):

$$\begin{pmatrix} \varepsilon_{zz} \\ \varepsilon_{xx} \\ \varepsilon_{yy} \\ \varepsilon_{xy} \end{pmatrix} = \begin{pmatrix} S_{11} & S_{12} & S_{13} & S_{14} \\ S_{21} & S_{22} & S_{23} & S_{24} \\ S_{31} & S_{32} & S_{33} & S_{34} \\ S_{41} & S_{42} & S_{43} & S_{44} \end{pmatrix} \begin{pmatrix} \sigma_{zz} \\ \sigma_{xx} \\ \sigma_{yy} \\ \sigma_{xy} \end{pmatrix} \tag{4.8}$$

(Note that the coordinate Oxyz presents global coordinate (z =1, x =2, y =3) as shown in the Figure 3-8)

The same methodology to determine the effective compliance matrix in Eq. (4.8) proposed in (Min and Jing, 2003; Yang et al, 2014) will be adopted here. Follow that, we assume that the Young modulus and Poisson ratios in the z-direction are remained as ones of the intact matrix ($\nu_{zx} = \nu_{zy} = \nu_m$, $E_z = E_m$). Correspondingly, we have $S_{12} = S_{21} = S_{13} = S_{31} = -\frac{\nu_m}{E_m}$ $S_{11} = \frac{1}{E_m}$.

The study of Min and Jing (2003) also revealed that the values of $S_{14}, S_{24}, S_{41}, S_{42}$ are small in compared with other components while S_{34}, S_{43} are equals to zero due to the fact that shear stress σ_{xy} does not affect the z-direction deformation. Thus, the compliance tensor in Eq. (4.8) can be rewritten in a more compact form:

$$\begin{pmatrix} \varepsilon_{zz} \\ \varepsilon_{xx} \\ \varepsilon_{yy} \\ 2\varepsilon_{xy} \end{pmatrix} = \begin{pmatrix} \frac{1}{E_m} & -\frac{\nu_m}{E_m} & -\frac{\nu_m}{E_m} & 0 \\ -\frac{\nu_m}{E_m} & S_{22} & S_{23} & 0 \\ -\frac{\nu_m}{E_m} & S_{32} & S_{33} & 0 \\ 0 & 0 & 0 & S_{44} \end{pmatrix} \begin{pmatrix} \sigma_{zz} \\ \sigma_{xx} \\ \sigma_{yy} \\ \sigma_{xy} \end{pmatrix} \tag{4.9}$$

Calculating the effective elastic properties of the fractured rock masses reduces to the determination of only the five components $S_{22}, S_{23}, S_{32}, S_{33}, S_{44}$ which can be conducted through three numerical experiments as illustrated in Figure (4-7). Let us consider a rectangular domain with the corresponding dimensions L_x (in x direction) and L_y (in y direction) and the sides of the domain are numbered from (1) to (4). We run three following loading cases (see Yang et al, 2014, Pouya and Ghoreychi 2001):

- Case a: Compression in x direction with free boundaries in y-direction: the boundary (1) is fixed in x-direction and a compressional stress $f_x^{(a)}$ is prescribed on the boundary (3). The average displacements U_x in the boundary (3) and U_y in boundaries (2), (4) are then calculated.
- Case b: Compression in y direction with free boundaries in x-direction: the boundary (2) is fixed in y-direction and a compressional stress $f_y^{(b)}$ is prescribed on the boundary (4). We calculate the average of displacements U_x of the boundaries (1), (3) and U_y of the boundary (4).
- Case c: Shear in xy-direction: a shear stress τ with the same magnitude but opposite direction is prescribed on each pair of the boundaries (1) and (3) as well as (2) and (4). The average displacement of all boundaries is then calculated.

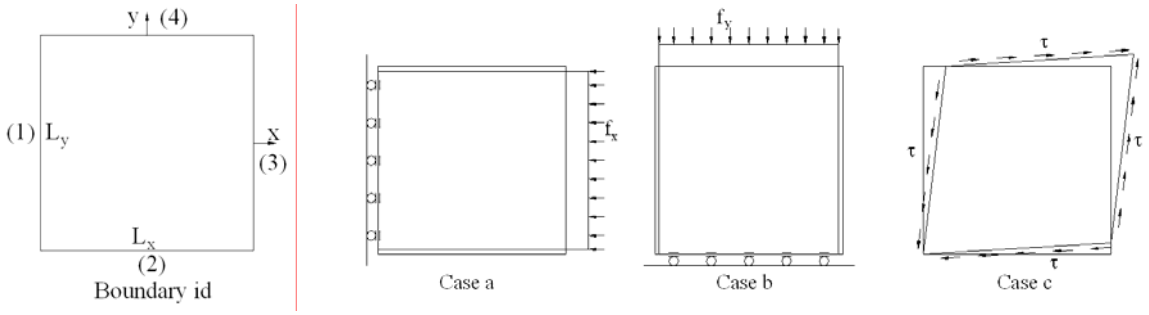

Figure 4-7 Sketch of side number and schematic diagram of three loading sets: (a) compression in x direction; (b) compression in y direction; (c) pure shear.

In case a, we have $\sigma_{zz}^{(a)} = \nu_m f^{(a)}$ by imposing $\varepsilon_{zz}^{(a)} = 0$. The equation (4.9) is reduced to:

$$\begin{aligned} \varepsilon_{xx}^{(a)} &= S_{22} f_x^{(a)} - \frac{\nu_m}{E_m} \nu_m f_x^{(a)} \\ \varepsilon_{yy}^{(a)} &= S_{32} f_x^{(a)} - \frac{\nu_m}{E_m} \nu_m f_x^{(a)} \end{aligned} \tag{4.10}$$

in which the two components S_{22} and S_{32} are calculated as function of Young modulus E_m and Poisson ratio ν_m of intact matrix:

$$\begin{aligned} S_{22} &= \frac{\varepsilon_{xx}^{(a)} + \frac{\nu_m}{E_m} \nu_m f_x^{(a)}}{f_x^{(a)}} \\ S_{32} &= \frac{\varepsilon_{yy}^{(a)} + \frac{\nu_m}{E_m} \nu_m f_x^{(a)}}{f_x^{(a)}} \end{aligned} \tag{4.11}$$

Similar to case a, two components S_{23} and S_{33} can be calculated from the case b as follows:

$$S_{23} = \frac{\varepsilon_{xx}^{(b)} + \frac{\nu_m}{E_m}\nu_m f_y^{(b)}}{f_y^{(b)}}$$
$$S_{33} = \frac{\varepsilon_{yy}^{(b)} + \frac{\nu_m}{E_m}\nu_m f_y^{(b)}}{f_y^{(b)}} \quad (4.12)$$

In theory, S_{32} must be equal to S_{23} due to the symmetric characteristic of the compliance tensor. However, numerical simulation would show a little difference between them and the representative value will be taken as the mean value of calculated ones.

Finally, the component S_{44} can be determined from the case c with:

$$S_{44} = \frac{2\varepsilon_{xy}^{(c)}}{\tau} = \frac{\gamma_{xy}^{(c)}}{\tau} \quad (4.13)$$

From these components of the effective compliance tensor, we can deduce without difficulty the effective Young modulus, Poisson ratio and shear modulus in xy plan of the equivalent medium:

$$E_x = \frac{1}{S_{22}}$$
$$E_y = \frac{1}{S_{33}}$$
$$\nu_{xy} = S_{23}E_y$$
$$\nu_{yx} = S_{32}E_x$$
$$G_{xy} = 1/S_{44} \quad (4.14)$$

4.5.2 Methodology for the determination of the effective permeability

The evaluation of the effective permeability of the fractured rock masses in each direction (x or y) is calculated with a constant hydraulic pressure gradient imposed on the boundaries of the corresponding direction (x or y) and no-flow boundaries of the other direction (see Figure 4-10). By adopting the Darcy's law for anisotropic and homogeneous porous media (Min et al., 2004a), the calculation is done from the following equation (gravity is ignored):

$$Q_x = A\frac{K_x}{\mu}\frac{\partial P}{\partial x} \text{ and } Q_y = A\frac{K_y}{\mu}\frac{\partial P}{\partial y} \quad (4.15)$$

where Q_x and Q_y are the flow rates at the boundaries of the corresponding x and y directions; A is the cross-sectional area; K_x and K_y are the permeability in the x and y directions, respectively; μ is the dynamic viscosity of fluid and P is the hydraulic pressure applied. In the numerical simulations, all terms on the right-hand side of equation (4.15), except for K_x and K_y, are specified while Q_x and Q_y are calculated numerically. Thus, without difficulty, K_x and K_y can be back-calculated using equation (4.16):

$$K_x = \frac{\mu Q_x}{A\frac{\partial P}{\partial x}} \text{ and } K_y = \frac{\mu Q_y}{A\frac{\partial P}{\partial y}} \tag{4.16}$$

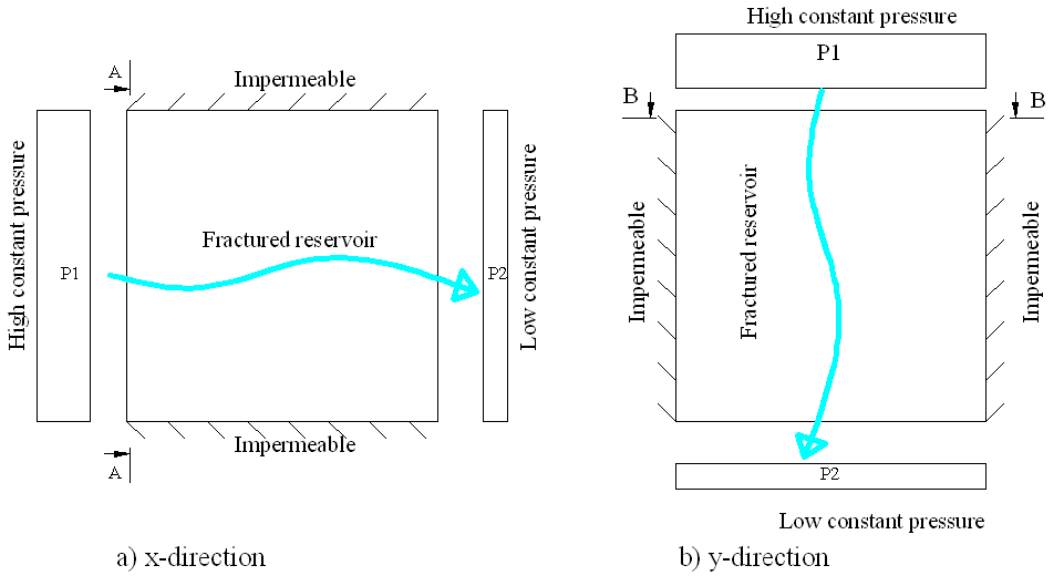

Figure 4-8 Boundary conditions for the effective permeability calculation

4.5.3 Effect of fracture-cell size on the effective properties

As discussed in the chapter 3, the accuracy of the EFC approach depends on the fracture-cell size *h*. In this part, the effect of this latter which can be represented through the effect of the local refinement level N (because of the relationship $h=L/2^N$) on the effective properties will be investigated.

In Figure 4-9 are presented a square sample ($L=L_x=L_y=2m$) of the Sellafield site. The DFN with and without dead-ends and isolated fractures was generated for the three cases of high, median and low density of fractures (the corresponding total number of fractures of these three cases are 73, 36 and 18). For the sake of clarity, all the necessary parameters of the matrix and fracture properties as synthetized previously are summarized in the table 4-6. Note

that, corresponding to the aperture 65(μm), the permeability of fracture is about $K_f=3.52*10^{-10}(m^2)$ while the permeability of intact matrix is $K_m= 2.4*10^{-15}$ (m^2).

Rock matrix	Bulk density ρ [kg/m3]	2750
	Young's modulus Eblock [GPa]	84.6
	Poisson ratio ν	0.24
	Biot modulus [GPa]	10.5
	Biot coefficient	0.8
	Permeability [m2]	$2.4*10^{-15}$
Fractures	Joint normal stiffness Kn [GPa/m]	434
	Joint shear stiffness Ks [GPa/m]	86.8
	Aperture [μm]	65
	Permeability [m2]	$3.52*10^{-10}$

Table 4-6: Rock matrix and fracture properties used in the numerical simulation of effective properties of rock masses

In Figure 4-10, as an illustration purpose, we present the contours of the isotropic Young's modus and isotropic permeability distributed in the high density DFN sample with and without dead-ends fractures. Although all the fractures own the same aperture, the isotropic Young's modulus and isotropic permeability in the fracture-cells of different fractures are not similar but depends on the orientation of the corresponding fracture (see the Eqs. (3.17) and (3.27)). The heterogeneity of the elastic properties and permeability of the fracture cells induces a heterogeneous distribution of stress (Figure 4.11) and pore pressure (4.12) in the fractured rock sample. The comparison of the isovalues of stress and pressure obtained from two cases of DFN with and without dead-ends show a significant disturbance due to the concentration of stress and pressure at the dead-ends of fractures. This observation can explain the difference of the effective properties calculated in these two cases of DFN as detailed below.

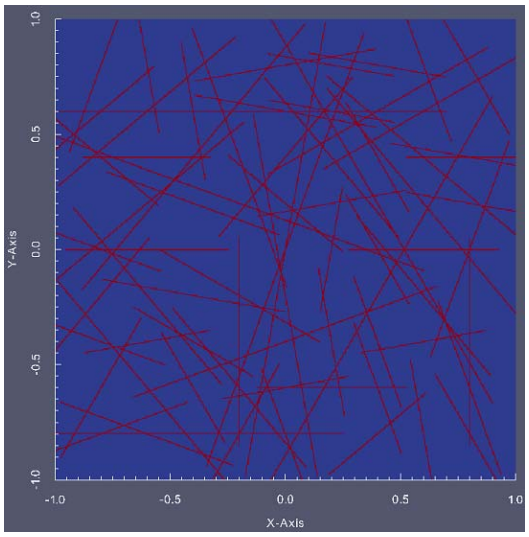

(a) high density sample with dead-ends

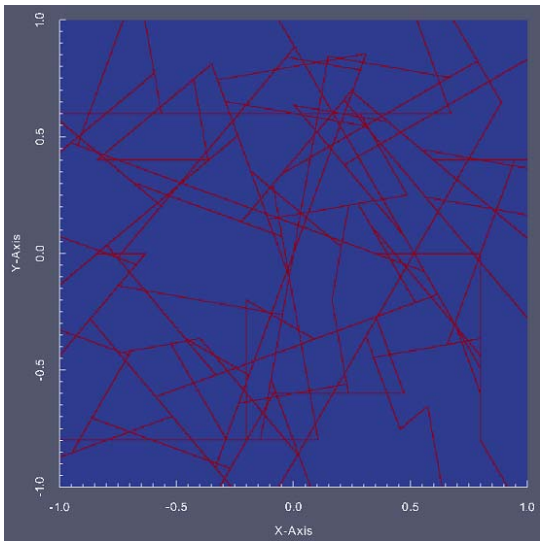

(b) high density sample without dead-ends

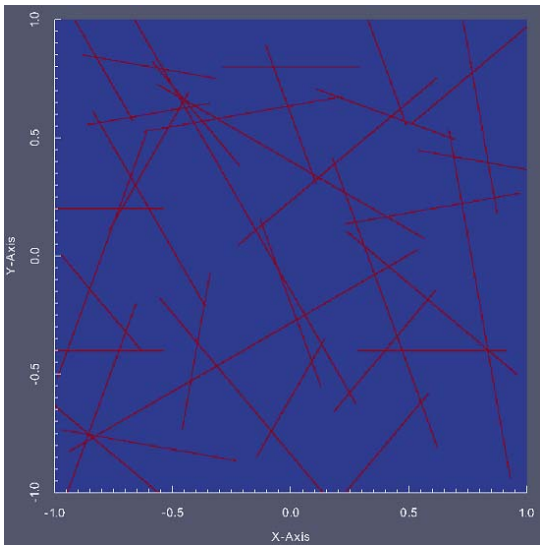

(c) median density sample with dead-ends

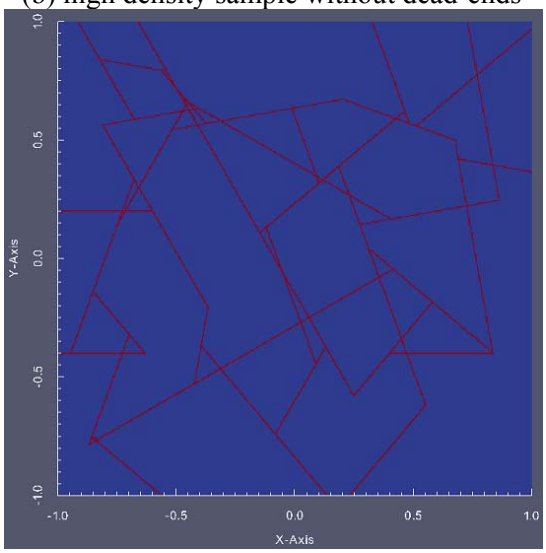

(d) median density sample without dead-ends

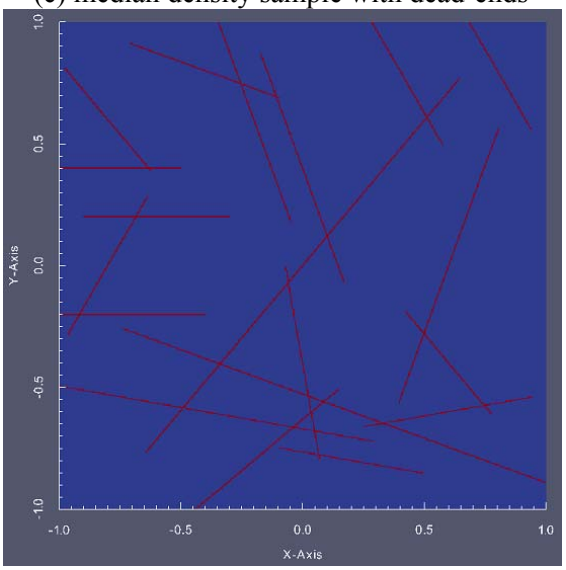

(e) low density sample with dead-ends

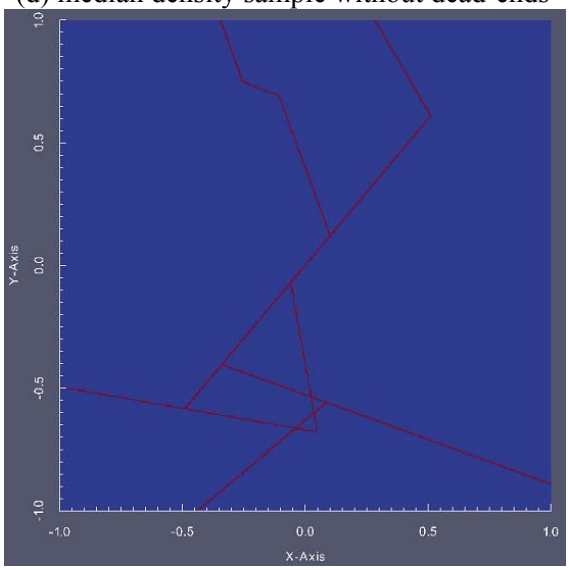

(f) low density sample without dead-ends

Figure 4-9: A 2m x 2m square sample of Sellafield rock masses: DFN in the sample with and without dead-ends fractures was generated with three cases of high, median and low density of fractures.

.

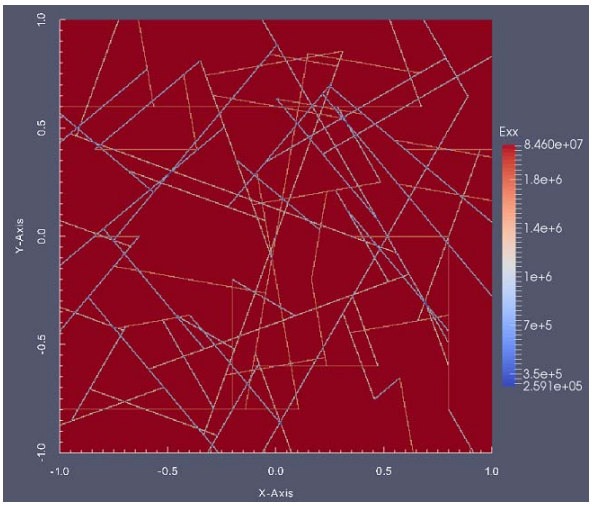

(a) Distribution of isotropic Young's modulus in the high density DFN sample without dead-ends

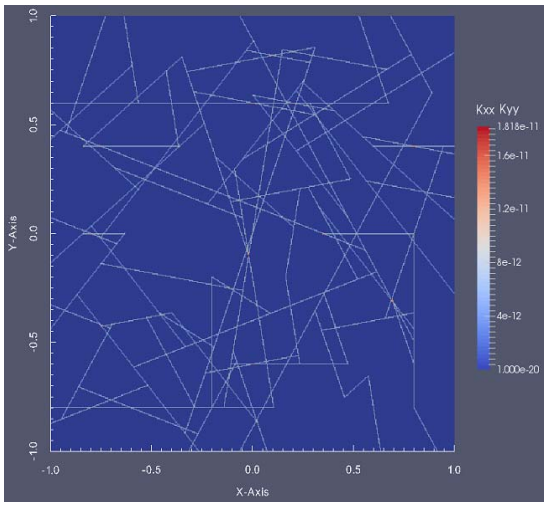

(b) Distribution of isotropic permeability in the high density DFN sample without dead-ends

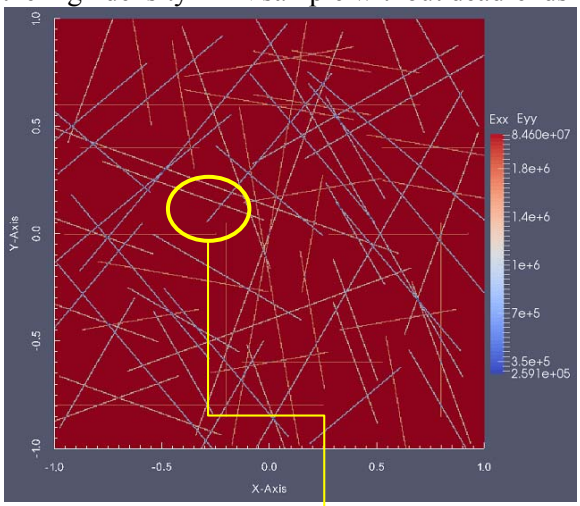

(c) Distribution of isotropic Young's modulus in the high density DFN sample with dead-ends

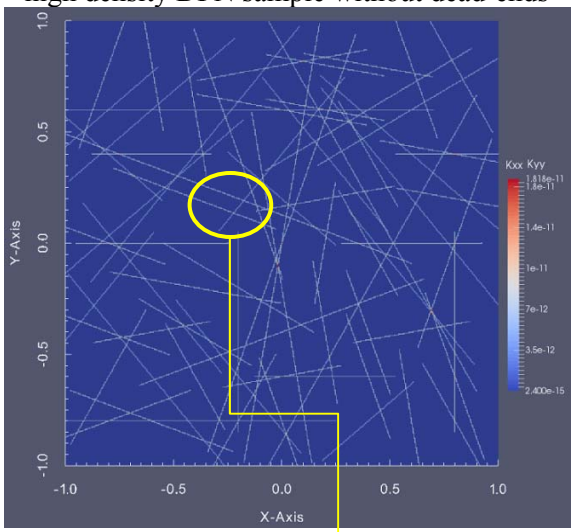

(d) Distribution of isotropic permeability in the high density DFN sample with dead-ends

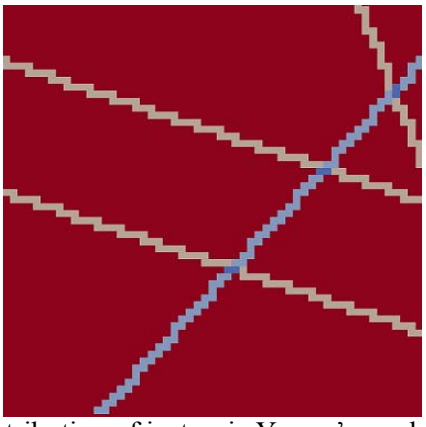

(e) Distribution of isotropic Young's modulus in the sample (zoom around fractures) (unit: kPa)

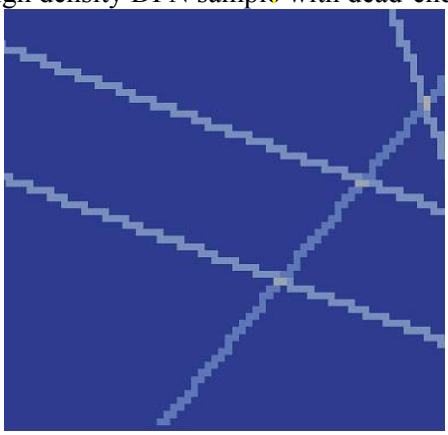

(f) Distribution of isotropic permeability in the sample (zoom around fractures) (unit:m^2)

Figure 4-10: Isovalue of isotropic Young's modulus (Ex=Ey) and isotropic permeability (Kx=Ky) of fracture cells and matrix cells for the high density DFN sample without dead-ends (a and b) or with dead-ends fractures (c and d) and a zoom around fractures (e and f)

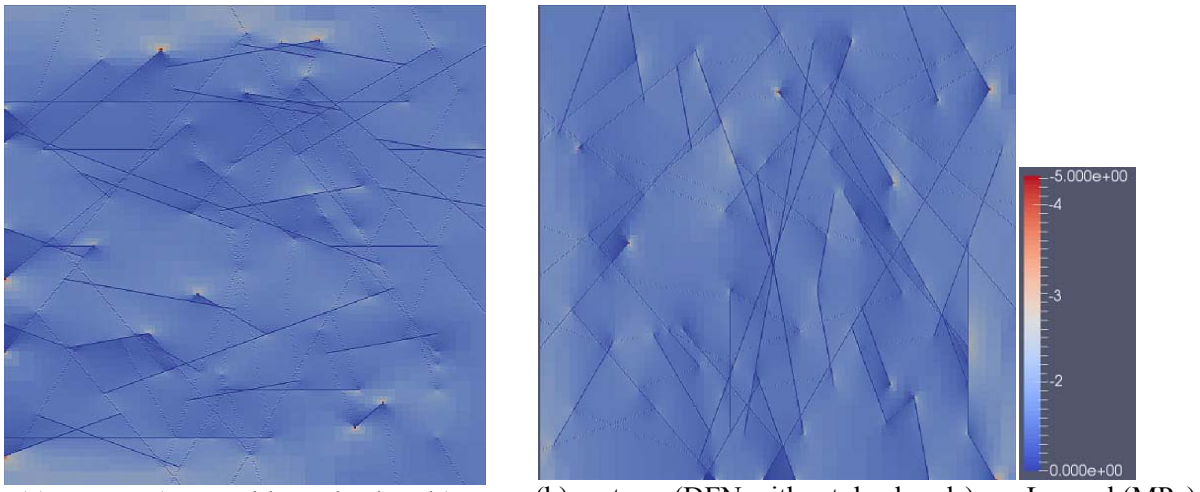

(a) x-stress (DFN without dead-ends) (b) y-stress (DFN without dead-ends) Legend (MPa)

(c) x-stress (DFN with dead-ends) (d) y-stress (DFN with dead-ends)

Figure 4-11 Isovalues of heterogeneous distribution of stress in the fractured rock masses: case of high density fractures without dead-ends (a,b) and with dead-ends (c,d).

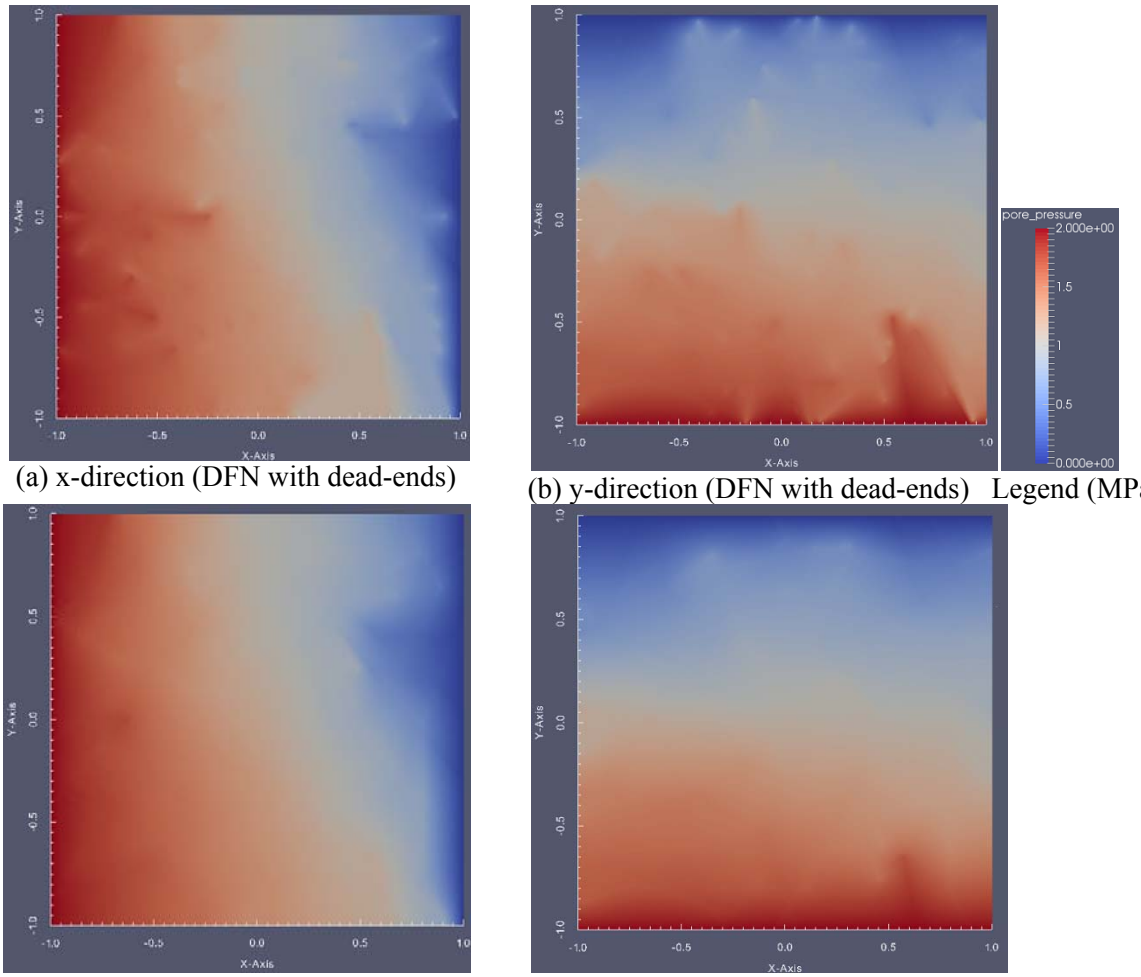

(a) x-direction (DFN with dead-ends) (b) y-direction (DFN with dead-ends) Legend (MPa)

(c) x-direction (DFN without dead-ends) (d) y-direction (FN without dead-ends)

Figure 4-12 Isovalues of the pore pressure in the fractured rock masses: case of high density fractures with dead-ends (a, b) and without dead-ends (c, d).

In Figures (4-13 and 4-14) are presented the results of the effective Young's modulus and permeability calculated with respect to two directions X and Y and with different levels of local refinement using the hanging node technique. A convergence of the obtained results can be noted for both types of DFN (with and without dead-ends fractures) in rock masses and with all cases of fractures density. For the most critical case (case of high density of fractures), a difference smaller than 10% can be stated when the local refinement is chosen from N=7 (case of DFN without dead-ends) or from N=8 (case of DFN with dead-ends). With respect to the decrease of fractures density (case of median and low density), the results (see Tables 4-7 and 4-8) show that the local refinement level N=6 (DFN without dead-ends) and N=7 (DFN with dead-ends) can be chosen to ensure a maximal difference of 10%. Moreover, as expected, the results presented in Figures (4-13 and 4-14) showed that the effective elastic properties decrease with respect to the fractures density while for the hydraulic problem a higher density will increase the effective permeability. A significant difference of the effective elastic properties obtained in two cases of DFN (with and without

dead-ends fractures) is also revealed. For example, at the local refinement N=8 (Table 4-9), this difference is most important in the case of low density (about 23%) and decreases to 17% in case of median density and is smallest in the case of high density of fractures (about 14 %). The results obtained in this work confirmed the discussion of Yang et al. (2014) who noted that ignoring of the dead-ends fractures can change the stress distribution (as shown in Figure 4-11) and induce a great deviation in determination of the effective compliance matrix. For the hydraulic problem, the difference of the effective permeability calculated in two cases of DFN with and without dead-ends is not significant. For all cases of fractures density, a difference smaller than 6% was noted.

Comparison of these results with those of previous work in the literature, show a general good agreement. For example, in the case of high density of fractures, our results of the effective Young's modulus (see Table 4-9) is about 28GPa (in both directions) which seems consistent with the results of (22GPa to 32 GPa) presented by Min and Jing (2003) who studied only the DFN without dead-ends. This consistence of results is also observed for the effective permeability when using EFC we obtain $K_x=1.02*10^{-13}\ (m^2)$ and $K_y=9.48*10^{-14}\ (m^2)$ which are in the range of $6*10^{-14}(m^2)$ to $1.8*10^{-13}(m^2)$ concluded in Min et al., 2004a and Baghbanan, 2008 by using the UDEC code.

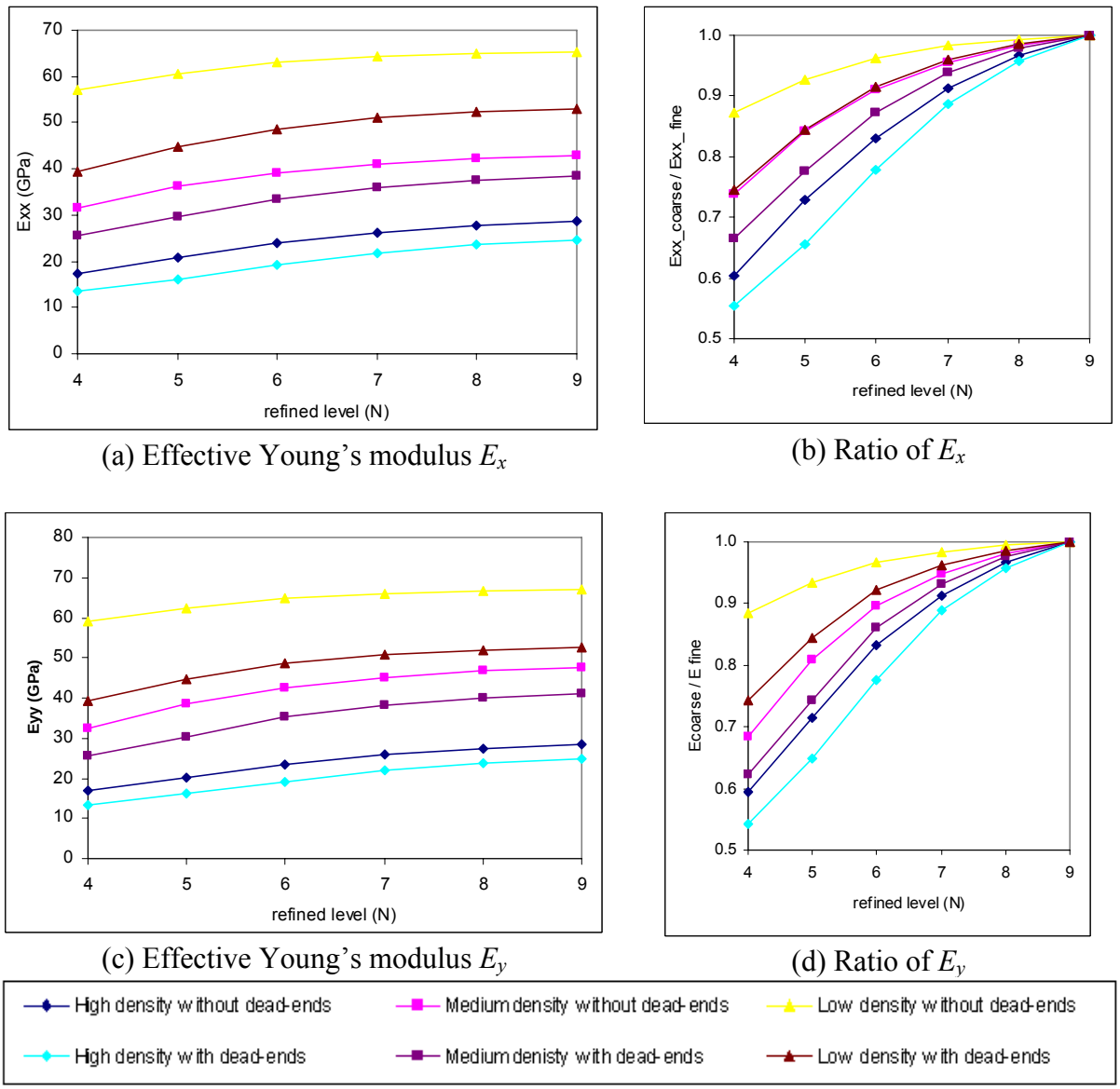

Figure 4-13: Effective Young's modulus E_x (a), E_y (c), and its corresponding ratio calculated with different sizes of fracture cells (local refinement level N<9) with respected to ones calculated with N=9.

Refined level (N)	Fracture-cell size (mm)	DFN sample without dead-ends			DFN sample with dead-ends		
		High	Medium	Low	High	Medium	Low
4	125	0.59	0.68	0.88	0.54	0.62	0.74
5	62.5	0.71	0.81	0.93	0.65	0.74	0.84
6	31.25	0.83	0.90	0.97	0.78	0.86	0.92
7	15.625	0.91	0.95	0.98	0.89	0.93	0.96
8	7.8125	0.97	0.98	0.99	0.96	0.98	0.99
9	3.90625	1.00	1.00	1.00	1.00	1.00	1.00

Table 4-7: The ratio of effective Young's modulus E_y calculated with different sizes of fracture cells (local refinement level N<9) with respected to ones calculated with N=9.

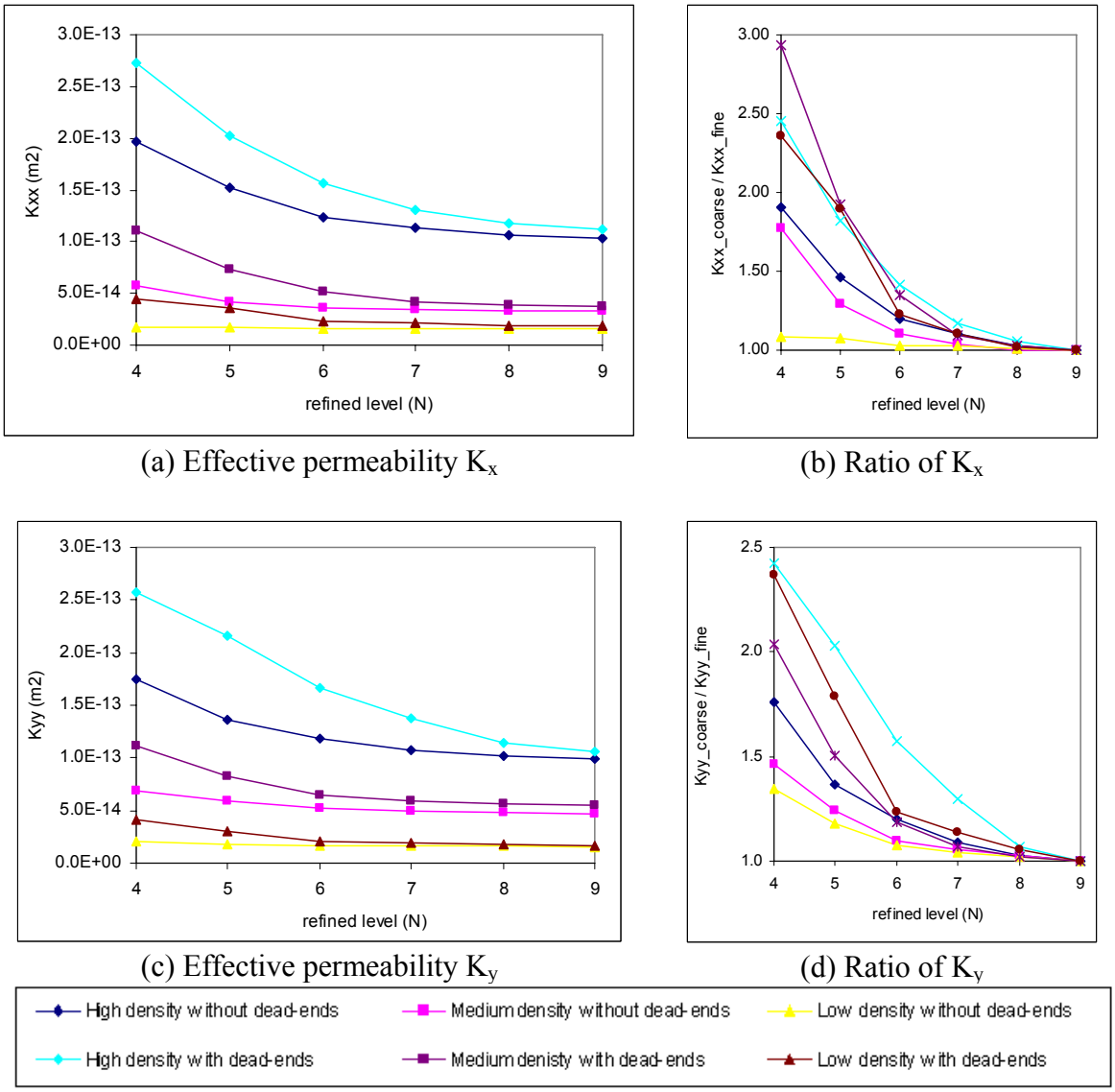

(a) Effective permeability K_x (b) Ratio of K_x

(c) Effective permeability K_y (d) Ratio of K_y

Figure 4-14: Effective permeability Kx (a), Ky (c), and its corresponding ratio calculated with different sizes of fracture cells (local refinement level N<9) with respected to ones calculated with N=9.

Refined level (N)	Fracture-cell size (mm)	DFN sample without dead-ends			DFN sample with dead-ends		
		High	Medium	Low	High	Medium	Low
4	125	1.90	1.77	1.09	2.45	2.93	2.61
5	62.5	1.47	1.29	1.07	1.82	1.93	2.09
6	31.25	1.20	1.10	1.03	1.41	1.35	1.15
7	15.625	1.10	1.04	1.03	1.17	1.09	1.09
8	7.8125	1.03	1.00	1.01	1.06	1.03	1.01
9	3.90625	1.00	1.00	1.00	1.00	1.00	1.00

Table 4-8: The ratio of effective permeability K_x calculated with different sizes of fractures cells (local refinement level N<9) with respect to ones calculated with N=9.

Case study	Sample	E_x (GPa)	E_y (GPa)	ν_{yx}	ν_{xy}	G_{xy} (GPa)
High density	With dead-ends	24.57	24.78	0.209	0.205	9.75
	Without dead-ends	28.66	28.35	0.215	0.214	11.26
	Relative ratio (with/without dead-ends)	***0.86***	***0.87***	***0.97***	***0.96***	***0.87***
Medium density	With dead-ends	33.42	35.19	0.242	0.232	13.43
	Without dead-ends	39.04	42.59	0.247	0.236	16.03
	Relative ratio (with/without dead-ends)	***0.86***	***0.83***	***0.98***	***0.98***	***0.85***
Low density	With dead-ends	51.01	50.82	0.225	0.230	20.16
	Without dead-ends	64.31	65.87	0.234	0.234	26.18
	Relative ratio (with/without dead-ends)	***0.79***	***0.77***	***0.96***	***0.98***	***0.77***

Table 4-9 Effective elastic properties (E_x, E_y, υ_{yz}, υ_{xy}, G_{xy}) in two cases of DFN with and without dead-ends fractures (results calculated at the local refinement level N=8).

DFN samples		Effective permeability (m^2)	
		K_x	K_y
High density	With dead-ends	1.11E-13	1.06E-13
	Without dead-ends	1.07E-13	1.02E-13
	Relative ratio (without/with dead-ends)	***0.96***	***0.96***
Medium density	With dead-ends	3.79E-14	5.47E-14
	Without dead-ends	3.58E-14	5.17E-14
	Relative ratio (without/with dead-ends)	***0.94***	***0.94***
Low density	With dead-ends	1.70E-14	1.72E-14
	Without dead-ends	1.62E-14	1.61E-14
	Relative ratio (without/with dead-ends)	***0.95***	***0.94***

Table 4-10 Effective permeability (K_x, K_y) in two cases of DFN with and without dead-ends fractures (results calculated at the local refinement level N=8).

4.5.4. Monte Carlo simulation of the effective properties of Sellafield fractured rock masses

The previous results discussed up to here are obtained using a realization of statistical properties (length, position) of cracks. To obtain the representative results, the Monte Carlo

simulation was conducted. More precisely, ten realizations of the REV of 5m (Figure 4-15) were generated and for each realization we calculate the effective properties of the fractured rock masses. Note that in this study, to complete the results in the literature (Min et al., 2003; Min et al., 200a; Marmier, 2007; Baghbanan 2008) who concentrated in the case of high density fractured rock masses, we consider only the case of median density of fractures and for all the calculations we use the local refinement level N=8.

The effective elastic properties and permeability calculated for all samples are summarized in Tables (4-11) and (4-12). The results showed an anisotropic behaviour of the equivalent medium of the fractured rock masses. However, the anisotropic degree, represented by the Young's modulus ratio (E_x/E_y) and permeability ratio (K_x/K_y), seems very moderate. These ratios determined from the mean values of ten realizations are respectively $E_x/E_y=1.02$ and $K_x/K_y=1.14$. Thus, the behaviour of the fractured rock mass in Sellafield site can be assumed isotropic.

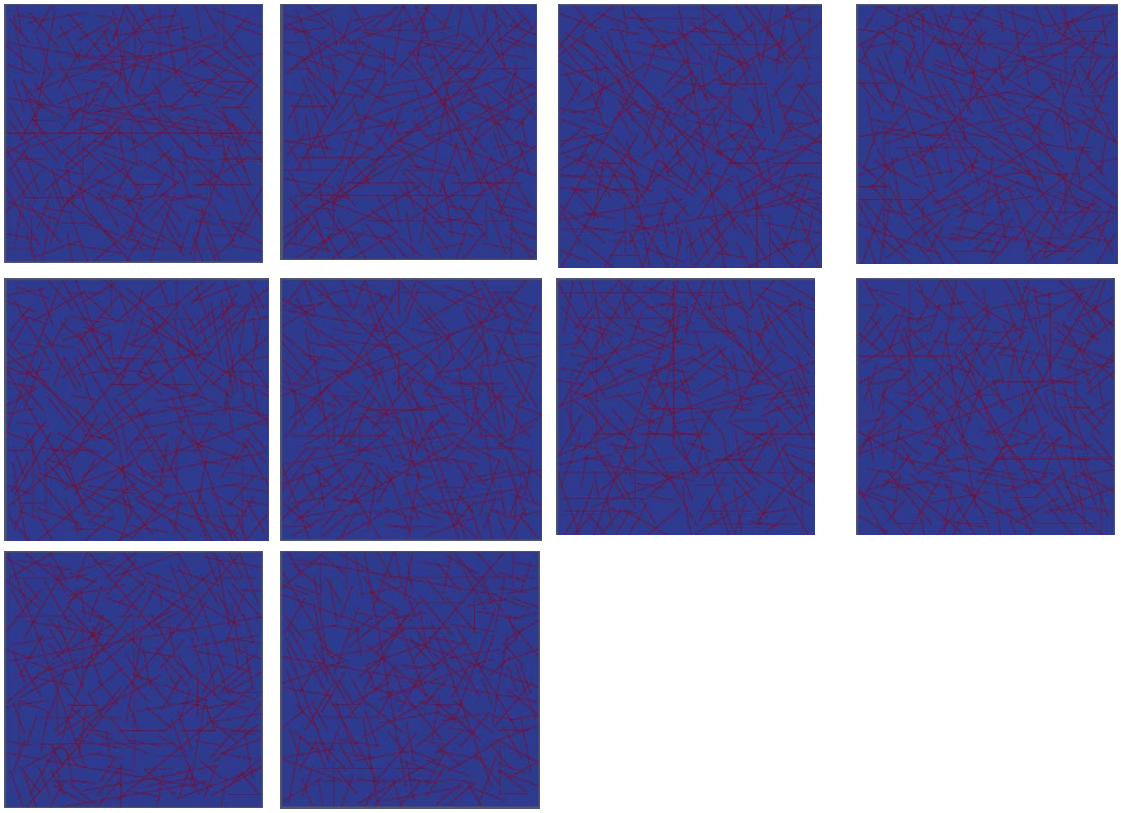

Figure 4-15: Ten realizations of the REV with 5m of size of the Sellafield fractured rock masses used in the Monte Carlo simulation of the effective properties.

Sample	E_x (GPa)	E_y (GPa)	ν_{yx}	ν_{xy}	G_{xy} (GPa)
1	34.01	32.47	0.222	0.231	12.86
2	32.59	31.24	0.229	0.237	12.74
3	32.34	32.23	0.236	0.237	12.99
4	33.58	32.45	0.220	0.231	12.82
5	31.53	31.68	0.236	0.237	12.73
6	32.77	32.19	0.229	0.233	12.81
7	33.79	33.51	0.222	0.225	12.88
8	33.78	34.37	0.225	0.222	13.14
9	32.97	32.17	0.227	0.235	12.81
10	33.32	33.36	0.226	0.225	12.86
Average	***33.07***	***32.57***	***0.227***	***0.231***	***12.86***
Standard deviation	0.740	0.879	0.005	0.005	0.114
Coefficient of variance (%)	***2.24***	***2.70***	***2.38***	***2.32***	***0.89***

Table 4-11 Effective elastic properties of the Sellafield fractured rock mass obtained from ten realizations

Sample	K_x (m2)	K_y (m2)
1	5.38E-14	4.04E-14
2	5.89E-14	4.77E-14
3	5.15E-14	4.49E-14
4	6.04E-14	5.12E-14
5	5.91E-14	5.34E-14
6	5.42E-14	4.92E-14
7	5.37E-14	4.89E-14
8	5.54E-14	5.51E-14
9	5.54E-14	5.20E-14
10	5.92E-14	4.96E-14
Average	***5.61E-014***	***4.92E-014***
Standard deviation	2.86E-15	4.03E-15
Coefficient of variance (%)	***5.10***	***8.19***

Table 4-12: Effective permeability of the Sellafield fractured rock mass obtained from ten realizations

4.6 Primary depletion modeling of fractured reservoir: effect of double porosity and double permeability

In this section, the EFC approach will be used to model a hypothetical reservoir whose natural fractures coincides with that of Sellafield site. The objective is to in one hand to demonstrate the capacities of EFC approach in modeling such complex problems and on the other hand to illustrate the effects of double porosity/double permeability media on the state evolution of a reservoirs. The choice to use the data of Sellafield is motivated only by the completeness of the data, which is unfortunately not valuable to us for a real reservoir. As such, further on, some variations on rock properties of Sellafield site (namely porosity) will be assumed in order to obtain typical values of these property for a reservoir rock.

The study consists of simulating the production of a vertical well (primary depletion) with 1m of diameter. To this end, the 2D plane strain assumption is adopted. Otherwise, to simplify the problem, only a quarter of the model will be considered (Figure 4-16). Regarding with the dimension of the well, the saturated reservoir of 200m-width and 200m-length (with respect to the center of well) was selected. The initial pore pressure and total isotropic horizontal stress are assumed respectively equal to 10.0 MPa and 24.46 MPa which corresponds to the values measured at the depth 725m in the Sellafield site (see sub-section 4.2.6 in this chapter). Otherwise, concerning the boundaries conditions, we consider that the top and right boundaries are closed and fixed while a zero-constant pressure is imposed on the wall of well.

The simulation will be conducted with different scenarios. As the first scenario, we replace the fractured medium by the homogeneous equivalent poro-elastic medium obtained from the previous section. This classical study case is largely adopted in the literature, particularly in the modeling of real field (Jensen et al., 1998; Lee et al., 2000; Marmier, 2007 and different references cited therein). However, the fact of using the equivalent medium in the modeling means that the porous space and permeability of rock matrix as well as ones of the fractures network are gathered and characterized through only a single porosity and a single permeability represented by the overall (effective) permeability as detailed in the last section. Thus this study case (called hereafter as homogenized model) consider only the effect of the single porosity and single permeability. The advantage and limitation of using the effective single continuum approach were discussed in (Jensen et al., 1998; Lee et al., 2000) by comparing with the traditional dual continuum model of Warren and Root (1963). These authors discussed that this approach can captures the baffled flow effect while the dual continuum approach is better equipped to enhance flow through the fracture system which is however limited for the models they used, in the regular and orthogonal fracture geometry. Otherwise, the unsteady-state flow effects between fracture and matrix (matrix – fracture

transfer) are not considered in the effective single continuum approach which however can be more easily addressed in the dual continuum model by using the matrix-fracture transfer functions (sugar cube-like matrix and fracture geometry). Thus, as detailed by Lee et al. (2000), the effective single continuum modeling approach can be applied when the unsteady-state between matrix and surrounding fractures is not a dominant feature. This is also the hypothesis adopted in the present work.

In the second scenario, the fractures are explicitly introduced in the model. The question of what fracture should be considered explicitly in a model is an open question. In fact, in every modeling approach (and this is valuable for all models not only for fractures), the discontinuities of lower scale than that of observation are neglected. For example when a rock sample is tested in laboratory the pores or cracks not detectable by naked observation are neglected. Where cracks in site are observed the cracks under a given value are simply neglected and the media under this scale is considered as continuum. Recall that for Sellafield the lower cut-off for crack distribution is 0.5m. Likewise in, in our model, only the long fractures with length superior of the REV size established before will be considered explicitly which limits the number of explicit fracture to the longest ones and with highest apertures (fractures with apertures much more important than the mean aperture of the DFN as described above will be taken into account explicitely). These fractures are embedded in the fractured matrix (matrix surrounds the DFN with uniform aperture of 65 μm) which is now replaced by the equivalent homogeneous medium as in the first scenario. This concept can be explained by the fact that in reality, the fractured rock mass is highly heterogeneous, and the assumption of using the uniform aperture of the fractures networks to simplify the modeling by using the equivalent medium through the upscaling approach can over/underestimate the problem. Otherwise, in such heterogeneous media, there is a high probability of the existence of several initial fractures/faults (or even induced fractures during drilling) with a large aperture. The consideration of these fractures in the classical upscaling approach can violate the notion of REV: if the REV is always existed and if it is the case what is the evolution of the REV size? The scenario proposed in this work can be an alternative approach to simplify the problem and matches well with the idea proposed by some other scholars (Lee et al., 2000; Li and Lee, 2008). In their work, Lee et al. (2000) proposed a hierarchical approach for modeling fluid flow in a naturally fractured reservoir with multiple length-scale fractures. They classified the fractures as short, medium-length and long fractures. The short and medium-length fractures were associated with the matrix through the homogenization technique to define the effective porous medium while the long fractures (considered as the major conduits) are separated and modelled explicitly in the model. The flexibility and performance of this hierarchical approach were demonstrated by these authors in the modeling complex fractured rock masses.

The second scenario will be separated in two cases which aim to investigate in more detail the effect of these fractures on a hypothetical well behaviour (well production notably). In the first case we consider that at least one of these long fractures intersects the well (called hereafter as conductive fractures model) and in the other case, any long fractures intersect the well (called as non-conductive fractures model) as highlighted in Figure 4-16. The implementation of these fractures in the model at the present stage seems easy by using the EFC approach based on the fracture cells concept. Note that each fracture-cell in the model represents a porous medium which has its own porosity and permeability and different with the ones of the fractured matrix. These models represent in effect the double porosity and double permeability medium to distinguish with the initial scenario based on the single effective medium. Otherwise, as mentioned above, in all calculations, we neglected the unsteady-state feature between matrix and fractures in this fractured matrix.

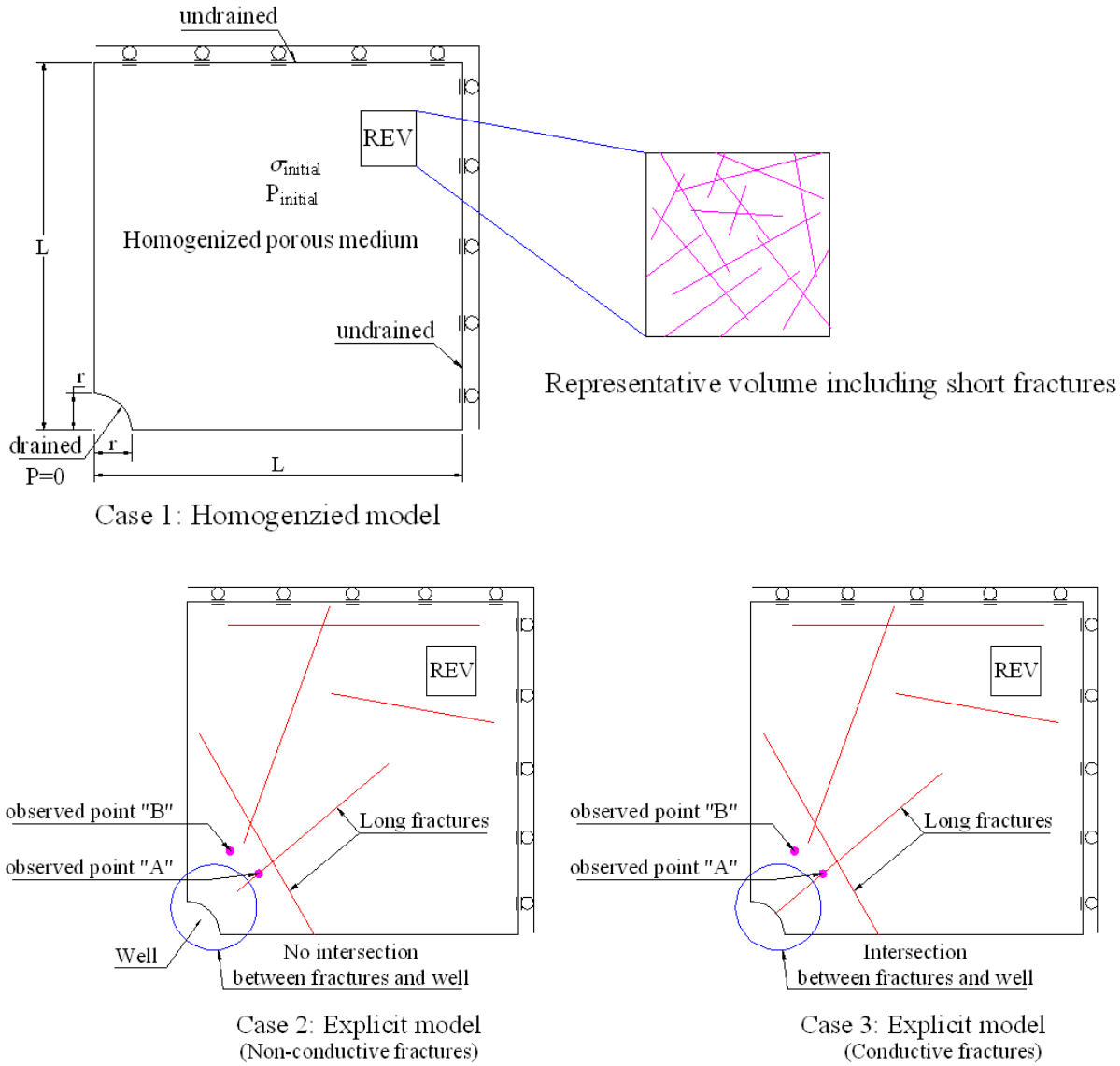

Figure 4-16 One quarter of the fractured reservoir model used in the well production simulation.

For these calculations, the following poro-elastic properties of the equivalent porous matrix and long fractures are chosen:

-For the equivalent fractured matrix: the effective properties calculated in the previous section will be used. As observed from these last calculations, the anisotropic degree of this fractured rock is low thus we can consider it as isotropic material. In this case, Biot modulus and Biot coefficient can be determined from the following equations:

$$b_{iso}^{\hom} = 1 - \frac{K_{iso}^{\hom}}{K_s} = 1 - \frac{E_{iso}^{\hom}}{3K_s(1-2\nu_{iso}^{\hom})};$$
$$\frac{1}{M^{\hom}} = \frac{b_{iso}^{\hom} - \varphi^{\hom}}{K_s} + \varphi^{\hom} c_f \qquad (4.17)$$

where K_s is bulk modulus of skeleton of rock matrix (K_s=271.2 GPa) and $\varphi^{\hom}$ is porosity of the homogenized porous matrix $\varphi^{\hom} = \varphi^0 + \varphi^{fractures}$ (the initial porosity of the intact matrix is taken as $\varphi^0 = 18.6\%$). The viscosity and compressibility of fluid (oil) are 0.01(Pa.s) and 5.0×10^{-10} (Pa^{-1}), respectively.

E_{hom} (GPa)	ν_{hom}	b_{hom}	M_{hom} (GPa)	K (m2)
32.82	0.229	0.87	10.4	5.3E-014

Table 4-13 Isotropic poro-elastic properties of the equivalent porous matrix (obtained from the effective properties of the fractured rock masses calculated in the previous section).

-For long fractures: as an example, only 6 fractures longer than 100m with 1mm of width are modeled explicitly (Figure 4-16). The properties of fractures like the normal and shear stiffness are taken to $k_n^{init} = 2.0\ GPa/m$ and $k_t^{init} = 0.4\ GPa/m$ at the initial state. The corresponding permeability of these fractures based on the cubic law is $K_f=8.33*10^{-8}\ (m^2)$.

In what it follows, for each model, the fluid flow simulation will be conducted. In this type of simulation, we consider that the fluid flow toward the well (drawdown effect) and hence well production (primary depletion) are from the contribution of both the permeable fractured matrix and long fractures. The mechanical effect will be ignored in the first stage by considering the constant aperture and hydraulic properties of long fractures and will be then considered (but in an implicit manner) in the second stage by varying the aperture and hydraulic properties of long fractures during the transient flow. More precisely, in the latter case, closure of fractures (updated aperture and permeability of fractures) will be taken into account as consequence of the mechanics effect. From several contributions (see Moinfar, 2013; Moinfar et al., 2013 and different references cited therein), it showed that

geomechanics can impact the fluid flow notably through the closure/opening of fractures which in turn induces a variation of the fractures' permeability. To account for this effect, many authors proposed to use an empirical stress-dependent function of the fractures aperture. Among different functions presented in the literature, the following relationship proposed by Bandis et al. (1983) and Barton et al. (1985) (called Bandis & Barton model) is the most commonly used:

$$\mathrm{w}_f = \mathrm{w}_{init} \frac{k_n^{init} \mathrm{w}_{init}}{k_n^{init} \mathrm{w}_{init} + \Delta\sigma_n^{'}} \tag{4.18}$$

Following this model, the closure/opening of fractures is principally affected by the effective normal stress acting on their surfaces (shear stress is neglected). In Eq. (4.18), w_{init} and k_n^{init} are the aperture and normal stiffness of fracture at the initial state; w_f is the actual fracture aperture calculated from the variation of the effective normal stress $\Delta\sigma_n^{'} = \sigma_n^{'} - \sigma_{n,o}^{'}$ ($\sigma_n^{'}$ and $\sigma_{n,o}^{'}$ indicate the actual and initial effective normal stress acting on the fracture plane). Otherwise, through the definition of the effective stress $\sigma_n^{'} = \sigma_n - b.p$ (we can consider as the simplest case $b=1$), if the variation of the total stress is negligible, the evolution of fracture aperture can be defined as function of the pressure drawdown $p_{drawdown}$:

$$\mathrm{w}_f = \mathrm{w}_{init} \frac{k_n^{init} \mathrm{w}_{init}}{k_n^{init} \mathrm{w}_{init} + p_{drawdown}} \tag{4.19}$$

This last equation will be used in our flow simulations to activate the fracture aperture w_f corresponding to the actual pressure ($p = p_{initial} - p_{drawdown}$) during the transient fluid flow. For the illustration purpose, this empirical relation is presented in Figure 4-17 by using the properties the long fractures as mentioned above. Note that, in our code, this pressure drawdown is calculated as the mean value of pressure drawdown in each fracture cell, it means that the fracture aperture and permeability will be updated at the end of each time step for each segment of fracture embedded in the fracture cell.

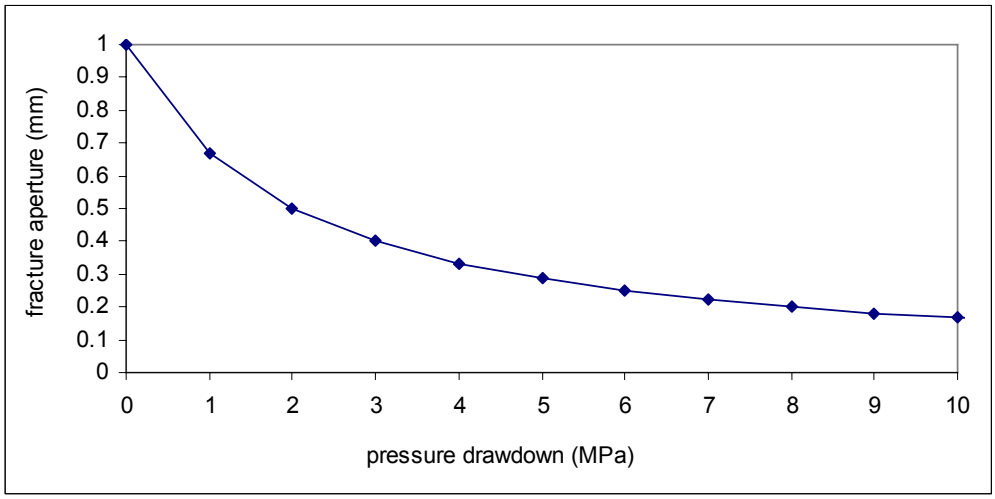

Figure 4-17 : Fracture aperture as function of pressure drawdown in fracture

The configuration of problems considered here is quite similar as ones studied in the work of Li and Lee (2008) (see also Moinfar et al., 2013). In their work, these last authors would like to elucidate the influence of well and long fractures intersection on the productivity of well. However, in comparison with this last contribution, there are some essential differences in the present study. In effect, to consider the communication between porous matrix and fractures, as well as fractures and well, Li and Lee (2008) used the transport index between matrix-fracture and the fracture transmissibility to the well. This later parameter is determined by using directly the Peaceman's productivity index (PI) which is largely used in practice for the well drilled in the medium without fracture intersection. For this purpose, these authors assumed that the pressure drop along the fracture inside the well block is negligible and the productivities from the fracture and well are superposed. This assumption means that the fractures connected with a well become part of extended well geometry. Otherwise, as the fracture surface is much larger than the well surface, the production from the fracture surface will be much larger than that from the well surface. Inversely, in the present work, we interest only the production calculated from the well surface. This well surface is explicitly considered in our model (see Figure 4-20) through which the production rate (fluid flux) will be calculated directly while the drop of pressure in the fractures is decided by the transient flow in their corresponding fracture cells.

In the Figures 4-18 and 4-19 are presented respectively the production rate and cumulative production of the well for the three considered models. As the first observation, we can note that there is a significant difference for the third case when the long fractures intersected with the well keeping their initial aperture during the simulation. With respect to the other case, the production rate of this last case is much higher (about twenty times) in the first days of production and drops quickly after one month. This statement is well illustrated in Figure 4-19 with a linear variation of the cumulative production which attaints finally its asymptotic

after this mentioned period. The difference of production rate is however much smaller (about four times) when the aperture of the conductive fractures is updated during the simulation by considering the geomechanical effects described through the Bandis and Barton model. A rapid drop of pressure in the conductive fractures in the firsts days induced a closure of aperture and hence induce the decrease the fractures permeability. Therefore, the production rate and cumulative production decrease versus elapsed time. The production is over at about 11 months (Table 4-14). The results obtained from homogenized model or non-conductive fractures model present no significant difference regardless of the aperture of fractures. The similar rate and cumulative production were stated in the whole simulation time with only moderate difference at the end days of the production process. The influence of the fracture closure as highlighted in the Figures (4-18 and 4-19) is really negligible. The production in the non-conductive models is finished at about 17 months while for the single effective medium scenario it is about 19 months.

For more information about the well behaviours in these studied scenarios, we presented in Figures (from 4-20 to 4-22) the distribution of pore pressure, fracture aperture determined at different instants (10h and 1 month) of fluid flow simulation. A drop of pressure in the fracture cells of the corresponding fracture intersected the well is well captured. Comparison with the case that the fracture aperture is updated, this drop is much more pronounced if the fracture aperture is kept constant during the simulation. It is important to note also that this drop is not instantaneous nor uniform in the fractures but mostly concentrated around the well (about 30m to 40m with respect to the center of well). It seems that the drop along the conductive fracture could play an important role on the productivity of well and cannot be neglected as assumed in the work of Li and Lee (2008). Corresponding to this latter case, the drawdown of the initial pressure ($p_{initial}=10MPa$) finish at the instant of 1 month as shown in Figure 4-21d. Besides, due to the rapid drawdown of pressure, the aperture of the conductive fractures decreases quickly which is about half of the initial aperture of 1mm after 10h and attains its maximal closure after 1 month (the corresponding final aperture about 0.2mm). All these observations are confirmed in Figures 4-23 and 4-24 in which the variation of pore pressure, fractures aperture and permeability at two predefined points (points A located at (38.3m, 32.14m) and B located at (25.0m, 43.30m)) in Figure 4-16 which located at the same positions on the three models) with respect to elapsed time are highlighted. A quite similar results of pore pressure evolution were noted for all studied case excepted for the conductive pressures case with constant aperture. The controlled point A which belongs to the long conductive fractures networks presents a drop of pressure at the very early instant. We observe also the drop of pressure at the controlled point B which has the same distance to the center of wellbore as the point A but belongs to the fractured matrix but this drop begins later at about 100h.

The results obtained in this part confirm the conclusion of Li and Lee (2008) who showed that the intersection of fractures and well plays a significant role on the well productivity. In this context, one observed a high production rate in the first stage which is followed by a quick drop in the second stage. This is also illustrated by the fact that the cumulative production will attain rapidly the maximum in comparison with the other cases of equivalent single medium or non-intersected well and fractures. The geomechanics effect described in an implicit manner by using a pressure-dependent function will reduce this production rate and delay the primary depletion time. As mentioned in the first paragraph of this section, the two scenarios considered here represent in effect the single porosity/single permeability medium and double porosity/double permeability. Thus, thanks for these simulations, we also highlighted the effect of these two concepts on the behaviour of the fractured reservoir.

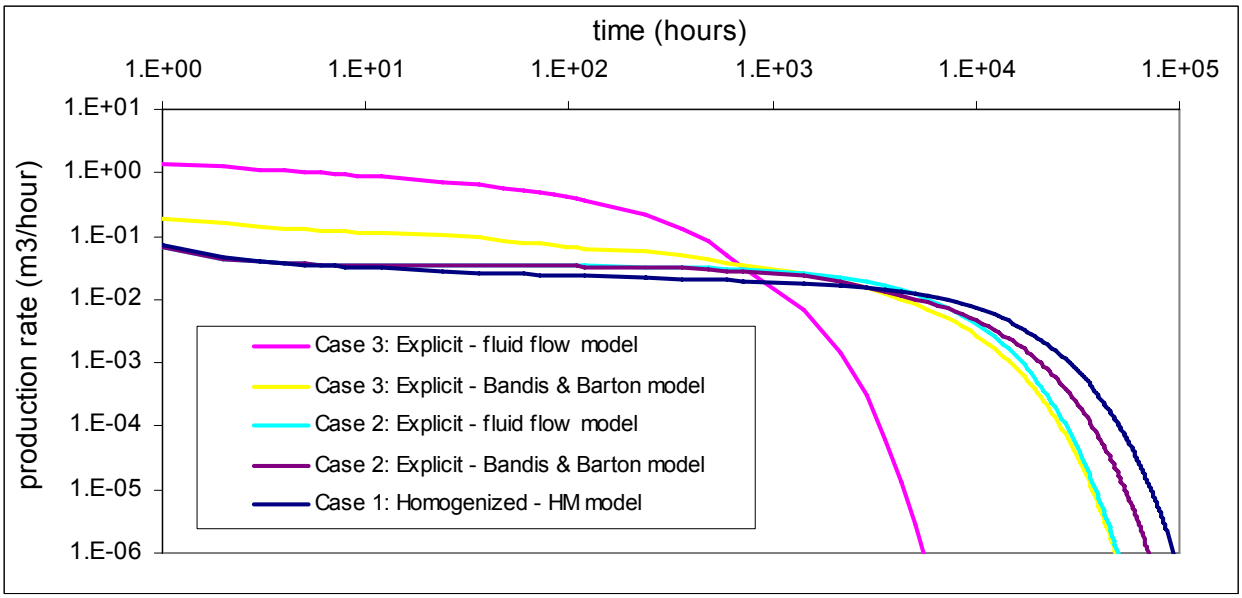

Figure 4-18 Production rate versus elapsed time

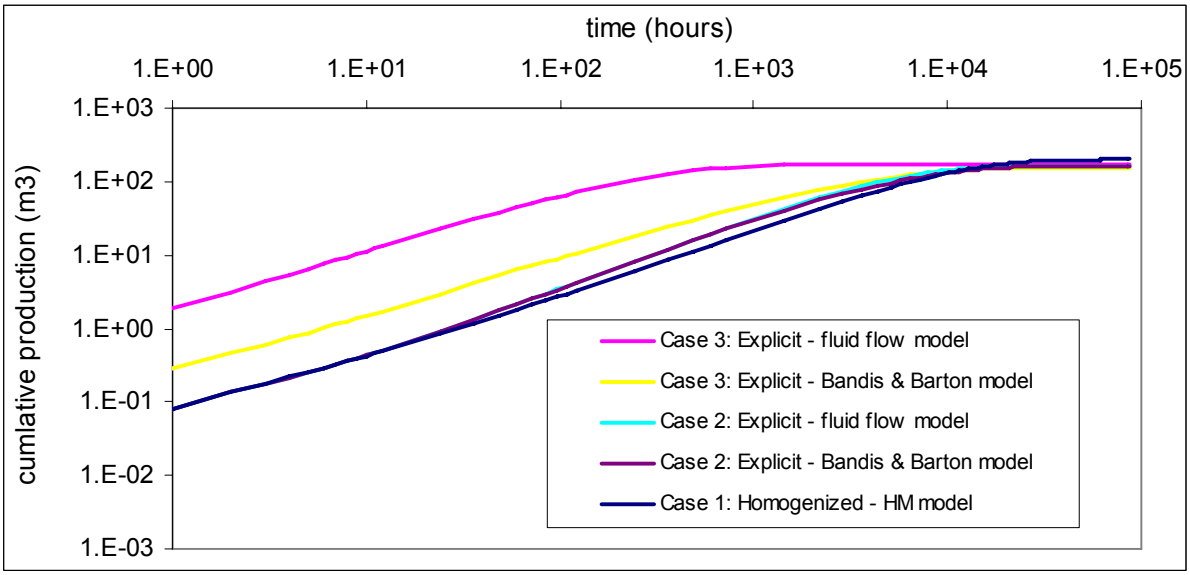

Figure 4-19 Cumulative production versus elapsed time

Models	Levels of coupling	Elapsed time (months)
Homogenized model	Coupled hydro mechanics	19
Conductive fractures model	Constant aperture	1
	Closure of aperture (Bandis and Barton model)	11
Non-conductive fractures model	Constant aperture	17
	Closure of aperture (Bandis and Barton model)	17

Table 4-14 Elapsed time at which the cumulative production attains its asymptotic value in different model

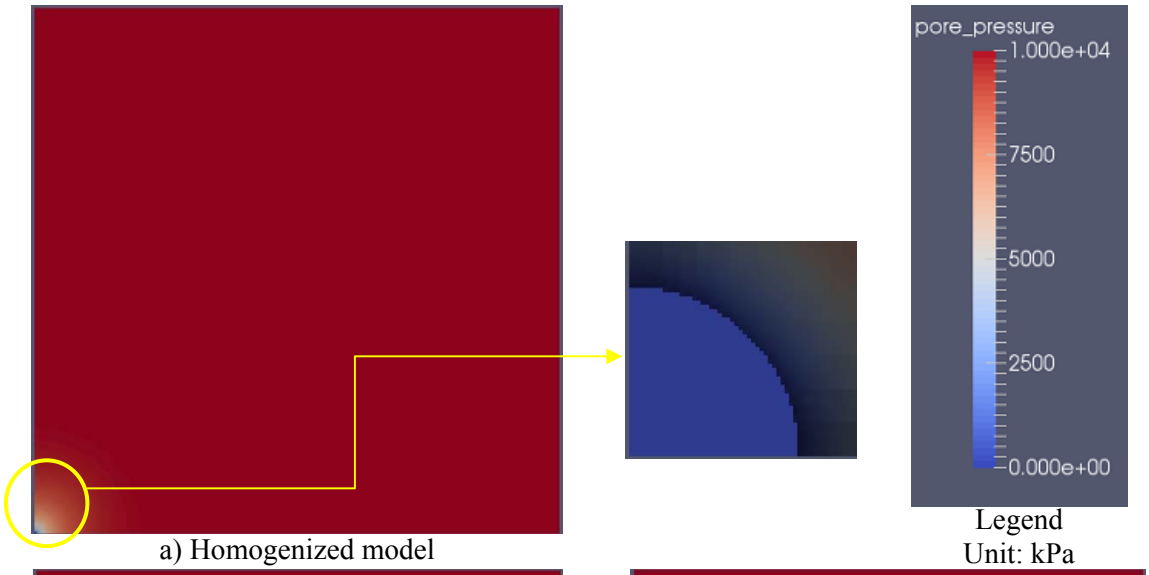

a) Homogenized model

Legend
Unit: kPa

b) Non-conductive fractures model with constant aperture

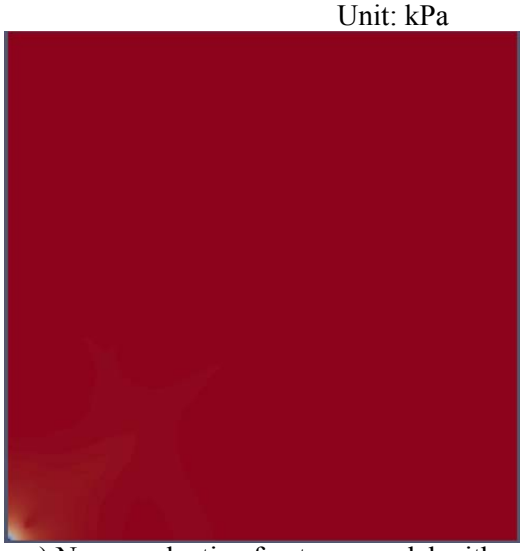

c) Non-conductive fractures model with closure (using Bandis & Barton model)

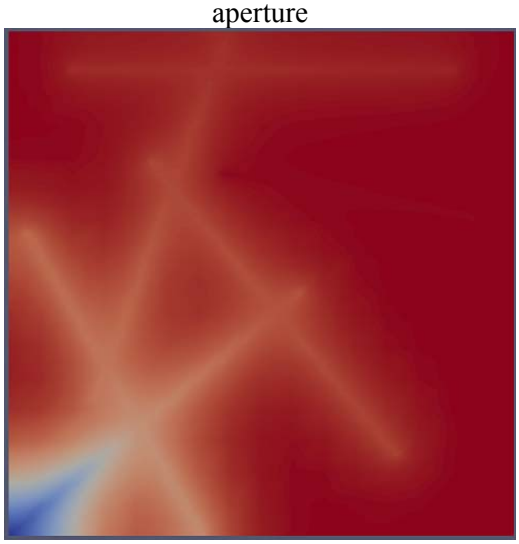

d) Conductive fractures model with constant aperture

e) Conductive fractures model with closure (using Bandis & Barton model)

Figure 4-20 Distribution of pore pressure in the model after 10 hours

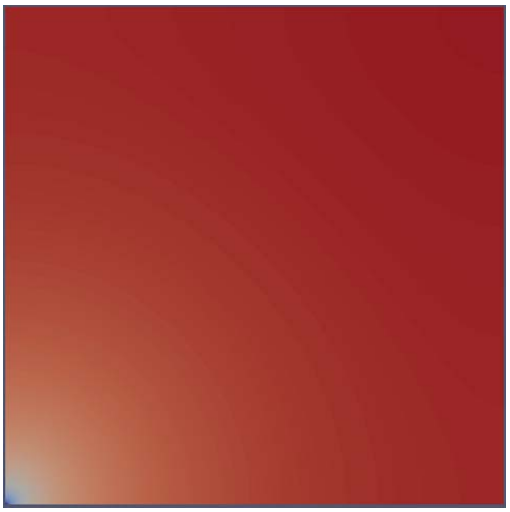

a) Homogenized model

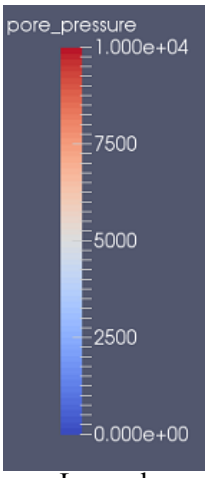

Legend
Unit: kPa

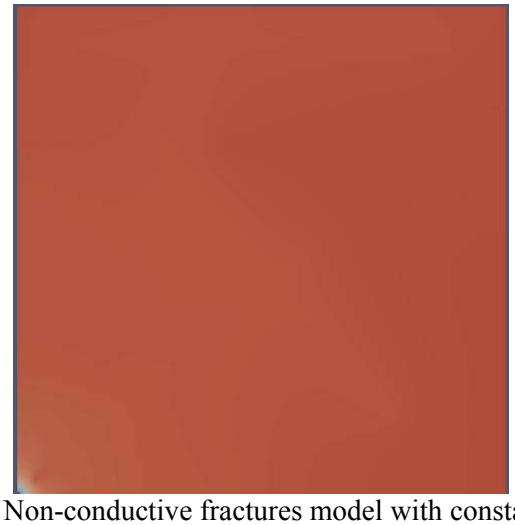

b) Non-conductive fractures model with constant aperture

c) Non-conductive fractures model with closure (using Bandis & Barton model)

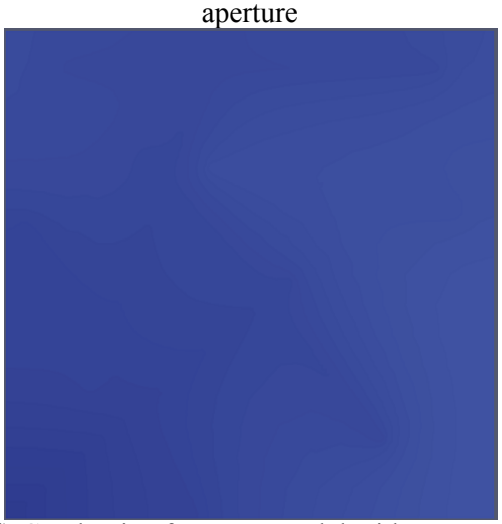

d) Conductive fractures model with constant aperture

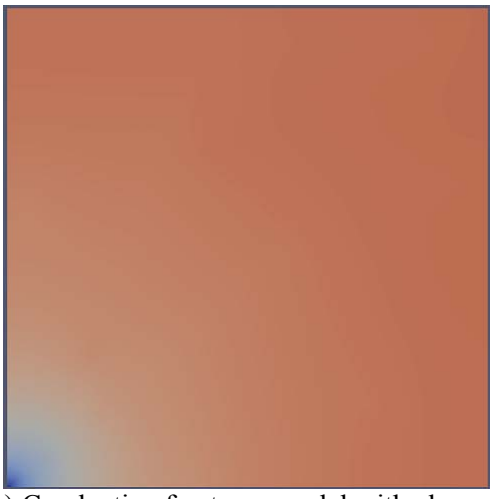

e) Conductive fractures model with closure (using Bandis & Barton model)

Figure 4-21 Distribution of pore pressure in the model after 720 hours (1 month)

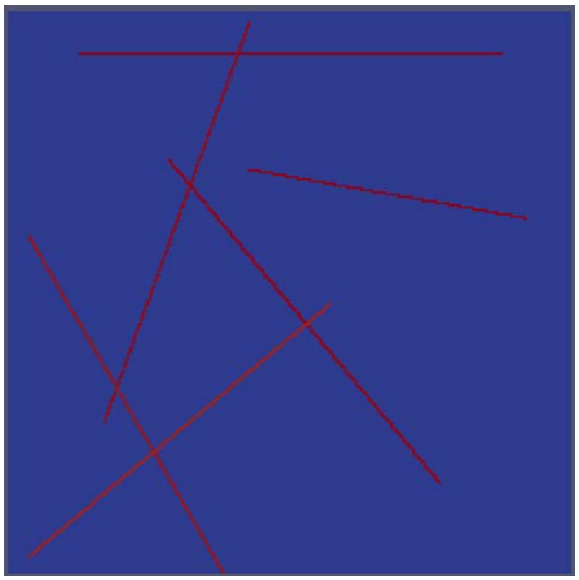

a) Non-conductive fractures model - 10 hours

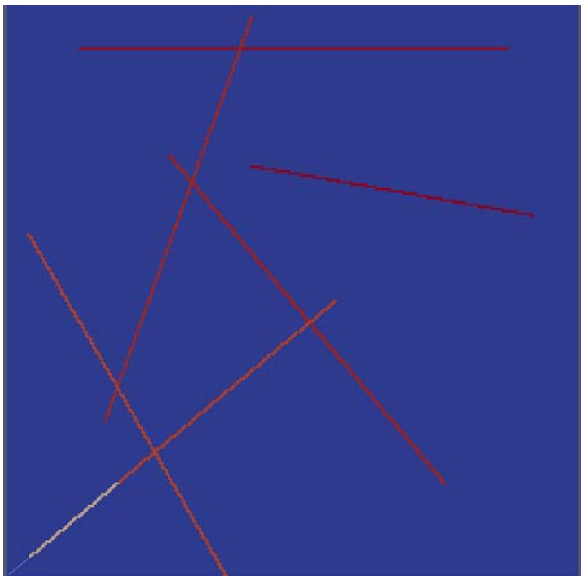

b) Conductive fractures model – 10 hours

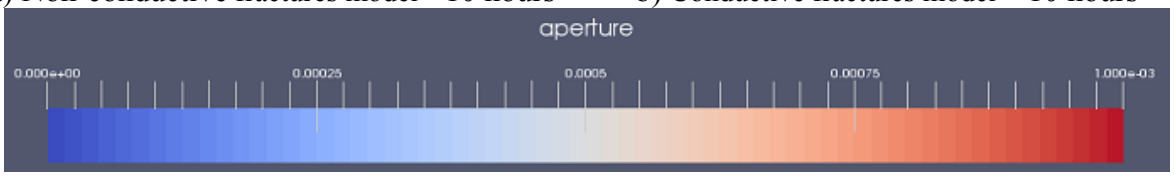

Legend, unit: meter

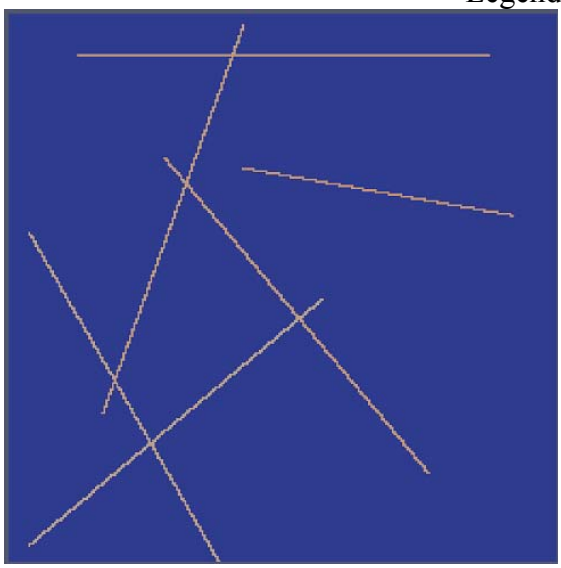

c) Non-conductive fractures model - 720 hours

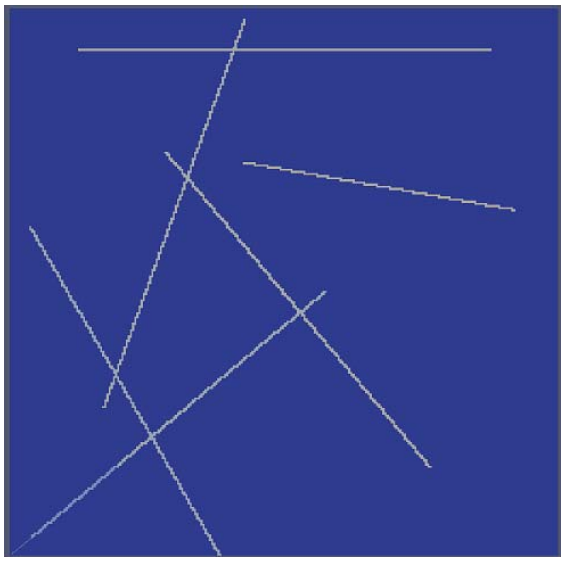

d) Conductive fractures model – 720 hours

Figure 4-22 Aperture distribution after 10hours and 720 hours in the explicit - Bandis & Barton model

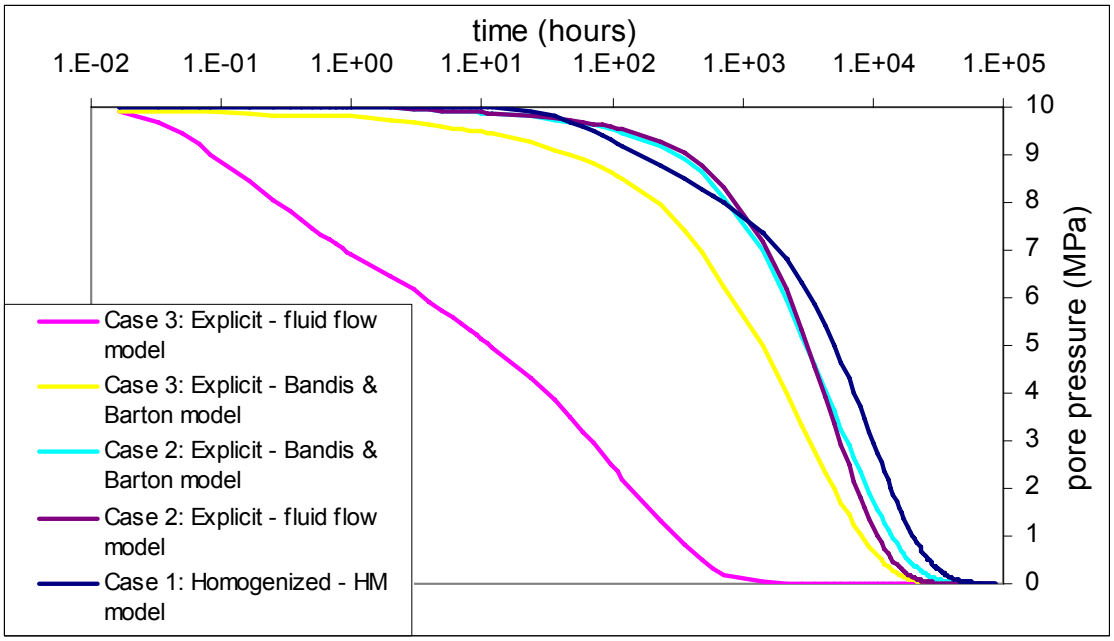

Figures 4-23 the variation of pore pressure at the controlled point A located on the fracture

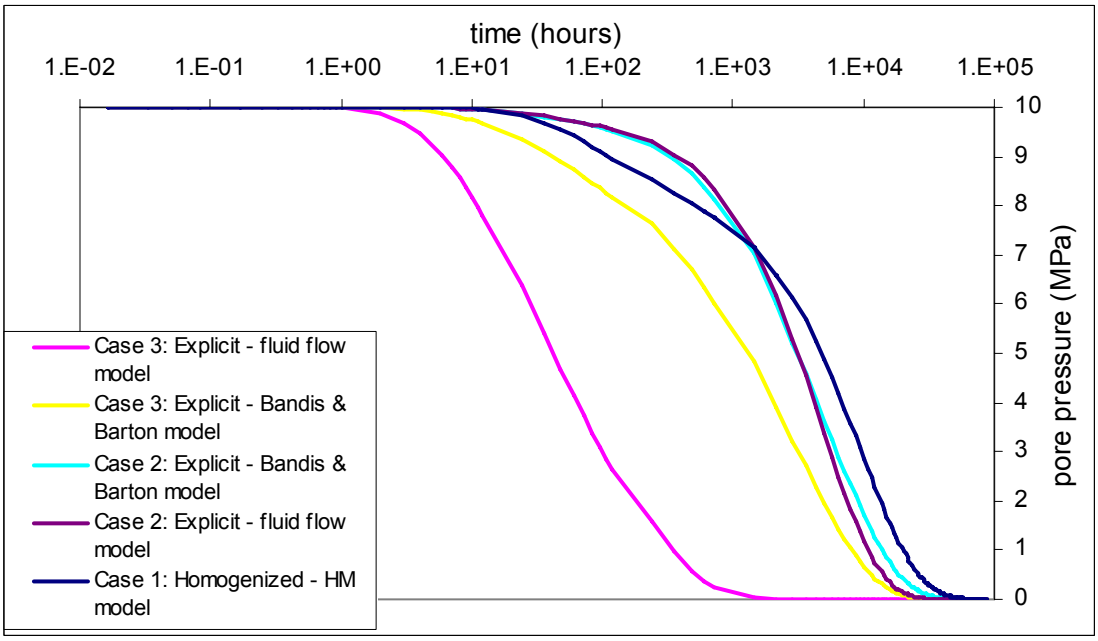

Figures 4-24 the variation of pore pressure at the controlled point B located on the fractured matrix-point

Finally, a parametric study was carried out which aim to highlight the effect of the initial normal stiffness on the closure and permeability of long conductive fracture and hence on the productivity of well. The results illustrated in Figure 4-25 and 4-26 show that the higher the initial normal stiffness of fractures is, the higher production rate is induced. The production is finishes earlier in the case that the initial normal stiffness is more important. These results can

be explained by the fact that the closure of aperture and the permeability of fractures is less affected when the normal stiffness increases.

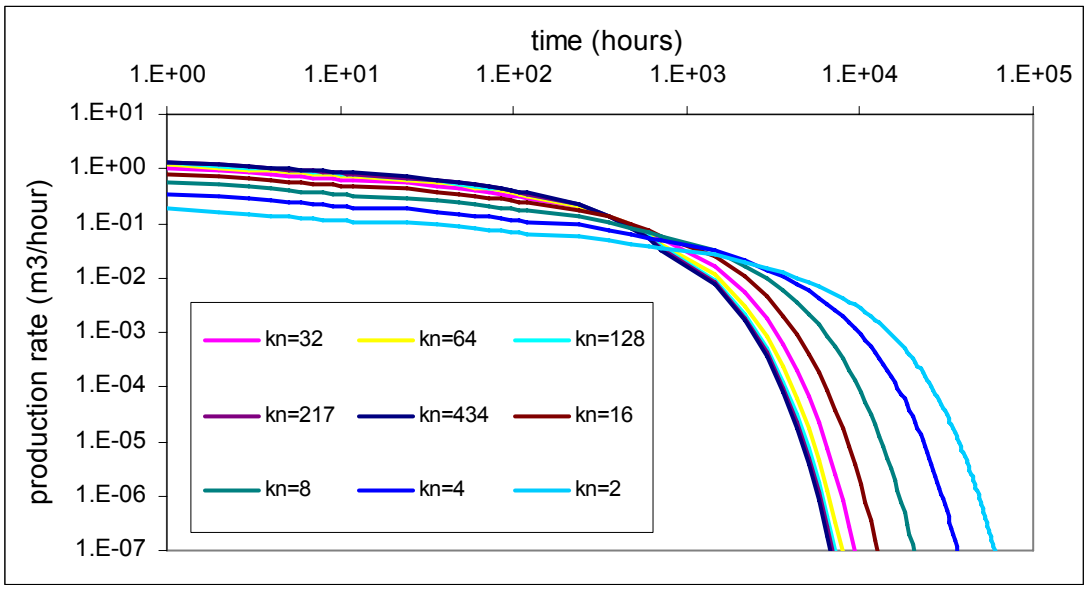

Figure 4-25 Production rate versus elapsed time in parametric study (kn)

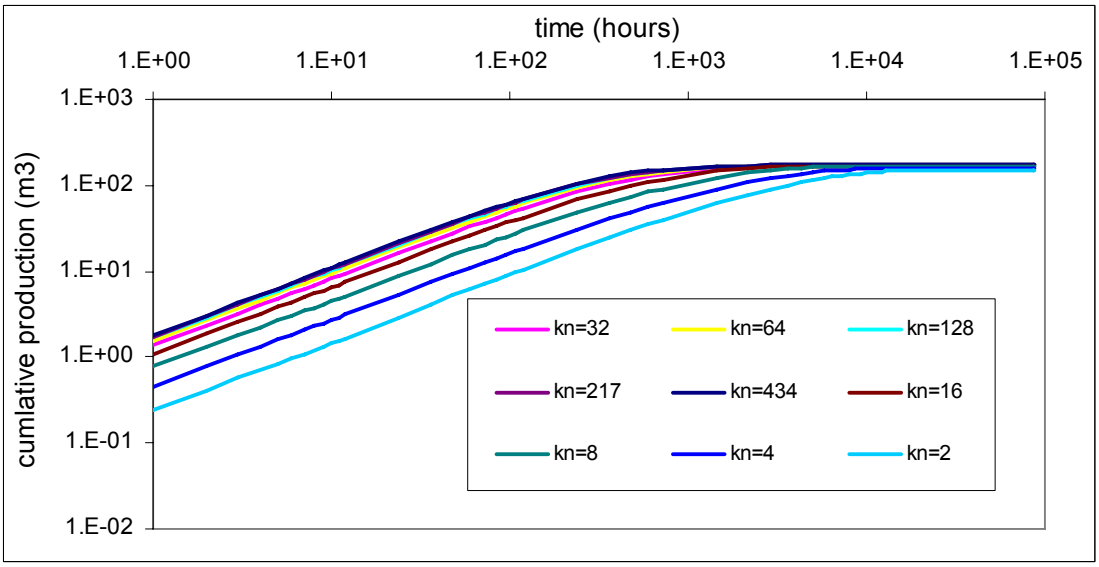

Figure 4-26 Cumulative production versus elapsed time in parametric study (kn)

4.7 Summary

In this chapter, the EFC approach is applied to model the fractured rock masses obtained from the real field. To this purpose, the Sellafiled site in UK is chosen thanks for its large accessible information. The synthetic data of this site is used to generate the DFNs in the model. The EFC approach in combination with mesh refinement based on the hanging node technique presents its performance to simulate this fractured rock owing a high density of

fractures. The Monte Carlo simulation was then conducted in which we applied the EFC approach to calculate the effective hydraulic and mechanical properties of this fractured rock (process known as homogenization technique). Both two cases of DFN with and without dead-ends fractures were considered in the present works which highlighted the necessary to consider the dead-end fractures on the behaviour of rock mass (particular for the mechanical behaviour). A consistence of the obtained results with ones presented in the literature was noted. Note however that these latter obtained principally from the UDEC code limit in case of the DFN without dead-ends fractures. The EFC approach was then used to simulate the primary depletion of the oil fractured reservoir. Different scenarios were considered. In the first scenario, all the contribution of fractures and intact porous matrix was represented through the single effective medium, result of the homogenization technique. In the second scenarios, we separate the contribution of the long fractures (considered as the major conduits) from the others of the DFN. This long fracture network embedded explicitly in the fractured matrix which is also obtained from the homogenization procedure as the first scenario. This scenario present in effect the double porosity and double permeability medium which represent respectively the fractured matrix and long fractures. Two configurations are studied in this scenario depending on the relative position of long fracture network with respect to the well. When the fractures intersect well, it can play a significant role on the productivity of well. Inversely, if the well is not intercepted by the long fractures, there is no significant difference between the single effective medium and double porosity/double permeability model. The geomechanical effect was considered implicitly in this work by using an empirical pressure-dependent of fracture aperture. As expected, the closure of fracture during production will reduce the production rate and delay the time production.

CONCLUSIONS AND PERSPECTIVES

The objectives of this work is to develop an approach of modeling the behaviour of double porosity and double permeability of fractured reservoir by taking into account explicitly the fractures network. The use of this approach to study the impact of the double porosity and the double permeability on behaviour of rock masses and fractured reservoirs was the second principal objective of the thesis.

After a review of existing literature, we observed that all modeling approaches developed so far fall either in the group of continuous approaches or in that of discontinuous approaches. The advantages as well as limitations of these two approaches are highlighted. The former approach has the advantage for solving problems of large scales with the help of REV properties and has been used since long time for different applications in the field. The later approach aims to take into account explicitly the fractures network in the medium. This approach can better investigate the local effects of fractures into fractured medium at small scale.

Borrowing the merits of these two approaches, in this work the embedded fracture continuum (EFC) approach was developed to model the fractured reservoir accounting for the hydro mechanical coupling. The principal idea of this approach lies on the notion of fracture-cell which was introduced in different works notably for the hydraulic simulation. The extension of this approach in the coupled HM problem reveals the necessity of determining the poroelastic properties of fracture-cell which contributes as the novelty of this work. The joint model was used as theoretical support for the determination of these properties. Some approximations for these calculated properties were then proposed in this work.

The implementation of this approach in the open library source code DEAL.II is conducted. For this purpose, in the first step, an iterative coupling strategy of the hydro-mechanical problem is chosen by profiting the two available modules in DEAL. II (step 8 for elastic mechanical problem and step 26 for the single-phase diffusion equation). Follow that, the developed code can easily switch from hydraulic calculation (H) to mechanical calculation (one-way coupling H-M) and vice versa (two-way coupling H-M). The accuracy of these developments in DEAL.II was investigated for different types of materials like isotropic, transversely isotropic poroelastic homogeneous and heterogeneous materials. Then, the discrete fracture network is introduced explicitly in the porous media. To this goal, the methodology to generate the fracture network based on the overall information of fractures such as distribution of fracture length, orientation and center is detailed. For the real fractured reservoirs owing a high density of fractures, the classical mesh refinement could increase significantly the number of degree of freedom and hence the computational time. To overcome this limitation, the developed code incorporates the hanging node technique which

allows to refine mesh locally on the area around fractures while preserving the use of simple cartesian grid mesh.

The accuracy of this EFC approach was investigated through different tests. The comparisons between the EFC approach and conformed mesh allow to validate the EFC approach using the isotropic approximation of the fracture-cell properties. It shows that ratio of fracture size with respect to the aperture of fracture play an essential role on the accuracy of the EFC approach. A good agreement of the results obtained from the conform-mesh method and from EFC approach (using the isotropic approximation proposed in this work) is observed if a sufficient local refinement of mesh is carried out.

The efficiency of the developed EFC approach was then demonstrated through the study conducted at industrial scale. An investigation of the effective mechanical and hydraulic properties of the fractured rock masses taken from the well-known Sellafield was conducted. Our results are consistent with ones presented in the literature using alternative approaches such as Distinct Element Method (DEM) implemented in the UDEC code and limited only in case of non-dead ends fractures. The EFC method presents among other the advantage of dealing with dead-ends fractures then can be accounted for in the DFN. Our results highlighted that the effective permeability determined from the fractures network with and without dead-ends are not much different (less than 6%) while regarding the effective mechanical properties these two DFN configurations present significant differences (up to 23%. Thus, ignoring of the dead-ends fractures can underestimate the effective properties of fractured rock mass.

As the second industrial application example, the EFC approach was used to simulate the primary depletion of an hypothetical oil fractured reservoir. Study was conducted as comparison among two scenarios of fractured rock mass: a single porosity and single permeability equivalent medium with the help of REV properties; a double porosity and double permeability medium in which a significant number of big fractures are explicitly introduced in the porous-fractured matrix with properties obtained from the homogenization procedure at the first scenario. The results show that when the long fractures intersect well (conductive fractures), it can play a significant role on the productivity of well. However, if the well is not intercepted by the long fractures (non-conductive fractures), there is no significant difference between the single effective medium and double porosity/double permeability model. The closure of fracture (consequence of the geomechanical effect on the behaviour of fracture) is also considered in this work by using an empirical pressure-dependent of fracture aperture. The results show that the closure of fracture during production will reduce the production rate and delay the time production.

As a first, immediate and short time perspective in continuity of this work is the evaluation of the pertinence of EFC method in comparison with the phase field method (PFM). The later one, was studied for a while during this work (not presented here) and presents some interesting features in modeling evolutionary fracture network (either fracture propagation or fracture opening/closing). The choice of EFC for our work is justified by its simplicity and the power of the method to deal with problems discussed here, for which EFC has clearly the advantage to PFM. If fracture propagation should be concerned the PFM is worthy to be re-evaluated. We have already observed that the use of PFM in simple configurations of crack propagation in porous media counting for hydro mechanical coupling, gives very good results. In perspectives, the feasibility of the extension of PFM for the case of intersecting fractures, or fractures in anisotropic porous media should be evaluated and compared with the perspectives to develop these features using EFC.

The presented EFC approach could be upgraded to the multiphase flow in which the hydraulic path will be needed some modification while mechanical path is remained. To upgrade the multiphase flow, the step 21 in DEAL.II developed for two-phase flow in simple porous media can be used as the starting point. The extension of the approach for fractured media and explicit presence of fracture, using EFC, seems a short-time perspective, once a theoretical model for multiphase flow in a fracture is adopted.

The software tool developed based on library DEAL.II could certainly be ameliorated and completed in many ways. To begin with, a more versatile input-output module should be developed. The concept of "fracture class" should be revisited in order to allow for a run-time updating of fracture-cell properties during variation of the fracture aperture. This update is for the moment performed using a special post-treatment and the Bandis & Barton model (Bandis et al., 1983 and Barton et al., 1985) and it is limited only on hydraulic properties.

The 3D extension of this work is quasi immediate and does not present a challenge other than computer capacities to deal with a high number of degree of freedom problem. In fact all theoretical and software elements are already in DEAL.II and only the 3D inherent difficulties (crack network visualization and apprehension, huge assembled matrix) could be seen as obstacles of such extension.

An extension of the EFC approach in the more general context of thermo-hydromechanical coupling can be done without difficulty using the same sequential coupling strategy used for HM coupling in this work. It basically consist initially to calculate thermal effective properties for the fracture-cell elements using the geometry and thermal properties of matrix and fracture. Then for problem solving, the temperature distribution as well as heat flux on the rock mass are calculated (much similar to hydraulic calculs). The mechanical effect of the temperature are calculate after. This order of T->M coupling is justified be done due to the

fact that the change of energy due to mechanical deformation is small and could be neglected Concerning the thermal effect to fluid flow (T->H), this coupling exists only in terms of changes in the fluid parameters (density, viscosity) with temperature. More sophisticated thermo-hydric coupling can be accounted for by modeling the convective heat transfer between the fluid flowing through the joints and the rock matrix.

While sequential coupling is used in our works (and has been suggested for further developments) a full coupling reformulation of problem could be worthy in some particular cases such as very long term transient problems , for which sequential coupling has a high cost in calculation time. This perspective however lead to fundamental changes of the philosophy of some key-stone concepts in DEAL.II and need a high investment in code developing.

REFERENCES

Abdallah G, Thoraval A., Sfeir A., Piguet J.P. (1995). Thermal Convection of Fluid in Fractured Media. Int. J. Rock Merh. Min. Sci. & Geomcch. Ahsrr. Vol. 32, No. 5, pp. 481- 490.

Abousleiman, Y., Cheng, A.H-D., Gui, L., Detoumay, E., & Roegiers. J.-C. (1996). Mandel's problem revisited. Géotechnique 46 (2), 187-195.

Almani, T., Kumar, K., Wheeler, M.F. (2016). Convergence Analysis of Multirate Fixed-stress split Iterative Schemes for Coupling Flow with Geomechanic. The Institute for Computational Engineering and Sciences, The University of Texas at Austin, Austin, Texas, ICES report 16-07.

Anderson J., Staub I., Knight L. (2005). Decovalex III/ Benchpar projects, Approaches to Upscaling Thermal-Hydro- Mechanical Processes in a Fractured Rock Mass and its Significance for Large-Scale Repository Performance Assessment, Summary of Findings, Report of BMT2/WP3

Arbogast, T. (1993). Gravitational forces in dual-porosity systems: I. Model derivation by homogenization. Transport in Porous Media, 13, pp 179-203.

Baghbanan, A. (2008). Scale and Stress Effects on Hydro-Mechanical Properties of Fractured Rock Mass. ISSN 1650-8602. PhD thesis, Royal Institute of Technology

Baghbanan, A. and Jing, L. (2008). Stress effects on permeability in a fractured rock mass with correlated fracture length and aperture. International Journal of Rock Mechanics & Mining Sciences; 45: 1320–1334

Bagheri, M. and Settari, A., (2008). Modeling of geomechanics in naturally fractured reservoirs. SPE Reservoir Evaluation and Engineering, Vol. 11, 108-118.

Bandis, S. C., Lumsden A. C. and Barton N. (1983). Fundamentals of rock joint deformation. Int. J. Rock Mech. Min. Sci. Geomech. Abstr., 20, 249-268.

Bangerth W. and Kanschat G. (1999). Concepts for object-oriented finite element software – the Deal.II library. Preprint 1999-43, SFB 359, Heidelberg.

Bangerth W. and Rannacher R. (2003). Adaptive Finite Element Methods for Solving Differential Equations. Birkh¨auser, Basel.

Bangerth W., Hartmann R. and Kanschat G., (2007). Deal.II — a general purpose object oriented finite element library, ACM Trans. Math. Software 33.

Bangerth, W., Burstedde, C., Heister, T. and Kronbichler, M. (2011). Algorithms and Data Structures for Massively Parallel Generic Finite Element Codes. ACM Trans. Math. Softw. 38.

Barenblatt, G. I., and Zheltov, Y. P. (1960). Fundamental equations of filtration of homogeneous liquids in fissured rocks. Dokl. Akad. Nauk SSSR, 13, pp 545-548.

Barton, N. (2013). Shear strength criteria for rock, rock joints, rockfill and rock masses: problems and some solutions. J. Rock Mech. Geotech. Eng., 5, 249-261.

Barton, N.R., Bandis, S.C., and Bakhtar, K., 1985, Strength, deformation and conductivity coupling of rock joints, International Journal of Rock Mechanics and Mining Sciences and Geomechanics, Abstract. 22 (3), 121-140.

Bear, J. (1972). Dynamics of fluids in porous media, 3rd edition. American Elsevier, USA.

Bear, J. and Berkowitz (1987). Groundwater fow and pollution in fractures rocks aquifers. Developments in Hydraulic Engineering No. 4, Elsvier.

Berkowitz, B. (2002). Characterizing flow and transport in fractured geological media: A review. Adv. Water Res., 25, 861-884.

Bibby, R. (1981). Mass Transport of Solutes in Dual-Porosity Media, Water resources research, vol 17, no.4, page 1075-1081,

Biot, M.A. (1941). General theory of three-dimensional consolidation, Journal of Applied physics, Vol. 12, No. 2, pp. 155-164.

Birkholzer J. and Karasaki K. (1996). FMGN, RENUMN, POLY, TRIPOLY: Suite of Programs for Calculating and Analyzing Flow and Transport in Fracture Networks Embedded in Porous Matrix Blocks, LBNL-39387

Blum, Mackay R. and Riley S. (2003). Coupled hydro-mechanical modelling of flow in fractured rock.

Blum, P, Mackay, R, Riley, M & Knight, JL (2005). Performance assessment of a nuclear waste repository: Upscaling coupled hydro-mechanical properties for far-field transport analysis, International Journal of Rock Mechanics & Mining Sciences, vol 42, pp. 781 – 792.

Bonnet, E., Bour O., Odling N., Main I., Berkowitz B., Davy P., and Cowie P. (2001). Scaling of fracture systems in geological media. Rev. Geophys., 39, 347-383.

Borden M.J., Verhoosel C.V., Scott M.A., Hughes T.J.R., Landis C.M (2012). A phase-field description of dynamic brittle fracture. Comput. Methods Appl. Mech. Engrg. 217–220: 77–95

Bornemann, F., Erdmann, B., and Kornhuber, R. (1993). Adaptive multilevel methods in three space dimensions. Int. J. Numer. Meth. Engrg. 36, 3187–3203.

Bornert M., Bretheau T., Gilormini P. (2001). Homogénéisation en mécanique des matériaux. 1: Matèriaux alèatoires élastiques et milieux périodiques. Hermes Sciences Europe Ltd

Botros, F. E., Hassan, A.E., Reeves, D.M. and Pohll G. (2008). On mapping fracture networks onto continuum, Water resources research, vol 44, W08435

Bruel, D. (1995). Modeling heat extraction from forced fluid-flow through stimulated fractured rock masses - evaluation of the Soultz-sous-Forets site potential. Geothermics, 24(3):439–450.

Brush D. and Thomson N.R. (2003). Fluid flow in synthetic rough-walled fractures: Navier-Stokes, Stokes, and local cubic law simulations. Water Resources Research, vol.39, no.4, 1085.

Cangiani A, Chapman J, Georgoulis E.H., and Jensen M. (2011). Implementation of the continuous-discontinuous galerkin finite element method. Numerical Mathematics and Advanced Applications 2011, page 315.

Cappa F., Guglielmi Y., Fenart P., Merrien-Soukatcho V. and Thoraval (2005). A, Hydromechanical interactions in a fractured carbonate reservoir inferred from hydraulic and mechanical measurements. International Journal of Rock Mechanics & Mining Sciences, 42, pp.287-306.

Cappa, F., Guglielmi Y., Rutqvist J., Tsang C.-F., Thoraval A. (2006), Hydromechanical modeling of pulse tests that measure both uid pressure and fracture-normal displacement of the Coaraze Laboratory site, France. International Journal of Rock Mechanics & Mining Sciences, 2006, 43, pp.1062-1082

Cappa, F., Guglielmi Y., Rutqvist J., Tsang C.-F., Thoraval A. (2008). Estimation of fracture flow parameters through numerical analysis of hydromechanical pressure pulses. Water resources research, vol. 44, w11408, doi:10.1029/2008WR007015, 2008

Chen Z., Huan G., Ma Y. (2006). Computational Methods for Multiphase Flows in Porous Media. Society for Industrial and Applied Mathematics, Philadephia.

Cheng A.H.-D. and Detourney E. (1998). A direct boundary element method for plane strain poroelasticity. Int. journal for numerical and analytical methods in geomechanics, vol 12, pp.551-572

Cheng, A.H-D. (1997). Material coefficients of anisotropic poroelasticity. Int. J. Rock Mech. Min. Sci., 34, 183-193.

Chin, L., Raghavan, R., and Thomas, L.K., (2000). Fully coupled geomechanics and fluid flow analysis of wells with stress-dependent permeability. SPE Journal, Vol. 5, 32-45.

Coussy O. (2004). Poromechanics. 1st ed., John Wiley & Sons Ltd.

Coussy, O., (1995). Mechanics of Porous Continua, John Wiley &: Sons, New York.

Cryer C.W. (1963). A comparison of the three-dimensional consolidation theories of Biot and Terzaghi. The Quarterly Journal of Mechanics and Applied Mathematics; 16(4):401–412.

Dang, H.L, Hoxha D., Do, D.P. (2016). A comparative study on modeling damage zone around underground excavation. 25th French Earth Sciences Conference (RST, la Réunion des Sciences de la Terre), Caen, France

Demkowicz L., Oden J., Rachowicz W., Hardy O. (1989). Toward a universal h-p adaptive finite element strategy, part 1. Constrained approximation and data structure, Computer Methods in Applied Mechanics and Engineering 77 (1–2) pp. 79 – 112.

Dershowitz W. S, and H. H. Einstein (1988). Characterizing rock joint geometry with joint system models. Rock Mech. Rock Eng., 21, 21-51.

Detournay E. and Cheng A.H.D., (1993). Fundamentals of Poroelasticity in Comprehensive Rock Engineering: Principles, Practice and Projects, Vol. II, Analysis and Design Method. C. Fairhurst, Pergamon Press, pp. 113-171.

Dietrich P., Helmig R., Sauter M., Hötzl H., Köngeter J., Teutsch G. (2005). Flow and Transport in fractured porous media,

Do, D.P., Tran, N.H., Hoxha D., Dang, H.L. (2017). Assessment of impact of hydraulic and poromechanic anisotropy in the fracture initiation pressure on high permeable rocks using a complex potential approach. International Journal of Rock Mechanics and Mining Sciences, vol. 100, page 108-123

Dormieux L., Kondo D., Ulm F.-J. (2006). Microporomechanics, John Wiley & Sons, Ltd.

Eloranta E. (2000). Decovalex II: The summary report of the Finnish contributions 1995–1999. Stuk-Yto-tr163, ISBN 951-712-379-5.

Eshelby J.D. (1957). The determination of the elastic field of an ellipsoidal inclusion, and related problems. Proc. Roy. Soc. Ser. A 241 (1957), 376–396

Figueiredo B., Tsang C.-F., Rutqvist J., Niemi A., (2015). A study of changes in deep fractured rock permeability due to coupled hydro-mechanical effects. International Journal of Rock Mechanics & Mining Sciences 79: 70–85

Figueiredo B., Tsang C.-F., Rutqvist J., Niemi A., (2017). Study of hydraulic fracturing processes in shale formations with complex geological settings. Journal of Petroleum Science and Engineering 152: 361–374

Formaggia L., Giovanardi B. and Scotti A. (2015). XFEM/Phase Field methods for crack propagation in brittle materials. X-DMS 2015 eXtended Discretization MethodS, Ferrara, Italy.

Gai X., (2004). A Coupled Geomechanics and Reservoir Flow Model on Parallel Computers. PhD thesis, the University of Texas at Austin

Ge S. (1997). A governing equation for fluid flow in rough fractures. Water Resour Res;33(1):53-61.

Gong Y., (2016). Importance of capillary heterogeneity in developing a representative reservoir model for shales with complex fractures. Master thesis, University of Oklahoma.

Gong, B. (2007). Effective models of fractured systems. PhD thesis. Standford university

Goodman, R.E. (1970). Deformability of joints. Paper presented at the Symposium for Determination of the In-Situ Modulus of Deformation of Rock.. Denver, Colorado, USA

Griffith A.A. (1921). The phenomena of rupture and flow in solids. Philos. Trans. R. Soc. Lond., vol 221, pp. 163–198.

Guerriero V. Mazzoli S., Iannace A., Vitale S., Carravetta A., Strauss C. (2013). A permeability model for naturally fractured carbonate reservoirs. Marine and Petroleum Geology 40, pp.115-134

Gutierrez, M., Lewis, R., and Masters, I., (2001). Petroleum reservoir simulation coupling fluid flow and geomechanics. SPE Reservoir Evaluation and Engineering, Vol. 4, 164-172.

Hao Y., Fu P., Johnson S.M., and Carrigan C.R. (2012. Numerical Studies of Coupled Flow and Heat Transfer Processes in Hydraulically Fractured Geothermal Reservoirs. GRC Transactions, Vol. 36, 2012

Heister T. (2011). A Massively Parallel Finite Element Framework with Application to Incompressible Flows. PhD thesis, University of Göttingen, Germany.

Heister T., Wheeler M.F., Wick T. (2015). A primal-dual active set method and predictor-corrector mesh adaptivity for computing fracture propagation using a phase-field approach. Comput. Methods Appl. Mech. Engrg. 290: 466–495

Hoek, E., and C. D. Martin (2014). Fracture initiation and propagation in intact rock. A review, J. Rock Mech. Geotech. Eng. 6, 287-300.

Huyakorn P., Lester B. H., Mercer J. W. (1983). An Efficient Finite Element Technique for Modeling Transport in Fractured Porous Media 1. Single Species Transport. Water resources research, Vol.19, No. 3, pp. 841-854.

Indraratna B., Ranjith P.G. and Gale W. (1999). Single phase water flow through rock fractures. Geotechnical and Geological Engineering 17: 211–240, Kluwer Academic Publishers.

IPCC Special Report and Cook P. (1999). IPCC Special Report on Carbon dioxide Capture and Storage, Chapter 5- underground geological storage.

Itasca (2006) (2012). Itasca Consulting Group Inc. https://www.itascacg.com/news/tags/flac3d

Jaeger J.C., Cook N. G.W. & Zimmerman R. W. (2007). Fundamentals of Rock Mechanics. Fourth Edition, ISBN-13: 978-0-632-05759-7, Blackwell Publishing

Janssen, B.; Kanschat, G. (2011). Adaptive multilevel methods with local smoothing for H1 - and Hcurl -conforming high order finite element methods. SIAM J. Sci. Comput.33(4).

Jensen C.L., Lee S.H., Milliken W.J., Kamath J., Narr W., Wu H.(1998). Field Simulation of Naturally Fractured Reservoirs Using Effective Permeabilities Derived From Realistic Fracture Characterization. SPE 48999, SPE Annual Technical Conference and Exhibition held in New Orleans, USA.

Jha B. (2005). A mixed finite element framework for modeling coupled fluid flow and reservoir geomechanics. M.S. thesis, Dept. Petroleum Eng., Stanford Univ.

Jiang J. and Younis R.M. (2015). Numerical study of complex fracture geometries for unconventional gas reservoirs using a discrete fracture-matrix model. Journal of Natural Gas Science and Engineering 26: 1174-1186

Jing, L. (2003). A review of techniques, advances and outstanding issues in numerical modelling for rock mechanics and rock engineering. Int. J. Rock Mech. Min. Sci., 40(3), 283-353.

Kachanov M. (1992). Effective elastic properties of a cracked solid: Critical review of some basic concepts. Appl. Mech. Rev., 45, 304-335.

Kalinina E.A., Klise K.A., McKenna S.A., Hadgu T. and Lowry T.S. (2014). Applications of fractured continuum model to enhanced geothermal system heat extraction problems. SpringerPlus 2014, 3:110, http://www.springerplus.com/content/3/1/110

Kanschat, G. (2004). Multi-level methods for discontinuous Galerkin FEM on locally refined meshes. Computers & Structures. 82.

Karimi-Fard M., Firoozabadi A. (2001). Numerical Simulation of Water Injection in 2D fractured Media. Using Discrete-Fracture Model.

Karlsson J. (2012). Implementing Anisotropic Adaptive Mesh Refinement in OpenFOAM. Master's Thesis in Computer Science, Algorithms, Languages and Logic, Chalmers University of Technology, Göteborg, Sweden.

Kazemi, H., Merrill, L. S., Porterfield, K. L., and Zeman, P. R. (1976). Numerical simulation of water-oil flow in naturally fractured reservoirs. SPE J., 16(6), pp 317-326.

Kim J. (2010). sequential methods for coupled geomechanics and multiphase flow. PhD thesis, Standford university.

Kim J. Tchelepi H.A., Juanes R, (2009), "Stability, Accuracy and Efficiency of sequential methods for coupled flow and geomechanics", the 2009 SPE Reservoir Simulation Symposium, Woodlands, Texas, USA.

Kim J., Tchelepi H.A., Juanes R. (2011), "Stability and convergence of sequential methods for coupled flow and geomechanics: Drained and undrained splits", Comput. Methods Appl. Mech. Engrg., vol 200, pp.2094-2116.

Kranzz R.L., Frankel A.D., Engelder T., Scholz C.H. (1979). The permeability of whole and jointed Barre Granite. International Journal of Rock Mechanics and Mining Science & Geomechanics Abstracts 16(4):225-234

Lee C.C, Lee C.H., Yeh H.-F., Lin H.-I. (2010). Modeling spatial fracture intensity as a control on flow in fractured rock. Environ Earth Sci, DOI 10.1007/s12665-010-0794-x

Lee S., Mikelic A., Wheeler M.F., Wick T., Phase-field modeling of proppant-filled fractures in a poroelastic medium, Comput. Methods Appl. Mech. Engrg. http://dx.doi.org/10.1016/j.cma.2016.02.008

Lee S.H., Jensen C.L., and Lough M.F. (2000). Efficient Finite-Difference Model for Flow in a Reservoir With Multiple Length-Scale Fractures. SPE 56752, presented at the 1999 SPE Annual Technical Conference and Exhibition held in Houston, 5–8 October.

Lei, Q. (2016). Characterisation and modelling of natural fracture networks: geometry, geomechanics and fluid flow, PhD thesis, Imperial College London.

Li, L. and Lee, S.H. (2008). Efficient field-scale simulation of black oil in a naturally fractured reservoir through discrete fracture networks and homogenized media. SPE Reservoir Evaluation and Engineering, Vol. 11, 750-758.

Liu F., Zhao L.-Q., Liu P.-L., Luo Z.-F., Li N.-Y. (2015), and Wang P.-S.. An Extended Finite Element Model for Fluid Flow in Fractured Porous Media. Mathematical Problems in Engineering.

Long, J. C. S., and Billaux D. M. (1987). From field data to fracture network modeling: An example incorporating spatial structure. Water Resour. Res., 23(7), 1201-1216.

Long, J. C. S., Gilmour, P., and Witherspoon P. A. (1985). A model for steady fluid flow in random three-dimensional networks of disc-shaped fractures. Water Resour. Res., 21(8), 1105-1115.

Long, J. C. S., Remer, J. S., Wilson, C. R., and Witherspoon, P. A. (1982). Porous media equivalents for networks of discontinuous fractures. Water Resour. Res., 18(3), 645-658.

Lorenz, J.C., (1999). Stress sensitive reservoirs, Journal of Petroleum Technology. Vol.51, 61-63.

Maghous S., Dormieux L., Kondo D. and Shao J.F. (2011). Micromechanics approach to poroelastic behavior of a jointed rock. Int. J. Numer. Anal. Meth. Geomech. DOI: 10.1002/nag.1087

Mainguy M. and Longuemare P. (2002). Coupling fluid flow and rock mechanics: formulations of the partial coupling between reservoir and geomechanics simulators. Oil Gas Sci Tech 57: 355–367.

Makurat, A. and Gutierrez, M., (1996). Fracture flow and fracture cross flow experiments. SPE 36732, SPE Annual Technical Conference and Exhibitions, Denver, CO, October 6-9.

Mandel J. (1953). Consolidation des sols (étude mathématique). Geotechnique; 3(7):287–299.

Marmier (2007). Changement d'échelle dans les modèles hydromécaniques couplés des réservoirs fracturés. PhD thesis, Lorraine university, France.

McKenna S.A. and Reeves P.C. (2006). Fractured Continuum Approach to Stochastic Permeability Modeling. The American Association of Petroleum Geologists. DOI:10.1306/1063815CA53234

Mestat P. (2001). Modélisation des Sols et des Ouvrages dans leur Environnement, Handbook of Ecole Nationale des Ponts et Chaussees

Mikelic A. Wheeler M.F., Wick T (2015). Phase-field modeling of a fluid-driven fracture in a poroelastic medium. Computational Geosciences, vol.19:1171–1195.

Mikelic A. Wheeler M.F., Wick T. (2014). A phase-field method for propagation fluid-filled fractures coupled to a surrounding porous medium. The Institute for Computational Engineering and Sciences, The University of Texas at Austin, Austin, Texas, ICES report 14-08

Min K.B., Jing L (2003). Numerical determination of the equivalent elastic compliance tensor for fractured rock masses using the distinct element method. Int J Rock Mech Min Sci;40(6):795-816

Min K.B., Jing L, Stephansson O. (2004a). Determining the equivalent permeability tensor for fractured rock masses using a stochastic REV approach: Method and application to the field data from Sellafield, UK. Hydrogeol;12(5):497-510.

Min K.B., Rutqvist J, Tsang CF, Jing L. (2004b). Stress-dependent permeability of fractured rock masses: a numerical study. Int J Rock Mech Min Sci;41(7):1191-1210.

Min K.B., Rutqvist J., Tsang CF, Jing L. (2005). Thermally induced mechanical and permeability changes around a nuclear waste repository—a far-field study based on equivalent properties determined by a discrete approach. International Journal of Rock Mechanics & Mining Sciences 42: 765–780

Mohammadnejad T and Khoei A.R. (2013). Hydro-mechanical modeling of cohesive crack propagation in multiphase porous media using the extended finite element method. Int. J. Numer. Anal. Meth. Geomech. 37:1247–1279

Moinfar A. (2013). Development of an Efficient Embedded Discrete Fracture Model for 3D Compositional Reservoir Simulation in Fractured Reservoirs, PhD thesis, The University of Texas at Austin;

Moinfar A., Sepehrnoori K., Johns R.T. and Varavei A. (2013). Coupled Geomechanics and Flow Simulation for an Embedded Discrete Fracture Model, SPE-163666-MS, https://doi.org/10.2118/163666-MS

Monteagudo, J., Rodriguez, A., and Florez, H., (2011). Simulation of flow in discrete deformable fractured porous media, SPE Reservoir Simulation Symposium, The Woodlands, TX, February 21-23.

Munier, R. (2004). Statistical analysis of fracture data adapted for modeling discrete fracture networks version 2. Rep. R 04-66, Swed. Nucl. Fuel and Waste Manage., Stockholm.

Namdari S., Baghbanan A., Habibi M.J. (2016). Effective of matrix permeability and fracture density on flow pattern in dual porous rock masses. conference paper.

Nelson (2001) R.A. Geologic Analysis of Naturally Fractured Reservoirs. ISBN 0-88415-317-7, Gulf Professional Publishing

Niemi, A., Kontio K., Kuusela-Lahtinen A., and Poteri A. (2000). Hydraulic characterization and upscaling of fracture networks based on multiplescale well test data. Water Resour. Res., 36(12), 3481–3497.

Nirex (1997a). Data summary sheets in support of gross geotechnical predictions. Nirex report SA/97/052, Harwell, UK.

Nirex (1997b). Evaluation of heterogeneity and scaling of fractures in the Borrowdale Volcanic Group in the Sellafield area. Nirex Report SA/97/028, Harwell, UK.

Nirex (1997c) Assessment of the in-situ stress field at Sellafield. Nirex Report S/97/003, Harwell, UK.

Ohman J. and Niemi A. (2003). Upscaling of fracture hydraulics by means of an oriented correlated stochastic continuum model. Water resources research, vol 39, no.10.

Parsons, R.W. (1966). Permeability of Idealized Fractured Rock., Soc. of Petroleum Engineers Journal, pp. 126-136, June.

Pouya A., Ghoreychi M. (2011). Determination of rock mass strength properties by homogenization. International Journal for Numerical and Analytical Methods in Geomechanics, Wiley, 2011, 25, pp.1285-1303

Raghavan, R. and Chin, L., (2004). Productivity changes in reservoirs with stress- dependent permeability. SPE Reservoir Evaluation and Engineering, Vol. 7, 308- 315.

Ranjbar, E., Hassanzadeh, H., and Chen, Z., (2011). Effect of fracture pressure depletion regimes on the dual-porosity shape factor for flow of compressible fluids in fractured porous media. Advances in Water Resources, Vol. 34, 1681-1693.

Raviart, P.A., Thomas, J.M. (1977). A mixed finite element method for 2nd order elliptic problems. Mathematical aspects of the finite element method. Lecture Notes in Mathematics, Vol. 606. Berlin, Heidelberg, New York.

Reeves, D. M., D. A. Benson, and M. M. Meerschaert (2008a). Transport of conservative solutes in simulated fracture networks: 1. Synthetic data generation. Water Resour. Res., 44, W05404, doi:10.1029/2007WR006069.

Reeves, D. M., D. A. Benson, M. M. Meerschaert, and H.-P. Scheffler (2008b). Transport of conservative solutes in simulated fracture networks: 2. Ensemble solute transport and the correspondence to operator-stable limit distributions. Water Resour. Res., 44, W05410, doi:10.1029/2008WR006858.

Reichenberger V., Jakobs H., Bastian P., Helmig R.(2006). A mixed-dimensional finite volume method for two-phase flow in fractured porous media. Advances in Water Resources 29: 1020–1036

Rekik A. and Lebon F. (2012). Homogenization methods for interface modeling in damaged masonry. Advances in Engineering Software, Elsevier, 46 (1), pp.35-42.

Renshaw C.E., Park J.C. (1997). Effect of mechanical interactions on the scaling of fracture length and aperture. Nature 386:482- 484.

Rheinboldt W. C. and Mesztenyi C. K. (1980). On a data structure for adaptive finite element mesh refinements. ACM Trans. Math. Softw. 6, 166–187.

Royer P., Auriault J.-L., Lewandowska J., Serres C. (2002). Continuum Modeling of Contaminant Transport in Fractured Porous Media. Kluwer Academic Plubishers.

Rutqvist J. and O. Stephansson, (2003). The role of hydromechanical coupling in fractured. rock engineering, Hydrogeol J 11, pp. 7–40.

Rutqvist J., Leung C., Hoch A., Wang Y., Wang Z. (2013). Linked multicontinuum and crack tensor approach for modeling of coupled geomechanics, fluid flow and transport in fractured rock. Journal of Rock Mechanics and Geotechnical Engineering 5: 18–31

Sahimi M., (2011). Flow and Transport in Porous Media and Fractured Rock: From Classical Methods to Modern Approaches. ISBN Print 978-3-527-40485-8, Willey-VCHVerlag GmbH & Co. KGaA, Boschstr. 12, 69469 Weinheim, Germany

Saidi, A.M. (1987). Reservoir engineering of fractured reservoir: fundamental and practical aspects. ISBN 2-095 143-09-6, Total edition press, Paris, France.

Sakhaee-Pour, A., and Wheeler. M.F. (2016). "Effective Flow Properties for Cells Containing Fractures of Arbitrary Geometry." SPE Journal 21 (03): 965-980. doi:http://dx.doi.org/10.2118/167183-PA.

Samier, P., Onaisi, A., and Fontaine, G., (2006). Comparisons of uncoupled and various coupling techniques for practical field examples. SPE Journal, Vol.11, 89-102.

Sarkar S., Toksöz M.N., and Burns D.R. (2004). Fluid Flow Modeling in Fractures. Earth Resources Laboratory Industry Consortia Annual Report.

Schwartz, F. W., and L. Smith (1988). A continuum approach for modeling mass transport in fractured media. Water Resour. Res., 24(8), 1360 – 1372.

Segura, J. M. and Carol, I. (2004). On zero-thickness interface elements for diffusion problems. International Journal for Numerical and Analytical Methods in Geomechanics, 28(9):947–962.

Settari A. and Walters D.A. (1999). Advances in Coupled Geomechanical and Reservoir Modeling With Applications to Reservoir Compaction. SPE Reservoir Simulation Symposium held in Houston, Texas

Settari, A. and Mourits, F.M., (1998). A coupled reservoir and geomechanical simulation systems. SPE Journal, Vol. 3, 219-226.

Shakiba M., (2014). Modeling and Simulation of Fluid Flow in Naturally and Hydraulically Fractured Reservoirs Using Embedded Discrete Fracture Model (EDFM). Master thesis, The University of Texas at Austin

Silberhorn-Hemminger (2002). Modeling of fracture aquifer systems: geostatistical analysis and deterministic-stochastic, fracture generation. PhD thesis, Institute for Water and Environmental Systems Modeling, University of Stuttgart.

Svensson, U. (2001a). A continuum representation of fracture networks: part I. Method and basic test cases. J. Hydrol., 250, 170–186.

Svensson, U. (2001b). A continuum representation of fracture networks: part II. Application to the Aspo Hard Rock Laboratory. J. Hydrol., 250, 187– 205.

Taleghani A.D. (2009). Analysis of Hydraulic Fracture Propagation in Fractured reservoirs: An improved model for the interaction between induced and natural fractures. PhD Thesis.

Tao, Q., Economides, C.A., and Ghasemi, A., (2009). Investigation of stress-dependent fracture permeability in naturally fractured reservoirs using a fully coupled poroelastic displacement discontinuity model. SPE 124745, SPE Annual Technical Conference and Exhibitions, New Orleans, LA.

Tatomir A.-B., (2007). Numerical Investigations of Flow through Fractured Porous Media. Master's Thesis, Universität Stuttgart.

Torres C. C. and Zhao J. (2009). Analytical and numerical study of the effect of water pressure on the mechanical response of cylindrical lined tunnels in elastic and elasto-plastic porous media. International Journal of Rock Mechanics & Mining Sciences, vol 46, pp.531-547.

Tran N.H. (2016). Hydro-mechanical behavior of deep tunnels in anisotropic poroelastic medium. PhD thesis, University of Orleans, France.

UDEC, Universal Distinct Element Code, http://www.itascacg.com/software/products/udec

UDEC's manual (1989). Mark Board Itasca Consulting Group, Inc. UDEC (Universal Distinct Element Code) Version ICG 1.5 User's Manual.

Van Golf-Racht, T. D. (1982). Fundamentals of Fractured Reservoir Engineering. Developments in Petroleum Science, no. 12, Elsevier Scientific Publishing Company, Netherlands.

Verruijt A. (2013). Theory and problems of poroelasticity. Available: http://geo.verruijt.net

Walpole, L. (1981). Elastic behavior of composite materials: theoretical foundations. Advances in applied mechanics 21, 169–242.

Wan J., (2002). Stabilized finite element methods for coupled geomechanics and multiphase flow. Ph.D. dissertation, Dept. Petroleum Eng., Stanford Univ.

Wang B. (2014). Parallel simulation of coupled flow and geomechanics in porous media. Ph.D. dissertation, Faculty of the Graduate School, University of Texas at Austin.

Warren, J. E., and Root, P. J. (1963). The behaviour of naturally fractured reservoirs. SPE J., 3(3), pp 245-255.

Watanabe N. (2011). Finite element method for coupled thermo-hydro-mechanical processes in discretely fractured and non-fractured porous media. Ph.D. dissertation, Faculty of Forest, Geo and Hydro Sciences, Dresden University of Technology.

Watanabe N. Wang W., Taron J., Görke U. J. and Kolditz O. (2012). Lower-dimensional interface elements with local enrichment: application to coupled hydro-mechanical problems in discretely fractured porous media. Int. J. Numer. Meth. Engng 2012; 90:1010–1034.

Watanabe N., Wang W., McDermott C.I., Taniguchi T., Kolditz O. (2010). Uncertainty analysis of thermo-hydro-mechanical coupled process in heterogeneous porous media. Comput mesh, vol 45, pp. 263-280.

Wheeler M.F. Wick T., Wollner W. (2014). An augmented-Lagangrian method for the phase-field approach for pressurized fractures. Comp. Meth. Appl. Mech. Engrg., vol 271, pp. 69–85.

Wick T. Wick T., Wollner W. Fluid-filled fracture propagation with a phase-field approach and coupling to a reservoir simulator. the SPE hydraulic fracturing technology conference, Texas, USA, Feb. 2014

Witherspoon P.A, Wang J.S.Y., Iwai K., Gale J.E. (1980). Validity of Cubic Law for fluid flow in a deformable rock fracture. Water resources research, 16: 1016-1024.

Woodbury, A. and Zhang, K. (2001). Lanczos method for the solution of groundwater flow in discretely fractured porous media. Advances in Water Resources, 24(6):621–630.

Xu Y. (2015). Implementation and Application of the Embedded Discrete Fracture Model (EDFM) for Reservoir Simulation in Fractured Reservoirs. Master thesis, The University of Texas at Austin

Yan X., Huang Z., Yao J., Li Y., Fan D. (2016). An efficient embedded discrete fracture model based on mimetic finite difference method. Journal of Petroleum Science and Engineering145:11–21

Yang J.P, Chen W.-Z., Dai Y.-H., Yu H.-D. (2014). Numerical determination of elastic compliance tensor of fractured rock masses by finite element modeling. International Journal of Rock Mechanics & Mining Sciences 70: 474–482

Zimmerman R.W. and Bodvarsson G.S. (1996). Hydraulic Conductivity of Rock Fractures Transport in Porous Media. 23: 1-30.

Zimmerman, R. W., and I. Main (2004). Hydromechanical behavior of fractured rocks, in Mechanics of Fluid-Saturated Rocks. edited by Y. Gueguen, and M. Bouteca, pp. 363-421, Elsevier, London.

APPENDIX A: BRIEFLY INTRODUCTION OF DEAL.II

Overall, there are some main modulus of DEAL.II presented in Fig A-1 including Triangulation, Finite Element, Quadrature, DoFHandler, Mapping, FEValues, Linear Systems, Linear Solvers and Output. The aim of these modules is outlined below.

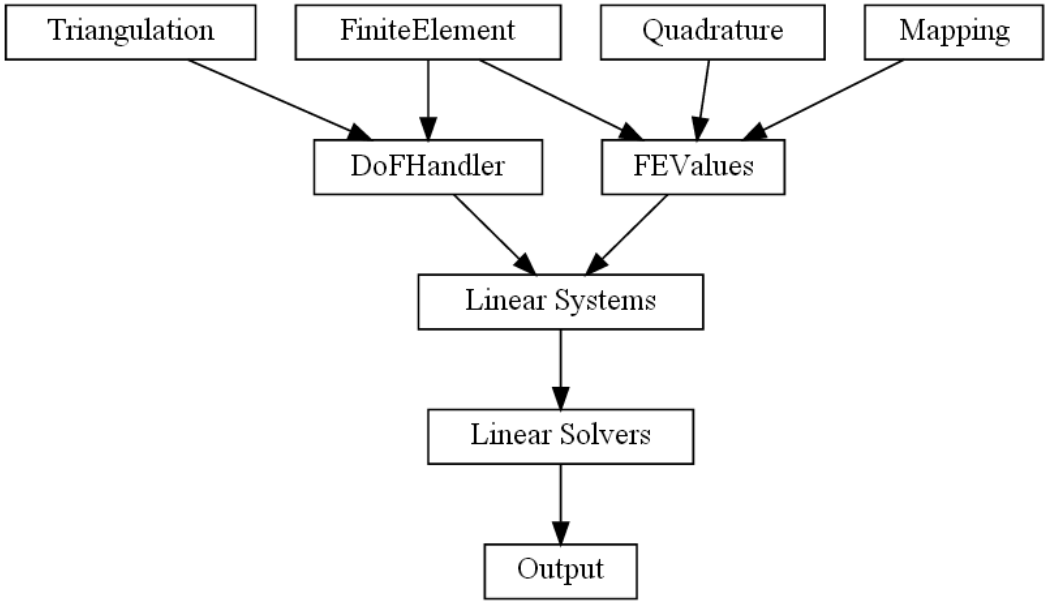

Figure A-1: Struture of modules in DEAL.II

Triangulation: Triangulations are collections of cells and their lower-dimensional boundary objects. Cells are images of the reference hypercube $[0, 1]^{dim}$ under a suitable mapping in the module on Mappings between reference and real cell.

Finite Element: Finite element classes describe the properties of a finite element space as defined on the unit cell. This includes, for example, how many degrees of freedom are located at vertices, on lines, or in the interior of cells. In addition to this, finite element classes of course have to provide values and gradients of individual shape functions at points in the unit cell.

Quadrature: As with finite elements, quadrature objects are defined on the unit cell. They only describe the location of quadrature points in the unit cell, and the weights of quadrature points thereon.

DoFHandler: DoFHandler objects are the confluence of triangulations and finite elements: the finite element class describes how many degrees of freedom it needs per vertex, line, or cell, and the DoFHandler class allocates this space so that each vertex, line, or cell of the triangulation has the correct number of them. It also gives them a global numbering.

Mapping: it is necessary to map the shape functions, quadrature points, and quadrature weights from the unit cell to each cell of a triangulation. They describe how to map points

from unit to real space and back, as well as provide gradients of this derivative and Jacobian determinants.

FEValues: The next step is to actually take a finite element and evaluate its shape functions and their gradients at the points defined by a quadrature formula when mapped to the real cell.

Linear Systems: If one knows how to evaluate the values and gradients of shape functions on individual cells using FEValues and friends, and knows how to get the global numbers of the degrees of freedom on a cell using the DoFHandler iterators, then the next step is to use the bilinear form of the problem to assemble the system matrix (right hand side) of the linear system. We will then determine the solution of our problem from this linear system.

Linear Solvers: In order to determine the solution of a finite-dimensional, linear system of equations, one needs linear solvers

Output: Finally, once one has obtained a solution of a finite element problem on a given triangulation, one will often want to post-process it using a visualization program.

To implement a FEM calculation of hydro mechanical coupling, following steps need to be done such as Mesh, Materials, Initial condition, boundary conditions, Solve and Output. We present these steps in the following items.

A-1 Mesh

In DEAL.II, A mesh can be thought of a collection of cells; if the mesh has been refined (possibly in an adaptive way), and then this collection is grouped into a hierarchy of refinement levels.

Note that DEAL.II only implements triangulations made up of linear, quadrilateral, and hexahedral cells; triangles and tetrahedral are not supported.

In general, the mesh can be established in two steps: grid generation and refined mesh.

Grid generation

There are three ways to create a mesh:

+ Creation by the GridGenerator class;

+ Reading from a file;

+ Creation by hand.

Firstly, the GridGenerator class provides functions that can generate the simplest and most common geometries automatically. For example, rectangular (or brick) geometry as well as

circles, spheres, or cylinders can generate with the functions in this class. http://www.dealii.org/8.4.1/doxygen/deal.II/namespaceGridGenerator.html

GridGenerator::hyper_cube (*triangulation*, *left*, *right*, *colorize*) or

GridGenerator::hyper_cube (*triangulation*, *left*, *right*) with *colorize* of false as default.

Initialize the given triangulation with a hypercube (line in 1D, square in 2D, etc) consisting of exactly one cell. The hypercube volume is the tensor product interval [*left, right*] ^{dim} in the present number of dimensions, where the limits are given as arguments. They default to zero and units, then producing the unit hypercube. If the argument *colorize* is false, all boundary indicators are set to zero ("not colorized") for 2d and 3d. If it is true, the boundary is colorized as in hyper_rectangle In 1d the indicators are always colorized, see hyper_rectangle().

GridGenerator::hyper_rectangle (*triangulation, p1, p2, colorize*) or

GridGenerator::hyper_rectangle (*triangulation, p1, p2*) with *colorize* of false as default.

Create a coordinate-parallel brick from the two diagonally opposite corner points: *p1* and *p2*. If the *colorize* flag is set, the boundary_ids of the surfaces are assigned, such that the lower one in x-direction is 0, the upper one is 1. The indicators for the surfaces in y-direction are 2 and 3, the ones for z are 4 and 5.

triangulation The Triangulation<dim, spacedim> to create. It needs to be empty upon calling this function. dim is the number of coordinate working on this Triangulation. spacedim is the number of all coordinates working on the code.

p1 First corner point.

p2 Second corner opposite to `p1`.

colorize Assign different boundary ids if set to true

An example

In 2-dimensional geometry:

```
Triangulation<2 > triangulation;
GridGenerator::hyper_cube (triangulation, 0,
1);
```

2D - a square

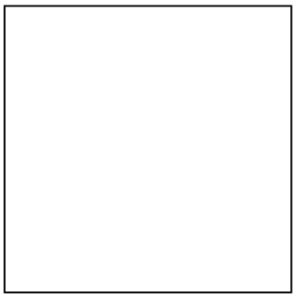

Or

```
Triangulation<2> triangulation;
Point<2>(0,0); Point<2>(1,1).
GridGenerator::hyper_rectangle
(triangulation, p1, p2);
```

In 3-dimensional geometry

```
Triangulation<3> triangulation;
GridGenerator::hyper_cube (triangulation, 0,
1);
```

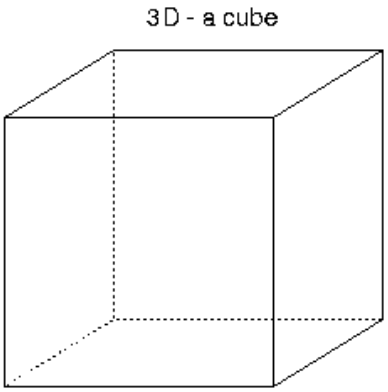

GridGenerator::hyper_cube_with_cylindrical_hole (*triangulation*, *inner_radius, outer_radius*, *L, repetitions, colorize*) or in 2-dimensional plane

GridGenerator::hyper_cube_with_cylindrical_hole (*triangulation, inner_radius, outer_radius*)

This class produces a square in the *xy*-plane with a circular hole in the middle. Square and circle are centered at the origin. In 3d, this geometry is extruded in z direction to the interval [0, L].

triangulation The triangulation to be filled.

inner_radius Radius of the internal hole.

outer_radius Half of the edge length of the square.

L Extension in `z-direction` (only used in 3d).

repetitions Number of subdivisions along the `z-direction`.

colorize Whether to assign different boundary indicators to different faces. The colors are given in lexicographic ordering for the flat faces (0 to 3 in 2d, 0 to 5 in 3d) plus the curved hole (4 in 2d, and 6 in 3d). If colorize is set to false, then flat faces get the number 0 and the hole gets number 1.

An example

In 2-dimensional geometry:

```
  Triangulation<2 > triangulation;
  GridGenerator::hyper_cube_with_cylindrical_hole (triangulation, 1, 2)
//Set manifold for circle
  double r=1; double fx;
  Point<2> p_center(0,0);
  Triangulation<2>::active_cell_iterator
                              cell = triangulation.begin_active(),
                              endc = triangulation.end();
```

```
  for (; cell!=endc; ++cell)
    for (unsigned int f=0; f<GeometryInfo<2>::faces_per_cell; ++f)
    {
      fx = (cell->face(f)->center()[0] - p_center[0])
            *(cell->face(f)->center()[0] - p_center[0])
            + (cell->face(f)->center()[1] - p_center[1])
              *(cell->face(f)->center()[1] - p_center[1]);
      if (fx <= (r*r)) cell->face(f)->set_all_manifold_ids (10);
     }
   static const SphericalManifold<2> boundary_description(p_center);
   triangulation.set_manifold (10, boundary_description);

//Mesh refinning
   triangulation.refine_global (2);
```

Result of running

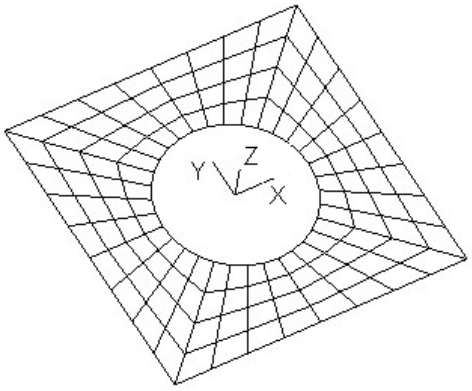

GridGenerator::subdivided_hyper_rectangle(*triangulation ,repetitions, left, right)*

Same as hyper_cube() but with the difference that not only one cell is created but each coordinate direction is subdivided into *repetitions* cells. Thus, the number of cells filling the given volume is $repetitions^{dim}$.

The above function, subdivided_hyper_rectangle, is active only in rectangular. It is a limitation on modeling fractured reservoir which fractures are clined. A development of that function is implemented by author for quadrilateral as below

void subdivided_hyper_quadrilateral (*triangulation, repetitions, p1, p2, p3, p4)*

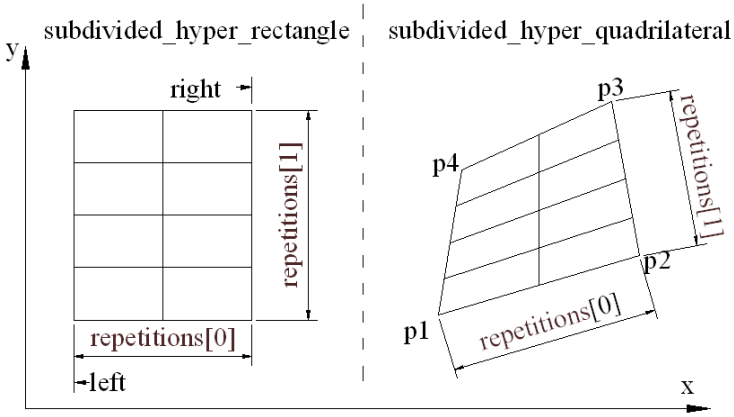

Figure A-2: Sketch of subdivided hyper rectangle and subdivided hyper quadrilateral

Secondly, it is possible to read in meshes from an input file in a number of different formats using the GridIn class. Using this class, it is possible to read meshes with several 10 or 100 thousand cells, although this is not really recommended: the power of adaptive finite element methods only comes to bear if the initial mesh is as coarse as possible and there is room for a number of adaptive refinement steps.

An example of reading a *.inp file

```
std::string grid_name;
grid_name = "rectangle.inp";
GridIn<dim> grid_in;
grid_in.attach_triangulation(triangulation);
std::ifstream input_file(grid_name.c_str());
grid_in.read_ucd(input_file);
```

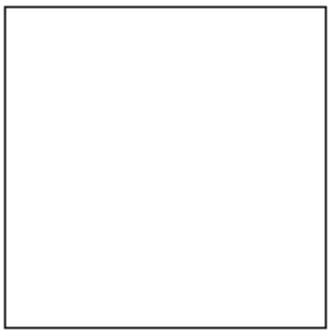

and the content of rectangle.inp file

```
4 5 0 0 0
0 0 0 0
1 1 0 0
2 0 1 0
3 1 1 0
0 1 quad 0 1 3 2
1 0 line 2 0
2 1 line 1 3
3 2 line 0 1
4 3 line 3 2
```

The third way is to create a mesh by hand, by building a data structure that describes the vertices and cells of triangulation. This is useful in cases of moderate complexity where a mesh can still be built by hand without resorting to a mesh generator, but where the domain is not one of those already supported by the GridIn class. In this method, the data structure is

built and handed to the *triangulation.* create_triangulation() function of the Triangulation class.

Besides the three method of grid generation, we can merge or remove the triangulation using the two command lines below

GridGenerator::merge_triangulations(*triangulation_1, triangulation_2, triangulation_result)*

Given the two triangulations, *triangulation_1, triangulation_2,* specified as the first two arguments, create the triangulation, *triangulation_result,* that contains the cells of both triangulation and store it in the third parameter. Previous content of *triangulation_result* will be deleted.

GridGenerator::create_triangulation_with_removed_cells(*input_triangulation, cells_to_remove, triangulation_result)*

This function creates a triangulation that consists of the same cells as are present in the first argument, except those cells that are listed in the second argument.

[in] input_triangulation The original triangulation that serves as the template from which the new one is to be created.

[in] cells_to_remove A list of cells of the triangulation provided as first argument that should be removed (i.e., that should not show up in the result.

[out] Triangulation_result The resulting triangulation that consists of the same cells as are in input_triangulation, with the exception of the cells listed incells_to_remove.

An example of merging and removing triangulation

```
Triangulation<2> tria_1, tria_2, tria_3;
// Tria_1
   std::vector< unsigned int > repetitions(2);
   repetitions[0] = 6;  repetitions[1] = 6;
   GridGenerator::subdivided_hyper_rectangle (tria_1, repetitions,
                                    Point<2>(0.0,0.0),Point<2>(12.0,12.0));
// Tria_2
   std::set< typename Triangulation<2>::active_cell_iterator >
                                                        cells_to_remove;
   Triangulation<2>::active_cell_iterator cell = tria_1.begin_active(),
                                          endc = tria_1.end();
   for (; cell!=endc; ++cell)
     for (unsigned int v=0; v< GeometryInfo<2>::vertices_per_cell; ++v)
          if ((cell->vertex(v)[0]==6.0) && (cell->vertex(v)[1]== 6.0))
```

```
                {
                    cells_to_remove.insert(cell);
                    break;
                }
   GridGenerator::create_triangulation_with_removed_cells (tria_1,
                                                cells_to_remove, tria_2);

// Tria_3
   GridGenerator::hyper_cube_with_cylindrical_hole(tria_3, 0.25, 2);
//Note that the center of result object always is (0,0,0), thus we need to
//move the result object if necessary.
   cell = tria_3.begin_active();    endc = tria_3.end();
   for (; cell!=endc; ++cell)
       for (unsigned int i=0; i<GeometryInfo<2>::vertices_per_cell; ++i)
            {
               Point<2> &v = cell->vertex(i);
               v(0) += 3.0;
               v(1) += 3.0;
             }
// Merge
   GridGenerator::merge_triangulations (tria_2, tria_3, triangulation);
```

Result of running

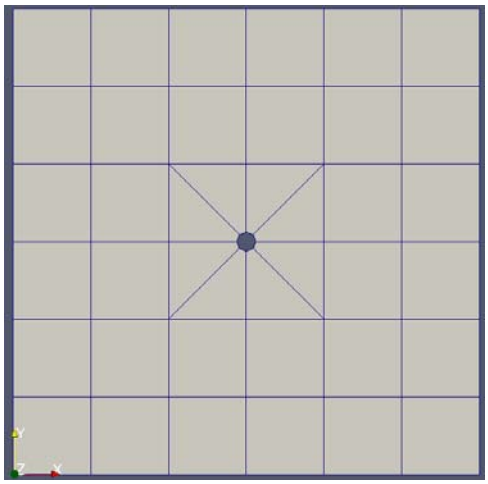

The grid which generated from DEAL.II can be outputted and stored in a *.inp file for other running by command line, write_ucd(), as below

```
std::ofstream out_ucd ("*.inp");
GridOut grid_out_ucd;
GridOutFlags::Ucd flags;
flags.write_faces = true;
flags.write_lines = true;
grid_out_ucd.set_flags (flags);
grid_out_ucd.write_ucd (triangulation, out_ucd);
```

Grid refinement and hanging nodes

The mesh obtained from the previous step, grid generation, will be assigned to level 0 of mesh structures. To smooth the mesh, grid refinement class can be applied. Principle of this class is that cells will be divided into two uniform parts per command time.

We can refine all cells of triangulation by command line *triangulation*.refine_global(*times*) or a part of cells which are already make up by a piece of code which used command line *triangulation*.execute_coarsening_and_refinement().

```
Triangulation<2>::active_cell_iterator cell =
            triangulation.begin_active(), endc = triangulation.end();
for (; cell!=endc; ++cell)
 if (cell is in boundary refined) cell->set_refine_flag();
triangulation.execute_coarsening_and_refinement();
```

More functions of grid refinement are available in the Triangulation class https://www.dealii.org/8.4.1/doxygen/deal.II/classTriangulation.html

All nodes and cells which are generated by refinement will be assigned to level 1, 2 …

In DEAL.II, hanging nodes is allowed for refining mesh and it is an strong point of this library.

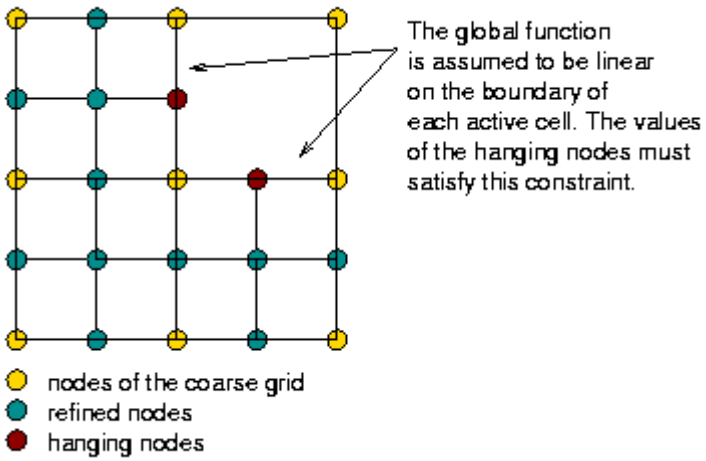

Figure A-3: Sample of hanging node and refined mesh in DEAL.II

Boundary identification

If mesh was generated by DEAL.II, the boundary indicator will be identified automatically in one id if *colorize* is false or in differential id number if *colorize* is true (see item 1)

Boundary indicator can be assigned in *.inp file or can be re-assigned during compile by a piece of code:

```
Triangulation<2>::active_cell_iterator cell = triangulation.begin_active(),
                                               endc = triangulation.end();
for (; cell!=endc; ++cell)
 for (unsigned int f=0; f<GeometryInfo<2>::faces_per_cell; ++f)
   if (cell->face(f) is in boundary id)
      cell->face(f)->set_boundary_indicator (id);
```

Note that the definition of positive vector for each boundary related to axis direction is presented in Figure D-2 of appendix D.

Group of cells

If mesh was obtained from importing a *.inp file, group of cells can be determined. Group of cells also can be assigned by a piece of code:

```
Triangulation<2>::active_cell_iterator cell = triangulation.begin_active(),
                                               endc = triangulation.end();
for (; cell!=endc; ++cell)
if (cell is in id group)cell->set_material_id(id);
```

A-2 Material

In DEAL.II, material properties are assembled in to system matrix and right hand side matrix.

In general case, but not in all cases, the finite element system equation will be formed:

$$\{M\}\{u\}=\{R\}$$

in which $\{M\}$ is the matrix of system obtained from material properties, mechanical behaviour, hydraulic behaviour, etc..

$\{u\}$ is the vector of degree of freedoms

$\{R\}$ is the vector of right hand side obtained from boundary conditions, initial condition, etc...

To calculate the $\{M\}$ and $\{R\}$ in conjunction with $\{u\}$, DEAL.II provide some classes to implement such as FESystem <dim>, DoFHandler<dim>, ConstraintMatrix, etc… The details of these classes are expressed in DEAL.II library and brief below.

FEM system setup

DEAL.II provides some finite elements such as scalar Lagrange finite element (FE_Q), discontinuous finite element (FE_DGQ), Raviart-Thomas (RT) elements (FE_RaviartThomas),

+ FE_Q yields the finite element space of continuous, piecewise polynomials of degree p in each coordinate direction.

+ FE_DGQ is a discontinuous finite element based on tensor products of Lagrangian polynomials.

+ FE_RaviartThomas generate vector fields with normal components continuous between mesh cells.

Addition, FESystem is used for combined finite element, for example

`FESystem<dim> fe(FE_Q<dim>(p), dim);` for `dim` finite elements of `FE_Q<dim>`, `p` is the polynomials of degree. `dim` is the number of spaces.

After, the degree of freedom needs to be distributed from triangulation by command line

```
DoFHandler<dim> dof_handler;
dof_handler.distribute_dofs (fe);
std::cout << " Number of active cells: " << triangulation.n_active_cells()
<< std::endl;
std::cout << " Number of degrees of freedom: " << dof_handler.n_dofs()
<< std::endl;
```

To constraint degree of freedoms in boundary conditions as well as hanging nodes in DEAL.II, ConstraintMatrix is built by following command lines:

```
ConstraintMatrix      constraints;
constraints.clear();
DoFTools::make_hanging_node_constraints (dof_handler, constraints);
constraints.close();
```

Shape function and constructing system matrix, right hand side matrix

DEAL.II provide some classes to control shape function and weight function in finite element method,

QGauss<dim> *quadrature_formula*`(n);`

Generate a formula with `n` quadrature points (in each space direction)

FEValues<dim, spacedim> *fe_values(fe, quadrature_formula, update_flags);*

For face elements:

QGauss<dim-1> *face_quadrature_formula*`(n);`

FEFaceValues <dim, spacedim> *fe_face_values(fe, face_quadrature_formula, update_flags);*

This allows us to evaluate values or derivatives of shape functions at the quadrature points of a quadrature formula when projected by a mapping from the unit cell onto a cell in real space.

Usually, an object of FEValues, FEFaceValues is used in integration loops over all cells of a triangulation (or faces of cells). A typical piece of code, adding up local contributions to the Laplace matrix looks like this:

```
FEValues values (mapping, finite_element, quadrature, flags);
for (cell = dof_handler.begin_active (); cell != dof_handler.end(); ++cell)
{
     values.reinit(cell);
     for (unsigned int q=0; q<quadrature.size(); ++q)
     for (unsigned int i=0; i<finite_element.dofs_per_cell; ++i)
     for (unsigned int j=0; j<finite_element.dofs_per_cell; ++j)
     A(i,j) += fe_values.shape_value(i,q) *
     fe_values.shape_value(j,q) *
     fe_values.JxW(q);
     ...
}
```

The functions of this class fall into different categories:

- shape_values(), shape_grad(), etc: return one of the values of this object at a time. These functions are inlined, so this is the suggested access to all finite element values. There should be no loss in performance with an optimizing compiler. If the finite element is vector valued, then these functions return the only non-zero component of the requested shape function. However, some finite elements have shape functions that have more than one non-zero component (we call them non-"primitive"), and in this case this set of functions will throw an exception since they cannot generate a useful result. Rather, use the next set of functions.
- shape_value_component(), shape_grad_component(), etc: This is the same set of functions as above, except that for vector valued finite elements they return only one vector component. This is useful for elements of which shape functions have more than one non-zero component, since then the above functions cannot be used, and you have to walk over all (or only the non- zero) components of the shape function using this set of functions.
- get_function_values(), get_function_gradients(), etc.: Compute a finite element function or its derivative in quadrature points.

- reinit: initialize the FEValues object for a certain cell. This function is not in the present class but only in the derived classes and has a variable called syntax. See the docs for the derived classes for more information.

From above loop, we can construct plural required matrices, vectors for finite element system equations.

Using MatrixCreator, VectorTools classes.

To get mass matrix and laplace matrix quickly, MatrixCreator and VectorTools class provides the functions to do it. At present there are functions to create the following matrices:

- create_mass_matrix: create the matrix with entries $m_{ij} = \int_{\Omega} a(x)\varphi_i(x)\varphi_j(x)dx$ by numerical quadrature. Here, $\varphi_i(x)$ is the basis function of the finite element space given and $a(x)$ is a function.
- create_laplace_matrix: create the matrix with entries $a_{ij} = \int_{\Omega} a(x)\nabla\varphi_i(x)\nabla\varphi_j(x)dx$ by numerical quadrature.

```
MatrixCreator::create_mass_matrix(dof_handler, Gauss<dim>(fe.degree+1),
                  mass_matrix, (const Function<dim> *)0, constraints);
MatrixCreator::create_laplace_matrix(dof_handler,QGauss<dim>(fe.degree+1,
                  laplace_matrix, (const Function<dim> *)0, constraints);
```

- create_right_hand_side: creation of right hand side vectors $f_{ij} = \int_{\Omega} f(x)\varphi_i(x)dx$ by numerical quadrature.

```
RightHandSide<dim> rhs_function();
VectorTools::create_right_hand_side(dof_handler, Gauss<dim>(fe.degree+1),
                                    rhs_function, tmp);
```

For other functions https://www.dealii.org/8.4.1/doxygen/deal.II/namespaceVectorTools.html https://www.dealii.org/8.4.1/doxygen/deal.II/namespaceMatrixCreator.html.

A-3 Initial condition and boundary conditions

A-3.1. Initial condition

There are two kinds of initial condition: direct initial condition, and indirect initial condition.

If variable has initial value, it is direct initial condition and can be assigned directly by command line

```
VectorTools::interpolate(dof_handler, InitialValues<dim>(initial_value),
```

```
                        solution);
```

in which `InitialValues<dim>(initial_value)` is a class written by user to control initial values. Normally, the form of `InitialValues` is as below:

```
template<int dim>
class InitialValues : public Function<dim>
  {
  public:
    InitialValues (const double init_p): Function<dim>()
    {
       _init_p = init_p;
    }
    virtual double value (const Point<dim> &p,
                          const unsigned int component = 0) const;
    double _init_p;
  };

 template<int dim>
 double InitialValues<dim>::value (const Point<dim> &p,
                                   const unsigned int component) const
  {
    Assert (component == 0, ExcInternalError());
    Assert (dim == 2, ExcNotImplemented());
    return _init_p;
  }
```

This method can be applied for pressure initial condition, displacement initial conditions.

If initial value is not for variable, indirect initial condition needs to be considered by a piece of code implemented by user.

A-3.2 Boundary conditions

a) Dirichlet boundary:

VectorTools::interpolate_boundary_values(*dof_handler, boundary_id, boundary_function, boundary_values);* or

VectorTools::interpolate_boundary_values(*mapping, dof_handler, boundary_id, boundary_function, boundary_values, component_mask);*

Compute Dirichlet boundary conditions. This function makes up a map of degrees of freedom subject to Dirichlet boundary conditions and the corresponding values to be assigned to them, by interpolation around the boundary. For each degree of freedom at the boundary, if its index already exists in *boundary_values* then its boundary value will be overwritten,

otherwise a new entry with proper index and boundary value for this degree of freedom will be inserted into *boundary_values*.

The flags in the last parameter, *component_mask* denote which components of the finite element space shall be interpolated. If it is left as specified by the default value (i.e. an empty array), all components are interpolated. As an example, assume that you are solving the Stokes equations in 2d, with variables (u,v,p) and that you only want to interpolate boundary values for the velocity, then the component mask should correspond to (`true,true,false`).

```
VectorTools::interpolate_boundary_values(dof_handler, boundary_id,
                                BoundaryValues<dim>(1), boundary_values);
MatrixTools::apply_boundary_values (boundary_values, system_matrix,
                                    solution, system_rhs);
```

If boundary is fixed, the `ZeroFunction<dim>(dim)` will replaced for `BoundaryValues<dim>(1)`

b) Neumann boundary

We need impose the Neumann boundary by a piece of code

```
for (unsigned int face_number=0;
      face_number<GeometryInfo<dim>::faces_per_cell; ++face_number)
 if (cell->face(face_number)->at_boundary()
      &&(cell->face(face_number)->boundary_indicator() == 3))
  {
   fe_face_values.reinit (cell, face_number);
   boundary_values.value_list(fe_face_values.get_quadrature_points(),
                              boundary_values);
   for (unsigned int q_point=0; q_point<n_face_q_points; ++q_point)
    {
     const Tensor<1, dim> neumann_value  = (boundary_values[q_point])*
                                    fe_face_values.normal_vector(q_point);
     for (unsigned int i=0; i<dofs_per_cell; ++i)
     {
      const unsigned int component_i=fe.system_to_component_index(i).first;
      cell_rhs(i) += (neumann_value[component_i] *
                      fe_face_values.shape_value(i,q_point)
                      * fe_face_values.JxW(q_point));
     }
    }
  }
```

What about the Neumann boundary in case Neumann value is 0?(to be answered later)

A-4 Solve

There are some methods of solving equations, the conjugate gradient method (SolverCG), the generalized minimal residual method (SolverGMRES), etc…

SolverCG:

SolverCG<> *cg (solver_control);*

*cg.*solve*(A,x,b,precondition);*

Solve the linear system Ax=b for x.

For example:

```
SolverControl           solver_control (1000, 1e-12);
SolverCG<>              cg (solver_control);
PreconditionSSOR<> preconditioner;
preconditioner.initialize(system_matrix, 1.0);
cg.solve (system_matrix, solution, system_rhs, preconditioner);
constraints.distribute (solution);
```

SolverGMRES

SolverGMRES<> *gmres (solver_control);*

*gmres.*solve*(A,x,b,precondition);*

Solve the linear system Ax=b for x.

For example

```
SolverControl solver_control(1000, system_rhs.l2_norm()*1e-12);
SolverGMRES<> gmres(solver_control);
PreconditionSSOR<> preconditioner;
preconditioner.initialize(system_matrix, 1.0);
gmres.solve(system_matrix, solution, system_rhs, preconditioner);
constraints.distribute(solution);
```

A-5 Output and post processing

A-5.1 Output results of variables

Class Dataout is the main class to provide output of data described by finite element fields defined on a collection of cells. The only thing this class offers is the function build_patches() which loops over all cells of the triangulation stored by the attach_dof_handler() function of the base class and converts the data on these to actual patches which are the objects that are later output by the functions of the base classes.

An example of outputting `solution` to `*.vtk` file

```
DataOut<dim> data_out;
```

```
data_out.attach_dof_handler (dof_handler);
data_out.add_data_vector (solution, solution_names);
data_out.build_patches ();
data_out.write_vtk (output);
```

A-5.2 Output of other items.

If other items such as velocity, stress need to be outputted, a calculation function needs to be implemented. There functions will be written in the post processing stage.

APPENDIX B: ANALYTICAL SOLUTION OF MANDEL'S PROPBLEM AND EXCAVATION PROBLEM

B-1 Mandel's problem

The geometry of Mandel's problem in anisotropic case is sketched in Figure B-1. A rectangular sample subjected to a constant applying stress at its top, through a rigid and frictionless plate of width 2a, with drainage to the two sides in lateral direction. (Mandel, 1963)

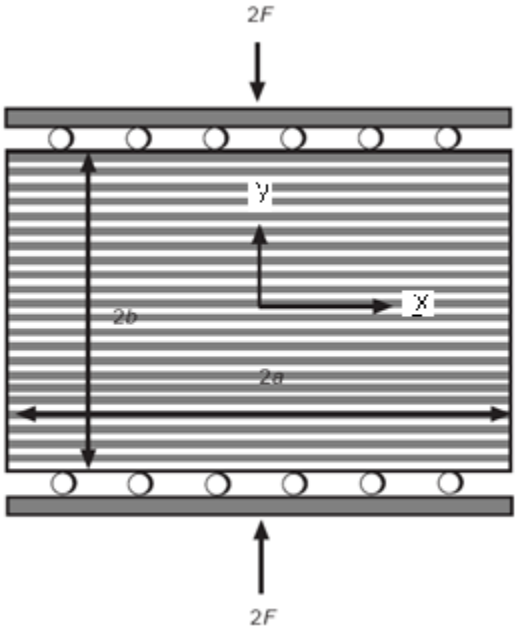

Figure B-1: Sketch of Mandel geometry in anisotropic case

The analytical solution is provided by Abousleiman et al, (1996) as briefly presented below

Pressure distribution on the x-coordinate is

$$p = \frac{2\mathrm{F}}{\mathrm{aA}_1}\sum_{i=1}^{\infty}\frac{\sin\alpha_i}{\alpha_i - \sin\alpha_i\cos\alpha_i}\left(\cos\frac{\alpha_i x}{a} - \cos\alpha_i\right)\exp\left(-\frac{\alpha_i^2 c_v t}{a^2}\right) \tag{B.1}$$

x-displacement on the x-coordinate (y=0) is

$$u_x = \left[\frac{F}{a}\frac{M_{13}}{M_{11}M_{33}\text{-}M_{13}^2} - \frac{2F}{a}\frac{b_x b_y M + M_{13}}{A_1 M(b_y M_{11} - b_x M_{13})}\sum_{i=1}^{\infty}\frac{\sin\alpha_i\cos\alpha_i}{\alpha_i - \sin\alpha_i\cos\alpha_i}\exp\left(-\frac{\alpha_i^2 c_v t}{a^2}\right)\right]x + 2F\frac{b_x}{A_2 M_{11}}\sum_{i=1}^{\infty}\frac{\cos\alpha_i}{\alpha_i - \sin\alpha_i\cos\alpha_i}\sin\left(\frac{\alpha_i x}{a}\right)\exp\left(-\frac{\alpha_i^2 c_v t}{a^2}\right) \tag{B.2}$$

y-displacement on the y-coordinate (x=0) is

$$u_y = -\frac{F}{a}\frac{M_{11}}{M_{11}M_{33}\text{-}M_{13}^2}\left[1+2\left(\frac{A_2}{A_1}-1\right)\sum_{i=1}^{\infty}\frac{\sin\alpha_i\cos\alpha_i}{\alpha_i-\sin\alpha_i\cos\alpha_i}\exp\left(-\frac{\alpha_i^2 c_v t}{a^2}\right)\right]y \tag{B.3}$$

In which

$$\begin{aligned}
&\frac{\tan\alpha_i}{\alpha_i}=\frac{A_1}{A_2}\\
&A_1=\frac{b_x^2M_{33}-2b_xb_yM_{13}+b_y^2M_{11}}{b_yM_{11}-b_xM_{13}}+\frac{M_{11}M_{33}-M_{13}^2}{M(b_yM_{11}-b_xM_{13})}\\
&A_2=\frac{b_yM_{11}-b_xM_{13}}{M_{11}}\\
&c_v=\frac{K_xMM_{11}}{\mu M_{11}^u}
\end{aligned} \tag{B.4}$$

For M_{ij} are the drained elastic moduli defined by the generalized Hook's law

$$\begin{aligned}
M_{11}&=\frac{E_x(E_y-E_x\nu_{yx}^2)}{(1+\nu_{zx})(E_y-E_y\nu_{zx}-2E_x\nu_{yx}^2)}\\
M_{12}&=\frac{E_x(\nu_{zx}E_y-E_x\nu_{yx}^2)}{(1+\nu_{zx})(E_y-E_y\nu_{zx}-2E_x\nu_{yx}^2)}\\
M_{13}&=\frac{E_xE_y\nu_{yx}}{E_y-E_y\nu_{zx}-2E_x\nu_{yx}^2}\\
M_{33}&=\frac{E_y^2(1-\nu_{yx})}{E_y-E_y\nu_{zx}-2E_x\nu_{yx}^2}\\
M_{55}&=G_{xy}
\end{aligned} \tag{B.5}$$

For properties of undrained material:

$$M_{ij}^u=M_{ij}+b_ib_jM \tag{B.6}$$

B-2 Excavation problem

The problem to be analyzed is represented in Figure B-2 (Torres and Zhao, 2009). A section of cylindrical tunnel of radius a is excavated in an elastic porous material characterized by Young's modulus E and Poisson's ratio υ. Axi-symmetry conditions for geometry and loading will be assumed (i.e., gravity will be disregarded), so the problem in Figure B-2 is

representative of the case of a deep tunnel excavated in elastic ground subject to uniform initial stresses.

Prior to excavation, the total stresses in the medium are uniformed and equal to $\sigma_V = \sigma_H$ and the pore pressures in the ground are also uniformed and equal to p_{ff}. The tunnel is then excavated and water is drained from inside the tunnel, leading to the non- uniform pore pressure distribution. We assume that the calculated area of simulation (2A x 2B) is large enough for the tunnel radius in which the pressure at boundary is kept constant of the far-field value p_{ff} in analytical solution (Torres and Zhao, 2009).

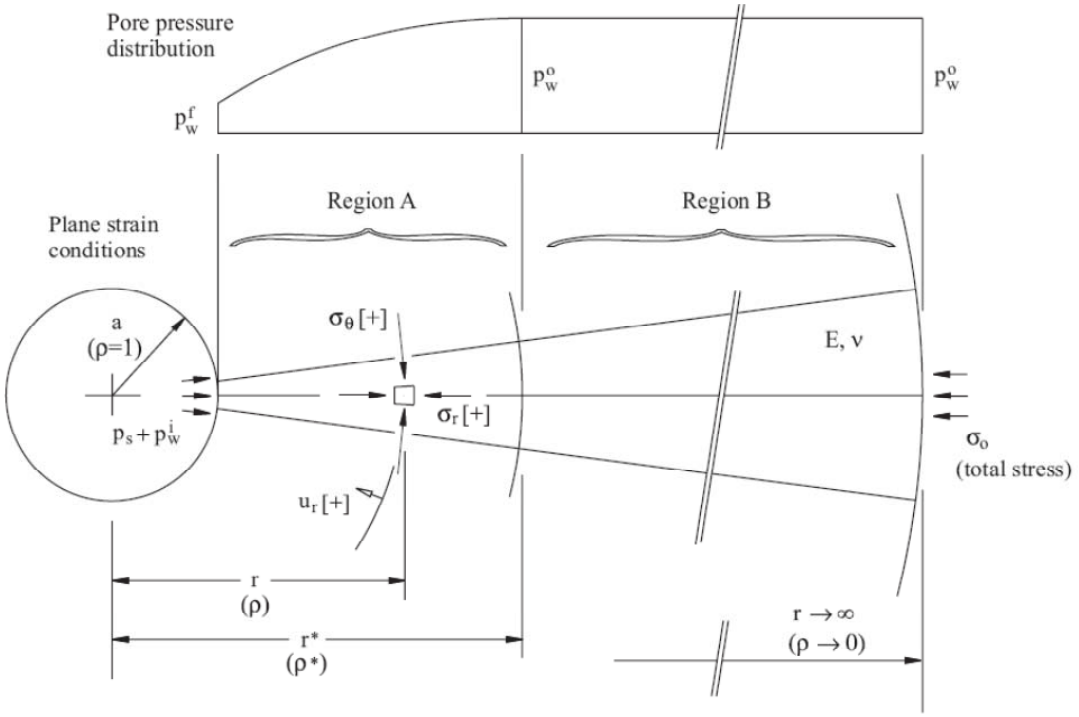

Figure B-2: The axi-symmetrical problem of excavation of a cylindrical tunnel in a saturated elastic porous material Torres and Zhao (2009)

The analytical solution:

The solution of the problem in Figure B-2 is expressed in terms of a transformed radial distance variable ρ, defined in terms of the radial distance r and the tunnel radius a as follows:

$$\rho = \frac{a}{r} \tag{B.7}$$

The pore pressure for region A and region B is as

$$p_w^{[A]}(\rho) = p_w^f + (p_w^0 - p_w^f)\frac{\ln\rho}{\ln\rho^*} \tag{B.8}$$

$$p_w^{[B]}(\rho) = p_w^0$$

The radial displacement for region A and region B are, respectively

$$u_r^{[A]}(\rho) = \frac{a}{2G}(\sigma_0 - p_s - p_w^i)\rho - \frac{a}{4(\lambda + 2G)}\frac{p_w^0 - p_w^f}{\rho \ln \rho}\left[2\ln \rho + (1-\rho^2)(1-2\ln \rho)\right]$$

$$u_r^{[B]}(\rho) = \frac{a}{2G}(\sigma_0 - p_s - p_w^i)\rho - \frac{a}{4(\lambda + 2G)}\frac{p_w^0 - p_w^f}{(\rho)^2 \ln \rho}\rho\left[1-(\rho)^2 + 2(\rho)^2 \ln \rho\right] \quad \text{(B.9)}$$

The radial effective stress for region A and region B are, respectively

$$\sigma_r'(\rho) = \sigma_r(\rho) - p_w(\rho)$$
$$= \sigma_0 - (\sigma_0 - p_s - p_w^i)\rho^2 + \frac{G}{2(\lambda + 2G)}\frac{p_w^0 - p_w^f}{\ln\rho}\left[2\ln\rho + (1-\rho^2)(1-2\ln\rho)\right] - p_w(\rho)$$

and

$$\sigma_\theta'(\rho) = \sigma_\theta(\rho) - p_w(\rho)$$
$$= \sigma_0 - (\sigma_0 - p_s - p_w^i)\rho^2 + \frac{G}{2(\lambda + 2G)}\frac{p_w^0 - p_w^f}{(\rho)^2 \ln\rho}\rho^2\left[1-\rho^2 + 2(\rho)^2\ln\rho)\right] - p_w(\rho) \quad \text{(B.10)}$$

APPENDIX C: DECOMPOSITION IN THE WALPOLE BASE

We introduce the Walpole base (Walpole, 1981) notations for fourth-order tensors with symmetry of transverse isotropic type. This base makes it possible, in particular, to carry out the double-contract product and inverting these tensor operations without great difficulty. The elements of the Walpole base are defined by

$$\begin{aligned}
\mathbb{E}_1(\underline{\xi}) &= \frac{1}{2} k^{\perp} \otimes k^{\perp} \\
\mathbb{E}_2(\underline{\xi}) &= k \otimes k \\
\mathbb{E}_3(\underline{\xi}) &= k^{\perp} \bar{\otimes} k^{\perp} - \mathbb{E}_1 \\
\mathbb{E}_4(\underline{\xi}) &= k^{\perp} \bar{\otimes} k + k \bar{\otimes} k^{\perp} \\
\mathbb{E}_5(\underline{\xi}) &= k \otimes k^{\perp} \\
\mathbb{E}_6(\underline{\xi}) &= k^{\perp} \otimes k
\end{aligned} \tag{C.1}$$

where $k = \frac{1}{\left|\underline{\xi}\right|^2} \underline{\xi} \otimes \underline{\xi}$ and $k^{\perp} = \boldsymbol{I} - \boldsymbol{k}$ with the condition $\underline{\xi} \neq 0$

The product doubly contracted two elements of the base of Walpole is given in the table below

	$\mathbb{E}_1(\underline{\xi})$	$\mathbb{E}_2(\underline{\xi})$	$\mathbb{E}_3(\underline{\xi})$	$\mathbb{E}_4(\underline{\xi})$	$\mathbb{E}_5(\underline{\xi})$	$\mathbb{E}_6(\underline{\xi})$
$\mathbb{E}_1(\underline{\xi})$	$\mathbb{E}_1(\underline{\xi})$	0	0	0	0	$\mathbb{E}_6(\underline{\xi})$
$\mathbb{E}_2(\underline{\xi})$	0	$\mathbb{E}_1(\underline{\xi})$	0	0	$\mathbb{E}_5(\underline{\xi})$	0
$\mathbb{E}_3(\underline{\xi})$	0	0	$\mathbb{E}_3(\underline{\xi})$	0	0	0
$\mathbb{E}_4(\underline{\xi})$	0	0	0	$\mathbb{E}_4(\underline{\xi})$	0	0
$\mathbb{E}_5(\underline{\xi})$	0	$\mathbb{E}_5(\underline{\xi})$	0	0	0	$2\,\mathbb{E}_2(\underline{\xi})$
$\mathbb{E}_6(\underline{\xi})$	$\mathbb{E}_6(\underline{\xi})$	0	0	0	$2\,\mathbb{E}_1(\underline{\xi})$	0

Any fourth-order isotropic transverse tensor can be represented in the base of Walpole:

$$\mathbb{A} = a_1 \mathbb{E}_1(\underline{\xi}) + a_2 \mathbb{E}_2(\underline{\xi}) + a_3 \mathbb{E}_3(\underline{\xi}) + a_4 \mathbb{E}_4(\underline{\xi}) + a_5 \mathbb{E}_5(\underline{\xi}) + a_6 \mathbb{E}_6(\underline{\xi}) \tag{C.2}$$

$\mathbb{A}$ is symmetric if $a_5 = a_6$. Consider a second tensor of fourth order, $\mathbb{B}$and note by *b1, .., b6* its components in the base of Walpole. The doubly contracted product of $\mathbb{A}$ by $\mathbb{B}$is:

$$\begin{aligned}\mathbb{A}:\mathbb{B} &= (a_1b_1+2a_6b_5)\mathbb{E}_1(\underline{\xi})+(a_2b_2+2a_5b_6)\mathbb{E}_2(\underline{\xi})+a_3b_3\mathbb{E}_3(\underline{\xi})\\ &+a_4b_4\mathbb{E}_4(\underline{\xi})+(a_2b_5+a_5b_1)\mathbb{E}_5(\underline{\xi})+(a_1b_6+a_6b_2)\mathbb{E}_6(\underline{\xi})\end{aligned} \tag{C.3}$$

The inverse of $\mathbb{A}$ is

$$\mathbb{A}^{-1}=\frac{a_2}{\Delta}\mathbb{E}_1(\underline{\xi})+\frac{a_1}{\Delta}\mathbb{E}_2(\underline{\xi})+\frac{1}{a_3}\mathbb{E}_3(\underline{\xi})+\frac{1}{a_4}\mathbb{E}_4(\underline{\xi})-\frac{a_5}{\Delta}\mathbb{E}_5(\underline{\xi})-\frac{a_6}{\Delta}\mathbb{E}_6(\underline{\xi}) \tag{C.4}$$

with $\Delta=a_1a_2-2a_5a_6$. This relation induces dynamically conditions of invertibility of the considered tensor.

The decomposition on $\mathbb{E}_n(\underline{\xi})$ of the identity of fourth order, $\mathbb{I}$, and isotropic tensors $\mathbb{K}=\mathbb{I}-\mathbb{J}$ and $\mathbb{J}=\frac{1}{3}i\otimes i$ are written

$$\begin{aligned}\mathbb{I} &= \mathbb{E}_1(\underline{\xi})+\mathbb{E}_2(\underline{\xi})+\mathbb{E}_3(\underline{\xi})+\mathbb{E}_4(\underline{\xi})\\ \mathbb{K} &= \frac{1}{3}\left(\mathbb{E}_1(\underline{\xi})+2\mathbb{E}_2(\underline{\xi})\right)+\mathbb{E}_3(\underline{\xi})+\mathbb{E}_4(\underline{\xi})-\frac{1}{3}\left(\mathbb{E}_5(\underline{\xi})+2\mathbb{E}_6(\underline{\xi})\right)\\ \mathbb{J} &= \frac{1}{3}\left(2\mathbb{E}_1(\underline{\xi})+\mathbb{E}_2(\underline{\xi})\right)+\frac{1}{3}\left(\mathbb{E}_5(\underline{\xi})+\mathbb{E}_6(\underline{\xi})\right)\end{aligned} \tag{C.5}$$

Green tensor $\Gamma^0(\underline{\xi})$ and $\Delta^0(\underline{\xi})$ are given by

$$\begin{aligned}\Gamma^0(\underline{\xi}) &= \frac{1}{\lambda_0+2\mu_0}\mathbb{E}_2(\underline{\xi})+\frac{1}{2\mu_0}\mathbb{E}_4(\underline{\xi})\\ \Delta^0(\underline{\xi}) &= \frac{2\mu_0(3\lambda_0+2\mu_0)}{\lambda_0+2\mu_0}\mathbb{E}_1(\underline{\xi})+2\mu_0\mathbb{E}_3(\underline{\xi})\end{aligned} \tag{C.6}$$

For tensor, $\mathbb{C}^0=3\lambda_0\mathbb{J}+2\mu_0\mathbb{I}$ (and $\mathbb{S}^0=\left(\mathbb{C}^0\right)^{-1}$), we have

$$\begin{aligned}\Gamma^0(\underline{\xi}):\mathbb{C}^0 &= \mathbb{P}(\underline{\xi})+\frac{\lambda_0}{\lambda_0+2\mu_0}\mathbb{E}_5(\underline{\xi})\\ \Delta^0(\underline{\xi}):\mathbb{S}^0 &= \mathbb{Q}(\underline{\xi})-\frac{\lambda_0}{\lambda_0+2\mu_0}\mathbb{E}_6(\underline{\xi})\end{aligned} \tag{C.7}$$

we have

$$\begin{aligned}\mathbb{I}-\Gamma^0:\mathbb{C}^0 &= \mathbb{Q}(\underline{\xi})-\frac{\lambda_0}{\lambda_0+2\mu_0}\mathbb{E}_5\\ \mathbb{I}-\Delta^0:\mathbb{S}^0 &= \mathbb{P}(\underline{\xi})+\frac{\lambda_0}{\lambda_0+2\mu_0}\mathbb{E}_6\end{aligned} \tag{C.8}$$

For all $a(\underline{\xi})$ satisfying the property $\underline{\xi} \neq 0 : \mathbb{Q}(\underline{\xi}) : a(\underline{\xi}) = 0$, we have $\forall \underline{\xi} : \mathbb{E}_n(\underline{\xi}) : a(\underline{\xi}) = 0$ for n=1,3,5. Therefore:

$$\forall \underline{\xi} \neq 0 : \Gamma^0(\underline{\xi}) : \mathbb{C}^0 : a(\underline{\xi}) = a(\underline{\xi}) \tag{C.9}$$

For all $a(\underline{\xi})$ satisfying the property $\underline{\xi} \neq 0 : \mathbb{Q}(\underline{\xi}) : a(\underline{\xi}) = 0$, we have $\forall \underline{\xi} : \mathbb{E}_n(\underline{\xi}) : a(\underline{\xi}) = 0$ for n=2,4,6. Therefore:

$$\forall \underline{\xi} \neq 0 : \Delta^0(\underline{\xi}) : \mathbb{S}^0 : a(\underline{\xi}) = a(\underline{\xi}) \tag{C.10}$$

APPENDIX D: MANUAL'S USER AND SOME EXAMPLES OF THE DEVELOPED CODE

In this appendix, we present the manual of the developed code as well as some examples of using it for example Mandel's problem in transversely isotropic porous media.

D-1 Manual

a) Overall parameters

To carry out all above items, a parameter file, *.prm, is provided; the structure of *.prm is divided into four main sections: `MESH SECTION, MATERIAL SECTION, INITIAL CONDITION AND BOUNDARY CONDITIONS` and `SOLVE SECTION.`

The purpose of this file is control all overall input data of simulation. Details of parameter data will be separately in detailed files

```
subsection MESH SECTION
  set geometry file                 =*.inp
  set geometry file in next stage   =*.inp
  set crack file                    = N/A
  set number global refinement      =?
  set number local refinement       =?
end

subsection MATERIAL SECTION
  set material file                 = *.txt
  set fluid viscosity               = ?
end

subsection INITIAL CONDITION AND BOUNDARY CONDITIONS
  set initial pressure              = ?
  set initial mechanics             = ?
  set boundary file                 = *.txt
end

subsection SOLVE SECTION
  set calculation type              = ?
  set time step parameter file      = *.txt
  set running stage                 = ?
end
```

Fig. D-1: Structure of input parameter file

The versatile software can be run from linux (Ubuntu) environment by command line:

```
./software_version parameter_file.prm
```

b) Detailed data of input parameters

(1) The detail of geometry (mesh) information is provided in `*.inp` file `triangulation.inp` for example. If we have stage calculation (for construction stage), the file of `geometry file in next stage` is provided.

The geometry file can be obtained from other softwares such as ABAQUS software or from the output, `write_ucd()`, of DEAL.II libarary or from manual implementation.

Structure of *.inp file

```
Number_of_nodes Number_of_cells_and_line 0 0 0
// provide all nodes in structure:
Node_id x y z     //Node_id is started from 0
x x x x
//provide all cells in structure
No. Cell_material_id Cell_type Node_id … //No. is started from 0
x x quad x x x x
//provide all lines of boundaries in structure
No. Boundary_id Node_id Node_id
x x line x x
```

(2) All kinds of materials are in `*.txt` file, for example in `material.txt` file.

Structure of `*.txt` file for all materials is formed

```
Number_of_materials
Material_id       Material_type
1     IO_M        E     ν
2     IO_H        K
3     IO_HM       E     ν     M     b     K
4     IT_M_Y      Exx   Eyy   νxz   νyx   Gxy
5     IT_H        Kxx   Kyy
6     IT_HM_Y     Exx   Eyy   νxz   νyx   Gxy   M     bxx   byy   Kxx   Kyy
7     Crack poi   kn    kt    b     w_aperture
```

(3) The initial condition can be set as default (no initial condition for mechanics and pressure, all are zero) if we `set initial pressure = 0` and `set initial mechanics  = N/A`.

We can calculate the initial condition by inputting value of initial pressure, inputting boundary conditions of mechanical behaviour in file `boundary.txt` and `set running stage = 0`.

We can read initial condition from the previous stage by

```
set initial pressure              = previous_stage
set initial mechanics             = previous_stage
```

(4) All boundary conditions are in `boundary.txt` file

Boundary conditions are provided in `*.txt` file with below form

```
Number_of_boundaries
Boundary_id Boundary_type
      M     dis_xx dis_yy normal_stress tangentiel_stress
      H     pressure flux
      HM    dis_xx dis_yy normal_stress tangentiel_stress pressure flux
```

The definition of positive vector for each boundary is related to axis direction in Fig 2-4

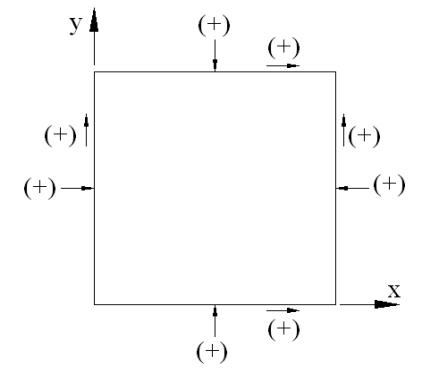

Fig. D-2: Definition of positive value of normal stress, tangential stress, flux

(5) For specified purpose, we can calculate separately mechanical only, hydraulic only in steady state or transient, one way hydro mechanical coupling, and hydro mechanical coupling in steady state or transient by

```
set calculation type          = HM_transient
                              #H_steady          #H_transient      #M
                              #HM_steady         #H1M_steady
                              #HM_transient      #H1M_transient
```

All time steps of calculation are provided in `*.txt` file with below form

```
Number_of_timestep_type
Timestep_id Staring_time Ending_time Time_step
```

c) Fractures assembled

The geometry of fractures is indicated one text file, cracks.txt for example, in which the structure of text file is below:

```
number_of_fractures
fracture_id fracture_type x_center y_center a_length b_length angle
…
```

For example in below file:

```
2
1 rec 2.40 2.93 1.22 0.15 45.89   #rec denotes for rectangular fracture
2 rec 6.63 2.39 1.42 0.05 26.11
```

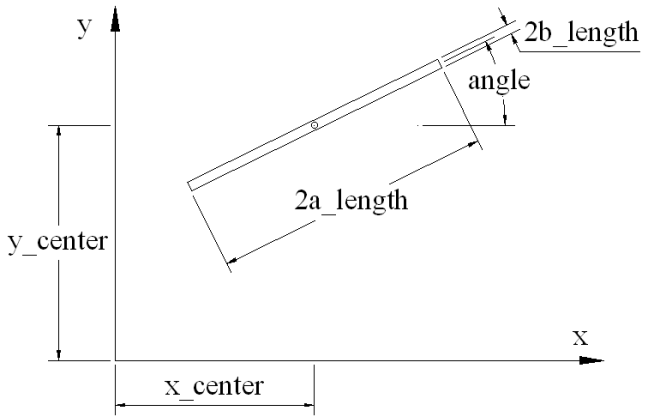

Fig. D-3: Sketch of inputted fracture.

D-2 Example of Mandel's problem (item 2.5.1)

The command line of running code is: `./HyMe_Fr_v1 parameter_2d.prm` in which the parameter file is below

```
subsection MESH SECTION
  set geometry file                 =meshes/triangulation.inp
  set geometry file in next stage   =N/A
  set number global refinement      = 4
  end

subsection MATERIAL SECTION
  set material file                 = meshes/material.txt
  set fluid viscosity               = 1.0e-9 #(MPa.s)
end

subsection INITIAL CONDITION AND BOUNDARY CONDITIONS
  set initial pressure              = 0
  set initial mechanics             = N/A
  set boundary file                 = meshes/boundary.txt
end

subsection SOLVE SECTION
  set calculation type              = HM_transient
  set time step parameter file      = meshes/time_step_parameter.txt
  set running stage                 = 1
end

subsection OTHER PARAMETERS
  set iterative accuracy            = 0.001
  set max no iterative steps        = 1000
end
```

Content of `meshes/triangulation.inp` file

```
4 5 0 0 0
1 0 0 0
2 0.1 0 0
3 0 0.1 0
4 0.1 0.1 0
1 1 quad 1 2 4 3
2 1 line 1 3
3 2 line 2 4
4 3 line 1 2
5 4 line 4 3
```

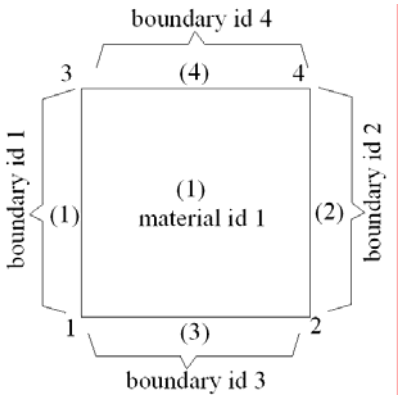

Content of `meshes/material.txt` file

```
1
1 IT_HM_Y 20600 17300 0.189 0.246 7320 15800 0.733 0.749 1E-19 2E-20
```

Boundary conditions are `meshes/boundary.txt` file with below form

```
4
1 HM N/A N/A N/A N/A N/A N/A
2 HM N/A N/A N/A N/A N/A N/A
3 HM N/A 0   N/A N/A N/A N/A
4 HM N/A N/A 10  N/A N/A N/A
```

All time steps of calculation are provided in `meshes/time_step_parameter.txt` file

```
1
0 0 1000 10
```

D-3 Example of Excavation problem (item 2.5.2)

Two stages were carried out in this test. The first one is setup the initial condition (initial pore pressure = 4.7 MPa, and total initial stress = 12.5 MPa); and the second one is excavation process.

D-3-1. Establish the initial condition

```
subsection MESH SECTION
  set geometry file                  = meshes/triangulation.inp
  set geometry file in next stage    = meshes/triangulation_with_tunnel.inp
  set crack file                     = N/A
  set number global refinement       = 2
  set number local refinement        = 0
  end

subsection MATERIAL SECTION
  set material file                  = meshes/material.txt
  set fluid viscosity                = 1.0e-9 #(MPa.s)
end

subsection INITIAL CONDITION AND BOUNDARY CONDITIONS
  set initial pressure               = 4.7  # (MPa)
  set initial mechanics              = N/A
  set boundary file                  = meshes/boundary.txt
end

subsection SOLVE SECTION
  set calculation type               = HM_steady
  set time step parameter file       = meshes/time_step_parameter.txt
  set running stage                  = 0
end

subsection OTHER PARAMETERS
  set iterative accuracy             = 0.001
  set max no iterative steps         = 1000
end
```

Content of `meshes/triangulation.inp` and `meshes/triangulation_with_tunnel.inp` files

`meshes/triangulation.inp`

```
39 28 0 0 0
1     8     0     0
2     8     8     0
3     0     8     0
4     2     0     0
5     1.414214    1.414214    0
6     0     2     0
7     24    0     0
8     24    24    0
9     0     24    0
10    8     4     0
11    4     8     0
```

`meshes/triangulation_with_tunnel.inp`

```
30 20 0 0 0
1     8     0     0
2     8     8     0
3     0     8     0
4     2     0     0
5     1.414214    1.414214    0
6     0     2     0
7     24    0     0
8     24    24    0
9     0     24    0
10    8     4     0
11    4     8     0
```

```
12    5     0     0
13    4.7071      4.7071      0
14    1.84776     0.765366    0
15    0     5     0
16    0.765366    1.84776     0
17    16    0     0
18    16    16    0
19    24    12    0
20    0     16    0
21    12    24    0
22    4.87114     2.36084     0
23    2.36084     4.87114     0
24    16    8     0
25    8     16    0
26    1     0     0
27    0.92388     0.382684    0
28    0.707106    0.707106    0
29    0.382684    0.92388     0
30    0     1     0
31    0     0     0
32    0.3   0     0
33    0     0.3   0
34    0.3   0.3   0
35    0.6   0     0
36    0.6   0.3   0
37    0     0.6   0
38    0.3   0.6   0
39    0.6   0.6   0
1 1 quad 22 13 5 14
2 1 quad 12 22 14 4
3 1 quad 10 2 13 22
4 1 quad 1 10 22 12
5 1 quad 23 15 6 16
6 1 quad 13 23 16 5
7 1 quad 11 3 15 23
8 1 quad 2 11 23 13
9 1 quad 24 19 8 18
10 1 quad 10 24 18 2
11 1 quad 17 7 19 24
12 1 quad 1 17 24 10
13 1 quad 25 21 9 20
14 1 quad 11 25 20 3
15 1 quad 18 8 21 25
16 1 quad 2 18 25 11
17 1 quad 26 4 14 27
18 1 quad 27 14 5 28
19 1 quad 28 5 16 29
20 1 quad 29 16 6 30
21 1 quad 32 34 33 31
22 1 quad 35 36 34 32
23 1 quad 34 38 37 33
24 1 quad 36 39 38 34
25 1 quad 26 27 36 35
26 1 quad 27 28 39 36
27 1 quad 28 29 38 39
28 1 quad 29 30 37 38
2 1 line 1 3
3 2 line 2 4
4 3 line 1 2
5 4 line 4 3
```


```
12    5     0     0
13    4.7071      4.7071      0
14    1.84776     0.765366    0
15    0     5     0
16    0.765366    1.84776     0
17    16    0     0
18    16    16    0
19    24    12    0
20    0     16    0
21    12    24    0
22    4.87114     2.36084     0
23    2.36084     4.87114     0
24    16    8     0
25    8     16    0
26    1     0     0
27    0.92388     0.382684    0
28    0.707106    0.707106    0
29    0.382684    0.92388     0
30    0     1     0
1 1 quad 22 13 5 14
2 1 quad 12 22 14 4
3 1 quad 10 2 13 22
4 1 quad 1 10 22 12
5 1 quad 23 15 6 16
6 1 quad 13 23 16 5
7 1 quad 11 3 15 23
8 1 quad 2 11 23 13
9 1 quad 24 19 8 18
10 1 quad 10 24 18 2
11 1 quad 17 7 19 24
12 1 quad 1 17 24 10
13 1 quad 25 21 9 20
14 1 quad 11 25 20 3
15 1 quad 18 8 21 25
16 1 quad 2 18 25 11
17 1 quad 26 4 14 27
18 1 quad 27 14 5 28
19 1 quad 28 5 16 29
20 1 quad 29 16 6 30
```

Content of `meshes/material.txt` file

```
1
0 IO_HM 4000 0.3 6000 1 1.333E-20
```

Boundary conditions are `meshes/boundary.txt` file with below form

```
4
1 HM 0 N/A N/A N/A N/A N/A
2 HM N/A N/A 12.5 N/A N/A N/A
3 HM N/A 0 N/A N/A N/A N/A
4 HM N/A N/A 12.5 N/A N/A N/A
```

All time steps of calculation are provided in `meshes/time_step_parameter.txt` file

```
1
0 0 1 1
```

The result of this stage is two text file which contained the information of the initial stage (Figure 2-11 and Figure 2-12)

D-3-2. Excavation stage

Note that we highlighted yellow color for the items which are changed in campared with the initial condition for easy reading.

```
subsection MESH SECTION
  set geometry file                  = meshes/triangulation_with_tunnel.inp
  set geometry file in next stage    = N/A
  set crack file                     = N/A
  set number global refinement       = 2
  set number local refinement        = 0
  end

subsection MATERIAL SECTION
  set material file                  = meshes/material.txt
  set fluid viscosity                = 1.0e-9 #(MPa.s)
end

subsection INITIAL CONDITION AND BOUNDARY CONDITIONS
  set initial pressure               = previous_stage
  set initial mechanics              = previous_stage
  set boundary file                  = meshes/boundary.txt
end

subsection SOLVE SECTION
  set calculation type               = HM_steady
  set time step parameter file       = meshes/time_step_parameter.txt
  set running stage                  = 1
end

subsection OTHER PARAMETERS
  set iterative accuracy             = 0.001
  set max no iterative steps         = 1000
end
```

Boundary conditions are `meshes/boundary.txt` file with below form

```
5
1 HM 0 N/A N/A N/A N/A N/A
2 HM N/A N/A 12.5 N/A 4.7 N/A
3 HM N/A 0 N/A N/A N/A N/A
4 HM N/A N/A 12.5 N/A 4.7 N/A
5 HM N/A N/A N/A N/A 0 N/A       #0: drained case and 4.7: undrained case
```

D-4 Example of effective properties (item 4.5.3)

Note that we highlighted yellow color for the items which are new in compared with the previous examples for easy reading.

```
subsection MESH SECTION
  set geometry file                 = meshes/triangulation.inp
  set geometry file in next stage   = N/A
  set crack file                    = meshes/cracks.txt
  set number global refinement      = 4
  set number local refinement       = 5
end

subsection MATERIAL SECTION
  set material file                 = meshes/material_fracture.txt
  set fluid viscosity               = 1.0e-6 #(kPa.s)
end

subsection INITIAL CONDITION AND BOUNDARY CONDITIONS
  set initial pressure              = 0  # (kPa)
  set initial mechanics             = N/A
  set boundary file                 = meshes/boundary.txt
end

subsection SOLVE SECTION
  set calculation type              = M   # or H
  set time step parameter file      = meshes/time_step_parameter.txt
  set running stage                 = 1
end

subsection OTHER PARAMETERS
  set iterative accuracy            = 0.001
  set max no iterative steps        = 1000
end
```

Content of `meshes/triangulation.inp` file

```
4 5 0 0 0
1 -1 -1 0
2 1 -1 0
3 -1 1 0
4 1 1 0
1 1 quad 1 2 4 3
2 1 line 1 3
3 2 line 2 4
4 3 line 1 2
5 4 line 4 3
```

Content of `meshes/cracks.txt` file

```
73
0 rec 0 0 1 0.000065 70
1 rec 0.4 0.2 1 0.000065 120
2 rec 0.4 -0.2 1 0.000065 60
3 rec 0 0 1 0.000065 80
37 rec 0.6 0.8 0.35 0.000065 110
38 rec -0.6 0 0.35 0.000065 0
39 rec -0.2 -0.8 0.35 0.000065 60
40 rec 0.8 0.4 0.35 0.000065 170
```

```
4 rec -0.2 0.6 0.9 0.000065 0
5 rec -0.2 0.2 0.85 0.000065 160
6 rec 0 -0.2 0.8 0.000065 100
7 rec -0.4 0.4 0.75 0.000065 50
8 rec 0 -0.4 0.7 0.000065 20
9 rec -0.4 -0.8 0.65 0.000065 0
10 rec 0.6 0.2 0.65 0.000065 130
11 rec -0.6 -0.6 0.6 0.000065 130
12 rec -0.2 0.4 0.6 0.000065 110
13 rec 0.4 0.6 0.55 0.000065 30
14 rec -0.6 0.2 0.55 0.000065 40
15 rec 0.6 0.4 0.55 0.000065 140
16 rec 0.6 0.6 0.5 0.000065 30
17 rec 0.8 0 0.5 0.000065 70
18 rec -0.6 0.6 0.5 0.000065 40
19 rec -0.6 -0.2 0.5 0.000065 130
20 rec 0 0.4 0.45 0.000065 50
21 rec 0.8 -0.4 0.45 0.000065 90
22 rec 0.6 -0.2 0.45 0.000065 130
23 rec -0.2 -0.4 0.45 0.000065 90
24 rec -0.2 -0.6 0.45 0.000065 130
25 rec 0.2 0.4 0.45 0.000065 130
26 rec -0.4 0.2 0.4 0.000065 160
27 rec 0 0.8 0.4 0.000065 10
28 rec -0.2 -0.2 0.4 0.000065 150
29 rec -0.8 0.8 0.4 0.000065 70
30 rec -0.6 -0.8 0.4 0.000065 160
31 rec 0.8 -0.6 0.4 0.000065 110
32 rec 0 0.6 0.4 0.000065 170
33 rec -0.4 -0.2 0.4 0.000065 170
34 rec -0.8 -0.8 0.4 0.000065 20
35 rec 0.8 0.8 0.35 0.000065 120
36 rec -0.8 -0.6 0.35 0.000065 60
```

```
41 rec 0.2 0.2 0.325 0.000065 10
42 rec -0.8 -0.2 0.325 0.000065 50
43 rec 0.2 -0.4 0.325 0.000065 100
44 rec 0.6 0 0.325 0.000065 0
45 rec 0 0.2 0.325 0.000065 140
46 rec 0.2 -0.6 0.325 0.000065 0
47 rec 0.6 -0.8 0.325 0.000065 100
48 rec -0.8 0.4 0.325 0.000065 140
49 rec 0 -0.8 0.3 0.000065 110
50 rec -0.4 -0.4 0.3 0.000065 150
51 rec 0.8 -0.8 0.3 0.000065 120
52 rec -0.4 0.6 0.3 0.000065 100
53 rec -0.8 -0.4 0.3 0.000065 160
54 rec 0.4 -0.4 0.3 0.000065 110
55 rec 0.4 -0.6 0.3 0.000065 110
56 rec 0.4 0.8 0.3 0.000065 170
57 rec -0.6 0.8 0.3 0.000065 100
58 rec -0.8 0.6 0.3 0.000065 40
59 rec 0.4 -0.8 0.275 0.000065 40
60 rec 0.6 -0.4 0.275 0.000065 10
61 rec -0.8 0 0.275 0.000065 160
62 rec 0.4 0 0.275 0.000065 120
63 rec 0.8 0.2 0.275 0.000065 170
64 rec 0.4 0.4 0.275 0.000065 120
65 rec -0.4 -0.6 0.275 0.000065 120
66 rec -0.6 0.4 0.275 0.000065 0
67 rec 0 -0.6 0.275 0.000065 10
68 rec 0.2 0 0.275 0.000065 80
69 rec 0.8 0.4 0.275 0.000065 0
70 rec -0.6 -0.4 0.275 0.000065 10
71 rec 0.2 0.6 0.275 0.000065 170
72 rec 0.2 0.8 0.275 0.000065 170
```

Content of `meshes/material.txt` file

```
2
0 IO_HM 84600000 0.24 20400000 0.8 2.4E-15
1 Crack poi 434000000 86800000 1 0.000065
```

Boundary conditions are `meshes/boundary.txt` file with below form

```
4
1 HM N/A N/A N/A N/A N/A N/A
2 HM N/A N/A N/A N/A N/A N/A
3 HM N/A 0 N/A N/A N/A N/A
4 HM N/A N/A 1000 N/A N/A N/A
```

All time steps of calculation are provided in `meshes/time_step_parameter.txt` file

```
1
0 0 1 1
```

Hong Lam DANG

MODÉLISATION DU COMPORTEMENT HYDROMÉCANIQUE DES RÉSERVOIRS FRACTURÉS À DOUBLE POROSITÉ ET DOUBLE PERMEABILITÉ

Résumé:

La modélisation des massifs rocheux fracturés est un problèmes important dans de nombreux secteurs industriels, y compris, mais sans s'y limiter à l'exploitation pétrolière et gazière. Dans la littérature, les roches fracturées sont reconnues comme des milieux à double porosité et double perméabilité dans lesquels le réseau de fractures fournit la perméabilité primaire et la matrice rocheuse la perméabilité sécondaire. L'idée de la dissociation de l'écoulement à l'intérieur du réseau de fractures et de la matrice, la double perméabilité, est toujours contestée pour les réservoirs fracturés. De nombreuses contributions sur cette question ont été présentées dans la littérature et les méthodes utilisées pourraient être classées dans deux approches principales : approches continues et discontinues. Chaque approche a ses avantages et ses limites. Pour surmonter les limites en gardant les avantages de ces deux approches, une approche nommée Embedded Fracture Continumm Approach (EFCA) qui emprunte le concept du modèle continu et intègre également l'effet des fractures explicites est considérée dans cette thèse. L'idée principale de cette approche repose sur le concept de la « cellule fracturée » représentant un milieu poreux qui a ses propres propriétés calculées à partir des propriétés de la matrice poreuse et des fractures qui la traversent. Le code de calcul développé dans le cadre de ce travail est basé sur la bibliothèque source DEAL.II. L'exactitude de l'EFCA a été étudiée à travers de différents tests. Plusieurs applications traitées dans ce travail comme la détermination des propriétés hydro-mécaniques effectives d'un site réel, estimation de la production de puits dans laquelle les fractures sont modélisées explicitement, démontrent la performance de l'EFCA dans la modélisation des roches fracturées ainsi que l'effet de la double porosité et de la double perméabilité aux comportements des réservoirs fracturés.

Mots-clés: réservoirs fracturés, réseau de fractures, modélisation hydromécanique, double porosité, double perméabilité, cellule de fracture, approche du continuum fracturé intégré, méthode des éléments finis, DEAL.II, nœud suspendu.

A HYDRO MECHANICAL MODELING OF DOUBLE POROSITY AND DOUBLE PERMEABILITY FRACTURED RESERVOIRS

Summary:

Fractured rock masses modeling is a challenge issue in many field of industry including but not limited to oil and gas exploitation. In the literature, fractured rock masse are in many cases recognized as double permeability medium in which fracture network provides the primary permeability and rock matrix plays as the second one. The idea of dissociation of flow inside the fracture network and the matrix, the double permeability, is still challenged for fractured reservoirs. Numerous contributions on this issue have been presented in the past could be cast in two main approaches: continuum media approach and discontinuous approach. Each approach has its advantages and limitations. To overcome the limitation and to take advantage of these two approaches, the Embedded Fractured Continuum Approach (EFCA) which borrows the concept of continuum models and also incorporates the effect of explicit fractures is considered in this thesis. The principal idea of this approach lies on the concept of fracture cell representing a porous medium that has their own properties calculated from the properties of porous matrix and fractures intersecting it. The development in this work was conducted by using the library source code DEAL.II. The accuracy of EFCA was investigated through different verifications. Through some applications: determination of effective hydro-mechanical properties of an actual site, estimation of well production in which necessary fractures are modeled explicitly, we demonstrate the performance of the EFCA in the modeling fractured rock masses as well as the effect of double porosity and double permeability on behaviours of fractured reservoirs.

Keywords: fractured reservoirs, fracture network, hydro-mechanical modeling, double porosity, double permeability, fracture cell, embedded fractured continuum approach, finite element method, DEAL.II, hanging node.

Laboratoire PRISME
08 rue Leonard de Vinci, 45072 Orléans Cedex 2